

MSU
3
2010



This is to certify that the
dissertation entitled

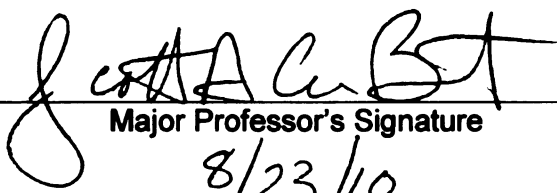
**HOLISTIC ELECTROCHEMICAL AND MECHANICAL
MODELING OF CORROSION-INDUCED CRACKING IN
CONCRETE STRUCTURES**

presented by

GOLI NOSSONI

has been accepted towards fulfillment
of the requirements for the

Doctoral degree in Civil Engineering


Major Professor's Signature
8/23/10
Date

PLACE IN RETURN BOX to remove this checkout from your record.
TO AVOID FINES return on or before date due.
MAY BE RECALLED with earlier due date if requested.

DATE DUE	DATE DUE	DATE DUE

**HOLISTIC ELECTROCHEMICAL AND MECHANICAL MODELING OF
CORROSION-INDUCED CRACKING IN CONCRETE STRUCTURES**

By

Goli Nossoni

A DISSERTATION

Submitted to
Michigan State University
in partial fulfillment of the requirements
for the degree of

DOCTOR OF PHILOSOPHY

Civil Engineering

2010

ABSTRACT

Holistic Electrochemical and Mechanical Modeling of Corrosion-Induced Cracking in Concrete Structures

By

Goli Nossoni

Corrosion of reinforcing bars (“rebars”) in concrete is the most destructive mechanism contributing to damage in concrete bridges in the U.S. Corrosion products that are formed are two to six times more voluminous than the corroding steel and the resulting expansion causes the concrete to crack and eventually spall thereby accelerating structural deterioration. The alkaline environment provided within concrete protects steel rebars from corrosion due to the passive layer that is formed on their surface. However, chloride ions from deicing salts or from a marine environment that diffuse to the surface of rebars destroy the passive layer and initiate corrosion. While considerable research has been devoted to predicting the time to corrosion initiation, studies on predicting the time to cracking of the concrete cover from the time of corrosion initiation have been far fewer. Much of the treatment has been empirical or based on a constant corrosion current.

This dissertation develops a holistic model of the electrochemistry of corrosion that accounts for the diffusion of oxygen, moisture and chloride through the concrete and rust layers, the densification of rust due to confinement, the diffusion of rust into the concrete pores, the development of internal pressure due to rust build-up, and cracking of the concrete cover. Experimentally measured anodic polarization curves for the corrosion of mild steel in alkaline media at varying chloride concentrations, the limiting cathodic

reaction, and models of the diffusion of oxygen and chloride through the concrete and rust layers, were used to determine the corrosion current in both the anodic and cathodic controlled regions. The boundary conditions, concrete quality, and cover thickness were included in the diffusion calculations. The relationship between the corrosion current and the pressure build-up due to the corrosion products for different concrete cover thicknesses and concrete quality was established through experiments using an accelerated corrosion test with an impressed current. Experiments were conducted to determine the conditions under which Faraday's Law could be used to accurately estimate the steel mass loss due to corrosion in the accelerated corrosion test. Results from the accelerated corrosion experiments were used to calibrate a model relating the rust build-up to the internal pressure generated on the concrete cover, allowing for the densification of rust due to confinement and the diffusion of rust into the concrete pores. Results from finite element analysis with an inelastic smeared crack concrete model were used to calibrate a simple analytical model of the critical internal pressure required to cause cracking of the concrete cover. The various sub-models were then linked together to predict the time for cracking of the concrete cover from the time of corrosion initiation.

Results from the model compare reasonably well with data reported in the literature from laboratory and field observations, as well as other models, although the variation in the data is considerable. The developed model was used to study the time for cracking of the concrete cover for different boundary conditions, concrete quality, and cover thicknesses. The model indicates that the time for corrosion initiation and the time from corrosion initiation to cracking of the concrete cover are comparable for certain boundary conditions and concrete quality.

DEDICATION

In childhood we strove to go to school
Our turn to teach, joyous as a rule
The end of the story is sad and cruel
From dust we came, and gone with winds cool

(Khayyam, Persian Poet, 1048-1131)

Those who have gone forth,
have fallen upon the dust of pride

To the soul of my grandfather, *Aga Joon*
and the soul of my grandmother, *Maman Bozorg*

ACKNOWLEDGMENT

*"In the Name of Allah, the Compassionate, the Merciful
Laudation is due the most High, the most Glorious.
Whose worship bridges the Gap and whose recognition breeds beneficence.
Each breath inhaled sustains life, exhaled imparts rejuvenation.
Two blessings in every breath, each due a separate salutation."
(Saadi, Persian Poet, 1184-1283)*

After God, I would like to express my deep appreciation to my advisors Prof. Harichandran and Prof. Barton for the encouragement, guidance, patience, and support they provided me throughout my PhD studies. Also, special thanks to the distinguished faculty members who served on my committee: Professors Burgueño, Soroushian, and Kutay for their support and useful suggestions.

Warm thanks to my family, especially my mother and my brother, Farid Nossoni, for their love, support, and patience throughout my life.

Sincere thanks to all of my friends who I shared my journey at MSU with. I would particularly like to thank Monther Dwaikat, Deepa Thandaveswara, Aradhana Sharma and Mahmoodul Haq, who provided friendship and support in good and down times; I am so grateful that they came along in my life and helped me to grow. I owe them a lot and they always will be a part of my life.

Thanks to the faculty and personnel in the CEE department for their support and help, especially Mr. Siavosh Ravanbakhsh.

Thanks to Professor Burgueño for suggesting the use of an FRP overlay for concrete repair, and to the Michigan Department of Transportation and the CEE department for their financial support.

TABLE OF CONTENTS

List of Tables	x
List of Figures	xi
Chapter 1 Introduction.....	1
1.1 Background.....	1
1.2 Problem Statement.....	3
1.3 Research Objectives.....	4
1.4 Layout of the Dissertation.....	5
Chapter 2 Literature Review	8
2.1 Introduction.....	8
2.2 Corrosion Mechanism.....	9
2.2.1 Corrosion Reaction	10
2.2.2 Pourbaix Diagram	12
2.2.3 Polarization	13
2.2.4 Passive Film and Depassivation.....	14
2.2.4.1 Effect of Chloride on Steel Behavior.....	16
2.2.5 Corrosion Rate Calculation with Polarization Curve.....	16
2.2.5.1 Anodic Polarization	16
2.2.5.2 Cathodic Polarization Curve.....	18
2.2.6 Growth of Rust Film	18
2.3 Corrosion of Steel in Concrete.....	19
2.3.1 Concrete Structure and Durability	21
2.3.2 Concrete Pore Solution	22
2.3.2.1 Chemical Composition.....	22
2.3.2.2 Transport Process.....	23
2.3.3 Chloride Diffusion	24
2.3.4 Basic Formulatio.....	25
2.3.5 Chloride Diffusion Coefficient	26
2.3.5.1 Effect of Aggregate.....	26
2.3.5.2 Temperature Dependence	27
2.3.5.3 Effect of Humidity	28
2.3.5.4 Effect of Chloride Concentration.....	28
2.3.6 Chloride Binding Capacity	29
2.3.7 Chloride Threshold	31
2.3.8 Oxygen Diffusion.....	31
2.4 Corrosion Rate	32
2.4.1 Corrosion Rate Models	32
2.4.1.1 Corrosion Rate in Carbonated Concrete	32
2.4.1.2 Corrosion Rate due to Chloride Diffusion	33
2.4.2 Corrosion Rate Monitoring Techniques.....	33
2.4.2.1 Half Cell Potential.....	34

2.4.2.2	Linear Polarization Technique.....	34
2.4.2.3	Gravimetric Technique (Weight Loss Method).....	36
2.4.2.4	Potentiodynamic/Static Polarization Measurement.....	37
2.5	Durability Model.....	38
2.5.1	Models for Predicting Concrete Cracking Time.....	38
2.5.1.1	Cady-Weyers's Deterioration Model.....	39
2.5.1.2	Bazant's Model for Time to Cracking.....	40
2.5.1.3	Morinaga's Model.....	41
2.5.1.4	Wang and Zhao's Model.....	42
2.5.1.5	Dagher and Kulendran's Model.....	42
2.5.1.6	Bhargava et al. Model.....	43
2.5.1.7	Maadawy and Soudki Cracking Model.....	43
2.5.2	Discussion of Existing Models.....	44
2.6	Corrosion and Repair.....	46
Chapter 3 Experimental Characterization.....		48
3.1	Introduction.....	48
3.2	Accelerated Corrosion Test.....	49
3.2.1	Accelerated Corrosion Testing Overview.....	50
3.2.1.1	Electrochemical Concepts.....	51
3.2.2	Experimental Tests.....	53
3.2.2.1	Accelerated Corrosion Test in Solution.....	53
3.2.2.2	Accelerated Corrosion Test in Concrete.....	55
3.3	Results and Discussion.....	56
3.3.1	Tests in Solution.....	56
3.3.1.1	Effect of Chloride Concentration.....	57
3.3.1.2	Effect of pH.....	58
3.3.1.3	Effect of Impressed Current Magnitude.....	59
3.3.1.4	Corrosion Mechanism.....	60
3.4	Calculation of Rust Thickness.....	63
3.4.1	Experimental Program.....	64
3.4.1.1	Specimen Preparation.....	64
3.4.1.2	Accelerated Corrosion Test and Test Set up.....	66
3.4.2	Measurement of Rust Thickness.....	68
3.5	Conclusions.....	73
Chapter 4 Electrochemical Modeling of Corrosion Rate in Concrete.....		76
4.1	Introduction.....	76
4.2	Polarization Curve.....	79
4.2.1	Experimental Anodic Polarization Curve.....	80
4.2.1.1	Test Set-Up.....	80
4.2.1.2	Three Electrode Cell.....	81
4.2.1.3	Measurement Technique.....	82
4.2.1.4	Mercury /Mercuryoxide Reference Electrode.....	83
4.2.2	Results and Discussion.....	84
4.2.2.1	Open Circuit Measurement.....	84

4.2.2.2	Potentiostatic Polarization Results.....	86
4.2.3	Model for Polarization Curve	96
4.2.4	Anodic Polarization Curve.....	96
4.2.5	Cathodic Polarization Curve.....	100
4.2.5.1	Effect of Chloride Concentration.....	101
4.2.5.2	Effect of Oxygen Concentration	102
4.2.5.3	Effect of pH.....	102
4.3	Initial Corrosion Rate.....	103
4.4	Limiting Corrosion Rate	109
4.4.1	Corrosion Scale.....	109
4.5	Corrosion Current	111
4.6	Calibration with Experimental Data	120
4.7	Results and Discussion	123
4.7.1	Effect of Boundary Condition.....	124
4.7.2	Effect of Water-Cement Ratio	127
4.7.3	Effect of Concrete Cover	128
4.7.3.1	Relationship between Corrosion Current and Rust Thickness	128
4.7.4	Comparison of Results with Literature.....	130
4.7.4.1	Experimental Data	130
4.7.4.2	Models.....	133
4.8	Summary and Conclusions	133

Chapter 5 Mechanical Modeling for Concrete Cover Cracking135

5.1	Introduction.....	135
5.2	Mechanistic Model of Concrete Cover Cracking	136
5.2.1	Development of Internal Pressure.....	137
5.2.2	Loss of Rust Thickness (δ_0)	139
5.2.3	Critical Pressure	141
5.3	Calibration and Validation with Finite Element Analysis	142
5.3.1	Finite Element Model	143
5.3.1.1	Geometry and Boundary Conditions	143
5.3.1.2	Concrete Material Model	145
5.3.1.3	Loading Condition	148
5.3.2	Finite Element Analyses	149
5.3.2.1	Strain-Pressure Relations.....	149
5.3.2.2	Critical Pressure	150
5.3.2.3	Effect of Concrete Cover vs. Bar Distance.....	151
5.4	Results and Discussion	152
5.4.1	Rust Thickness Growth.....	152
5.4.1.1	Rust Build-Up	153
5.4.1.2	Rust Diffusion into Pores.....	156
5.4.2	Stress in Concrete Cover.....	157
5.4.3	Cracking Time, t_2	158
5.4.3.1	Effect of Boundary Condition.....	159
5.4.3.2	Effect of Concrete Quality	160
5.4.3.3	Effect of Concrete Cover	161

5.4.4	Comparison of Results with the Literature	161
5.4.5	Effect of Time t_1 Compared to t_2	163
5.5	Summary and Conclusions	165
Chapter 6	Effect of Concrete Repairs on Corrosion Behavior.....	171
6.1	Introduction.....	171
6.2	Overview of Patching System.....	172
6.2.1	Traditional Patch.....	173
6.2.2	Patch and FRP Overlay	174
6.3	Experimental Test	176
6.3.1	Sample Preparation	176
6.3.1.1	Surface Preparation.....	179
6.3.1.2	Repair of the Specimens	179
6.3.2	Installing Stain Gages	180
6.3.3	Test Set-Up	181
6.3.4	Results and Discussion	182
6.3.4.1	Crack Path.....	182
6.3.4.2	Strain Gage Readings.....	184
6.3.4.3	Crack Pattern.....	184
6.3.4.4	Mass Loss.....	187
6.4	Corrosion Modeling in Repaired Concrete	189
6.4.1	Corrosion Rate	190
6.4.2	Cracking Pressure	191
6.5	Summary and Conclusions	193
Chapter 7	Summary, Conclusions, and Recommendations for Future Research..	195
7.1	Introduction.....	195
7.2	Significance of Research.....	195
7.3	Summary, Conclusions	198
7.3.1	Effect of Chloride Ions on Steel Behavior	198
7.3.2	Corrosion Current	199
7.3.3	Concrete Cracking	200
7.3.4	Effect of Repair on Corrosion Rate	201
7.3.5	Experiments on Accelerated Corrosion Test and Rust Thickness Growth	202
7.4	Recommendations for Future Research	203
APPENDIX.....	205
REFERENCES.....	211

LIST OF TABLES

Table 2-1: Ionic Concentration Measured in the Pore Solution Extracted from Cement Paste and Mortar (mmol/L).	23
Table 2-2: Activation Energy for Various Cement Pastes.....	28
Table 2-3: Guidance for Interpretation of Results from Half-Cell Surveying.....	34
Table 2-4: Guideline for Interpreting Results from the Linear Polarization Method	36
Table 3-1: Solution Properties	54
Table 3-2: Mix Proportion of Concrete	66
Table 4-1: Solution Properties (Bertolini et al. 2002).....	81
Table 4-2: Parameters used in Equation 4-2	86
Table 4-3: Parameter used on Equation 4-3 and 4-4.....	95
Table 4-4: Parameters used in Equation 4-6	99
Table 4-5: Weight and Volume of Various Corrosion Products (Bhagava et al. 2005) .	110
Table 4-6: Different Concentrations Boundary Conditions (lb/in ³)	124
Table 4-7: Geometry	124
Table 4-8: Corrosion Current Guide (Broomfield 1996).....	133
Table 5-1: Case Study on Finite Element to calibrate a factor in asymmetric situation.	154
Table 6-1: Mechanical and Fresh Properties of Concrete.....	178
Table 6-2: Mechanical and Physical Properties of the Glass FRP and Patch Material used	187
Table 6-3: Average Mass Loss for Each Group in the Corrosion Test.....	188

LIST OF FIGURES

Figure 2-1: Corrosion process on steel bar surface.....	11
Figure 2-2: Pourbiax diagram for iron (Pourbiax 1976).....	12
Figure 2-3: General polarization curve for iron (Jones; 1992)	13
Figure 2-4: Corrosion of steel in water solution as a function of OH ⁻ concentration and pH level (Shalon and Raphael 1959)	15
Figure 2-5: Effect of chloride ions on steel polarization curve (Jones 1992).....	17
Figure 2-6: Water content in pore as a function of relative humidity (Bertolini et al 2004).....	24
Figure 2-7: Diffusion of chloride in concrete	25
Figure 2-8: Predicted total, bounded and free chloride after 50 years (Glass and Buenfeld 2000).....	30
Figure 2-9: Effect of chloride and pH in liquid phase (ACI 1975).....	31
Figure 2-10: Chloride corrosion deterioration process for a concrete element with a mean cover depth of 2 in.	39
Figure 2-11: Caddy and Weyer's deterioration model	40
Figure 3-1: Comparison between real mass loss and that estimated using Faraday's Law (Nossoni and Harichandran 2007)	52
Figure 3-2: Accelerated corrosion test set-up in: (a) solution, and (b) concrete.....	54
Figure 3-3: Accelerated corrosion test results in solution with pH of (a) 13.95, (b) 13.70 and (c) 13.46.....	57
Figure 3-4: Effect of pH on the accelerated corrosion test results for different chloride concentration.....	60
Figure 3-5: Comparison between $n = 2$ and $n = 3$	61
Figure 3-6: Appearance of anode, cathode and solution after 15 minutes of testing at chloride concentrations of: (a) 0 mMol, (b) 250 mMol, and (c) 500 mMol	62
Figure 3-7: Accelerated corrosion test in concrete for different chloride concentration..	64

Figure 3-8: Test Specimens	67
Figure 3-9: Test set up under microscope.....	68
Figure 3-10: Rust thickness over time for specimens with $k = 3, 4,$ and 6	70
Figure 3-11: Experimental test results for rust thickness under the microscope for specimens with $k = 3$	71
Figure 3-12: Experimental test results for rust thickness under the microscope for specimens with $k = 4$	72
Figure 3-13: Experimental test results for rust thickness under the microscope for specimens with $k = 6$	73
Figure 4-1: Damage as a function of time (not to scale).....	77
Figure 4-2: Corrosion rate model.....	79
Figure 4-3: Steel electrode	80
Figure 4-4: Potentiostat operation.....	82
Figure 4-5: Mercury/ mercury oxide electrode	83
Figure 4-6: Variation of the open circuit potential as function of time, the parameters are given in	85
Figure 4-7: Effect of electrode rotation on the current	87
Figure 4-8: Polarization curve for different chloride concentrations.....	89
Figure 4-9: Experimentally determined oxidation polarization curves for steel at different $[\text{Cl}^-]/[\text{OH}^-]$ ratios.....	93
Figure 4-10: Pitting corrosion potential as a function of $[\text{Cl}^-]/[\text{OH}^-]$ ratios, parameters are given in Table 4-3.....	94
Figure 4-11: Passive current as a function of $[\text{Cl}^-]/[\text{OH}^-]$ ratios.....	96
Figure 4-12: Calculated anodic polarization curve from mode	97
Figure 4-13: Change in steel polarization due to varying $[\text{Cl}^-]/[\text{OH}^-]$ ratio (polarization surface)	99
Figure 4-14: Effect of oxygen concentration on cathodic polarization curve	102

Figure 4-15: Effect of pH on the cathodic polarization curve.	102
Figure 4-16: Variation of corrosion current with χ	104
Figure 4-17: Comparison between experimental data and model, and the corrosion current	105
Figure 4-18: Corrosion scale model (adapted from Jones 1992, Sarin et al. 2004).....	111
Figure 4-19: Oxygen diffusion path.....	112
Figure 4-20: Effect of K_p factor on oxygen diffusion coefficient.....	117
Figure 4-21: Flowchart of the model	118
Figure 4-22: Time to cracking as function of K_p , using the model.	120
Figure 4-23: Model calibration results for $k_r = 3$	121
Figure 4-24: Model calibration results for $k_r = 4$	121
Figure 4-25: Model calibration results for $k_r = 6$	121
Figure 4-26: Comparison between model and experiment of rust thickness over time..	123
Figure 4-27: Corrosion current for BC1	126
Figure 4-28: Corrosion current for BC2	127
Figure 4-29: Corrosion current for BC3	127
Figure 4-30: Corrosion current for W/C of 0.4.....	129
Figure 4-31: Corrosion current for W/C of 0.5.....	129
Figure 4-32: Corrosion current for W/C of 0.6.....	130
Figure 4-33: Corrosion Current and rust thickness for BC2.....	131
Figure 4-34: A comparison between literature test data and proposed model.....	132
Figure 4-35: Field measurement of corrosion current (Broomfield 1996)	134
Figure 5-1: Diffusion of rust inside concrete	141
Figure 5-3: Geometry of the FE models: (a) experimental unit, and (b) real structure ..	145

Figure 5-4: Typical concrete uni-axial stress-strain curve in (a) tension and (b) compression (ABAQUS User Manual).....	148
Figure 5-5: Stress-strain curve used for the concrete.....	149
Figure 5-6: Rust thickens vs. pressure from model and FEM	151
Figure 5-7: Critical pressure for different k_r ratios	153
Figure 5-8: Effect of concrete cover and bar distance on type of damage: (a) cover < half of bar distance, and (b) cover > half of bar distance.....	154
Figure 5-9: Finite element result for unsymmetrical situation.....	155
Figure 5-10: Rust growth over time for different w/c ratio and $k_r = 6$	156
Figure 5-11: α coefficient for different conditions	157
Figure 5-12: β coefficient for different conditions	157
Figure 5-13: Comparison Between Model and Equation 5-22	157
Figure 5-14: Pressure loss due to rust diffusing into concrete pores	158
Figure 5-15: Reduction in pressure as a percentage of the final pressure	159
Figure 5-16: Hoop stress from model for different k_r . (a) $k_r = 3$, (b) $k_r = 4$, and (c) $k_r = 6$	161
Figure 5-17: Effect of water cement ratio on concrete cracking time: (a) BC1 and (b) BC2.....	163
Figure 5-18: Effect of concrete cover on cracking time (a) BC1 and (b) BC2.....	164
Figure 5-19: Comparison between proposed model and literature	166
Figure 5-20: Comparison between time t_1 and t_2 for different conditions: (a) BC1 and (b) BC2	168
Figure 6-1: Corrosion test specimens	177
Figure 6-2: Steel bars after degreasing and cleaning.....	178
Figure 6-3: Specimens (a) before and (b) after sand blasting.....	179
Figure 6-4: Experimental setup for the corrosion test	181

Figure 6-5: Samples from each group after 6 weeks of accelerated corrosion testing ...	182
Figure 6-6: Crack pattern due to corrosion	183
Figure 6-7: Maximum strains in the corrosion test along the crack path for crack pattern 1	184
Figure 6-8: Maximum strains in the corrosion test along the crack path for crack pattern 2	184
Figure 6-9: TCI along crack pattern 1.....	185
Figure 6-10: TCI along different crack pattern 2.....	186
Figure 6-11: Corrosion mass loss for each group.....	188
Figure 6-12: Bars after six weeks of accelerated corrosion testing (a) Group 1 (b) Group 2 & 3.....	189
Figure 6-13: Corrosion rate for different patching system, BC2 and a) w/c = 0.4, b) w/c = 0.5 and c) w/c = 0.6	190
Figure 6-14: Geometry of the FE model with and without FRP.....	192
Figure 6-15: Concrete cover cracking for different condition for BC2, and $k_r = 6$	193

Chapter 1

Introduction

1.1 Background

Corrosion of reinforcing bars (“rebars”) in concrete is the most destructive mechanism contributing to damage in reinforced concrete bridges in the U.S. (Weyers et al. 1993). Corrosion reduces the strength, durability, and service life of reinforced concrete structures. Concrete can provide very good protection to embedded steel rebars due to its high alkalinity. In an alkaline medium a passive layer forms on the steel surface and protects rebars from further corrosion. However, in the presence of chloride ions the passive layer is disrupted or destroyed and steel spontaneously corrodes (Townsend et al. 1981, and Verbeck 1975). As the reinforcement corrodes, it expands causing cracking of *concrete* and spalling. Chloride concentration, temperature, relative humidity, cover

thickness, and concrete quality are the major factors affecting the rate of corrosion. The transformation of metallic iron to rust can result in an increase in volume of up to 600%, depending on the final rust form (Mehta 1993). The deterioration caused by corrosion of reinforcing steel in concrete structures has been recognized as one of the greatest maintenance challenges (Beaudette 2001). Corrosion should therefore be treated before it becomes a significant problem. Since the presence of both air and water is required for the corrosion activity to continue, corrosion may slow down considerably if a barrier could reduce the diffusion of moisture and harmful substances such as chloride ions and carbon dioxide through the concrete.

There are two main sources from which chloride ions can diffuse into a concrete structure. Structures in marine environments are constantly exposed to brackish sea water, especially in the splash zone. Another source is deicing salts used on roadways in the U.S. Since the late 1960's, the use of the deicing salts in the U.S. has increased greatly (Liu 1960). It has been reported (Fasullo 1992) that more than 40% of total highway bridges in the U.S. are structurally deficient or functionally obsolete. Approximately 20% of the total estimated repair cost is due to corrosion deterioration of concrete bridges. Through the effective use of deterioration models, improved design and cost effective repair strategies that can increase the life of concrete structures can be developed.

Modeling the corrosion rate, understanding the corrosion reactions that take place inside concrete, and the effect of chloride in destroying the passive layer and initiating corrosion has attracted the attention of scientists for over 50 years. While considerable research has been done in this area and many analytical, numerical and empirical models

have been proposed, the corrosion of steel in concrete still has many unknown elements and holistic electrochemical- mechanical models are lacking.

1.2 Problem Statement

The corrosion problem starts with the diffusion of chloride ions or carbon dioxide into the concrete to create conditions that overcome the protection offered by the existence of a passive film on the surface of steel in an alkaline concrete medium. This work focuses on corrosion initiation by chloride ions. Once chloride ions diffuse through the concrete cover and the chloride concentration adjacent to the steel reaches the threshold that can damage or destroy the passive layer, corrosion starts and continues until eventually the concrete cover cracks.

While various aspects of corrosion of steel in concrete from chloride diffusion to concrete cracking have been studied, the phase that has received the greatest attention is the diffusion of chloride ions into the concrete, since in many situations this takes the longest time.

The second phase of the corrosion process is from the initiation of corrosion to concrete cracking. Study of this phase involves modeling the electrochemistry of the corrosion rate and mechanical modeling of the concrete cracking and in a disciplinary context lies at intersection between chemistry and mechanics.

The third and final phase of corrosion is from the initiation of cracking until spalling of the concrete cover after which repair and rehabilitation of the concrete is necessary. This phase is the fastest since the concrete is already cracked and the corrosion

rate becomes high due to increased availability of oxygen, water and other necessary ions.

This dissertation focuses on the second phase of corrosion of steel in concrete, and includes electrochemical concepts of the effect of chloride on depassivation of the steel, corrosion rate modeling that accounts for the diffusion of oxygen, water, chloride ions, and rust build up, the diffusion of rust products, and mechanical effects of the pressure increase. All of these effects are modeled to predict the time to first cracking of the concrete cover.

1.3 Research Objectives

The objectives of this research were:

- To experimentally investigate the effect of chloride ions on the depassivation of steel in alkaline media.
- To model the corrosion rate of steel in concrete due to the effect of chloride ions from the initial rate to the limiting rate.
- To model the rust thickness growth, pressure developed and time to cracking of the concrete cover.
- To study the effect of different repair systems on the corrosion current and to propose a new system for repairing corrosion-damaged concrete structures.

Experimental investigations for calibrating models and understanding some fundamental concepts were necessary as part of the research. When possible, finite *element* analysis and validation based on the literature was used in lieu of experiments.

1.4 Layout of the Dissertation

This dissertation has seven chapters. Chapter 1 provides an introduction and outlines the research objectives.

Chapter 2 contains a detailed literature review on experimental and analytical studies of all three phases of corrosion of steel inside concrete. Models of diffusion of chloride ions into concrete, electrochemical concepts of corrosion of steel due to chloride, passivation and depassivation, and different models are included. However, the literature review focuses mainly on areas related to the research objectives: the electrochemical concepts of steel behavior in alkaline media with and without the presence of chloride ions; a detailed review on different corrosion rate models; instruments available to measure the corrosion rate; concrete cracking models; and a comprehensive discussion on the limitations of existing models.

Chapter 3 contains a detailed description of experiments needed to better understand the impressed current accelerated corrosion test and validate the use of Faraday's Law to calculate the mass loss in the test. This understanding was important to establish conditions for the accelerated corrosion test in which all the impressed current was expended on corrosion rather than on other reactions. The second part of the chapter describes the accelerated corrosion test conducted under a microscope to provide data to calibrate the model developed later, and to establish the relationship between the corrosion current and rust thickness build-up.

Chapter 4 presents different stages in the development of the corrosion current model focusing mainly on electrochemical aspects. Both experimental and theoretical work is described, starting with a comprehensive investigation on the effect of chloride

ions on the electrochemical behavior of steel passivation and depassivation, finding an empirical equation to estimate the initial corrosion rate, and development of a theoretical model for the corrosion limiting current that controls the greater part of corrosion during the second phase of corrosion. The results of the model are compared with previous research.

Chapter 5 develops the mechanical model, including the effect of corrosion current on the time to cracking of the concrete cover. The rust thickness growth, the diffusion of rust products into concrete pores and the generation of internal pressure is modeled first. Finite element analysis of concrete cracking due to internal pressure, derivation of the critical pressure required to cause cracking, and establishment of a relationship between the critical pressure and concrete strength are then described. The time to cracking of the concrete cover is established based on these results, validated using data from the literature, and compared to results from models proposed by others. Finally, the duration of the two main phases of the corrosion process diffusion of chloride until initiation of corrosion (t_1), and corrosion until cracking (t_2) are compared for different conditions using the developed model.

Chapter 6 present a study on concrete repairs and the effect of corrosion on the traditional patching repair system as well as a proposed more durable concrete repair procedure using a fiber reinforced polymer (FRP) overlay as a secondary reinforcement and barrier. Experimental tests and 3-D finite element studies conducted to assess this new dual repair system under corrosion are described. Also, adjustment of the proposed corrosion model so that it could be used to study corrosion in repaired systems and

compare them with corrosion in real undamaged concrete and experimental test results is described.

Finally, Chapter 7 presents the summary and conclusions of the findings, and recommendations for future study in this field.

Chapter 2

Literature Review

2.1 Introduction

Studies on the corrosion of reinforcing steel (“rebars”) in concrete structures have been widely reported in the literature over the last several decades. Corrosion is one of the major durability problems in concrete structures, mainly when the rebar is exposed to chlorides from the surrounding environment. Carbonation of the concrete due to the penetration of acidic gasses into the concrete is the other major cause of reinforcement corrosion. Beside these, there are other factors that affect rebar corrosion, some related to the concrete quality (such as water cement ratio, cement content, impurities in concrete ingredients, presence of surface cracks), and others related to the external environment (*such* as moisture, oxygen, temperature, and bacterial attack). Assessment of the extent of

corrosion is usually carried out using various electrochemical techniques. Prediction of the remaining service life of a corroding reinforced concrete (RC) structure is commonly based on empirical models and experimental methods (Ahmad 2003). Here, a comprehensive literature review is presented on many aspects of corrosion of steel rebars in concrete and some existing durability models for predicting the time for cracking of the concrete cover.

2.2 Corrosion Mechanism

Corrosion is the destructive result of the chemical reaction between metals or metal alloys and the environment. Corrosion science is the study of the electrochemical process that occurs during corrosion. Nearly all metallic corrosion processes involve the transfer of electronic charge in aqueous solution (Jones 1992). Thus the corrosion of metals is an electrochemical reaction. Corrosion of steel embedded in concrete also is an electrochemical process (Ahmad 2003). According to thermodynamic laws, there is a strong tendency for compounds in a high energy state to transfer to low energy states. All interactions between the metal element and the environment are governed by the free energy change ΔG available to it, and for a spontaneous reaction to occur ΔG must be negative. At room temperature most chemical components of metals have a lower value of ΔG (more negative) than uncombined metals. Nevertheless, most metals have an inherent tendency to corrode.

2.2.1 Corrosion Reaction

In the electrochemical corrosion reaction, there are two reactions which occur at the metal/liquid interface: the electron producing reaction (oxidation) at the anode; and the electron consuming reaction (reduction) at the cathode. Five essential components are involved in a basic corrosion cell.

Anode: The anode usually corrodes by losing electrons and dissolution of the metal. The anodic reaction depends on the pH of the pore solution of the concrete, presence of aggressive ions, and the potential at the surface (Ahmad 2003). The general anodic reaction for steel corrosion is:



Cathode: The cathodic reaction must consume the electrons produced at the anode and the exact reaction depends on the availability of oxygen and the pH of the solution. The following reduction process occurs in concrete:



Electrolyte: The solution that conducts electricity.

Metallic path: Metallic connection between the anode and cathode which allows the current to flow.

Current: Electrons flow through the rebar from the anode to the cathode, and the rate of flow is conventionally measured as current. The current is related to the rate of the anodic and cathodic reactions. The current will reach its limit when one of the reactions reaches its maximum rate due to limitation in availability of a required species.

For corrosion of steel in concrete, the steel acts both as the anode and the cathode and the pore solution acts as the electrolyte.

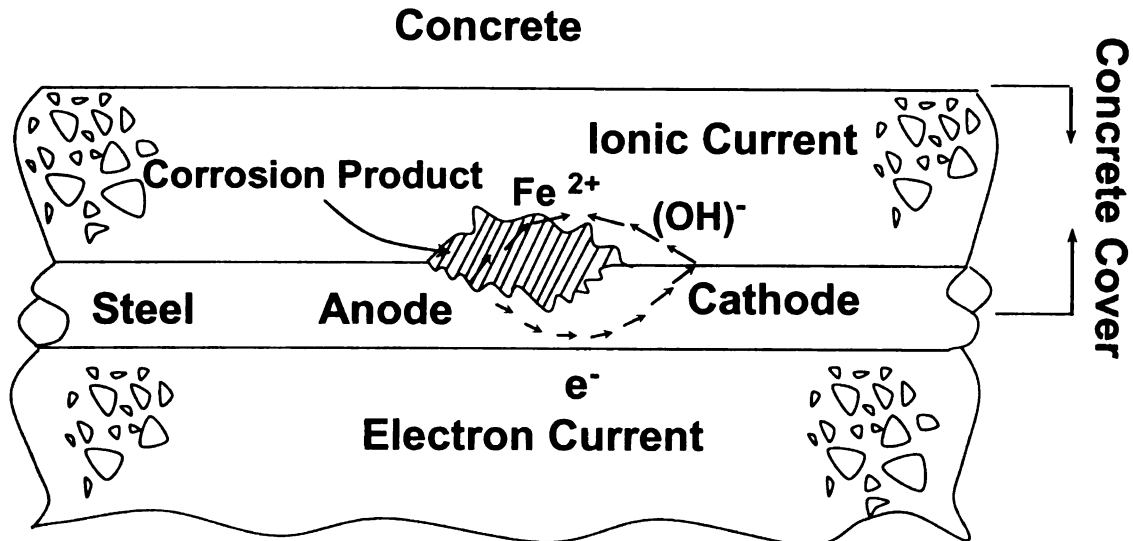


Figure 2-1: Corrosion process on steel bar surface

The actual mass loss due to corrosion is due to the reaction that takes place at the anode. The iron atoms ionize to Fe^{2+} ions according to Equation 2-1 and are dissolved in the pore solution around the steel bar. The electrons are deposited on the rebar surface and raise its electrochemical potential. The electrons then flow through and along the steel to a lower potential region (cathode) as shown in Figure 2-1. The free electrons are consumed in the cathodic reaction as shown in Equation 2-2. The electrochemical character of the corrosion process is demonstrated by the flow of current in the closed loop as shown in Figure 2-1. The rate of electron flow within the steel bar results from the difference in potential and determines the rate of corrosion.

2.2.2 Pourbaix Diagram

Based on thermodynamic data on the reactions between metal and water, Pourbiax developed potential versus pH diagrams which indicate thermodynamically stable phases as a function of electrode potential and pH (Pourbiax 1976). The Pourbiax diagram for iron is shown in Figure 2-2.

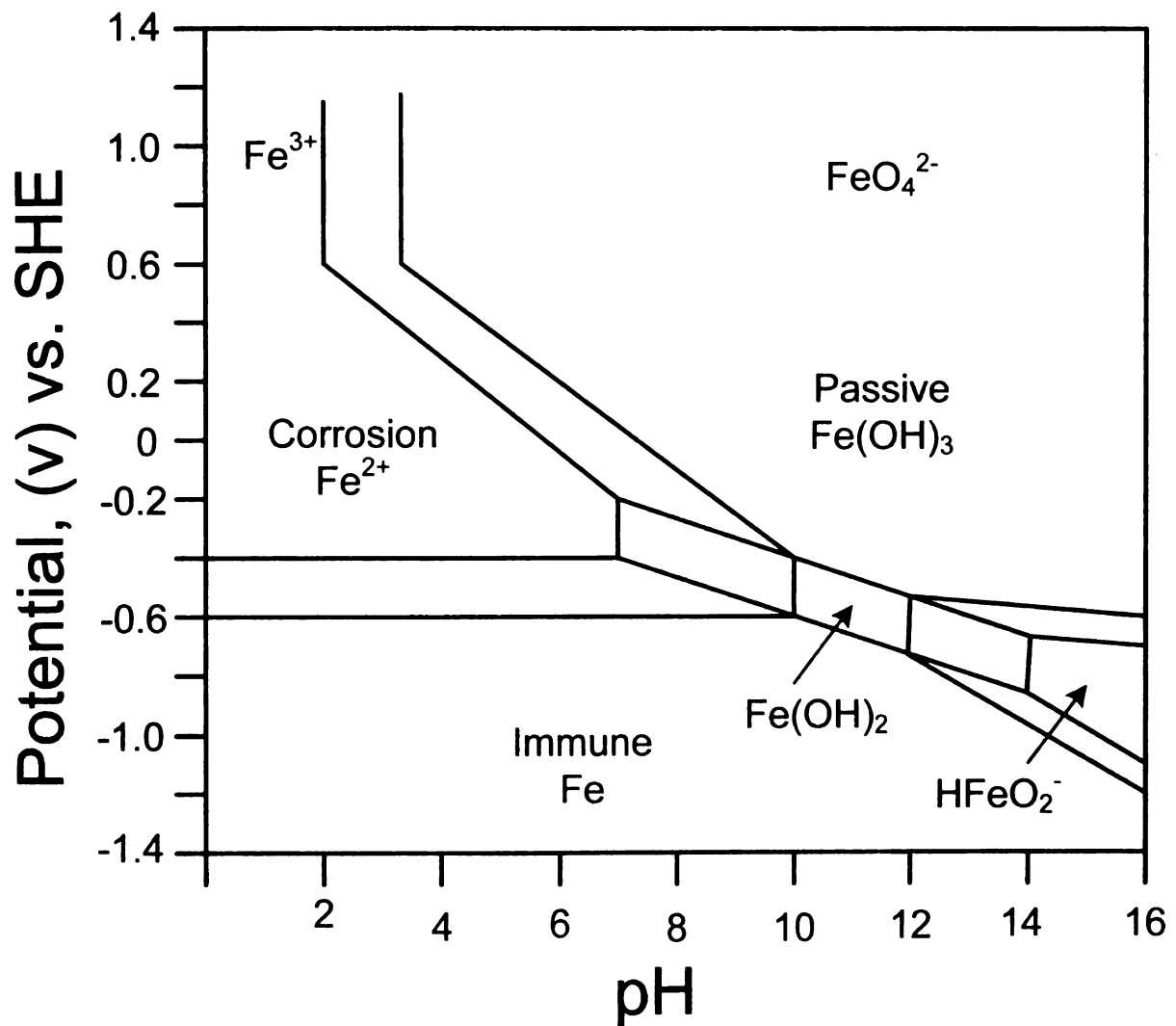


Figure 2-2: Pourbiax diagram for iron (Pourbiax 1976)

The three general regions are regions of corrosion, passivity and immunity. A soluble product is formed under a range of acidic conditions and a narrow range of very

alkaline conditions. These are regions of corrosion. Between these two regions a passive region exists due to the formation of an insoluble film. In the third immune region, the metal is thermodynamically stable and no corrosion will occur. The Pourbiax diagram provides a strong thermodynamic basis for understanding corrosion reactions. There are two main limitations on use of the diagram. One arises from the lack of kinetic data and the other, which is more important for the corrosion of steel, is the purity of the environment. In practice, corrosion occurs when the environment is contaminated.

2.2.3 Polarization

The difference between the potential of an electrode with and without current is called electrochemical polarization. This polarization is represented by the over potential defined as:

$$\eta = E - e \quad (2-3)$$

where η is the potential change from the equilibrium half-cell electrode potential, e , caused by the net surface for the half-cell reaction. Figure 2-3 shows an illustration of a typical potentiodynamic curve for iron.

The logarithm of the current is plotted as a function of the

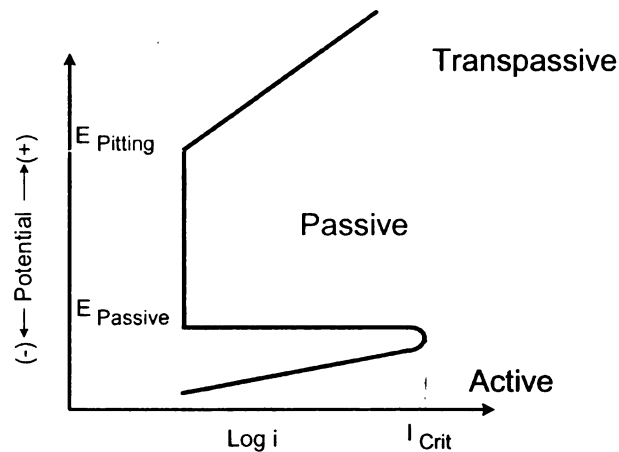


Figure 2-3: General polarization curve for iron (Jones; 1992)

applied potential. For cathodic polarization, electrons are supplied to the surface, and a

build-up in metal due to the slow reaction causes the surface potential, E , to become negative to e . Hence η is negative by definition. For anodic polarization, electrons are removed from the metal, a deficiency results in a positive potential change due to the slow liberation of electrons by the surface reaction, and η must be positive.

2.2.4 Passive Film and Depassivation

Passivity is defined as a condition of corrosion resistance due to the formation of a thin surface film under oxidizing conditions. Passivity has been studied for over 140 years (Jones 1992). The lack of fundamental understanding of passive film properties has delayed the control and prevention of localized forms of corrosion that results from breakdown of the passive film. The structure favored by most investigators for the thin passive film on iron (steel) is an inner layer of Fe_3O_4 under an outer layer of $\gamma\text{-Fe}_2\text{O}_3$ (Jones 1992). Effective passivation can also be obtained with conventional steel if it is in contact with an aqueous solution in which the concentration of hydroxide ions (OH^-) is high enough. This is indicated in

Figure 2-4 which shows the results of a series of experiments in which the extent of steel corrosion is plotted against the OH^- ion concentration. The level of the hydroxide ion concentration required to maintain passivity is not constant but varies with the presence of other ions (Bentur et. al 1998). When the steel is passive, a small amount of corrosion current maintains the passive layer, and this current decreases as the passive layer becomes stronger with time in an alkaline medium (Princeton Applied Research 2002). Due to this effect, the passive current measured at an early age for steel in concrete with

no chloride can be ten-fold higher than that for the same concrete with no chloride after 10 years.

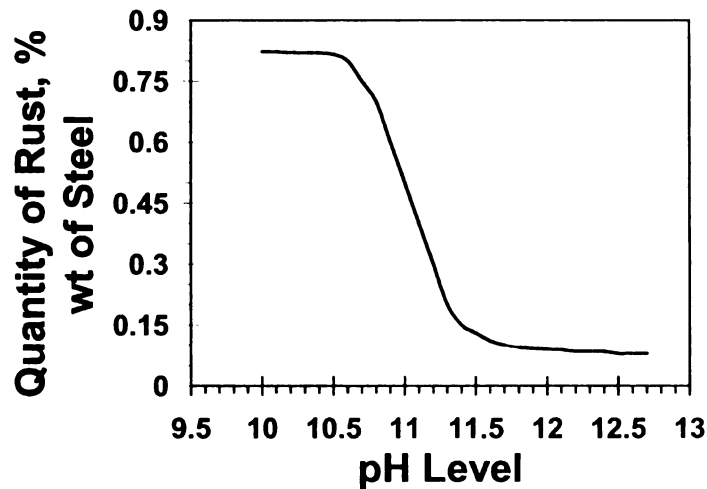


Figure 2-4: Corrosion of steel in water solution as a function of OH^- concentration and pH level (Shalon and Raphael 1959)

The strength of the passive film depends on the alkalinity of the solution or concrete environment (Thangavel and Rengaswamy 1998).

The maintenance of passivity requires a certain electrochemical environmental condition, and breakdown of the passive film is usually brought about by changes in this condition or mechanical force. Steel is passive inside alkaline media. Destruction of the passive film in steel reinforcement embedded in concrete and the onset of active corrosion can arise due to two causes: carbonation of the concrete, or chloride diffusion. When the $\chi = [\text{Cl}^-]/[\text{OH}^-]$ ratio reaches a certain value (reported to be about 0.6), corrosion will start (Mindess et al. 2003). However, there is no electrochemical interpretation of this value and it was obtained from experimental testing or field investigation. Knowing the effect of chloride on the corrosion of steel in alkaline media is very important for predicting the lifetime of concrete structures.

2.2.4.1 Effect of Chloride on Steel Behavior

The presence of chloride in the environment generally increases the potentiodynamic or potentiostatic anodic curve at all potentials. But the most singular feature is the dynamic increase in current at the critical potential, E_{pit} , as shown schematically in Figure 2-5. This increase in current density above E_{pit} measures low voltage anodic dissolution within pits, which initiate and become visible at the critical potential. The more noble E_{pit} is, the more resistant the alloy is to pitting. As Figure 2-5 shows, an increase in the chloride concentration generally decreases the passive potential range and increases the passive current density.

2.2.5 Corrosion Rate Calculation with Polarization Curve

The corrosion rate can be calculated from the anodic and cathodic polarization curves using the mixed potential theory.

2.2.5.1 Anodic Polarization

The anodic potentiodynamic polarization plot can yield important information such as: (a) the ability of the metal to spontaneously passivate in the particular medium; (b) the potential region over which the metal remain passive; and (c) the corrosion rate in the passive region (Princeton Research Group 2002). The plot can be divided into the three regions shown in Figure 2-3 the active, passive and transpassive regions.

The active region is the linear part in the semi-logarithmic plot, called the Tafel region, where the iron or steel corrodes. The accepted model to describe this part of the curve is the Tafel equation:

$$\eta = \beta \log\left(\frac{i}{i_0}\right) \quad (2-4)$$

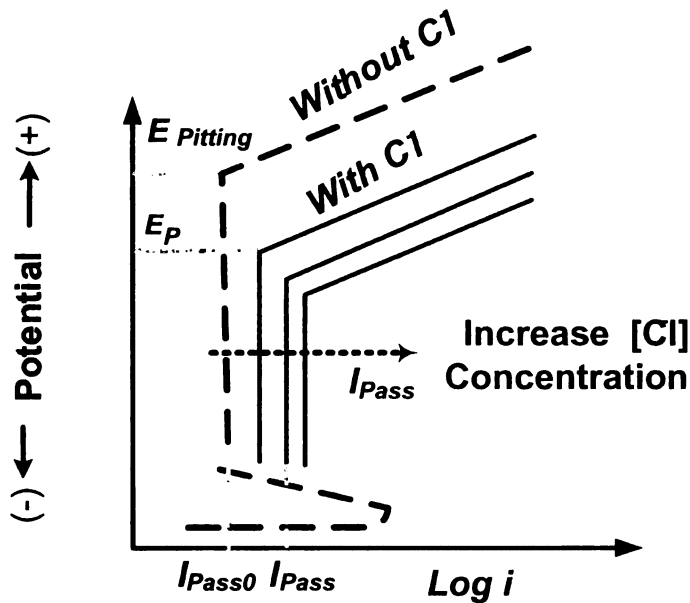


Figure 2-5: Effect of chloride ions on steel polarization curve (Jones 1992)

where η is the over potential, β is the Tafel constant, and i_0 is the exchange current density.

The constants β and i_0 need to be determined experimentally for different solutions. The plot is linear up to the critical current, i_{crit} . The passive region

begins after i_{crit} . The loss of chemical reactivity occurs under certain environmental conditions due to the formation of a thin oxide layer that according to the Pourbiax plot is stable at this pH. The passive region continues until E_{pit} , where the transpassive region starts. This region is also linear in the semi-logarithmic plot.

For knowing the behavior of steel in alkaline media and the change of this behavior in the presence of chloride ions, it is necessary to know the polarization curve of

steel. Only from the polarization curve is it possible to evaluate the passivation current and pitting corrosion current.

2.2.5.2 Cathodic Polarization Curve

When the cathodic half-cell reaction is controlled by the rate of change of electron flow, the cathodic polarization curve is said to be under activation or charge transfer control. As mentioned in the previous section, the active part of the polarization curve is controlled by the Tafel equation, Equation 2-4. The cathodic reduction reaction cannot exceed a certain rate due to the limitation of diffusion of species to the solution. The threshold current is called the limiting current. The limiting current density can be calculated through:

$$i_L = \frac{DnFC_B}{\delta} \quad (2-5)$$

where n is 4 for the reduction of oxygen in the corrosion reaction, F is Faraday's constant, D is the diffusion coefficient of the reduction species toward the cathode, C_B is the concentration of the reduction species at the boundary, and δ is the thickness of the diffusion layer.

2.2.6 Growth of Rust Film

The growth of corrosion products may follow a linear or parabolic law depending on the properties of rust oxides (Speller 1951). For a metal that does not form a protective oxide film, the rate of growth of the oxide film remains constant, i.e.,

$$y = k.t \quad (2-6)$$

where k is a constant, y is the oxide film thickness, and t is the corrosion time.

For a metal that forms a protective oxide film, the rate of corrosion will depend on the diffusion of corrodant through the film. As the film thickens with time, the rate of corrosion will continuously decrease and the corrosion film thickness follows a parabolic law:

$$y^2 = kt \quad (2-7)$$

where k is a constant related to the diffusion coefficient of the products and reactant.

However, the general relation between the corrosion film thickness and time is not as simple as described above, and it is more appropriate to express it as (Tomoshov 1966)

$$y^n = kt \quad (2-8)$$

Unfortunately, no experimental results exist to calibrate the k and n coefficients. Also, both coefficients depend on factors that are not addressed in the literature.

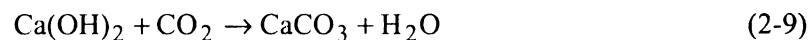
2.3 Corrosion of Steel in Concrete

In general, good quality concrete of appropriate mix proportions, compaction and curing provides an excellent protective environment for steel. The physical protection is afforded by the cover concrete acting as a physical barrier to the ingress of aggressive species. Chemical protection is provided by the highly alkaline solution present within the pore structure of the cement paste matrix. The range of high pH values of typical concrete (12.5-13.5) is within the pH domain in which the insoluble oxides of iron are

thermodynamically stable (see Figure 2-2). This is the reason that steel is passive inside concrete and protected from further corrosion.

The porous nature of concrete allows aggressive species to diffuse through it. Some of these diffused species have the ability to break down the passive film and initiate corrosion. Two effects can accelerate the corrosion process:

1. Carbonation of concrete: Carbonation of concrete is a reaction between acidic gases present in the atmosphere or dissolved in water and the products of cement hydration (Emmons 1994, ACI 1992). Carbonation occurs in concrete because the calcium bearing phases present are attacked by the carbon dioxide in the air and are converted to calcium carbonate. Cement paste contains 25-50% calcium hydroxide (Ca(OH)_2) by weight, which means that the pH of the fresh cement paste is at least 12.5. The pH of a fully carbonated paste is about 7. The chemical reaction corresponding to carbonation is:



This reaction produces calcium carbonate (CaCO_3) and is accompanied by shrinkage.

Concrete carbonation is a function of humidity, concrete permeability, and the concentration of carbon dioxide. Carbonated concrete has properties that can be considered both beneficial and detrimental to concrete performance. Favorable effects of carbonation are increased strength, hardness, and dimensional stability. Adverse effects of carbonation can be a porous and less wear resistant surface. Probably the most detrimental effect is a reduction in the concrete alkalinity, from a pH of around 13 to a

pH of around 10 (ACI 1992). When the pH of concrete approaches 10, the passivity of steel is destroyed and more rapid corrosion may occur (Emmons 1994).

Carbonation can be recognized in the field by the presence of a discolored zone in the surface of the concrete. The color may vary from light gray that is difficult to recognize to strong orange that is easy to recognize. Carbonation can be visualized by using phenolphthalein. Under an optical microscope carbonation can be recognized by the presence of calcite crystals and the absence of calcium hydroxide, ettringite and unhydrated cement grains. Porosity is unchanged or lower in the carbonated zone

2. Deicing salt: Chloride ions have a well-documented detrimental role on reinforced concrete as mentioned earlier. Chloride ions are considered to be the major cause of premature corrosion of steel reinforcement. The chloride ions disrupt the performance of the passive oxide film on the reinforcement, in turn promoting corrosion (ACI 1996). This work focuses mainly on the effect of chloride on corrosion initiation and the corrosion rate.

2.3.1 Concrete Structure and Durability

Concrete has a complex structure and contains a heterogeneous distribution of different types and amounts of solid phases, pores and microcracks. In addition, the structure of concrete can also change with time, humidity of the environment, and temperature. Concrete is inherently a durable material. Its durability is influenced most by the water/cement (w/c) ratio because it strongly impacts the permeability of the cement paste. High permeability of concrete allows moisture, water, and chemicals that can degrade concrete or reinforcing steel to diffuse into it (Mindess 2003).

The modeling of fluid movement within unsaturated cement-based material is difficult because of the complexity of its microstructure. The flow of water through cement paste obeys Darcy's Law for flow through a porous medium, namely,

$$j = K_P \frac{h}{x} \quad (2-10)$$

where j = rate of flow of water, h = pressure head (hydraulic pressure), x = thickness of specimen, and K_P = permeability coefficient. The relationship between the pressure head and saturation can be expressed according to the Van Genuchten relationship (Coussy et al. 2004)

$$S = [1 + (ah)^n]^{-m} \quad (2-11)$$

where a , n and m are empirical parameters, S = saturation, and h = pressure head or macroscopic capillary pressure. When saturation is almost 100% the capillary pressure is almost zero, and when the saturation is low the capillary pressure is high. Water flows from high pressure to low pressure zones (Monlouis et al. 2004).

2.3.2 Concrete Pore Solution

2.3.2.1 Chemical Composition

The chemical composition of the solution in the pores of hydrated cement paste depends on the composition of the concrete, mainly the type of cement. As mentioned before, it also depends on the exposure condition, e.g., changes due to carbonation or penetration of salts. Table 2-1 shows the ionic concentration measured in the pore solution of cement pastes, mortar and concrete of Ordinary Portland cement (OPC)

(Bertolini et al. 2004). In non-carbonated and chloride free concrete, the concentration of hydroxide ions $[\text{OH}^-]$ varies from 0.1 M to 0.9 M due to the presence of sodium and potassium oxide in cement as well as the calcium hydroxide produced by the hydration reaction of cement (Barneyback and Diamond 1981). The hydroxide concentration shown in Table 2-1 yields pH values of 13.4 to 13.9.

Table 2-1: Ionic Concentration Measured in the Pore Solution Extracted from Cement Paste and Mortar (mmol/L).

Cement	Water binder	Age	Sample	$[\text{OH}^-]$	$[\text{Cl}^-]$	$[\text{Na}^+]$	$[\text{Ca}^+]$	$[\text{K}^+]$
OPC	0.45	28	Paste	470	n.a	130	1	380
OPC	0.5	28	Mortar	391	3	90	<1	288
OPC	0.5	28	Paste	834	n.a.	271	1	629
OPC	0.5	192	Mortar	351	n.a.	38	1>	241
OPC	0.5	84	Paste	589	2	n.a	n.a.	n.a
OPC	0.5	84	Paste	479	3	n.a.	n.a.	n.a

Penetration or addition of chloride-bearing salts changes the chemical composition of the pore solution, depending on the type of the salt, and due to the chemical or physical binding effect of chloride and hydroxyl ions.

2.3.2.2 Transport Process

The actual quantity of water in the pores of concrete depends on the humidity of the surrounding environment. Figure 2-6 shows the schematic representation of the water content in the pores of concrete at equilibrium as a function of relative humidity of the environment (Bertolini et al. 2004). The amount of water in the concrete pore system is very important since it acts as an electrolyte in the corrosion of reinforcing steel. The presence of oxygen is also necessary for the cathodic reaction. If the pore volume of the

concrete is only partially filled with water, the transport of oxygen to the steel surface will be easier, whereas when the concrete is saturated, the transport of oxygen must occur through the pore solution. The diffusion coefficient of oxygen in water is four orders smaller than that in air. Kobayashi (1991) reported that when the moisture content of concrete is lowered from 80% to 40%, the value of the oxygen diffusion coefficient

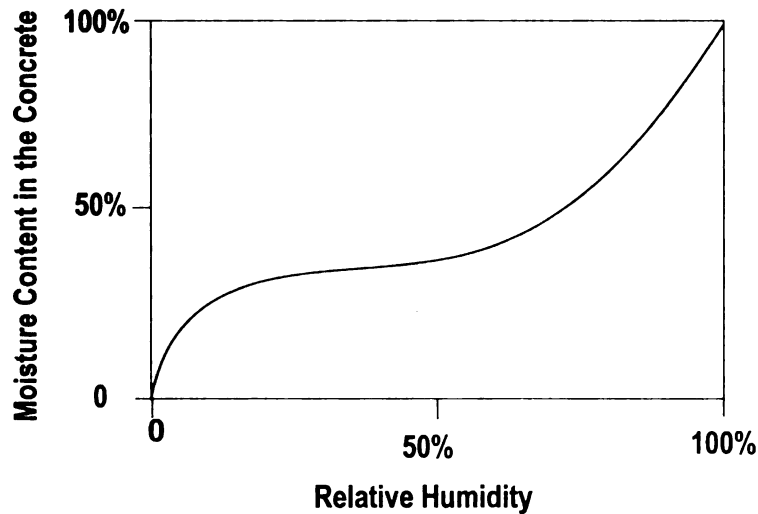


Figure 2-6: Water content in pore as a function of relative humidity (Bertolini et al 2004).

increases by a factor of 15.

This is the primary reason that the corrosion rate is very low for concrete structures below seawater.

The water content also affects the chloride diffusion coefficient discussed next.

2.3.3 Chloride Diffusion

The chloride content at the steel surface has a significant effect on the corrosivity of steel in concrete. The penetration of harmful substances, such as chloride ions, into concrete occurs through two mechanisms: capillary action and ionic diffusion (Collepordi et al. 1972, Page et al. 1981).

When concrete is dry or semi-dry, ions migrate along with water under the influence of capillary action. The rate of penetration of chloride under capillary action is much faster than through ionic diffusion. Capillary action was explained earlier for

movement of liquid inside porous media such as concrete. When concrete is wet to near saturation, ionic migration occurs primarily through the diffusion process.

2.3.4 Basic Formulation

The diffusion of chloride into concrete has been studied by numerous researchers. The diffusion process is complex, many factors are involved, and no model can be considered to be “correct” in an absolute sense. However, a good model provides additional insight into behavior. A simple model is used in this work to estimate the depassivation time and corrosion rate that are dependent on the chloride concentration. Diffusion generally follows Fick’s Second Law:

$$\frac{\partial C_{Cl}}{\partial t} = D_{Cl} \frac{\partial^2 C_{Cl}}{\partial x^2} \quad (2-12)$$

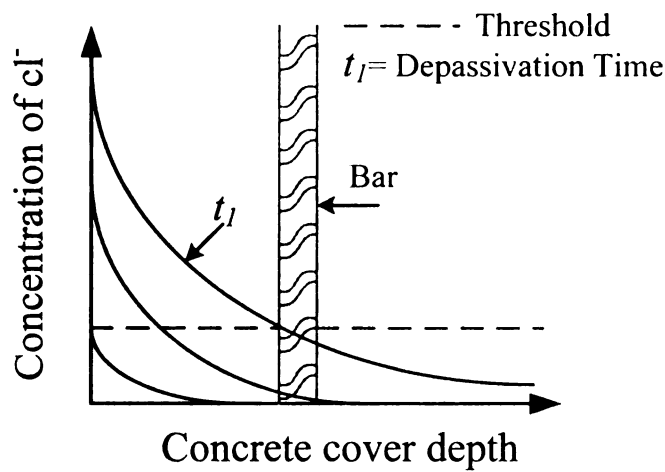


Figure 2-7: Diffusion of chloride in concrete

where C_{Cl} is the concentration of chloride ions (mass of chloride ions per unit volume of concrete), and D_{Cl} is the chloride ion diffusion coefficient.

2.3.5 Chloride Diffusion Coefficient

The chloride diffusion coefficient is assumed to be highly dependent on pore humidity, temperature, degree of hydration, percentage of aggregate content and the chloride concentration. The diffusion coefficient can be expressed by (Ababneh et al. 2003):

$$D_{Cl} = f_{Cl} D_m \times F(h) \times F(T) \times F(C) \times F(g_i) \quad (2-13)$$

where f_{Cl} and D_m can be calculated using Equations 2-14 and 2-15 , and $F(h)$, $F(T)$, $F(C)$, and $F(g)$ are correction factors that account for humidity, temperature, concentration, and aggregate, respectively, and are explained later.

$$D_m = \frac{2 \left[1 - (V_P - V_P^c) \right]}{S^2} (V_P - V_P^c) f \quad (2-14)$$

where V_P is the porosity of cement paste and S is the specific surface area (surface area/bulk volume) , $V_P^c = 3\%$ and $f = 4.2$ (Martys et al. 1994).

$$f_{Cl} = \left[\frac{1}{4} + \frac{(28+t)}{300} \right] \left(\frac{w}{c} \right) + \frac{28-t_0}{62500} \quad (2-15)$$

where t_0 is the time in days, and for concrete older than 28 days $t_0 = 28$ days.

2.3.5.1 Effect of Aggregate

The effective diffusivity of concrete can be obtained using the theory of composite materials. Christensen (1979) developed a composite model based on a three-

phase model and Fick's First Law. When the diffusivity of cement paste and aggregate are obtained, the effective diffusivity of concrete can be evaluated on the basis of the composite sphere model (Ababneh et al. 2003):

$$F(g_i) = \left\{ 1 + \frac{g_i}{[(1 - g_i)/3] - [D_m / (D_i - D_m)]} \right\} \quad (2-16)$$

where D_i and D_m = diffusivity of inclusions (aggregate) and matrix (cement paste), respectively, and D_i can be taken as $1 \times 10^{-12} \text{ cm}^2/\text{s}$, and g_i = volume fraction of the inclusions, which depends on the configuration of the two constituent phases, the microstructure feature of each phase, and other factors described.

2.3.5.2 Temperature Dependence

Temperature has a significant effect on the rate of diffusion in more than one aspect. First, the temperature changes the adsorption heat. Second, temperature increases the frequency of thermal vibration of the diffusant, which can be taken into account by the Arrhenious Law (Martys et al 1994):

$$F(T) = \exp\left[\frac{U}{R} \left(\frac{1}{T_0} - \frac{1}{T}\right)\right] \quad (2-17)$$

where T_0 and T = reference temperature and current temperature, respectively ($^{\circ}\text{K}$), R = gas constant, and U = activation energy for the diffusion process. U has been found to depend on the water cement (w/c) ratio and the cement type (Page et al. 1981, Collepardi et al. 1972). Some test results on the value of U for various w/c ratios are shown in Table 2-2.

Table 2-2: Activation Energy for Various Cement Pastes

w/c Ratio	U	
	Ordinary portland cement (KJ/mol)	Cement with pozzalans (KJ/mol)
0.4	41.8 ± 4.0	–
0.5	44.6 ± 4.3	41.8
0.6	32.0 ± 2.4	–

2.3.5.3 Effect of Humidity

The effect of relative humidity on the chloride diffusion coefficient is accounted for by $F(h)$. The model proposed by Bazant and Najar (1972), initially developed for moisture diffusion, can be used:

$$F(h) = \left[1 + \frac{(1-H)^4}{(1-H_c)^4} \right]^{-1} \quad (2-18)$$

where H_c = critical humidity level at which the diffusion coefficient drops halfway between its maximum and minimum values = 0.75. $F(h)$ is very important for characterizing the coupling between moisture diffusion and chloride penetration.

2.3.5.4 Effect of Chloride Concentration

In diffusion, the movement of ions is restricted by the electrostatic field induced by the other ions present in the solution. The factor accounting for the dependence of the chloride diffusion coefficient on the free chloride concentration is (Xi and Bazant 1999):

$$F(C) = (1 - k_{ion}(C_f)^m) \quad (2-19)$$

where k_{ion} and m are two constants that were calibrated by Xi and Bazant (1999) to be

$$k_{ion} = 8.333 \text{ and } m = 0.5.$$

2.3.6 Chloride Binding Capacity

When chloride ions enter concrete, some of them will bind to the internal surfaces of the cement paste and aggregate. These are called bound chloride ions. The free chloride ions diffuse freely through the concrete. Steel corrosion in concrete is related only to the free chloride content and not to the total chloride content. The governing equation of Fick's Law should therefore be expressed in terms of the free chloride content (Xi et al. 1999):

$$\frac{dC_f}{dt} = \frac{dC_f}{dC_t} \text{div}[D_{Cl} \cdot \text{grad}(C_f)] \quad (2-20)$$

$$\frac{dC_f}{dC_t} = \frac{1}{1 + (dC_f / dC_t)} \quad (2-21)$$

where dC_f/dC_t = binding capacity. The binding of chloride by the cement in concrete affects the rate of chloride ingress and chloride threshold levels, and thereby affects the time to chloride-induced corrosion initiation (Glass and Buenfeld 2000). The total chloride concentration, C_t , is the sum of the free chloride concentration, C_f , and the bound chloride concentration, C_b :

$$C_t = C_f + C_b \quad (2-22)$$

The adopted model for chloride diffusion which considers the binding effect is (Glass and Buenfeld 1998)

$$C_b = \frac{\alpha.C_f}{1 + \beta.C_f} \quad (2-23)$$

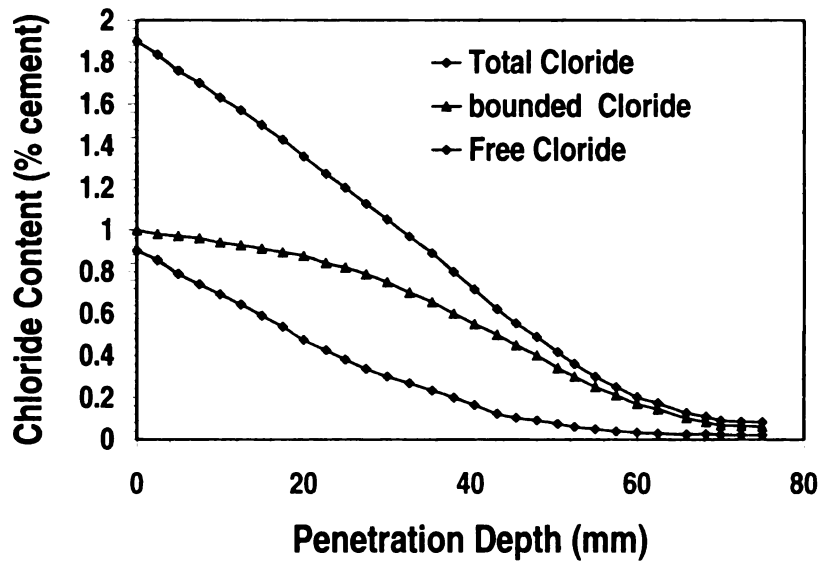


Figure 2-8: Predicted total, bounded and free chloride after 50 years (Glass and Buenfeld 2000).

where α and β are empirical constants, mostly dependent on the C_3A content of the cement.

Experimental results show that increasing the C_3A content of cement

increases the binding capacity. The model shows that from the total chloride penetrated into concrete, up to 74% can be bound, and even up to 78% can be bound by increasing the depth. An increase in chloride binding results in a decrease in free chloride concentration at all depths within the concrete. Figure 2-8 shows the prediction of the model for concrete with low C_3A after 50 years (Glass and Buenfeld 2000).

2.3.7 Chloride Threshold

The amount of chloride required to initiate corrosion depends on the pH of the solution in contact with the steel surface. A wide range of chloride threshold concentrations have been reported in the literature generally varying from 1.2 to 2.5 kg.m³ in some Asian country (Yoshiki et al. 2001) and 0.6 to 0.7 kg.m³ in the US

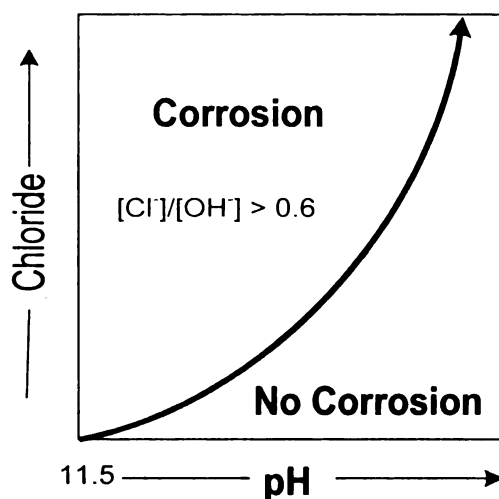


Figure 2-9: Effect of chloride and pH in liquid phase (ACI 1975)

(Browning 2007). It was also reported that corrosion will start when the $[Cl^-]/[OH^-]$ reaches 0.6 (Mindess 2003).

2.3.8 Oxygen Diffusion

The diffusion coefficient of the dissolved oxygen in concrete also depends on the w/c ratio, and decreases with the reduction of the w/c ratio. The ratio of the diffusion coefficient of oxygen to that of chloride ions increases from a value close to one in permeable paste, to a value of 15 in low-permeable paste (Ngala 1994).

No model seems to exist in the literature for the variation of the diffusion coefficient of oxygen in concrete as a function of different environmental conditions such as relative humidity and temperature, and also the effect of different components of cement paste and concrete. However, Nagal (1994) showed that the diffusion coefficient

of oxygen for a given capillary porosity in ordinary Portland cement (OPC) with 30% fly ash is about 30% smaller than that in OPC.

2.4 Corrosion Rate

Modeling the corrosion rate in concrete is difficult. There are a few mathematical models for corrosion due to carbonation of concrete based on the oxygen limiting current (Liang et al. 2005), but there appears to be no model for the rate of corrosion of steel in concrete due to the effect of chloride concentration. There are only a few experimental methods to measure the corrosion rate after corrosion begins (Liu 1996).

2.4.1 Corrosion Rate Models

2.4.1.1 Corrosion Rate in Carbonated Concrete

Liang (2005) proposed a model assuming that corrosion is only a result of carbonation of concrete and the oxygen limiting current, and that diffusion of oxygen into the concrete obeys Fick's Second Law of diffusion.

He expressed the corrosion current as

$$i_{corr} = \frac{n_{O_2} F D_{O_2} C_{O_2}}{D} \quad (2-24)$$

where $n_{O_2} = 4$, F = Faraday's constant (96,485 Columb/mol), C_{O_2} = concentration of the oxygen at the boundary, and D_{O_2} = coefficient for diffusion of oxygen into carbonated concrete, and D is the depth of carbonation calculated from

$$D = \alpha \cdot t^{\lambda} \quad (2-25)$$

where α = carbonation velocity, λ = empirical coefficient, and t = time in minutes.

2.4.1.2 Corrosion Rate due to Chloride Diffusion

Liu (1996) developed an empirical equation for the corrosion current of steel in concrete under chloride attack. This purely empirical model is based on curve fitting to experimental data obtained over 5 years from a corrosion monitoring technique explained later. He expressed the corrosion current as

$$\ln(i_{corr}) = A + B \ln[Cl^-] + \frac{C}{T} + DR_c + Et^{0.25} \quad (2-26)$$

where A , B , C , D , and E are empirical coefficients, $[Cl^-]$ = chloride concentration at the surface of the bar, T = temperature at the steel surface, R_c = ohmic resistance of concrete, and t = time in years.

The main shortcoming of this model is that it is purely empirical and all the coefficients need to be calibrated using experimental data. Also, the model was calibrated using readings from a commercially available corrosion rate monitoring instrument, which raises questions about the accuracy of the results, since these instruments can yield results that differ by a factor of 10.

2.4.2 Corrosion Rate Monitoring Techniques

Corrosion of steel embedded in concrete is not visually evident until the damage is externally visible as rust spots, cracking or spalling. In order to predict the service life of reinforced concrete structures and to determine the need for repair or rehabilitation, it is necessary to have a mathematical model that can predict the stress and strain distribution due to the corrosion.

Due to the special electrolytic characteristics of concrete, it is difficult to develop accurate corrosion monitoring devices for use with reinforced concrete structures. Nevertheless, some electrochemical techniques such as half cell potential and linear polarization are used to monitor corrosion of steel in concrete.

2.4.2.1 Half Cell Potential

Corrosion causes an electrical potential to be generated and the half-cell provides a method of detecting this. The ASTM C 876 procedure presents the test method and measurement interpretation of the reading potential. As shown in Table 2-3, the more negative the reading, the greater the possibility of corrosion.

Table 2-3: Guidance for Interpretation of Results from Half-Cell Surveying

E_{corr} (Cu/CuSO₄)	Probability of Corrosion
> -0.20 V	Greater than 90% probability of no corrosion
0.35 to -0.20 V	Corrosion activity uncertain
< 0.35 V	Greater than 90% probability of active corrosion

Since the potential of the half cell can be a function of a large number of variables, it is not possible to obtain a quantitative corrosion rate or corrosion current from this method and the potential does not provide any information on the amount of corrosion. Further, the validity of interpretations of half cell potential readings has been questioned in some situations, such as in saturated concrete (Elsener and Bohni 1991, and Pathmanaban 1981).

2.4.2.2 Linear Polarization Technique

The term linear polarization refers to linear regions of the polarization curve along which slight changes in current applied to a corroding metal in an ionic solution causes

corresponding changes in the potential of the metal. The relationship between the potential and current is assumed to be linear and the slope of the relationship is called the polarization resistance (Stearn et al. 1958).

The corrosion current is given by

$$R_P = \left(\frac{\Delta E}{\Delta I} \right)_{\Delta E \rightarrow 0} \quad (2-27)$$

$$i_{corr} = \frac{\beta_a \beta_c}{2.3 R_P (\beta_a + \beta_c)} \quad (2-28)$$

where β_a and β_c are the anodic and cathodic Tafel slopes. As shown in Figure 2-3, the polarization curve for iron is divided into active, passive and transpassive regions. The linear part of the curve (active region) is called the Tafel region where the Tafel equation holds (Jones 1992). Due to this relationship, the method is also called the Tafel method of measuring the corrosion rate.

The linear polarization technique has been widely used to measure the corrosion current density both in the laboratory and in the field (Hope et al 1985, Carassiti et al. 1991). The general guideline for interpreting results from the linear polarization method is summarized in Table 2-4. However, the results obtained from this method can vary by a factor of 10 compared to the corrosion current obtained from tests and hence the results from this method are not very reliable (Liu 1996).

In this method, at least one decade of linearity on the semi-log plot is desirable for good accuracy in the determination of i_{corr} . This may be difficult to achieve when concentration polarization effects are likely, such as in the corrosion of steel in concrete

where i_{corr} is always equal to the limiting current for the concentration polarization with diffusion control.

Table 2-4: Guideline for Interpreting Results from the Linear Polarization Method

$i_{\text{corr}} (\mu\text{A}/\text{cm}^2)$	Corrosion State
< 0.2	No damage expected (passive)
0.2-1.0	Damage possible in 10-15 years (low corrosion)
1.0-10	Damage possible in 2-10 years (moderate)
> 10	Damage possible in less than 2 years (high corrosion)

Also, when the steel is passive in the absence of chloride ions, i_{passive} can be measured using the polarization resistance method, although not knowing the correct value of the Tafel slope can yield results that vary by a factor of two (Winston Revie 2000). There also can be a significant error in the measurement of i_{passive} when the passive current is close to or less than the reduction exchange current density, i_0 . Hence, this method must be used with care. Since the corrosion current, i_{corr} , is equal to the anodic passivation plateau current (Carnot et al. 2002), the Tafel form does not hold at the anode. Consequently the Tafel equation (Equation 2-29).

$$\eta = \beta \log\left(\frac{i}{i_0}\right) \quad (2-29)$$

can not be used to calculate the corrosion current in the passive stage

2.4.2.3 Gravimetric Technique (Weight Loss Method)

This technique is a destructive method. The steel bars in specimens are weighed before and after corrosion occurs. Details of the test procedure for preparing, cleaning, and evaluating corrosion test specimens are described in ASTM G1 (2002). The

difference in the weight is a quantitative average of the amount of corrosion. The average corrosion rate may be obtained as follows:

$$\text{Corrosion Rate} = \frac{K \times W}{A \times T \times D} \quad (2-30)$$

where K = a constant, T = exposure time, A = surface area, W = mass loss, and D = density of corroding metal. The instantaneous corrosion rate cannot be measured in this technique, but only the mean rate during the period of the test. This is the most accurate method of determining total corrosion in laboratory experiments. Although this method is very time consuming and only applicable to laboratory studies, it is useful as a reference for checking results from electrochemical methods.

2.4.2.4 Potentiodynamic/Static Polarization Measurement

The potentiodynamic/static anodic polarization curve is a characterization of the metal by its current vs. potential relationship. The metal specimen is scanned slowly in the positive direction as it corrodes and forms an oxide coating. Investigation of passivation tendencies and the effect of inhibitors or oxidizers on metals are easily performed with this technique. A potentiodynamic anodic polarization curve such as Figure 2-3 can yield important information such as:

1. The ability of the material to spontaneously passivate in a particular medium.
2. The potential region over which the specimen remain passive and the pitting potential.
3. The corrosion rate in the passive region.

According to Princeton Applied Research (1982) the only reliable technique for studying the passivation and depassivation of metals is the anodic polarization curve.

Unfortunately, there is no data in the literature for the steel polarization curve in alkaline media with and without chloride. This technique has been used to study the pitting corrosion of stainless steel in the presence of chloride ions (Egamy and Badaway 2004).

2.5 Durability Model

Different deterioration models can be used to predict the service life of concrete structures due to corrosion-induced damage (Tuutti 1982, Caddy et al. 1983, Bazant 1979, Morinaga et al. 1989, Allan 1995, Bhargava et al. 2005, Maddaway 2007). Quantitative prediction of the time to cracking is useful for establishing the overall deterioration model to predict service life. Mathematical models (Kssir 2002, Du et al. 2006), and empirical equations (Morinaga 1989) for predicting the time to cracking have been proposed. Due to the complexity of the corrosion process in concrete, the observed data from the field and laboratory deviate significantly from predictions using existing models. It is necessary to establish quantitative relationships among the factors that control the time to cracking, so that the time to corrosion cracking and delamination of the concrete cover can be better predicted.

2.5.1 Models for Predicting Concrete Cracking Time

There are different models for predicting the service life of concrete elements due to corrosion damage of steel reinforcement. Tuutti (1982) suggested a model for predicting the service lives of reinforced concrete structures (see Figure 2-10). The maximum acceptable corrosion level is related to the appearance of cracks. The

deterioration process consists of two periods: initiation and propagation. The length of the initiation period can be estimated from the time required for aggressive species to

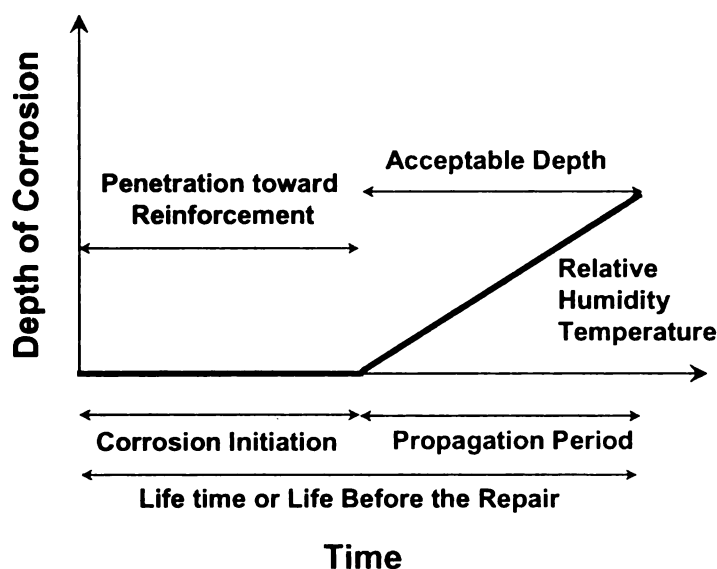


Figure 2-10: Chloride corrosion deterioration process for a concrete element with a mean cover depth of 2 in.

reach reinforcement surfaces and trigger active corrosion, while that of the propagation period can be taken as the time elapse until repair becomes mandatory. Caddy and Weyers (1983) developed a qualitative deterioration model based on field and laboratory data that

has been used to estimate the time to rehabilitate concrete bridge decks. The quantitative prediction of time to cracking is useful for establishing the overall deterioration model to predict the service life. Mathematical models (e.g., Bazant 1979), empirical equations (e.g., Morinaga 1989), or finite element models (e.g., Wang; 1993, and Dagher 1992) for predicting the time to the cracking of concrete cover have been proposed over the past three decades. Due to the complexity of the corrosion process in concrete, the observed data from the field and laboratory deviate significantly from existing models. To better predict the time to corrosion cracking of cover concrete, it is necessary to establish quantitative relationships among all the factors that affect the corrosion.

2.5.1.1 Cady-Weyers's Deterioration Model

Cady and Weyers (1983) proposed a determination model to estimate the remaining life of concrete bridge components in a corrosive environment. The model predicts the percentage of the entire deck that is deteriorated. The total area of spalls, delaminations, asphalt patches, and crack lengths multiplied by a tributary width are combined to calculate total damage.

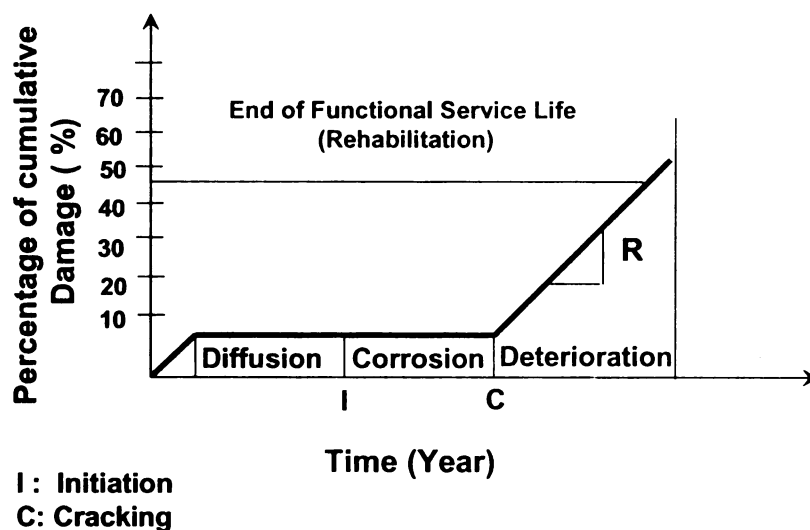


Figure 2-11: Caddy and Weyer's deterioration model

According to Cady-Weyers's model, the corrosion rate is the key to predicting the time to cracking. The corrosion rate is largely controlled by the rate of oxygen

diffusion to the cathode, resistivity of the pore solution, and temperature. Their model involved three different stages: diffusion, corrosion, and deterioration.

2.5.1.2 Bazant's Model for Time to Cracking

Based on the theoretical electrochemical model for corrosion, Bazant (1979) suggested a simplified model to calculate the time to corrosion cracking of the concrete cover. The model considers the volume expansion due to the formation of hydrated red rust, $\text{Fe}(\text{OH})_3$, over the residual rebar core. When the corrosion reaches steady state with

a constant rate, the deformation of concrete at cracking can be related to the duration of the steady state corrosion by

$$t_{corr} = \rho_{corr} \frac{D \Delta D}{P J_r} \quad (2-31)$$

where ρ_{corr} is the combined density of steel and rust, D is the diameter of the bar, ΔD is the increase in the bar diameter, P is the perimeter of the rebar, and J_r is the instantaneous corrosion rate. According to Bazant's model, the time to cracking is a function of corrosion rate; cover depth, spacing, and certain mechanical properties of concrete. Unfortunately, Bazant's model has never been validated experimentally. The predicted time to cracking calculated from Bazant's model is much shorter than observed values (Newhouse 1996, Peterson 1993).

2.5.1.3 Morinaga's Model

Morinaga developed an empirical model based on field and laboratory data to compute the amount of corrosion, Q_{corr} , which causes the concrete cover to crack. The expression to estimate Q_{corr} is

$$Q_{corr} = 0.602 \left(1 + \frac{2C_v}{D} \right)^{0.85} D \quad (2-32)$$

where C_v is the concrete cover, and D is the diameter of the bar. The time to cracking is estimated as

$$t_{corr} = \frac{Q_{corr}}{i_{corr}} \quad (2-33)$$

where i_{corr} is the corrosion current and t_{corr} is the corrosion time.

According to Morinaga's equation, the time to cracking is a function of the corrosion rate, concrete cover, and reinforcement size, but no expression for i_{corr} is given in this model. This model predicts an even shorter time than Bazant's model for concrete cracking.

2.5.1.4 Wang and Zhao's Model

Wang and Zhao (1993) suggested a step method of using finite element analysis to determine the thickness of the corrosion products, Δ , corresponding to the time when the surface concrete cracks. Further, by analyzing a large amount of laboratory data, they established an empirical equation to determine the ratio of the thickness of corrosion products to the depth of the rebar as a function of the cubic compression strength of concrete:

$$\frac{\Delta}{H} = \gamma = 0.33 \left(\frac{D}{C_p} \right)^{0.565} f_{cu}^{1.436} \quad (2-34)$$

The time to corrosion cracking of the concrete cover is then calculated as

$$t_{\text{corr}} = \frac{H}{P_r} \quad (2-35)$$

where P_r is the penetration rate of the rebar due to corrosion.

2.5.1.5 Dagher and Kulendran's Model

Dagher and Kulendran (1992) also performed finite element modeling of corrosion damage in concrete. This numerical model is rather versatile in terms of estimating the radial bar expansion D , and includes: (a) a number of options for modeling crack formation; (b) the ability to accept any shape of corrosion around the bar; and (c) the ability to incorporate dead and live load stresses and initial shrinkage and temperature cracks in the analysis. However, this work requires further development to make it capable of service life prediction (Ahmad 2003).

2.5.1.6 Bhargava et al. Model

Bhargava et al. (2005) also developed a mathematical model for cracking of the concrete. The problem was modeled as a boundary value problem wherein the governing equations are expressed in terms of the radial displacement and the analytical solutions are presented considering a simple two-zone model for the cover concrete that may be cracked or uncracked. First, porous zone that is assumed to exist around the steel reinforcement and the surrounding concrete is not subjected to any pressure until the porous zone fills up with rust products. The model assumes that this porous zone takes care of the problem of evenly applied pressure on the concrete cover, and the cracking occurs when the hoop stress exceeds the tensile strength of the concrete. A bilinear model was used for the tensile strength of concrete and the effect of softening due to opening of cracks. The internal pressure and corrosion current were considered and an equation to predict the cracking time was presented.

2.5.1.7 Maadawy and Soudki Cracking Model

Maadawy and Soudki (2007) also worked on the initiation time for concrete cover cracking. The model predicts the time from corrosion initiation to corrosion cracking. A relationship between steel mass loss and internal radial pressure caused by the expansion of corrosion products was developed. The concrete around a corroding steel reinforcing bar was modeled as a thick-walled cylinder with a wall thickness equal to the smallest concrete cover. The concrete ring was assumed to crack when the tensile stresses in the circumferential direction at every part of the ring has reached the tensile strength of concrete. The internal radial pressure at cracking was then determined and related to the steel mass loss. Faraday's Law was then utilized to predict the time from corrosion initiation to corrosion cracking. The model accounts for the time required for corrosion products to fill a porous zone before they start inducing expansive pressure on the concrete surrounding the steel reinforcing bar. The cracking time of the concrete was expressed as

$$T_{cr} = \left[\frac{7117.5(D + 2\delta_0)(1 + \nu + \psi)}{iE_{ef}} \right] \left[\frac{2Cf_{ct}}{D} + \frac{2\delta_0 E_{ef}}{(1 + \nu + \psi)(D + 2\delta_0)} \right] \quad (2-36)$$

where D = the diameter of the steel reinforcement, δ_0 = the thickness of the porous zone, ν = the Poisson's ratio of concrete, i is the corrosion current, E_{ef} is the effective elastic modulus of the concrete cylinder, and

$$\psi = \frac{D'^2}{2C(C + 2D')} \quad (2-37)$$

$$D' = D + 2\delta_0 \quad (2-38)$$

2.5.2 Discussion of Existing Models

It is well-recognized that both corrosion rate and cover depth have a large effect on the time to cracking as shown in Bazant's and Morinaga's equations. As mentioned earlier, the estimated time to cracking predicted by existing models is significantly shorter than those observed in field and laboratory studies. This may be related to the complexity and properties of the corrosion products and corrosion processes. Also, none of these models account for the fact that some of the corrosion products will diffuse into the concrete while some account for a very thin porous layer surrounding the steel bar that is first filled by the corrosion products. However, no measurement of the porous layer was made and the thickness of this layer was simply assumed based on the general interfacial transition zone (ITZ) for concrete. The models also use a simple linear function to describe the relationship between growth of rust products and time, which may be the reason why the time to cracking due to corrosion is underestimated. They do not consider the fact that corrosion may slow down after some time due to the lack of oxygen and the presence of a thick rust layer. Also, some of the models were purely mechanical models, did not calculate the corrosion current, and the calibration and validation of the model was based on cracking of concrete under accelerated corrosion induced by an external current impressed through the steel bar to be corroded.

Corrosion is an electrochemical process, and strongly dependent on environmental factors (temperature, relative humidity, rainfall, etc.) and properties of the concrete. These factors act simultaneously on the corrosion process during the service life of the structure, and interact with one another. The interaction model for the corrosion rate has not been well-established due to the complexity of the problem and the lack of

long term corrosion data. It is necessary to develop a model of the corrosion rate that accounts for changes in the environmental conditions, and one that is not simply a steady-state model. For corrosion-induced cracking of concrete it is also essential to develop a model of the pressure build-up due to rust production and calculate the stress and strain distributions around the corroded bar, so that the service life of the reinforced concrete structure can be better predicted.

Much of the research related to corrosion in concrete has been done using the accelerated corrosion test. There is no standard specification for the accelerated corrosion test, and all of its complexities are not well understood. A clear understanding of the electrochemical reactions involved in the accelerated corrosion test is necessary for its effective and accurate use.

2.6 Corrosion and Repair

Corrosion reduces the strength, durability, and service life of reinforced concrete structures. As the reinforcement corrodes, it expands causing cracking of concrete and spalling. The deterioration caused by corrosion of reinforcing steel in concrete structures has been recognized as one of the greatest maintenance challenges (Beaudette 1991). Corrosion should therefore be treated before it becomes a significant problem. Since the presence of both air and water is required for the corrosion activity to continue, corrosion may slow down considerably if a barrier could reduce the diffusion of moisture and harmful ions like chloride and carbonate through the concrete. In many cases a patching approach to concrete repair is adopted in which the damaged concrete is removed, the reinforcing steel is cleaned, and the area is patched with a patching compound. However,

in many situations repairs of this nature will accentuate corrosion in the adjacent steel bar. This phenomenon is often referred to as “ring anode” corrosion (Beaudette 1991). Ring anode corrosion results from electrochemical incompatibilities between the repair and the concrete substrate. Differences between the base concrete and repair can create an electrical potential difference which drives a new corrosion cell across the interface between the patch and the concrete substrate. Factors that can lead to this corrosion problem include differences in chloride ion content, pH, and permeability (Beaudette 1991). These factors may lead to increased corrosion in the repaired part, especially at the interface of the patch and concrete substrate, and consequently cause damage to the patch material. Even for the most promising patching products the cracking and full or partial delamination of the patching material from the concrete substrate due to corrosion is generally unavoidable, and can lead to premature failure of the patch.

Chapter 3

Experimental Characterization

3.1 Introduction

This chapter focuses on the experimental investigation of the corrosion of steel bars in concrete. Corrosion is a very long term process in nature, and studying the effect of the corroding bar on the concrete may take years. Due to the long time required for natural corrosion, an accelerated corrosion test using impressed current is used in this study to evaluate the effect of corrosion damage on concrete structures. Accelerated corrosion has been used by other researchers (Batis and Routoulas 1999, Hart 1979). This chapter first presents results of a comprehensive study performed on the accelerated corrosion test using different chloride concentrations and potential levels to determine the

accuracy of using Faraday's law on estimating the mass loss in accelerated corrosion tests. After determining the conditions under which Faraday's Law will give the most accurate results, accelerated testing was conducted to investigate the growth of the rust layer over time, the pressure induced by the rust products on the concrete cover, and eventually the time for the cracking of the concrete cover.

The accelerated corrosion test was conducted under a microscope to measure the rust thickness as a function of time under a constant applied current. Also, the effect of the rust growth layer on the pressure and consequently on the stress and strain distribution in the concrete cover was investigated.

The results of the experimental investigation on corrosion presented in this chapter were used to calibrate and validate the model presented later.

3.2 Accelerated Corrosion Test

Accelerated corrosion testing using an impressed current is often used to study the effect of corrosion in a reasonable time frame. In this method the mass loss is calculated using the circulated charge and Faraday's Law. Although accelerated corrosion testing has been used extensively, no standard test procedure exists, and researchers use a variety of applied potentials and chloride concentrations (Lee et al. 2000). A careful study has not been performed to assess whether Faraday's Law yields accurate results of mass loss at any arbitrary voltage and chloride concentration. The accuracy of using Faraday's Law to estimate the mass loss in accelerated corrosion tests was investigated in this study. The test was done with steel electrodes in solution as well as in concrete. The purpose of the study was to establish guidelines for accelerated corrosion testing and to minimize the

error when estimating the mass loss using Faraday's Law. This can also help researches better understand the electrochemistry associated with the test.

3.2.1 Accelerated Corrosion Testing Overview

In accelerated corrosion testing an external power supply is used to impress current through reinforcing bars. The moisture and chloride in the concrete specimens and the impressed current induces corrosion in the anodic reinforcing bars in an accelerated fashion. Usually, the applied voltage across each specimen remains constant during the test. The impressed current is monitored during the test and Faraday's Law is used to estimate the overall mass loss of the anodic steel bar assuming that the entire current passed through the anode oxidizes the steel (Pantazopoulou and Papoulia 2001).

Since the current has to be transmitted from the anode to the cathode and the electrical resistance of dry concrete is very high, specimens are usually wetted with salt water to increase the electrical conductivity between the anode and the cathode. Researchers have used salt water with NaCl content varying from 3% to 5% by weight of solution to wet the specimens for short periods of time (Boyar et al. 1990, Baiyasi and Harichandran 2001). There appears to be no basis for the concentration of NaCl used and in some cases even unsalted water has been used with the chloride added to the concrete mixture. It is not clear why salt is needed when the anodic bars are forced to corrode with an impressed current. Also, the applied voltage used by researchers has varied from a minimum of 12 V (Baiyasi and Harichandran 2001) to a maximum of 60 V (El Maaddawy 2006). Since no standard test method exists for accelerated corrosion testing,

it is also not apparent whether Faraday's Law gives a reasonable estimate of the mass loss under all test conditions.

3.2.1.1 Electrochemical Concepts

The accelerated corrosion test is based on the assumption that all of the current passing between the electrodes produces ferrous ions at the anode as in natural corrosion i.e,



The mass loss will be proportional to the current passed and is calculated using Faraday's Law:

$$\Delta m = \frac{A_m}{nF} \int_0^T I(t) dt \quad (3-2)$$

where Δm = steel loss in grams , $I(t)$ = measured current in amperes at time t , T = duration of the test in seconds, A_m = atomic mass of Fe , n = valency (assuming that the rust product is mainly $\text{Fe}(\text{OH})_2$, $n = 2$), and F = Faraday's constant (96485 coulomb per mol). In natural corrosion of iron, the cathodic reaction is the reduction of oxygen to hydroxide ions according to:



In accelerated corrosion testing attention is not paid to the cathodic reaction since focus is mainly on the anodic reaction. However, knowledge of the reactions that take place at both the anode and the cathode clarifies the entire processes involved in the test. Only few studies have compared the real mass loss and that estimated through Faraday's

Law (El Maaddawy et al. 2006). Figure 3-1 shows the comparison between the real mass loss and that estimated using Faraday's Law in one study using accelerated corrosion test specimens (Harichandran and Nossoni 2007, 2008).

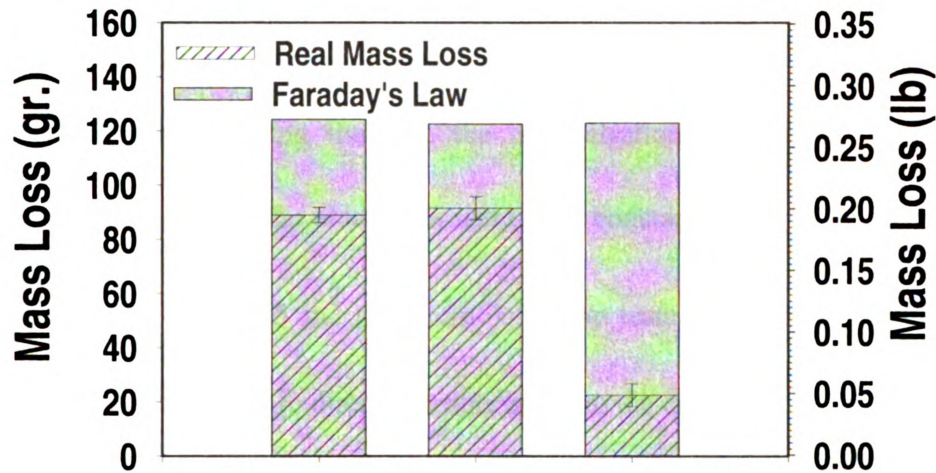


Figure 3-1: Comparison between real mass loss and that estimated using Faraday's Law (Nossoni and Harichandran 2007)

In this test, all the specimens were exposed to the same wetting and drying cycles with 3.5% salt solution, and the impressed current was approximately the same for all specimens. The anode and the cathode consisted of steel bars embedded within the concrete. However, three type of specimen were used: (1) regular concrete control specimens; (2) specimens repaired along one surface with a polymer concrete patch; and (3) specimens repaired with both a polymer concrete patch and a fiber reinforced polymer (FRP) sheet along one surface. As Figure 3-1 shows, the error in using Faraday's Law varied from 27% to 84% in this particular study. The results of this test provided the motivation to study the accelerated corrosion test in greater detail.

3.2.2 *Experimental Tests*

Comprehensive experiments were conducted using the accelerated corrosion test. Since it is difficult to control the environment precisely and inspect the anodic and cathodic reactions when the test is performed on concrete specimens with embedded electrodes, the accelerated corrosion test was initially performed in a solution. Two parameters were varied during the test: the concentration of chloride ions, and the current. The surface area of the electrodes were kept constant at 0.542 in^2 (3.5 cm^2) for the tests in solution and 2.25 in^2 (14.5 cm^2) for the tests in concrete, so the current densities for each test type were directly proportional to the currents.

Two different constant currents of 0.25 A, and 0.5 A were used for tests in three different solutions having pH values of 13.95, 13.70 and 13.50, the chloride concentration was varied from 0 to 1000 mMol, and 3 test specimens were used for each combination. For the concrete specimens, two constant currents of 0.025 A and 0.25 A and four different chloride concentration were used, and 6 specimens were tested for each combination.

3.2.2.1 Accelerated Corrosion Test in Solution

Concrete has a very high pH (12.5-13.5). The same species as in the concrete pore solution were used to formulate the solutions in which steel electrodes were immersed. Table 1 shows the concentration of the species for the different concrete pore solutions reported in the literature (Bertolini et al. 2004).

Table 3-1: Solution Properties

	[Na(OH)] (mMol)	[Ca(OH) ₂] (mMol)	[K(OH)] (mMol)	Calculated pH
Solution 1	271	1.0	629	13.95
Solution 2	130	0.0	380	13.70
Solution 3	85	0.0	228	13.49

The test was done using constant current control and the voltage was monitored.

Regular #3 reinforcing steel bars were used as the anode and the cathode.

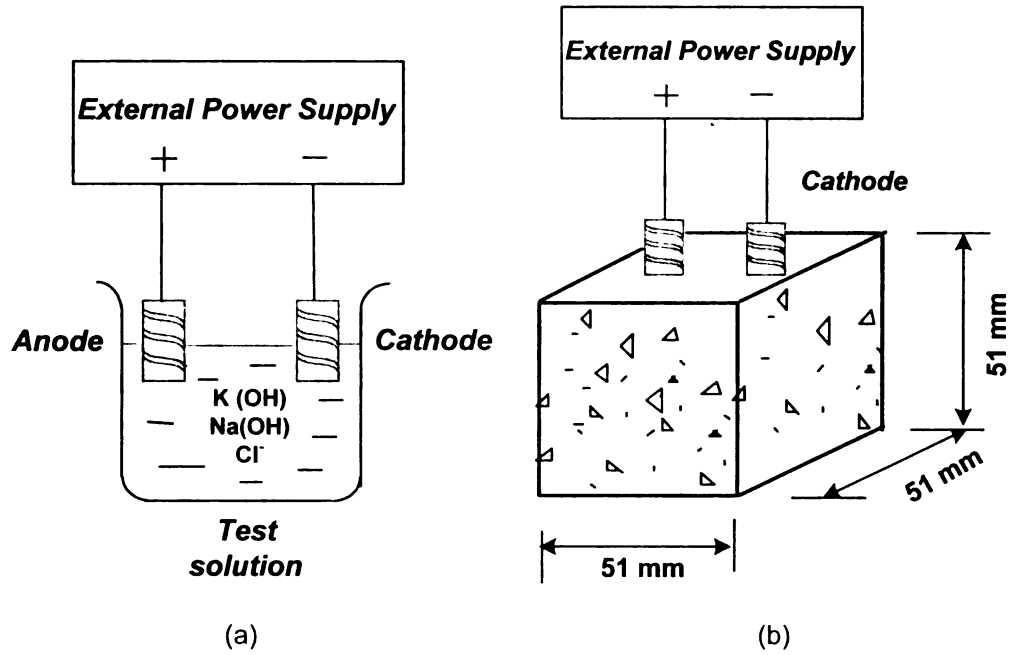


Figure 3-2: Accelerated corrosion test set-up in: (a) solution, and (b) concrete

Figure 3-2 (a) shows the set up for the test in solution. The anode was weighed before and after the test according to ASTM G1-90 (2002), and the mass loss was calculated using both Faraday's Law and the measured weights. The accuracy of Faraday's Law was characterized using the current efficiency defined as:

$$\text{Current efficiency} = \frac{\text{current inducing corrosion}}{\text{total current}} = \frac{m_R}{m_F} \quad (3-4)$$

where m_R = real mass loss, and m_F = mass loss calculated using Faraday's Law. The solution was discarded after each test and a fresh solution was used, and the distance between the two electrodes was kept constant. Since high current densities were used compared to the size of the specimens for the test conducted in the solution, the current was impressed only for 20 minutes. The pH of the solution close to the anode and cathode was also monitored during the test to monitor the change in the pH of the solution adjacent to the anode and cathode.

3.2.2.2 Accelerated Corrosion Test in Concrete

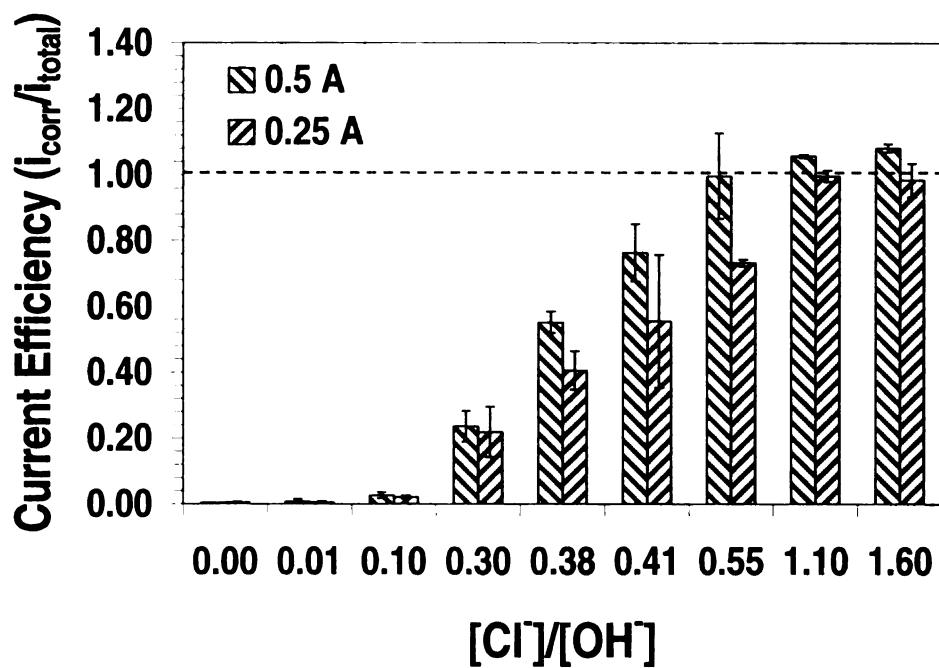
The accelerated corrosion test was also conducted on concrete specimens. A standard concrete mix with Type I cement, water cement ratio of 0.4, and cement factor of 500- kg/m^3 with a maximum aggregate size of 3/8 of an inch (9.5 mm) was used. Small concrete cubes with dimensions of $2 \times 2 \times 2$ in ($51 \times 51 \times 51$ mm) and two #3 bars electrodes were used, with one bar as an anode and the other as a cathode, and a constant distance of 1 in (25 mm) between the electrodes. Figure 3-2(b) illustrates the test set-up. Four different chloride concentrations of zero, low (0.5%), medium (3.5%), and high (saturated) were used. The specimens were immersed in salt solutions of different concentrations for one week to obtain steady-state conditions before conducting the test. The specimens needed to be in a steady state condition at the beginning of the test to avoid any variation in chloride concentration adjacent to the anode due to diffusion (Austin et al. 2004). Since the electrical resistance of concrete is much higher than that of the solutions, only two fixed currents of 0.025A and 0.25 A were used and the voltage

was monitored. The effect of chloride concentration on the anodic reaction was studied using the current efficiency defined in Equation 3-4. Specimens were immersed in deionized water with K(OH) dissolved to improve electrical conductivity. K(OH) having a pH of 9 was used instead of salt to improve the conductivity so that the chloride concentration adjacent to the anode would not increase and introduce error when cracks occurred. Each test lasted for two days for the current of 0.025 A and 8 hours for the current of 0.25 A. Both the anode and the cathode were weighed before and after each test. The steel outside the concrete experienced some corrosion during the curing period. The mass loss of the cathode was subtracted from the mass loss of the anode to compensate for the corrosion that occurred prior to testing and to estimate the mass loss due to accelerated corrosion testing only.

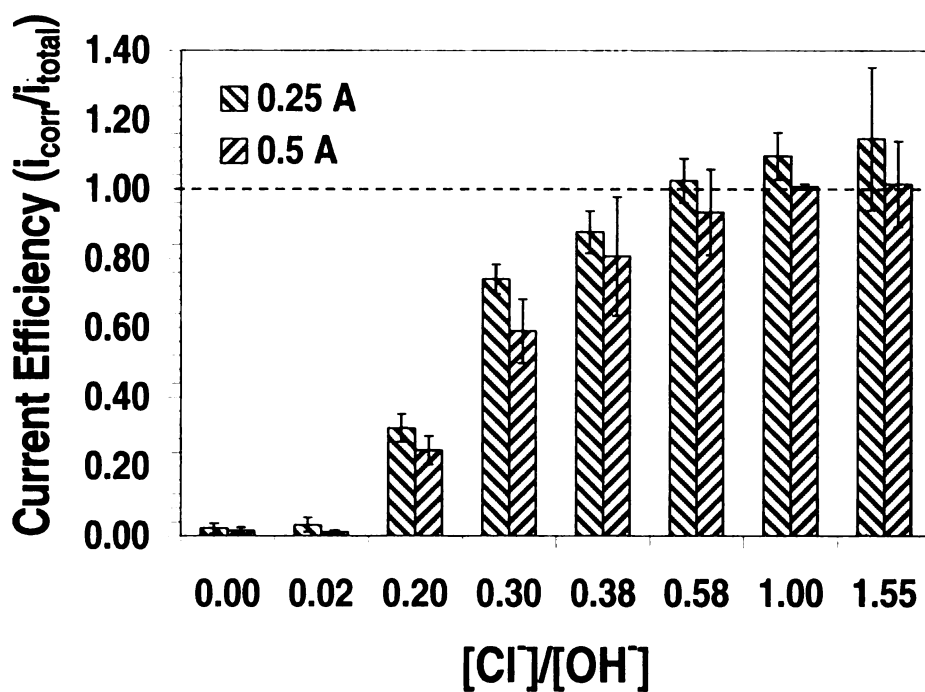
3.3 Results and Discussion

3.3.1 Tests in Solution

The current efficiency as a function of the $[\text{Cl}^-]/[\text{OH}^-]$ ratio for the accelerated corrosion test in solution are presented in Figure 3-3 for different solutions. The values shown are the average of the replicate results obtained at each current and chloride concentration. The 95% confidence interval for each set of measurements is shown as error bars in the figures. Calculated efficiencies of greater than 1.0 at high chloride concentrations are probably due to natural corrosion of specimens during the test or measurement error.

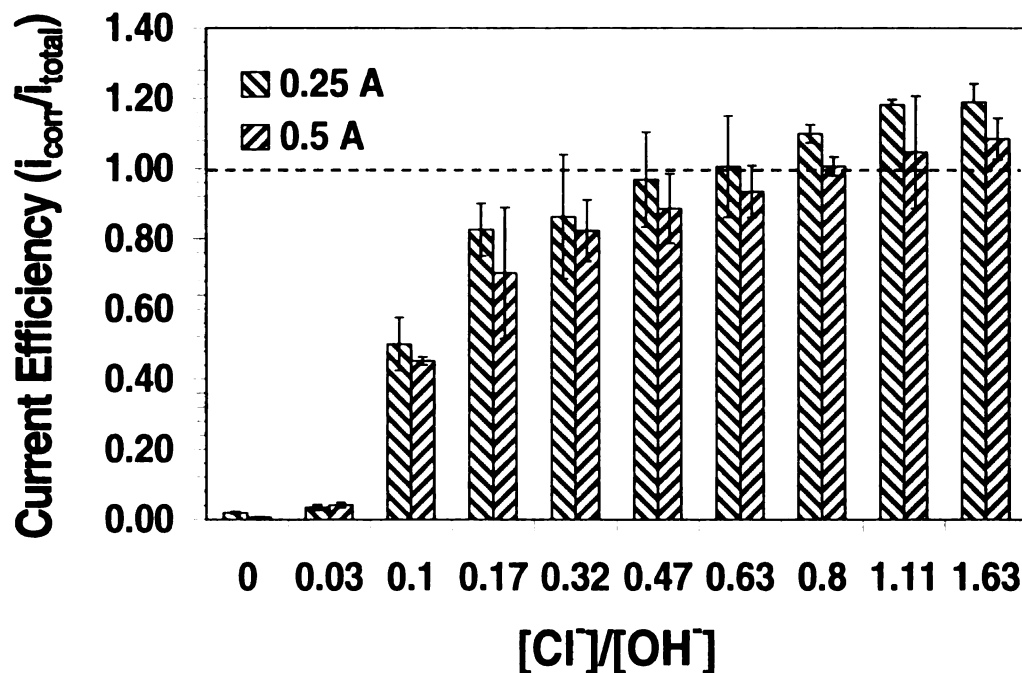


(a)



(b)

Figure 3-3: Accelerated corrosion test results in solution with pH of (a) 13.95, (b) 13.70 and (c) 13.46



(c)

Figure3-3 cont'd: Accelerated corrosion test results in solution with pH of (a) 13.95 , (b) 13.70 and (c) 13.46

3.3.1.1 Effect of Chloride Concentration

The current efficiency increases as the chloride concentration increases, and decreases as the current increases and depends on the pH of the solution. These observations indicate that the anodic reaction is highly dependent on the chloride concentration, and when there is no chloride or when the concentration of chloride compared to hydroxide ions is very low, the current does not oxidize the steel as indicated in Equation 3-1. Therefore another reaction must take place at the anode when the chloride concentration is very low, and at least two reactions must occur when the chloride concentration is moderate.

Figure 3-3(a) shows that oxidation of steel at the anode gradually increases as the concentration of chloride increases. The current efficiency increases until it reaches 1.0 when $\chi = [\text{Cl}^-]/[\text{OH}^-] \approx 0.55$. The current efficiency is only 0.73 when the current is 0.5 A, and the current efficiency reaches 1.0 only at $\chi = 1.10$. This shows that higher chloride concentrations are required when the impressed current is high if most of the current is to oxidize the steel.

Figure 3-3(b) and (c) show that at lower pH values less chloride is needed to initiate corrosion, and the oxidation of iron is the primary reaction even at smaller value of χ . Figure 3-3(b) shows that for a pH of about 13.70, χ should be almost 0.6 for the current efficiency to reach 1.0. Figure 3-3(c) shows that when the pH is 13.50, oxidation of steel is the primary reaction even at the low χ value of 0.35, but a χ value of about 0.6 is still required for the current efficiency to become 1.0.

3.3.1.2 Effect of pH

Figure 3-4 shows a direct comparison of the current efficiency for all three solutions for an impressed current of 0.25 A. For a given χ value, when the pH of the solution is lower the current efficiency is higher. This means that a smaller chloride concentration is needed to initiate corrosion at lower pH values. Thus both pH and the $\chi = [\text{Cl}^-]/[\text{OH}^-]$ ratio affect the current efficiency in accelerated corrosion testing. However, even at lower pH values, the $[\text{Cl}^-]/[\text{OH}^-]$ ratio needed to reach the current efficiency of 1.0 is about 0.55 to 0.65, and is very similar to the ratio that is needed for natural corrosion to begin in normal concrete.

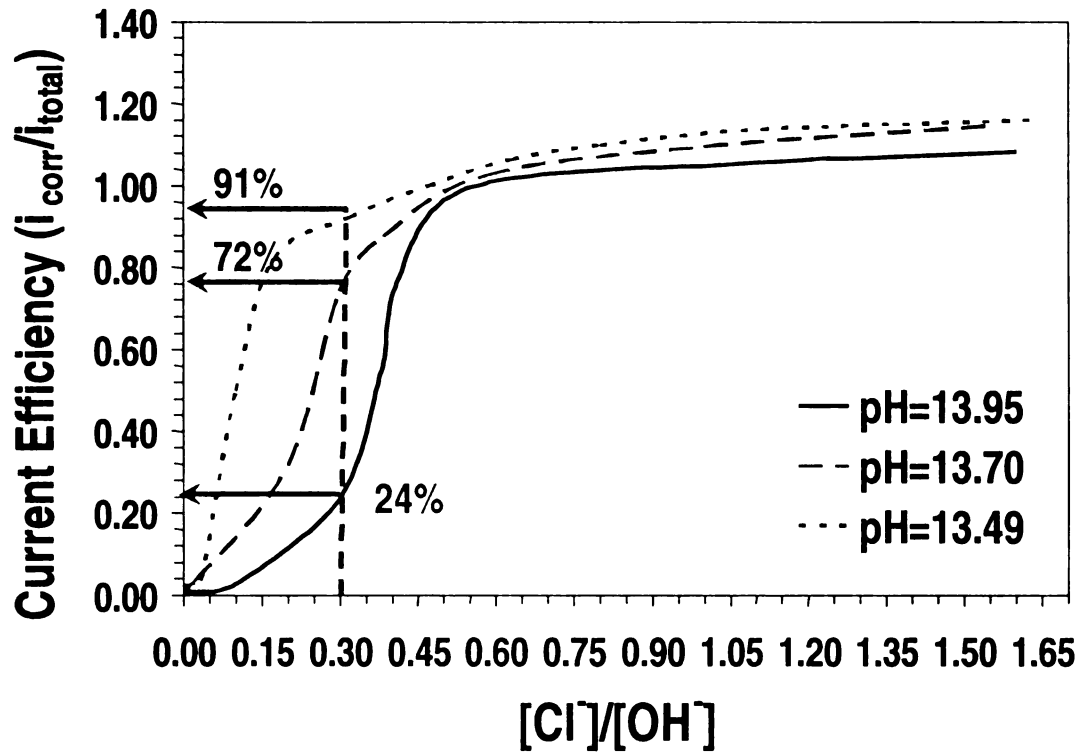


Figure 3-4: Effect of pH on the accelerated corrosion test results for different chloride concentration

3.3.1.3 Effect of Impressed Current Magnitude

At high current densities, it is possible that the oxidation at the anode produces either predominantly Fe^{3+} ions, or both Fe^{2+} and Fe^{3+} ions, so that n will be greater than 2 in Equation 3-1, and the mass loss calculated using Faraday's Law will be smaller than that obtained with $n=2$. In this case, the calculated current efficiencies will be higher.

Figure 3-5 shows a comparison of the current efficiency for $n = 2$ and $n = 3$ for the current of 1 A in the solution with a pH of 13.95. The difference between the two mass loss calculations may explain the drop in current efficiency at the high current of 0.5 A in Figure 3-3 for any given chloride concentration. However, as Figure 3-5 shows, for $[\text{Cl}^-]/[\text{OH}^-] > 0.55$ the current efficiency becomes significantly larger than 1 for $n = 3$

and is less than 1 for $n = 2$, indicating that at high current densities Fe^{3+} is most likely produced in the first oxidation reaction in addition to Fe^{2+} . Figure 3-3 indicates that at lower current densities, Fe^{2+} appears to be the predominant product of steel oxidation.

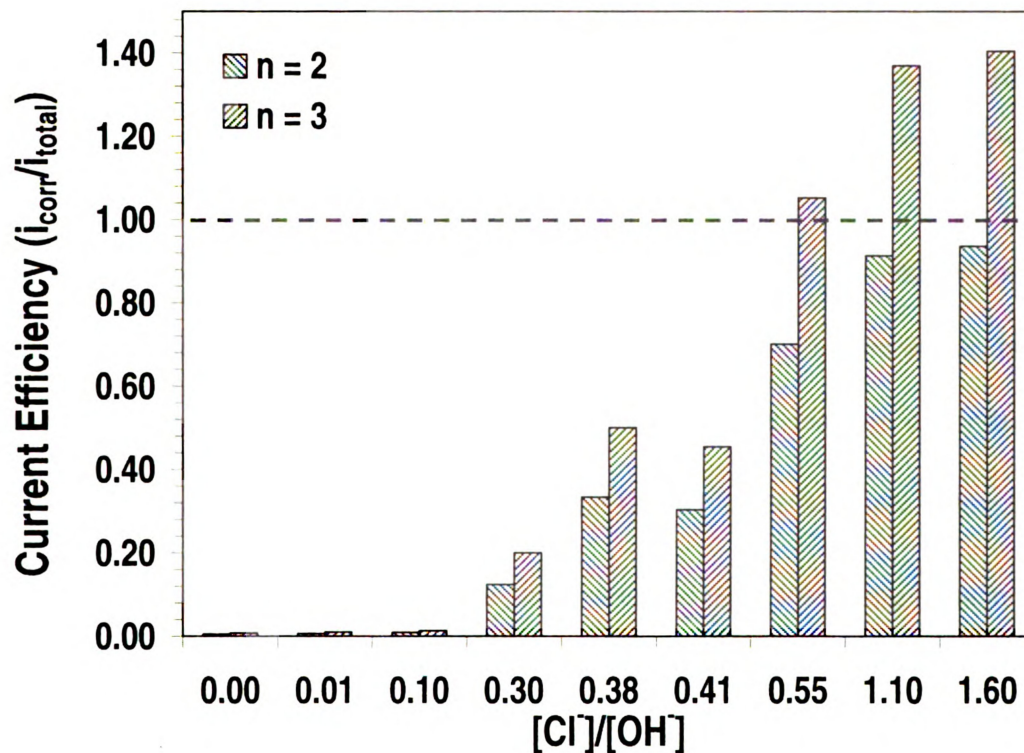
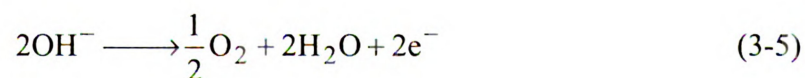


Figure 3-5: Comparison between $n = 2$ and $n = 3$

3.3.1.4 Corrosion Mechanism

Figure 3-6 shows the appearance of the anode, cathode and solution for three different chloride concentrations for the test in solution having a pH of 13.95. When no chloride exists in the solution the only reaction that takes place is the splitting of water to produce oxygen at the anode and hydrogen at the cathode according to the reactions



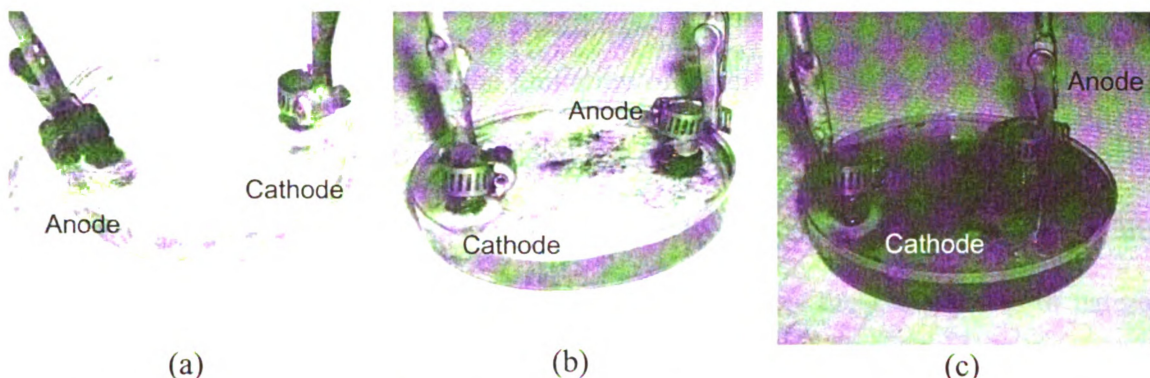
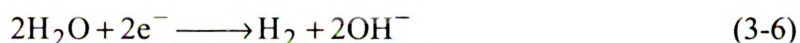


Figure 3-6: Appearance of anode, cathode and solution after 15 minutes of testing at chloride concentrations of: (a) 0 mMol, (b) 250 mMol, and (c) 500 mMol



With increasing chloride concentration the reaction at the anode gradually changes to oxidation of steel. There is a competitive reaction at the anode between oxidation of steel and oxygen production, and the rate of each reaction depends on the chloride concentration or $\chi = [\text{Cl}^-]/[\text{OH}^-]$ ratio and the pH of the solution. When there is insufficient chloride and the χ value is low, the calculated mass loss using Faraday's Law will not be accurate, since only a part of the impressed current oxidizes the steel at the anode.

Tests in Concrete

The results of the accelerated corrosion tests in concrete are presented in Figure 3-7 for impressed currents of 0.025 A and 0.25 A, and follow the same trend as the results of the tests in solution. The error bars show the 95% confidence interval for each measurement. When no chloride exists in the system, the current efficiency is about 0.30 and 0.35 for the currents of 0.025 A and 0.25 A, respectively, and increases to 0.6 and 0.52 when the chloride concentration is increased to 0.5%. It is somewhat surprising that

for the test in concrete some oxidation of steel occurs even when there is no chloride present. This is most likely due to the limitation of water in concrete. When the splitting of water exhausts all the water available in the concrete adjacent to the anode, the only reaction that can take place is oxidation of the steel. The current efficiencies slightly greater than 1.0 obtained for high chloride concentrations is most likely due to natural corrosion during the test or measurement error yielding measured mass losses greater than those estimated through Faraday's Law.

Nevertheless, the results indicate a significant error between the real mass loss and the mass loss calculated using Faraday's Law for both current densities. During the accelerated corrosion test in concrete, hydrogen bubbled out of the concrete surrounding the cathode and a small amount of oxygen was observed at the anode. The splitting of water produces half as much oxygen as hydrogen (see Equations 3-5 and 3-6) and it is more difficult to observe the oxygen produced at the anode for the test in concrete.

As Figure 3-7 indicates, when the chloride concentration is increased to 3.5%, the current efficiency increases to 1.0 for the low current and to 0.86 for the high current. When the water is fully saturated with chloride, the current efficiency for the high current also reaches almost 1.0. However, as shown in Figure 3-1, even a 3.5% salt solution may not result in full current efficiency when the diffusion of chloride and water is restricted. As with the tests in the solution, the generally lower current efficiency for the higher current may be due to the production to Fe^{3+} in addition of Fe^{2+} . However, differences in the current efficiencies for the two currents are not statistically significant at the 95% confidence level for all chloride concentration other than 3.5%.

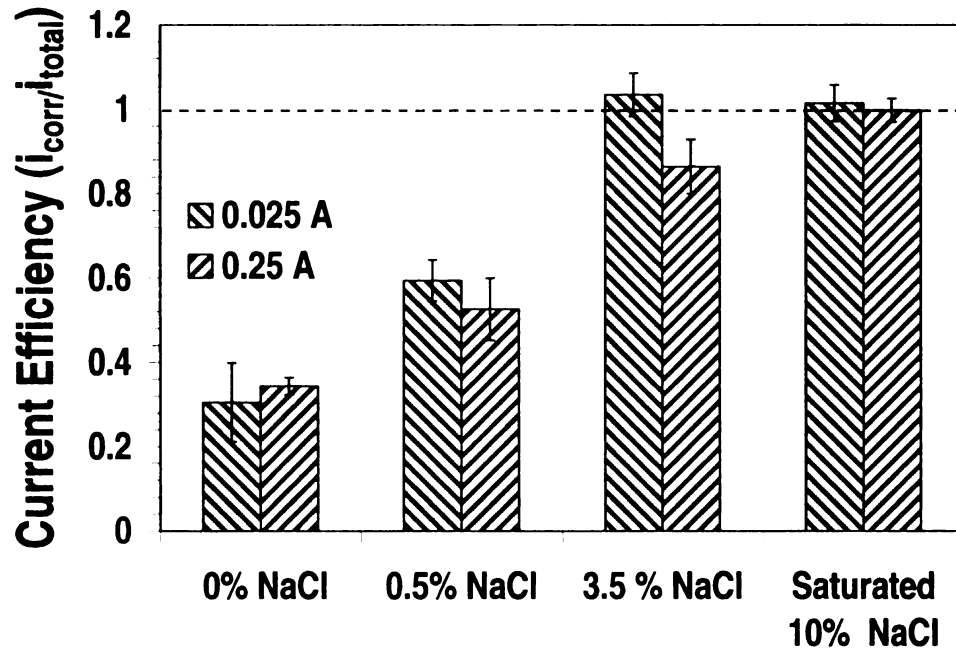


Figure 3-7: Accelerated corrosion test in concrete for different chloride concentration

3.4 Calculation of Rust Thickness

When steel corrodes the rust products have a volume of 2 to 6 times that of the original volume of the steel. The rust products accumulate around the steel bar, and the expansion of the corrosion products apply pressure on the concrete cover that eventually leads to cracking of the concrete cover. The thickness of the rust product has a direct relationship with the applied pressure, but is not necessarily linear during the corrosion time. The thickness of the rust layer depends on many factors such as the volume fraction of different rust products, which in turn depends on the availability of oxygen and water in the system, the confinement pressure exerted by the concrete on the steel bar, diffusion of the rust products into the concrete pores surrounding the steel bar, and current density.

The mechanical properties and the composition of the rust layer are not well known (Care et al. 2008). The main aim of this part of the experimental study was to estimate the cracking time and thickness of the rust layer as a function of the corrosion current density. The thickness of the rust layer was not generally measured in the past as a function of the corrosion current. Only Care et al. (2008) attempted to measure the property of the rust layer along with the rust thickness at different times during the accelerated corrosion test for steel in mortar. Their results had vast variations. However, they did not report the time to cracking of the concrete and the rust thickness at which the concrete cracked. Also the results were based only on one test and there was no repetition in their work or in the literature to confirm their findings. The tests performed in this study were to confirm their results and fill in the missing gaps.

3.4.1 Experimental Program

Experiments were conducted to measure the rust thickness as a function of current density up to the time of cracking of the concrete. The rust thickness was measured under the microscope using photographs were taken at different time intervals, and the time to cracking was obtained as a function of the measured rust thickness. The results of this experiment were used to calibrate the concrete cover cracking model developed in the next chapter.

3.4.1.1 Specimen Preparation

The concrete mix used is shown in Table 3-2. The cement was Portland cement Type I and the maximum coarse aggregate was 3/8". The maximum aggregate size was chosen to be small due to the small dimensions of the specimens. No chloride was added

to the mix. The concrete had a 7-day compressive strength of 6,000 psi and a 28-day strength of 8,300 psi. The specimens were cast in small cylindrical shapes having a thickness of one inch with a #4 carbon steel bar in the middle to serve as an anode. The diameter of the cylinder was chosen to yield the k ratio given by.

$$k = D / d \quad (3-7)$$

to be 3, 4, and 6, where D is the diameter of the concrete cylinder and d is the diameter of the steel bar. Figure 3-8 shows the schematic of the test specimens.

Table 3-2: Mix Proportion of Concrete

	<i>lb/yd</i> ³
Water	385
Cement	939
Sand	1233.5
Gravel	1282.5
Water-Cement Ratio	0.41
Sand-Cement Ratio	0.76

Three #1 carbon steel wires to be used as cathodes were placed equine distant from each other and the anode, close to the outer edge of the specimen as shown for each specimen size, tests were conducted on triplicates specimens.

As explained earlier, a minimum amount of salt is needed even in the accelerated corrosion test so that all the impressed current is consumed in oxidizing the steel bar. Therefore, the test specimens were soaked in 3.5% NaCl by weight for one week before testing. This allowed the chloride concentration at the bar surface to reach a sufficient amount to yield a current efficiency of 1.0.

Before testing, each specimen's top surface was polished with grade 400 sand paper and then cleaned with methanol to expose the steel bars (anode and cathodes). The bottom surface was coated with epoxy to prevent the corrosion products from escaping out from the concrete. Also, the surfaces of the steel bars that were not embedded inside

the concrete and were needed for the electrical connection as shown Figure 3-8 were coated with epoxy to prevent any corrosion in this part and to prevent any variation in current density due to change in electrodes surface area.

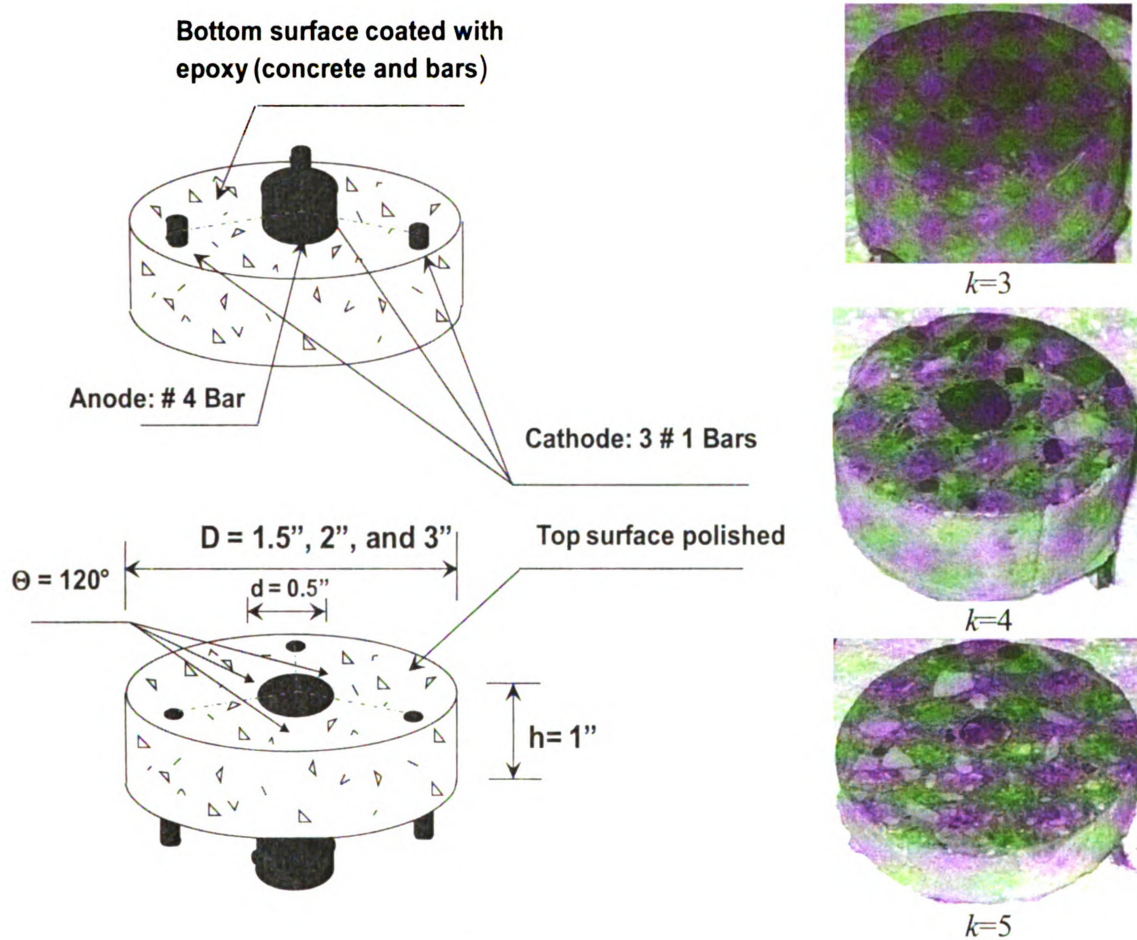


Figure 3-8: Test Specimens

3.4.1.2 Accelerated Corrosion Test and Test Set up

As explained earlier, the accelerated corrosion test consisted of impressing an anodic current to the rebar so that it corrodes in a short time. Figure 3-9 shows the test set up for the accelerated corrosion test under the microscope. A power supply (60-120 V, 0.5-0.25 A) was used to apply a constant and direct current between the anode and cathodes. The applied current was limited to 0.05 A yielding a current density of 0.0045 A/cm^2 .

An optical microscope with a magnification of 25 to 100 was used to capture images of the concrete and steel interface to estimate the rust layer thickness. After immersion in salt water for a week the specimens were surface dried and the test was conducted in a dry condition. This is a more realistical natural condition and prevents any escape of rust product outside the concrete during the test. Initial images were taken before the test began. When the current was impressed, images were captured at 15 to 30 minute intervals depending on the size of specimens. The test was stopped and images of different parts of the steel and concrete interface were captured.

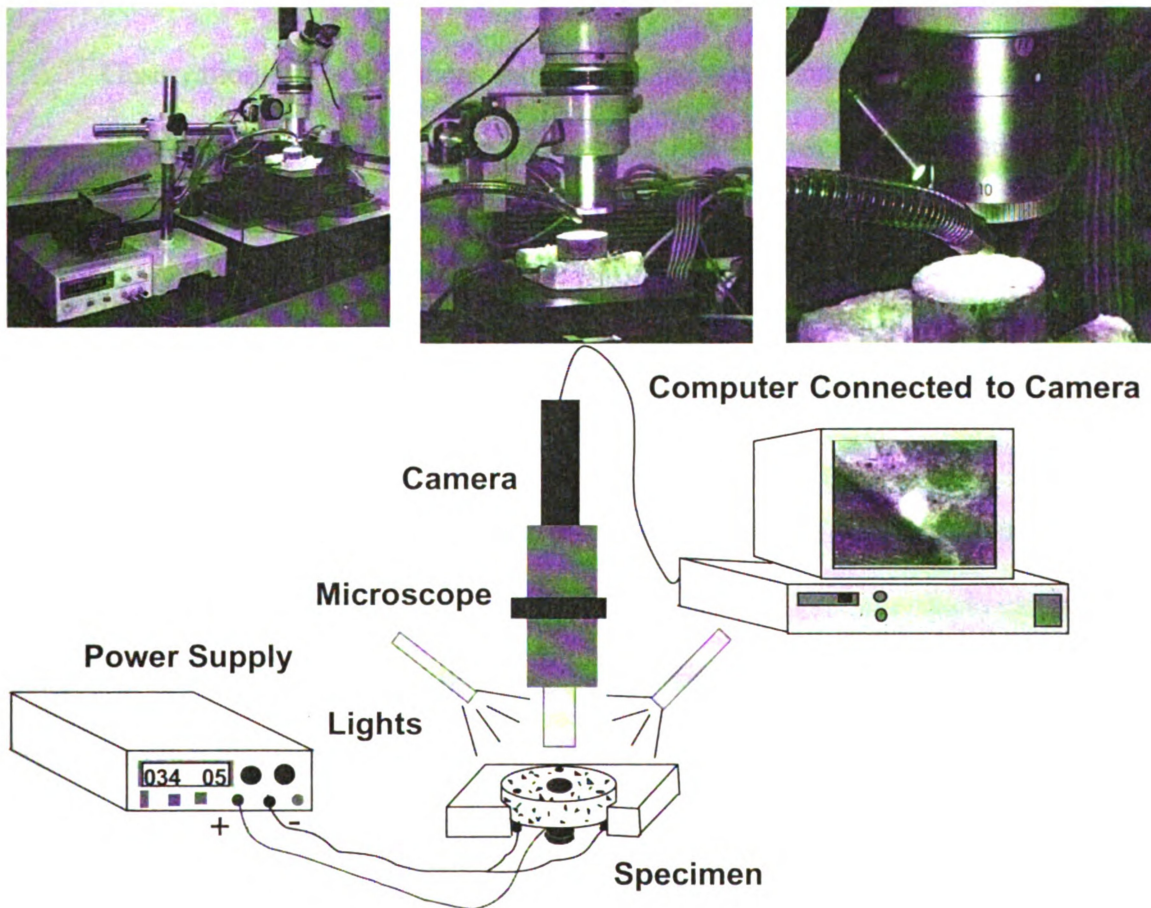


Figure 3-9: Test set up under microscope

Before capturing images the specimen's surface was polished again with sand paper and cleaned with methanol. Methanol was used to minimize damage of the rust layer during the polishing stage since it has minimum reaction with rust. The test was continued up to the first cracking of the concrete and the rust thickness was measured when cracking initiated. Although the main purpose of the test was to estimate the rust thickness and time to concrete cracking as a function of the applied current, the test was continued even after concrete cracking.

3.4.2 Measurement of Rust Thickness

Observation of the specimens subjected to the accelerated corrosion test under the optical microscope allowed measurement of the rate of rust thickness build up as a function of applied current density and time. Figure 3-10 to Figure 3-13 show that during the first 15 minutes of the test no identifiable rust layer can be observed. It is likely that during the first 15 minutes the rust mostly diffused into the micro pores around the steel bar.

After about 30 minutes the rust layer became visible, mostly around the areas where some rust had already accumulated in the pores. The rust thickness was not uniform around the steel bar and the areas surrounding the micro pores had a thicker rust layer than other areas. Figure 3-11 to Figure 3-13 show the build up of the rust layer over time for specimens with different k ratios. Figure 3-10 indicates the time to first cracking of the concrete and the measured rust thickness at that time.

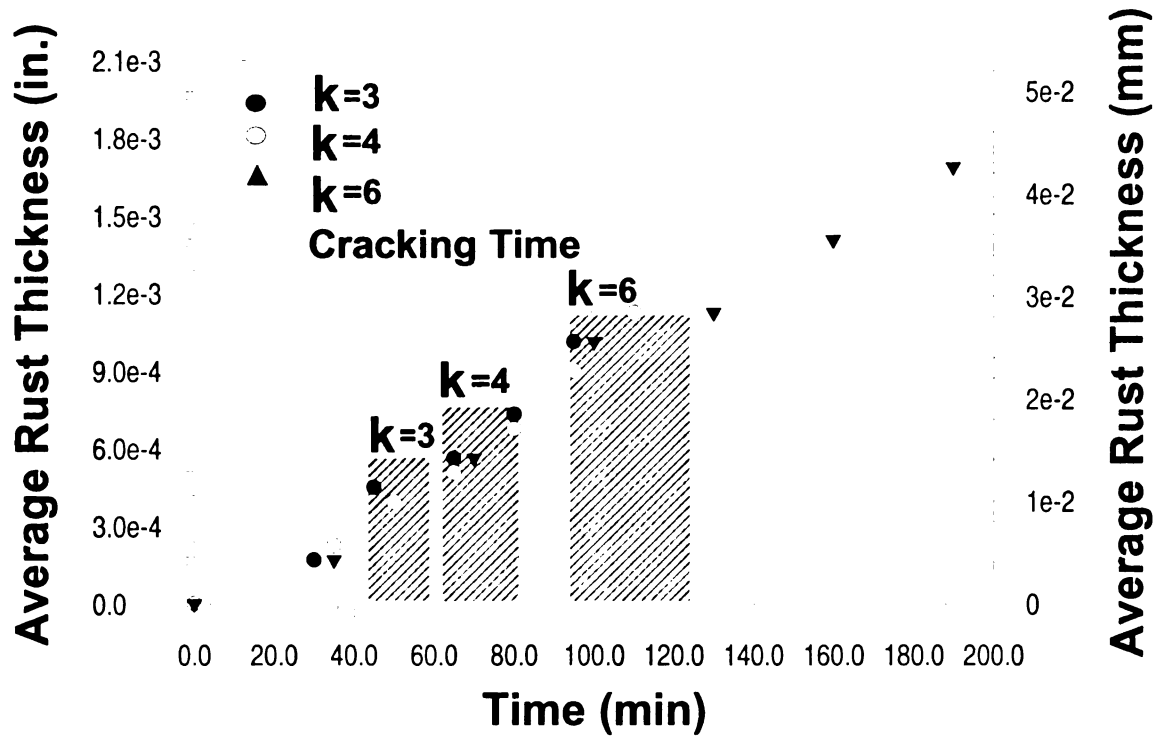


Figure 3-10: Rust thickness over time for specimens with $k = 3, 4,$ and 6

For the $k = 3$ specimens, it took almost 45 to 60 minutes for the first crack to appear, at which time the average rust thickness around the steel bar was between 0.00046 to 0.00056 in., and in some places reached a maximum of 0.0009 in. at 60 minutes. The first crack opened suddenly in the concrete cover. The thickness of the crack in some cases was very thin and it had to be identified using the microscope. Also, the rust thickness was not uniform around the bar. The ratio of the maximum thickness to the average thickness at some points was about 1.65. After cracking of the concrete cover the variation of rust thickness around the steel bar decreased. This may be different than for natural corrosion, since in natural corrosion the concentration of rust products increases locally around the crack opening due to the increased availability of oxygen and moisture.

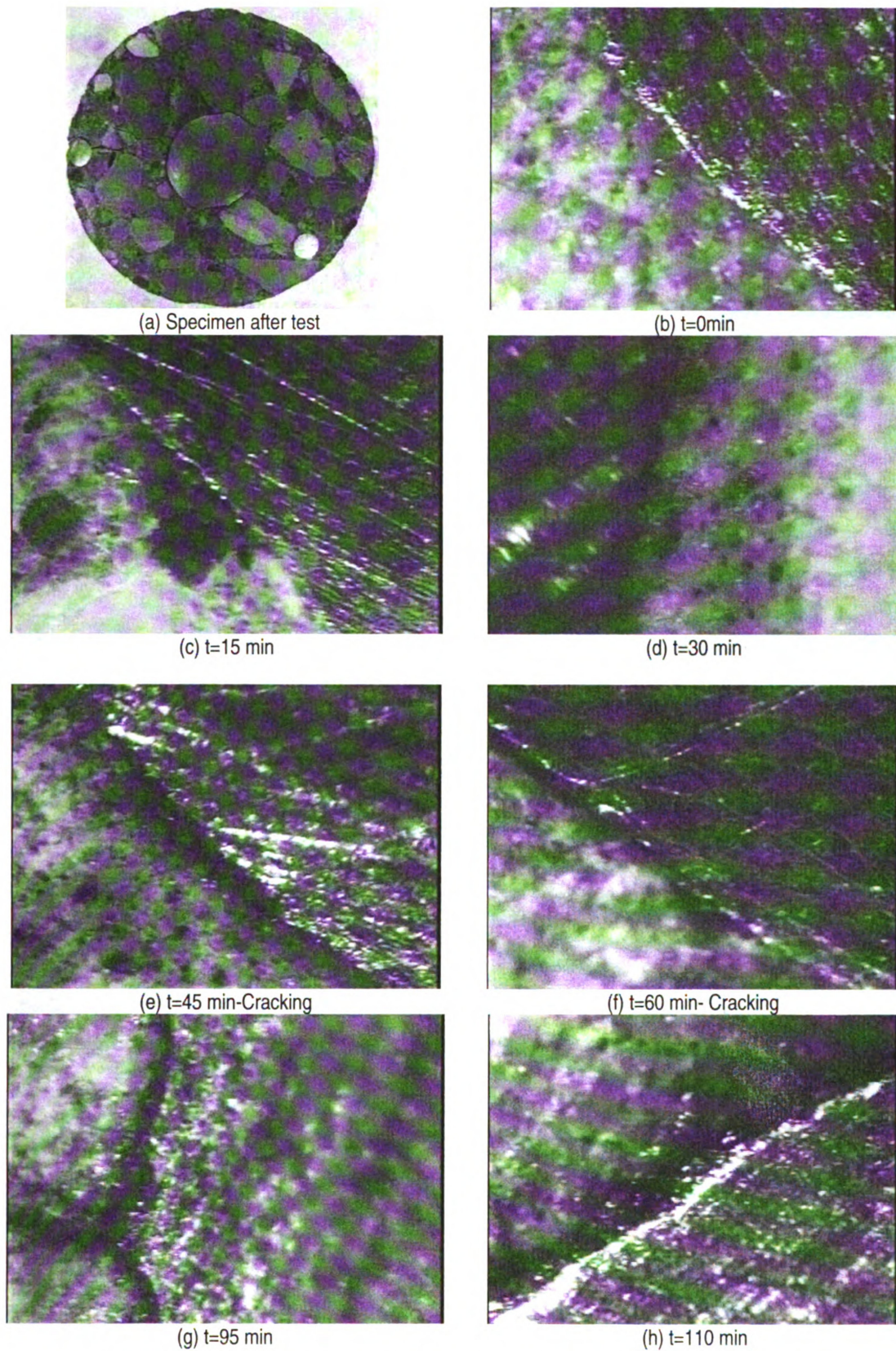
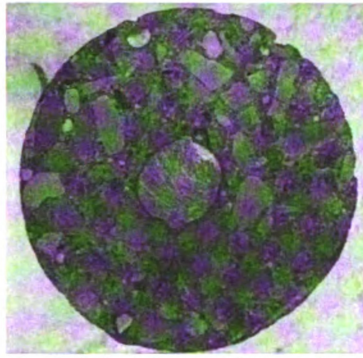
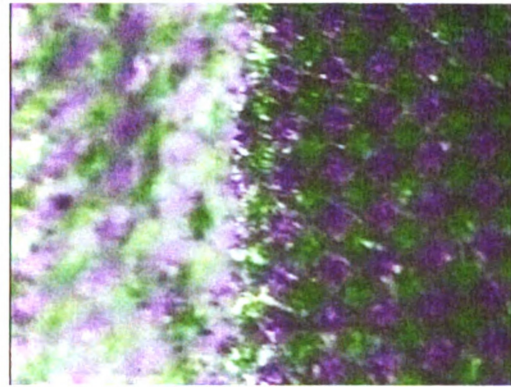


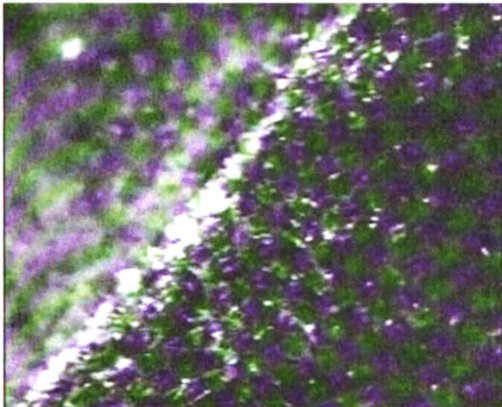
Figure 3-11: Experimental test results for rust thickness under the microscope for specimens with $k = 3$



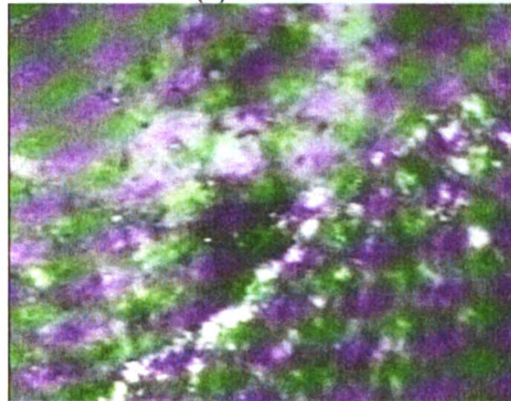
(a) Specimen after test



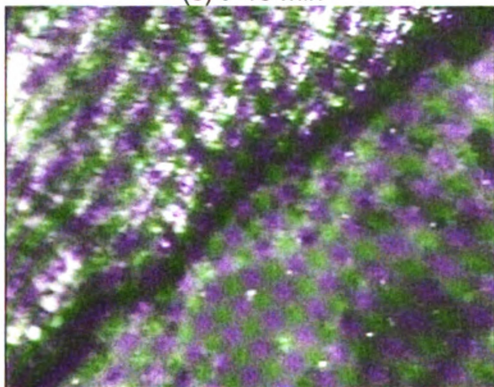
(b) $t = 0$ min



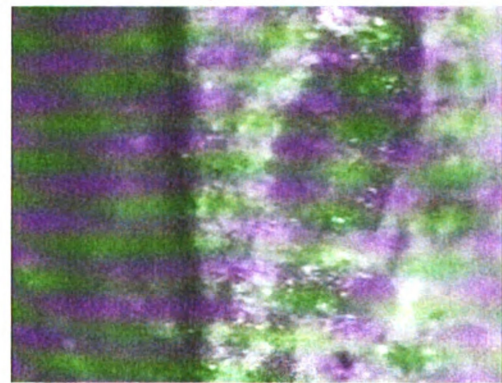
(c) $t = 15$ min



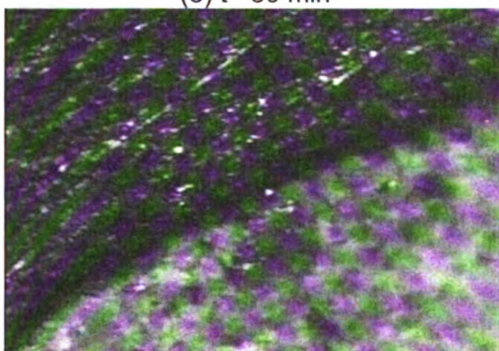
(d) $t = 35$ min



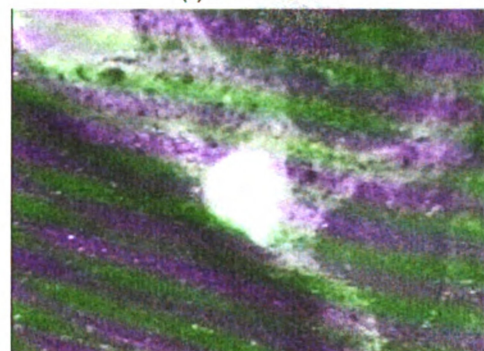
(e) $t = 50$ min



(f) $t = 65$ min

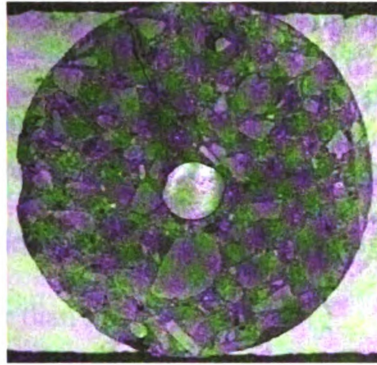


(g) $t = 80$ min-Cracking

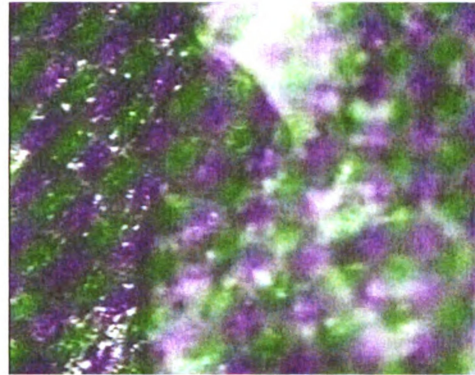


(h) $t = 95$ min

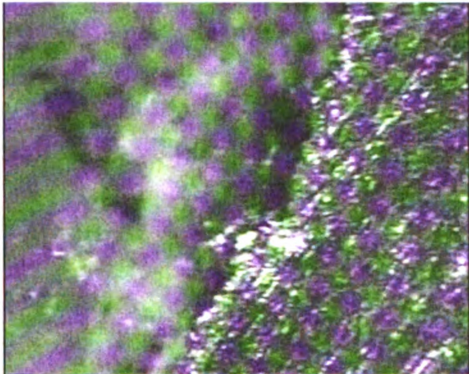
Figure 3-12: Experimental test results for rust thickness under the microscope for specimens with $k = 4$



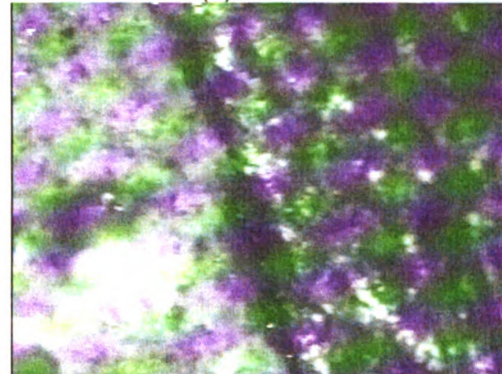
(a) Specimen after test



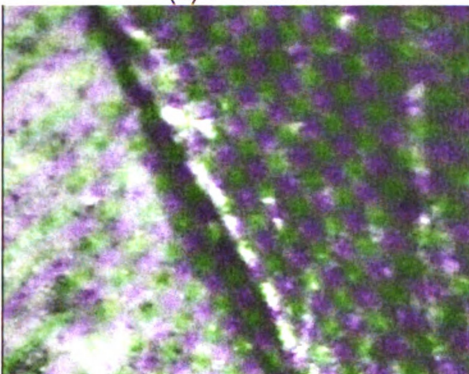
(b) $t=0\text{min}$



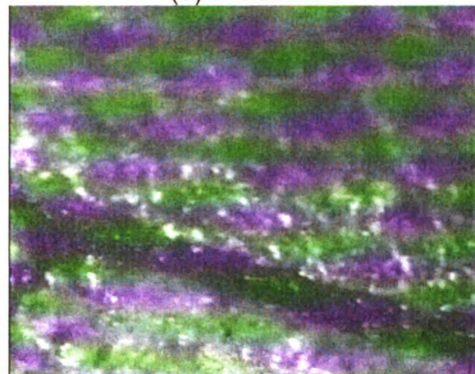
(c) $t=35\text{ min}$



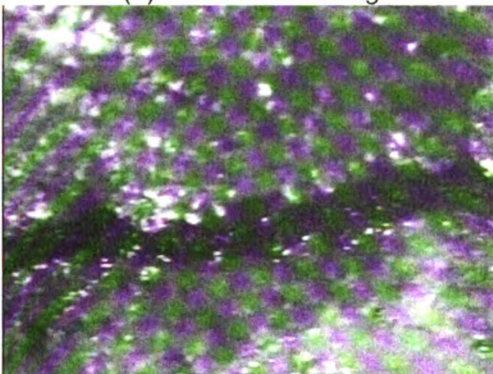
(d) $t=70\text{ min}$



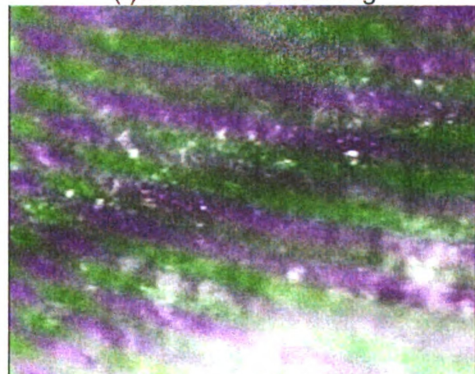
(e) $t=90\text{ min-Cracking}$



(f) $t=115\text{ min-Cracking}$



(g) $t=130\text{ min-Cracking}$



(h) $t=160\text{ min}$

Figure 3-13: Experimental test results for rust thickness under the microscope for specimens with $k = 6$

For $k = 4$ it took between 65 to 80 minutes for the first crack to appear at which time the average rust thickness around the bar was between 0.00057 to 0.00082 in. However, in some locations the maximum thickness reached 0.0011 in. at 80 minutes and the ratio of the maximum to average rust thickness ratio was almost 1.4, which is quite smaller than the ratio for $k = 3$.

Finally, for $k = 6$ it took about 95 to 125 minutes for the first crack to open at which time the average rust thickness was about 0.0009 to 0.00129 in. The maximum rust thickness was 0.0014 in. in some places at $t = 125$ minutes, and the maximum to average rust thickness ratio of 1.08 was less than that for $k = 4$ and 3. The growth of the average rust thickness with time is given in Figure 3-10.

As Figure 3-10 shows, the rust thickness had an approximately linear relationship with time in this experiment since the corrosion current was constant, but it may not be the case on real corrosion when the corrosion current may vary with time. More detail on modeling of the corrosion current and growth of the rust thickness is discussed in later chapters.

3.5 Conclusions

This chapter focused on the experimental tests that were needed for developing a more accurate model for corrosion-induced cracking of concrete. A comprehensive experimental investigation was performed on accelerated corrosion testing to investigate the accuracy of using Faraday's Law to calculate mass loss, since this test was used to calibrate the relationship between corrosion current and rust thickness, and establishing a situation where Faraday's Law gave accurate results was very important. Tests were performed in both

solution and concrete to better understand the reactions that take place at the anode and cathode. The solution was chosen to be similar to the pore solution of concrete. The results of the tests in solution and concrete had similar trends, and indicated that Faraday's Law does not always give accurate estimation of the mass loss. The accuracy depends on the chloride concentration in the system as well as the impressed current. Two competing reactions, the oxidation of steel and production of oxygen due to the splitting the water, occur at the anode. When the chloride concentration exceeds the amount required for natural corrosion to begin (i.e., $[\text{Cl}^-]/[\text{OH}^-] \geq 0.6$) and when there is no limitation of water in the system, the current efficiency (ratio of the real mass loss to the mass loss calculated using Faraday's Law) is close to unity. In this situation, Faraday's Law may be used to accurately estimate the mass loss in the accelerated corrosion test as long as the current is not too high.

Accelerated corrosion testing was performed under a microscope to establish the relationship between rust thickness and corrosion current. The test was done under conditions where all the corrosion current would be spent on corrosion rather than on splitting water to oxygen and hydrogen. The results indicated that the accumulated rust thickness varied approximately linearly with until cracking of the concrete cover. The linear relationship between rust thickness and time may not hold under natural corrosion as discussed in the next chapter. The results of the test under the microscope are used in subsequent chapters to calibrate and validate the corrosion current and concrete cover-cracking model.

Chapter 4

Electrochemical Modeling of Corrosion Rate in Concrete

4.1 Introduction

Reinforced concrete is one of the most common construction materials. High quality concrete is a very durable material and should remain maintenance free for many years when it is properly designed. Steel reinforcement is used to improve the tensile strength of concrete structures, and more generally the mechanical resistance. The high alkalinity of concrete can prevent the reinforcing steel from any corrosion inside concrete; in other words steel is passive inside concrete. Depassivation of steel reinforcement embedded in concrete and the onset of active corrosion can arise due to two causes: carbonation of the concrete, or chloride diffusion. Corrosion will commence for a good quality concrete when the pH of the pore solution is about 13.5 when the

$[\text{Cl}^-]/[\text{OH}^-]$ ratio reaches about 0.6 (Mindess and Young 2003) However, there is little electrochemical interpretation of this condition and it was obtained from field investigations. Alosuso et al. (2002) related the chloride threshold to the pitting potential of reinforcing steel in concrete. A deeper understanding of the effect of chloride on the corrosion of steel in alkaline media is necessary for predicting the lifetime of concrete structures. Corrosion of reinforcement in concrete structures results in damage in the form of expansion, cracking and eventually spalling of the concrete cover (Bhargave et al. 2005).

The aim of this chapter is to evaluate the corrosion rate of steel in concrete due to chloride penetration and the availability of oxygen in the concrete pores. The corrosion process is very complex and modeling is often based on observation or speculation rather than a clear understanding of the physical and chemical processes involved (Palle 2002). For the corrosion of reinforcement due to chloride penetration, the damage in the concrete can be divided into the following stages (see Figure 4-1):

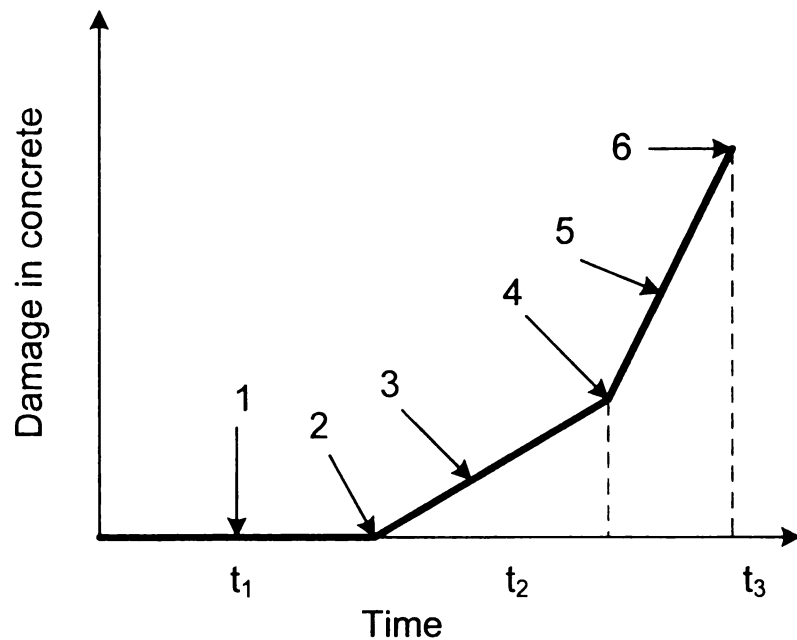


Figure 4-1: Damage as a function of time (not to scale)

1. Depassivation time due to chloride penetration (*time t_0-t_1*)
2. Initiation of corrosion (*time t_1*)
3. Development of corrosion products (*time t_1-t_2*)
4. Initiation of concrete cover cracking (*time t_2*)
5. Crack propagation (*time t_2-t_3*)
6. Spalling (*time t_3*)

The deterioration steps 1 and 2 are well understood, and are presented in numerous papers. Steps 3 to 6 have been addressed by some researches, but they generally did not address the corrosion rate or assumed it to be constant and independent of the environmental condition (El Maaddawy and Soudki 2007). The fundamental behavior of steel corrosion in highly alkaline media in the presence of chloride ions is poorly understood. It is therefore desirable to develop an electrochemical/mechanical model of the corrosion process based on the fundamental behavior of steel inside concrete and until cracking initiates.

This work focuses on predicting the rate of corrosion based on a fundamental understanding of the electrochemical corrosion reaction, and the effect of chloride and oxygen concentrations on both the anodic and cathodic reactions. Since a significant amount of corrosion products diffuse into the concrete pores before concrete cracking occurs (Du et al. 2006), the mechanical model addresses this issue along with others.

Corrosion of steel in concrete consists of two stages as Figure 4-2 shows. The first stage is anodic control and can be ignored in some cases compared to the second stage since it is very short even though corrosion rate is higher. In the first stage the corrosion rate increases until the corrosion current reaches a limiting stage. In the second stage the current is limited by cathodic control. This is the corrosion current often measured by

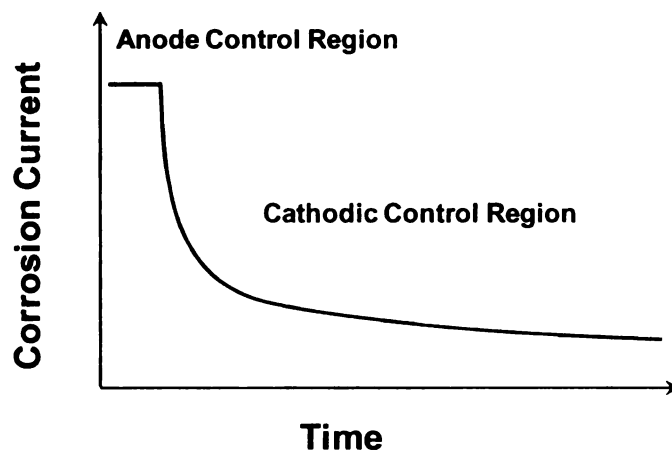


Figure 4-2: Corrosion rate model

researchers (Liu 1996).

Thereafter, the corrosion current will gradually and very slowly decrease until cracking of the concrete. In this chapter, an electrochemical model for the corrosion rate for both stages is developed empirically and

theoretically.

4.2 Polarization Curve

Proposing a model or measuring the initial corrosion rate is almost impossible without knowing the effect of chloride on the depassivation of steel. As explained in the literature review, the polarization curve can be used to measure the corrosion rate. For this purpose it is necessary to measure the effect of the chloride ion concentration on the anodic and cathodic polarization curves and consequently on the corrosion rate. While the Tafel equation describes the polarization curve in the active region, there is no equation that explains the anodic polarization curve in the passive and transpassive regions, they must be measured experimentally. A comprehensive experimental test was

done to measure the effect of different chloride concentrations on the behavior of steel in alkaline media and then a semi-empirical model for the initial corrosion rate is proposed.

4.2.1 *Experimental Anodic Polarization Curve*

No theoretical model exists to illustrate the corrosion behavior of steel in the passive and transpassive regions. The only available model for the polarization curve is the Tafel equation that is only valid for the active part of the curve at the limiting potential. The polarization curve of steel in the passive and transpassive region and the changes of this behavior with chloride concentration need to be determined experimentally.

4.2.1.1 Test Set-Up

A three-electrode cell was used to study the electrochemical behavior of steel in alkaline media with and without chloride ions. Experiments were carried out with disc electrodes made of mild steel cut from #3 reinforcing bars with an exposed surface area of approximately 0.02759 in^2 (0.178 cm^2), sealed with an alkaline resistant epoxy resin in a Teflon tube. Impurity elements in structural steel as quoted by ASTM A36 are 0.26%-0.29% carbon, 0.6%-0.9% magnesium, 0.04% phosphorous, 0.05% sulfur, and 0.4% silicon. The electrode surface was polished up to Grade 2400 with Sic paper and cleaned with acetone and distilled water prior to measurement. Figure 4-3 shows a photograph of the electrode. The solution was chosen to have a

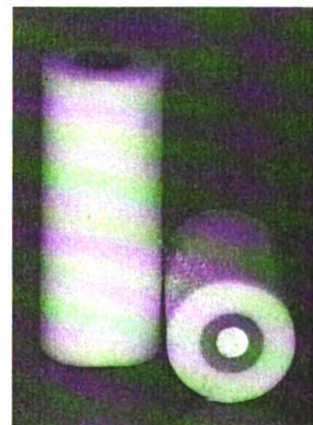


Figure 4-3: Steel electrode

composition and pH similar to concrete pore solution. The solution properties and concentration of the species is given in Table 4-1 (Bertolini et al. 2002), and the solution was prepared using distilled water. The measured pH of the chloride-free solution was 13.64, and was comparable to the theoretical value of 13.5. The chloride concentration was varied from 0 to 600 mMol, yielding $\chi = [\text{Cl}^-]/[\text{OH}^-]$ values of 0 to 1.91. The experiments were carried out at room temperature (25 ± 2 °C) under oxygen free conditions which were achieved by purging the cell for 30 minutes with nitrogen prior to each experiment.

Table 4-1: Solution Properties (Bertolini et al. 2002)

	[Na(OH)] (mMol)	[Ca(OH) ₂] (mMol)	[K(OH)] (mMol)	[Cl ⁻] (mMol)	pH
Test Solution	85	1.0	228	Varied from 0 to 600	13.50

The pH of the solution for different chloride concentrations was also measured. All potentials were measured with reference to the mercury/mercury oxide reference electrode. The potentiostatic experiments were carried out by applying a constant potential in the range of -0.2 to 0.8 V at 0.1V intervals. The current transient at each applied potential was recorded for a period of 30 minutes, after which the steady state minimum current was reached.

4.2.1.2 Three Electrode Cell

Usually the three electrode cell as shown in Figure 4-4 is used for a typical electrochemical corrosion measurement. The test cell includes a metal specimen (commonly called the working electrode) and the solution in which the specimen is to be

tested. The reference electrode is in contact with the solution, and a counter electrode is used to supply the current to the working electrode during the test.

The heart of the ECHM corrosion measurement system is the potentiostat. As shown in Figure 4-5, a potentiostat can be viewed as a “black box” which performs two main functions:

- It controls the potential difference between the working electrode and reference electrode. i.e., it imposes an applied potential (E_{app}).
- It measures the current flow between the working electrode and counter electrode.

This is the i_{total} measurement. In addition, the potentiostat makes the value of E_{app} and i_{total} available for recording.

4.2.1.3 Measurement Technique

Most corrosion measurements involve a scan of the working electrode potential and measure the resulting current. This is referred to as a potentiodynamic scan, since the applied potential continuously changes. It is

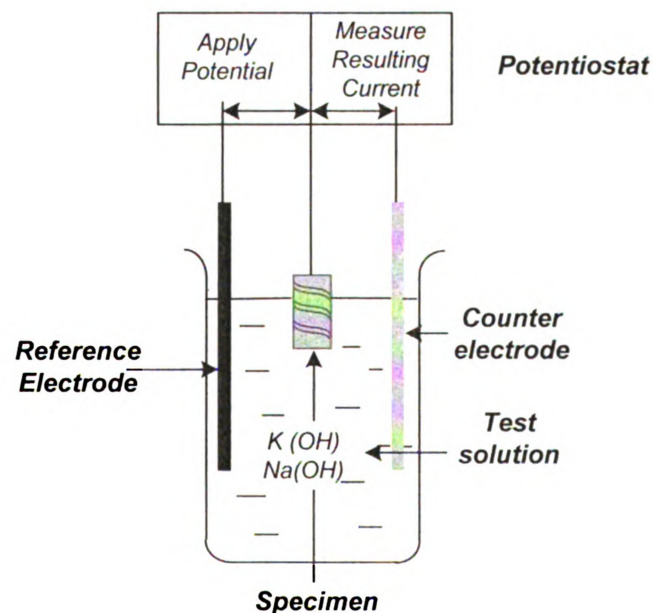


Figure 4-4: Potentiostat operation

useful sometimes to maintain a constant potential and measure the resulting current as a function of time. This kind of experiment is called a potentiostatic measurement. In this study the potentiostatic measurement technique was chosen since it was necessary to let the electrodes reach a steady state current for these measurements. It is also possible to control the current at the working electrode and measure the resulting potential. If the current is varied by the controlling instrument, the measurement is called a galvanodynamic scan. If a constant current value is maintained and potential vs. time is measured, the experiment is called galvanostatic.

4.2.1.4 Mercury/Mercuryoxide Reference Electrode

The mercury/mercury oxide reference electrode is designed for use in strongly alkaline media to produce stable and reproducible results. It is usually constructed with 100% plastic with no glass parts, which would corrode in alkaline solutions. Figure 4-5 shows a photograph of the mercury/mercury oxide reference electrode used in this test.

The potential of the Hg/HgO reference electrode can be calculated from the potential of the cell, which depends on

the alkaline base solution that is usually potassium hydroxide at different concentrations.

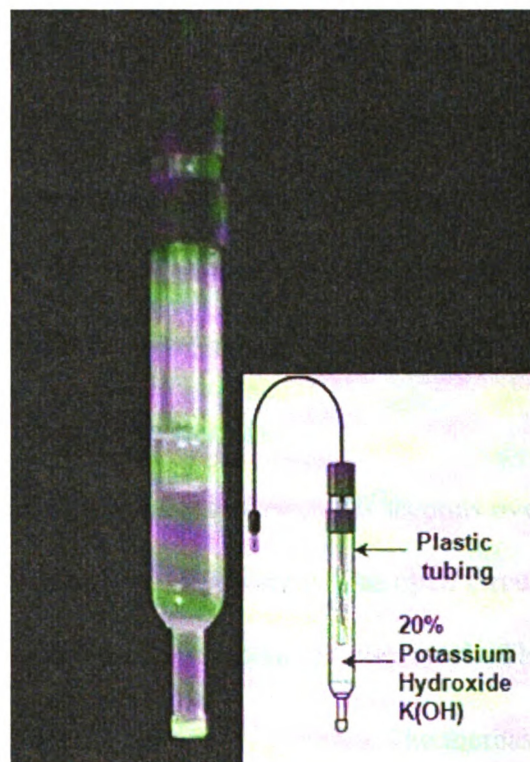
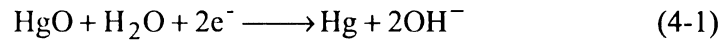


Figure 4-5: Mercury/ mercury oxide electrode

The potential of the electrode changes as the concentration of potassium hydroxide inside the electrode changes. The reference electrode used in this test was Hg/HgO with a 20% potassium hydroxide filling solution. The reaction that occurs at the electrode is:



which has a potential difference of $E_0 = +0.098 \text{ V}$ compare to a normal Hydrogen electrode at 25°C.

4.2.2 Results and Discussion

4.2.2.1 Open Circuit Measurement

One of the factors that can lead to understanding the long term passivation behavior of steel in concrete is the open circuit potential, which is related to the rate of passivation of steel in concrete. The passive current of steel inside concrete when there is no chloride concentration decays with time due to the strengthening and thickening of the passive layer. Tests were conducted to establish the rate of passivation of steel in concrete.

The corrosion potential of the steel electrode was recorded every 30 seconds over a period of 3 hours in alkaline solution with no chloride concentration. The open circuit potential became more positive with time indicating passivation of the steel. The variation of the electrode potential, E_{open} , with time is shown in Figure 4-6. The increase in potential can be represented by:

$$E_{open} = \begin{cases} \alpha_1 + \beta_1 \log t & t < 10\text{min} \\ \alpha_2 + \beta_2 \log t & t \geq 10\text{min} \end{cases} \quad (4-2)$$

where α is a constant, β is the rate coefficient for passive film growth, and t is the time in minutes (Egamy et al. 2004). After immersion over a long period, the surface became completely covered with the passive film, the passivation current decreased and the electrode potential increased rapidly (not shown in Figure 4-6). This behavior is similar to the passivation behavior of stainless steel in alkaline media at low pH (Egamy et al. 2004).

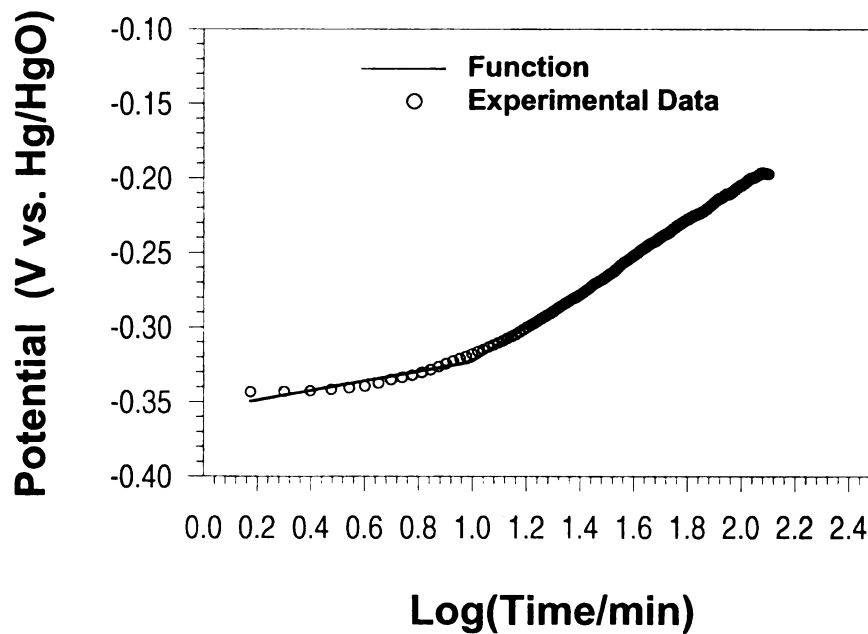


Figure 4-6: Variation of the open circuit potential as function of time, the parameters are given in

As shown in Figure 4-6, the potential as a function of time consists of two straight line segments with different slopes. The first segment with the smaller slope for $t < 10$ minutes occurs when the passive layer is forming and the potential grows gradually. After the first 10 minutes, the entire surface area of the electrode is passive and the passive layer becomes thicker. It is expected that when the passive film reaches its maximum thickness after some time, the potential should reach a steady state. This result indicates

that the passive current for steel in fresh concrete can be considerably more than that for steel in very old concrete, due to formation of the thick passive layer. The current that is needed to maintain the passive layer is less in old concrete. However, in fresh concrete the passive oxide layer is forming and this yields a higher current density.

Table 4-2: Parameters used in Equation 4-2

	Parameter	Value (Error)
t < 10 min	α_1 (V)	-3.55×10^{-1} (2.30×10^{-3})
	β_1 (V)	3.22×10^{-2} (2.17×10^{-3})
t > 10 min	α_2 (V)	-4.41×10^{-1} (5.00×10^{-4})
	β_2 (V)	1.18×10^{-1} (2.80×10^{-4})

4.2.2.2 Potentiostatic Polarization Results

The potentiostatic technique was used to measure the polarization curve for steel in alkaline solution with and without chloride. The test was done by using no rotation of the working electrode for better simulation of real corrosion of steel in concrete. The effect of electrode rotation was also studied to evaluate this effect on the results. For the potentiodynamic measurement the potential was fixed between -0.2 and 0.8 V and the current was measured for a 30 minute duration until it reached the steady state value. The final current as a function of the potential was plotted to obtain the polarization curve for steel in different solutions.

Effect of Electrode Rotation

Figure 4-7 shows the effect of electrode rotation speed (ω , rpm) on the passivation current density for different chloride concentrations. The test was conducted

at a potential of 0.3 V and the measured current was in the plateau region for all cases. Figure 4-7 indicates that the passive current changes linearly with $\omega^{0.5}$. However, the rotation of the electrode does not affect the measured current considerably for either high or low chloride concentrations, possibly due to the high concentration of the species in the electrolyte. The slight increase in the current for low chloride concentrations may be due to faster diffusion of the chloride to the electrode surface that increases the chloride

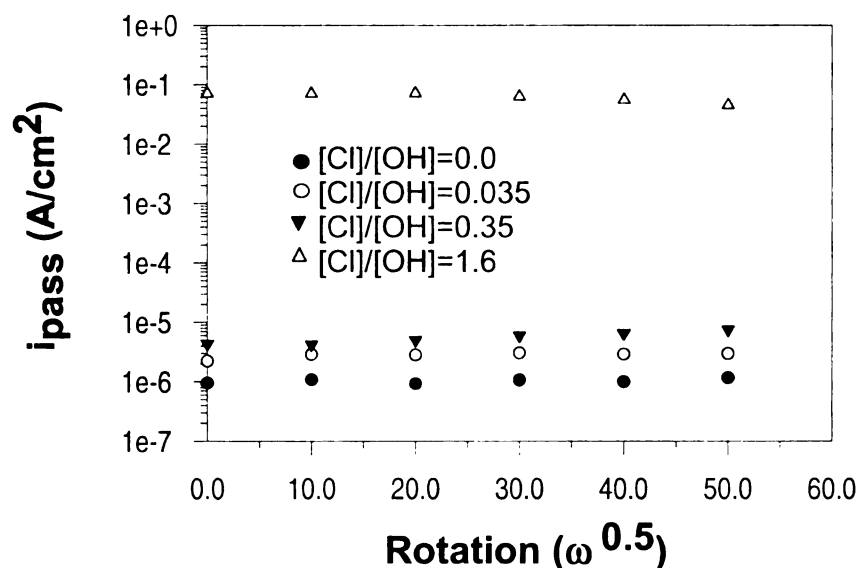


Figure 4-7: Effect of electrode rotation on the current

concentration in its vicinity, thereby increasing the passivation current. The slight decrease in the limiting current at high chloride concentration may also be due to the

earlier deposition of corrosion products on the electrode surface that limit the diffusion of other species to the electrode surface.

Effect of Chloride Ion Concentration

Figure 4-8 presents the potentiostatic results of the anodic polarization curves for steel in alkaline solution at different chloride concentrations. As expected and shown schematically in Figure 2-4 in Chapter 2, in the absence of chloride ions, the steel

electrode is passive over the wide potential range extending from about -0.2 V to 0.6 V. At higher potentials, a sharp increase in current due to transpassivity was recorded. When chloride concentration was zero, the passivation current is very low around 10^{-6} A/cm². This current can be higher or lower depending on the exposure time to the alkaline solution as explained in the previous section.

When the chloride concentration increases, the passive current also increases. When $[\text{Cl}^-]$ reaches 250 mMol, and correspondingly the $\chi = 0.35$, the passivation current density increased to 3×10^{-5} A/cm², indicating reduced passivity. However, the change in the pitting potential, E_{pit} , remained small for $0 < \chi < 0.6$. Under these conditions, no visible corrosion products were observed on the working electrode surface after the test. For $\chi > 0.6$, E_{pit} shifted to the more active (negative) region, and decreased dramatically from 0.6 V to about 0.1 V when χ increased from 0.96 to 1.91 . At $\chi \geq 0.96$, the passive region vanished gradually, and E_{pit} could not be established within the experimental potential window.

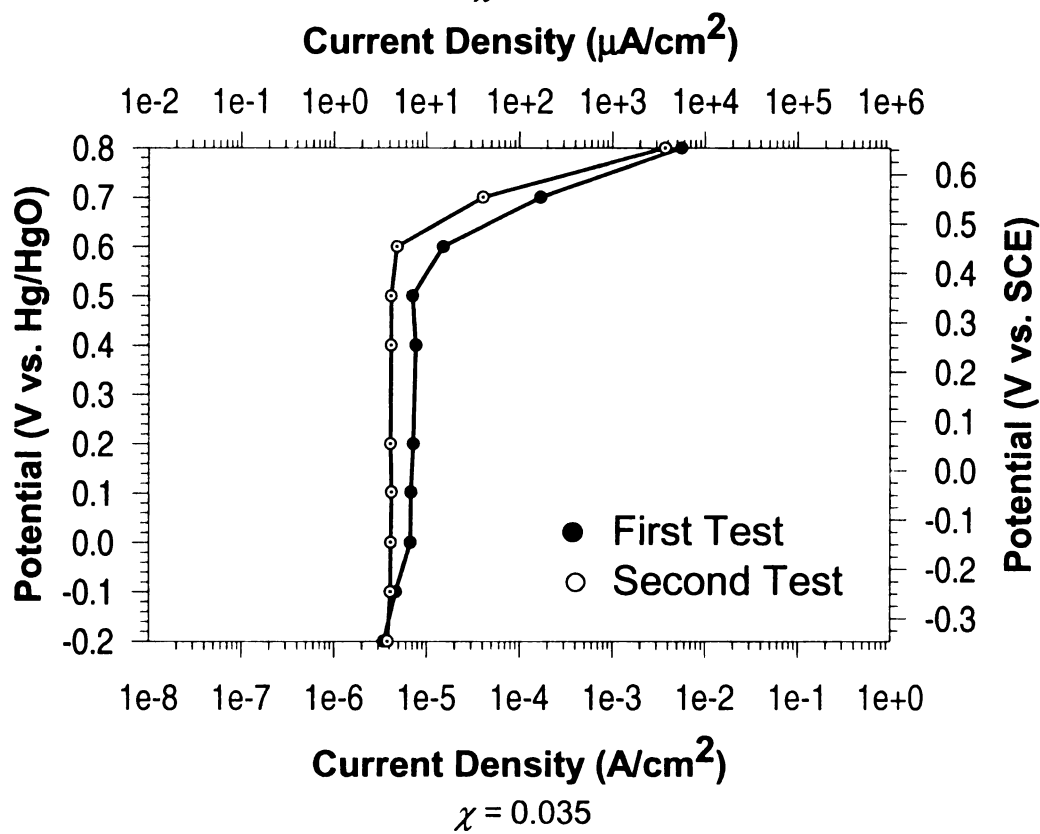
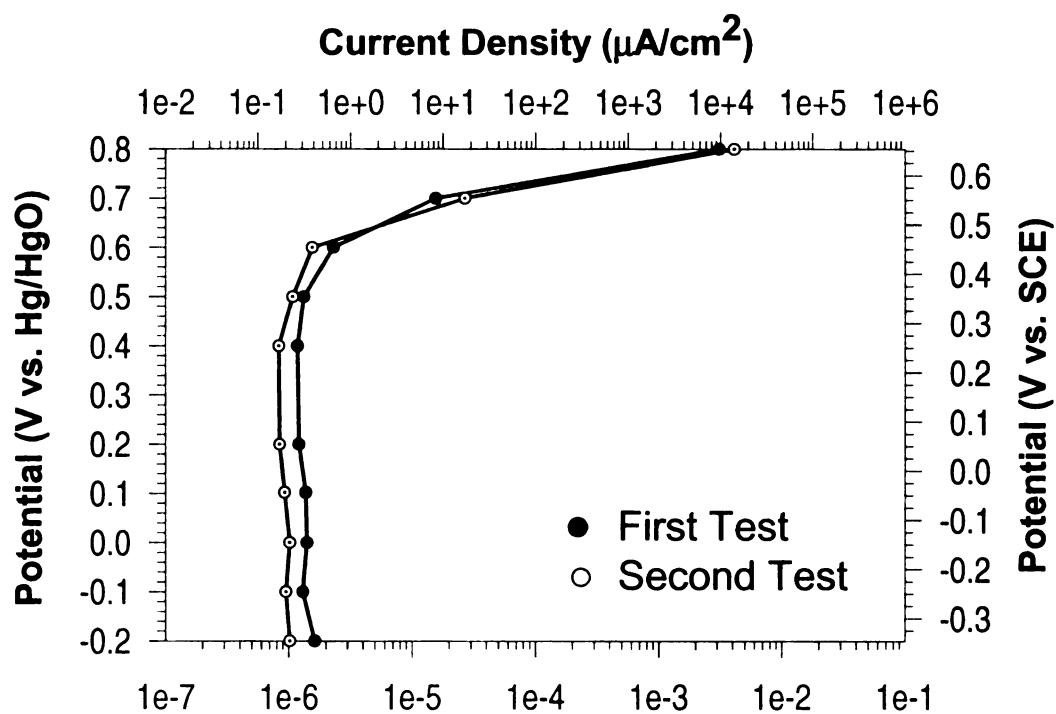


Figure 4-8: Polarization curve for different chloride concentrations

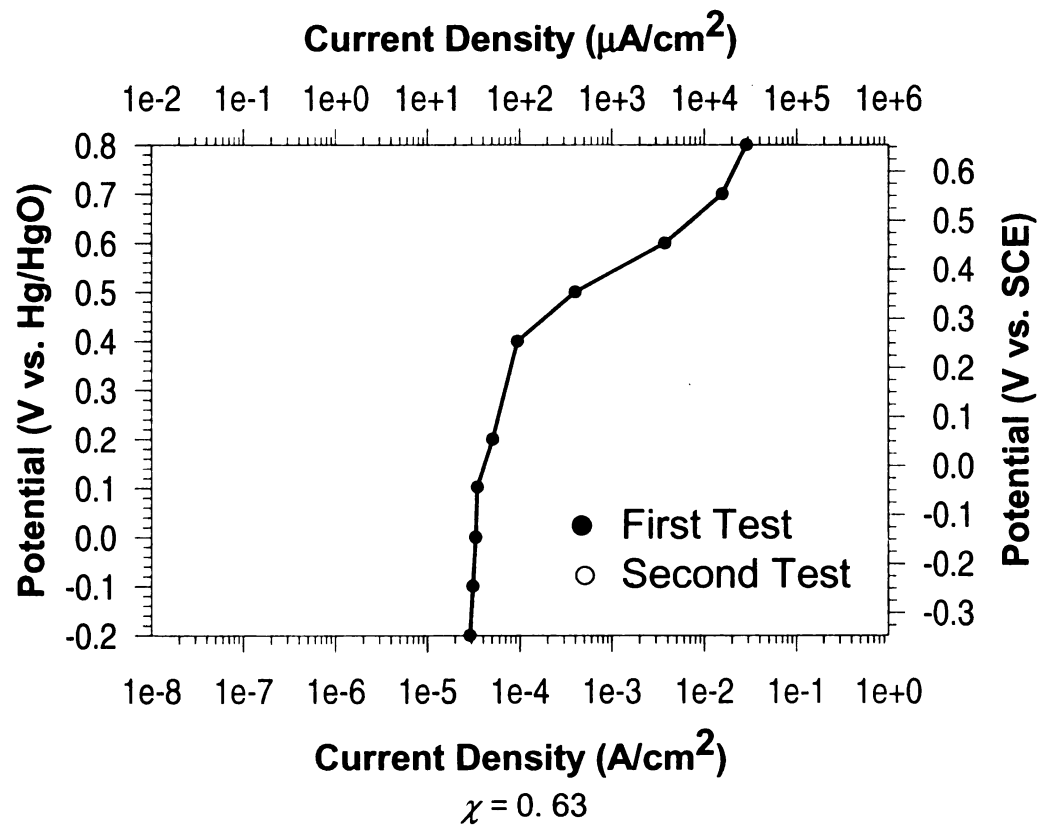
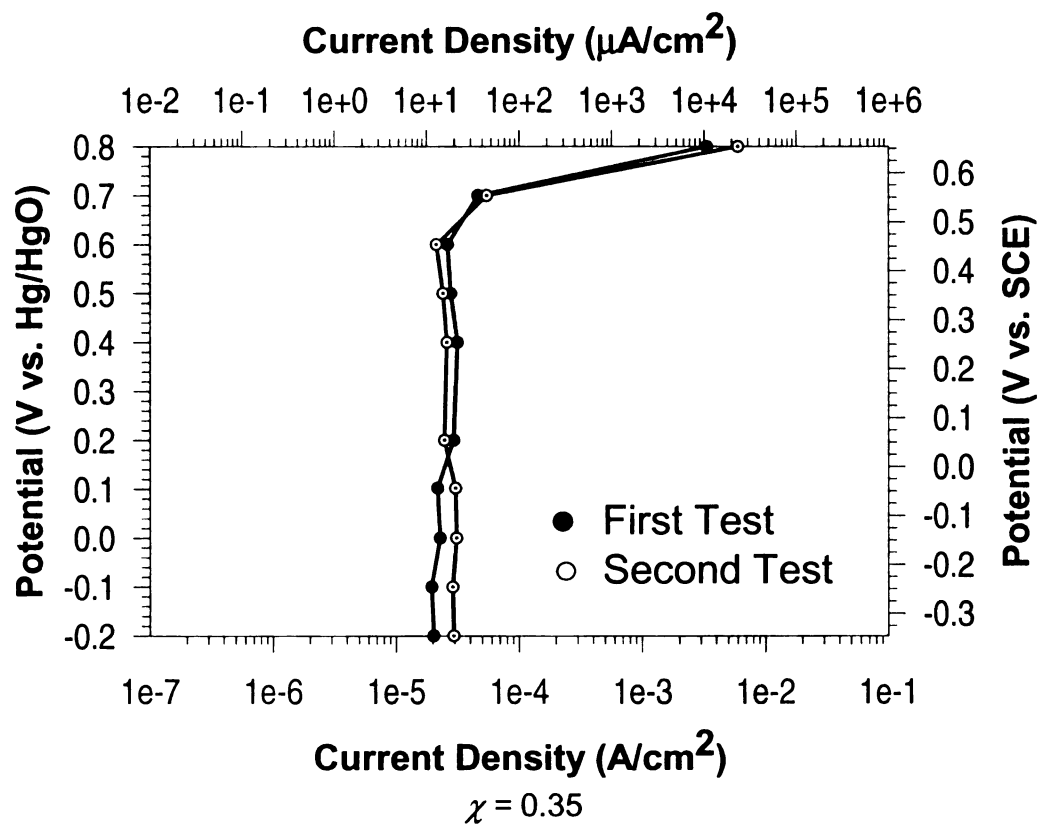


Figure 4-8 Cont'd: Polarization curve for different chloride concentrations

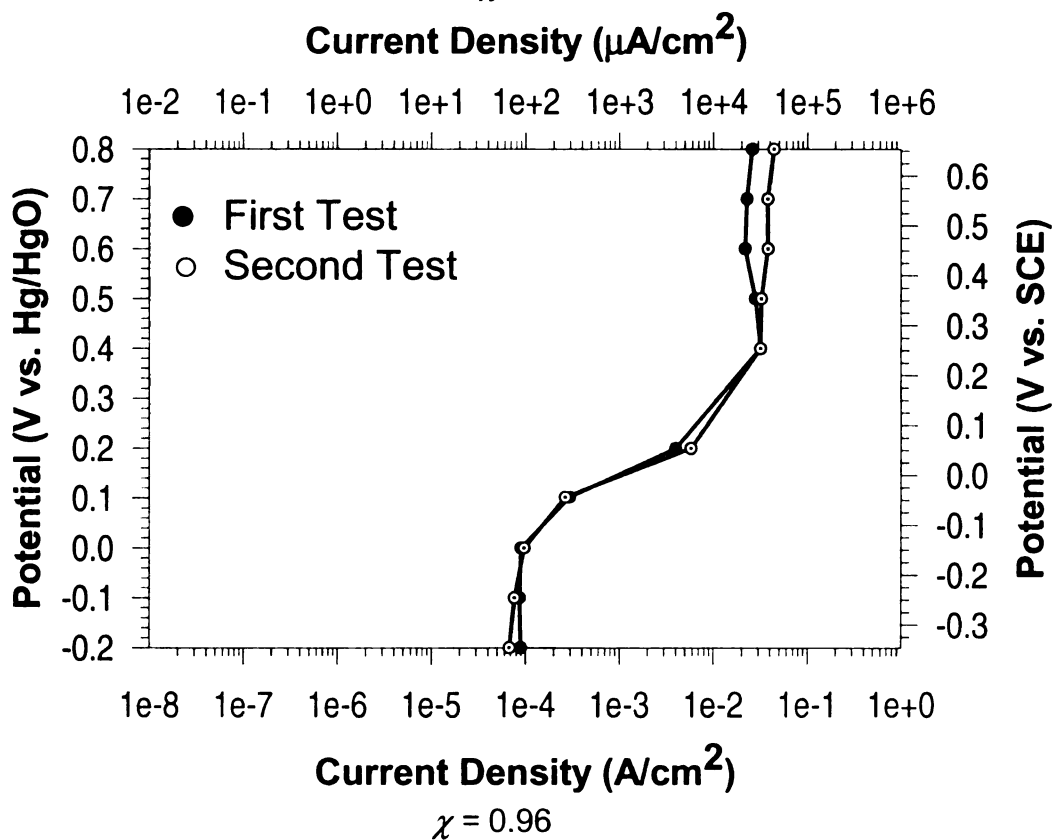
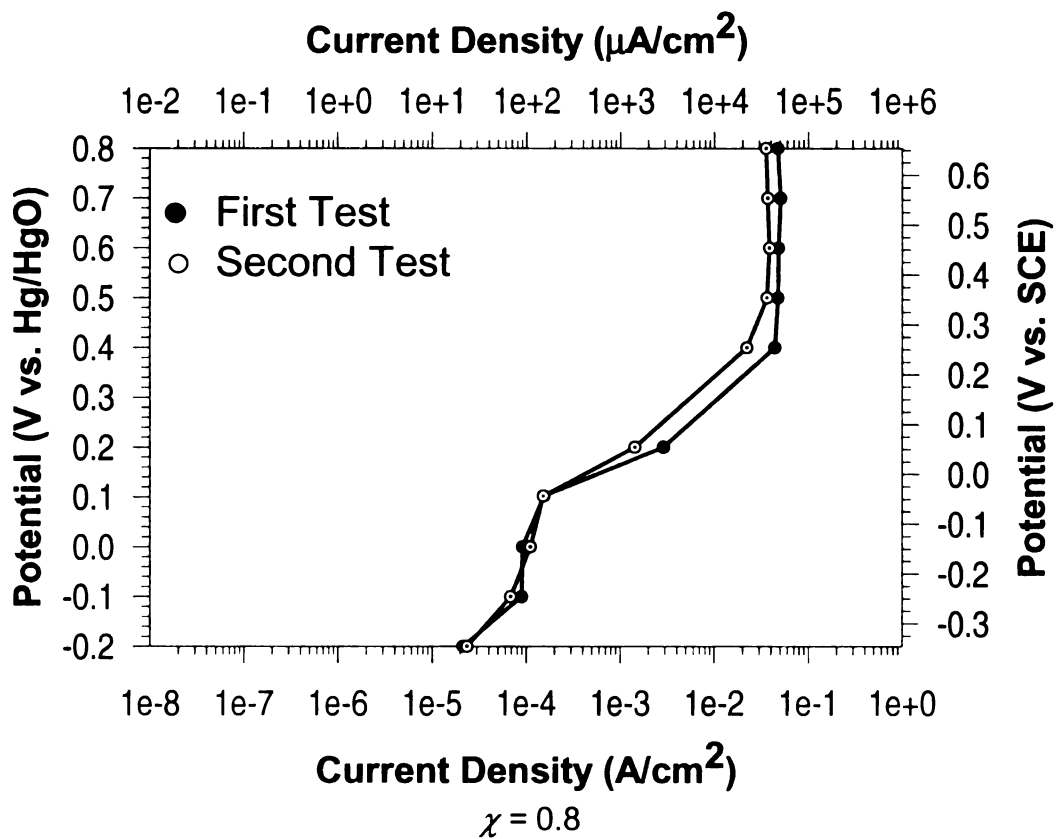


Figure 4-8 Cont'd: Polarization curve for different chloride concentrations

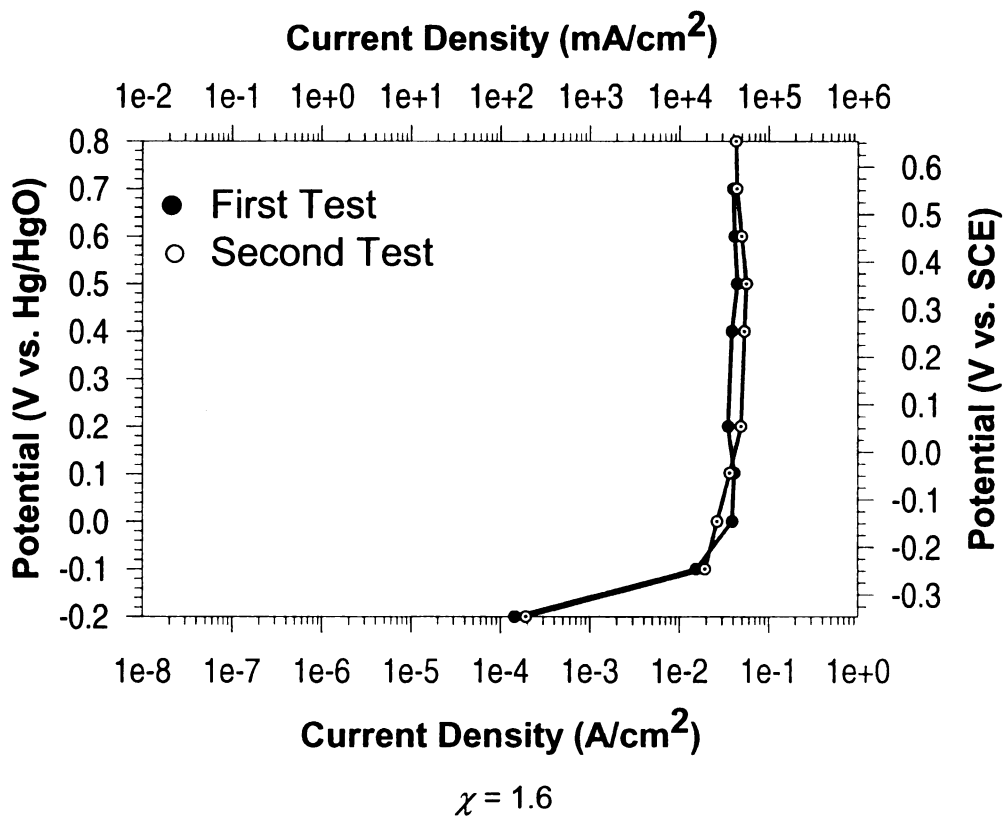
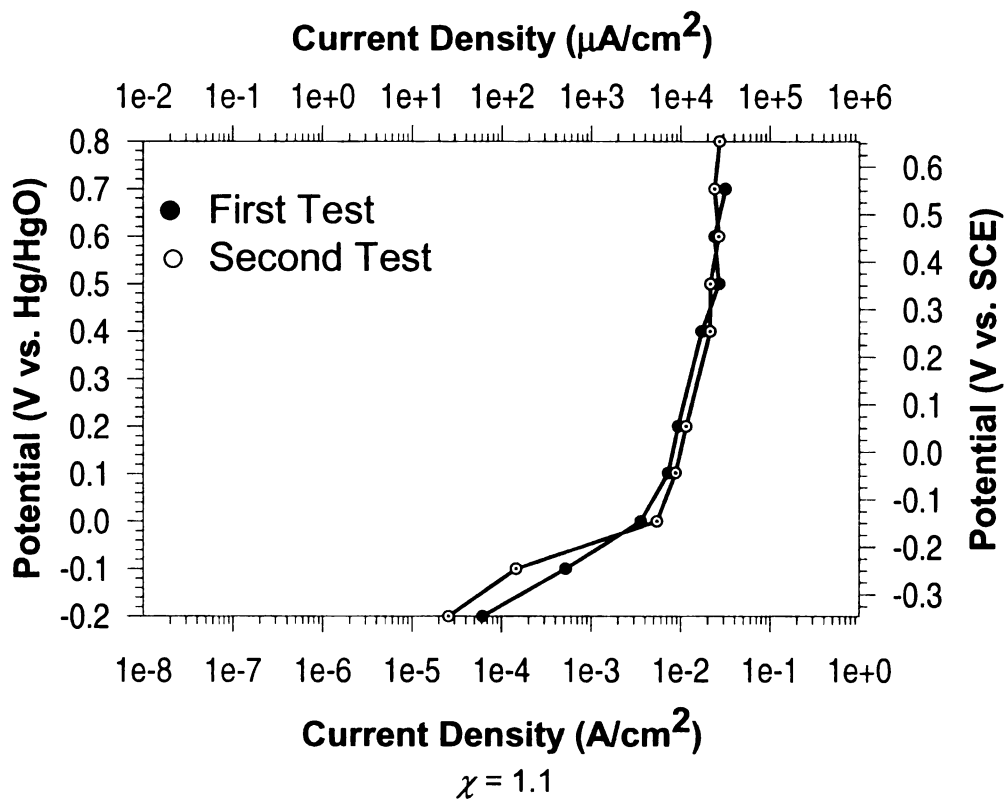


Figure 4-8 Cont'd: Polarization curve for different chloride concentrations

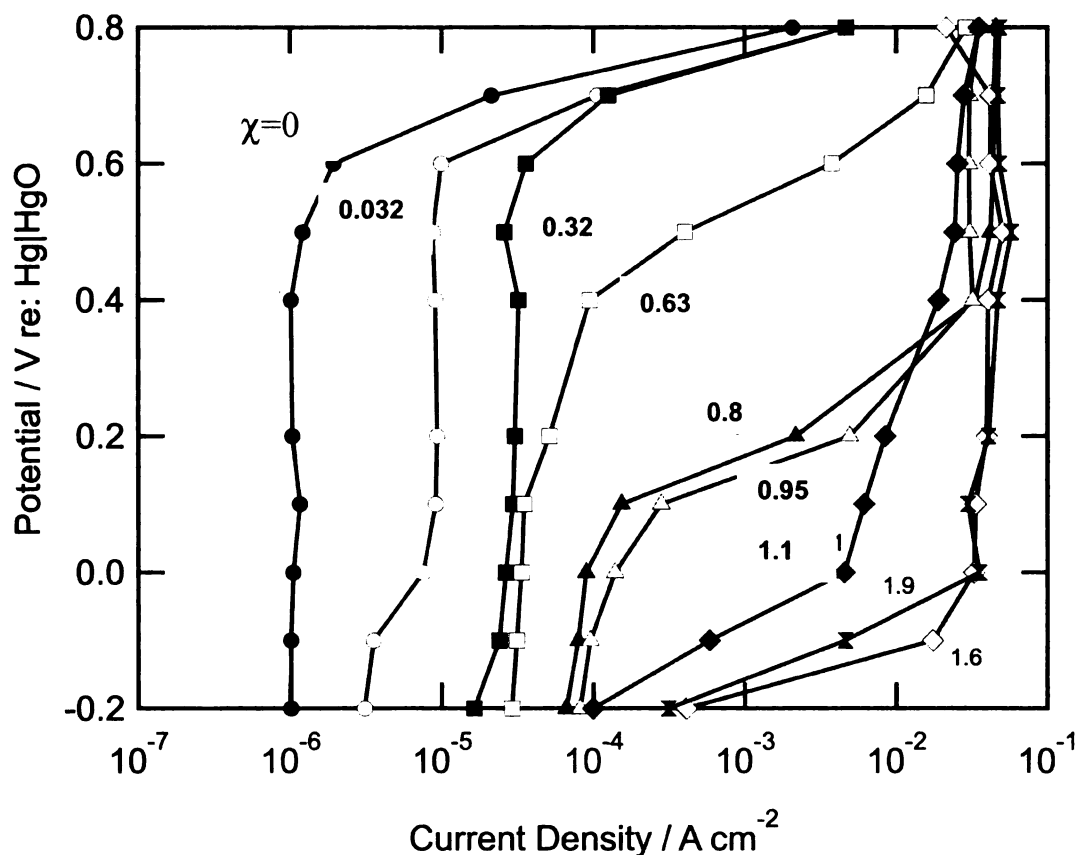


Figure 4-9: Experimentally determined oxidation polarization curves for steel at different $[\text{Cl}^-]/[\text{OH}^-]$ ratios

The plateau region above the pitting potential was most likely due to the mass transfer limitation of products or reactants. No stirring was used in the test in order to better simulate field conditions of steel embedded in concrete.

Change of Potential

The pitting potential, E_{pit} , was determined from the polarization curve at the point where a stable increase in the current density occurred. Figure 4-10 shows, on a log scale, the relationship between E_{pit} and χ , which can be represented as

$$E_{\text{pit}} = a\chi^n + e_0 \quad (4-3)$$

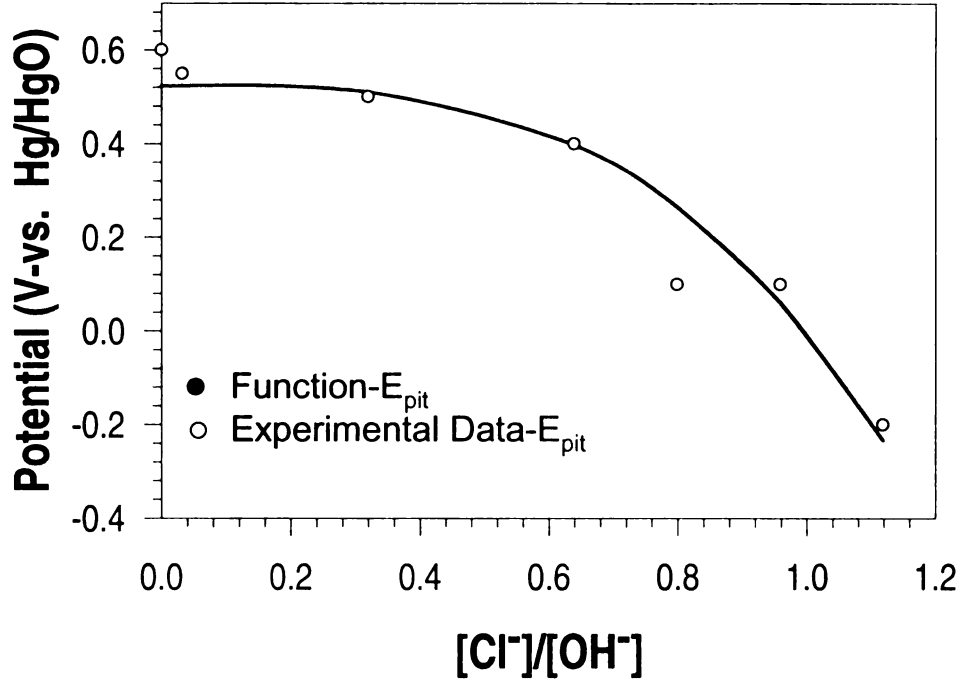


Figure 4-10: Pitting corrosion potential as a function of $[\text{Cl}^-]/[\text{OH}^-]$ ratios, parameters are given in Table 4-3

The results in Figure 4-10 reveal that when χ is smaller than 0.6, the pitting potential does not change considerably and pitting may only occurs in the transpassive region when the potential is high, or no pitting occurs at all suggesting that at such a low chloride concentration the Cl^- ions are not able to depassivate the steel. However, for $\chi > 0.6$, the pitting corrosion drops dramatically to a very low potential and the passivation region of the graph vanishes. In this situation, pitting can occur at a very low potential at which steel was passive earlier.

Table 4-3: Parameter used on Equation 4-3 and 4-4

Equation	Parameter	Value (Error)
Equation 4-3	n	2
	a (V)	-6.00×10^{-1} (5.46×10^{-2})
	e_0 (V)	5.77×10^{-1} (3.57×10^{-2})
Equation 4-4	b (A/cm ²)	4.62×10^{-5} (1.62×10^{-6})
	i_0 (A/cm ²)	1.05×10^{-6} (9.56×10^{-7})

Change in Passive Current

The passive current density, i_{pass} , was determined from the low potential plateau region of the polarization curve. Figure 4-11 shows the relationship between i_{pass} and χ , which can be expressed as

$$i_{\text{pass}} = b\chi + i_0 \quad (4-4)$$

where i_0 is a constant that depends on the nature of the electrode and the environment.

The increase in i_{pass} when χ is small indicates that although the amount of chloride is insufficient to trigger pitting corrosion, it can nevertheless increase the amount of current needed to maintain the passive layer. At $\chi = 1.1$, the passive region ceases to exist in the potential range considered (−0.2 V to 0.8 V).

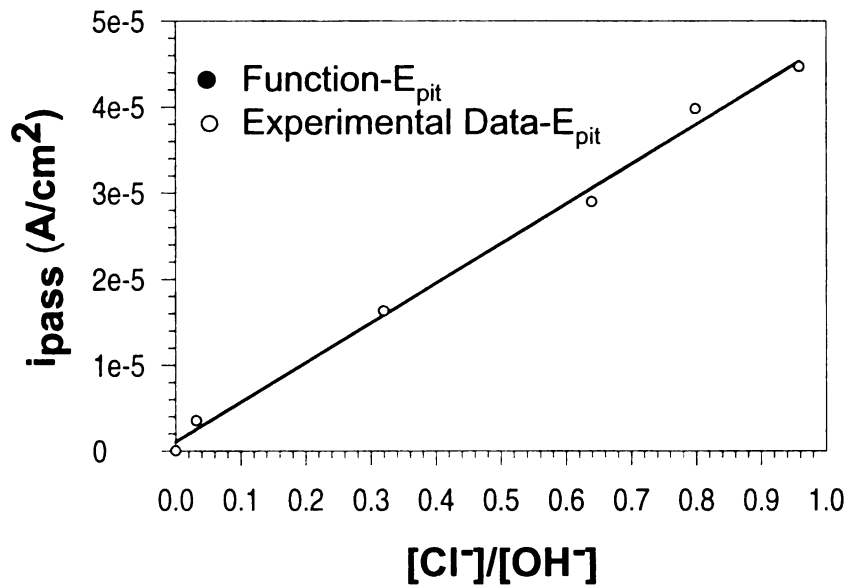


Figure 4-11: Passive current as a function of $[\text{Cl}^-]/[\text{OH}^-]$ ratios

4.2.3 Model for Polarization Curve

In any corroding system, to study the corrosion rate and corrosion current, both the anodic and cathodic polarization curves are needed according to mixed potential theory. The anodic polarization curve and the effect of chloride concentration on it was studied experimentally. The polarization curve for steel was dependent on the chloride concentration and χ . The following section presents the anodic polarization curve model as a function of χ . However, the anodic polarization curve by itself is not enough to estimate the corrosion rate. It can yield the passive current and the overall behavior of steel at different potentials. The cathodic polarization curve is needed along with the anodic polarization curve to estimate the corrosion current. Due to this reason, the cathodic polarization curve and the effect of chloride on it is also presented in this chapter.

4.2.4 Anodic Polarization Curve

As Figure 4-9 shows, the polarization curve for steel in alkaline media is a function of the chloride concentration. The anodic polarization curve can be divided into three main regions: the passive region, the transpassive region, and the limiting region. The proposed model for the anodic polarization curve as a function of chloride concentration is:

$$E - E_{\text{pit}} = \beta_p \log\left(\frac{i}{i_{\text{pass}}} - 1\right) - \beta_l \log\left(\frac{i}{i_{\text{lim}}} - 1\right) \quad (4-5)$$

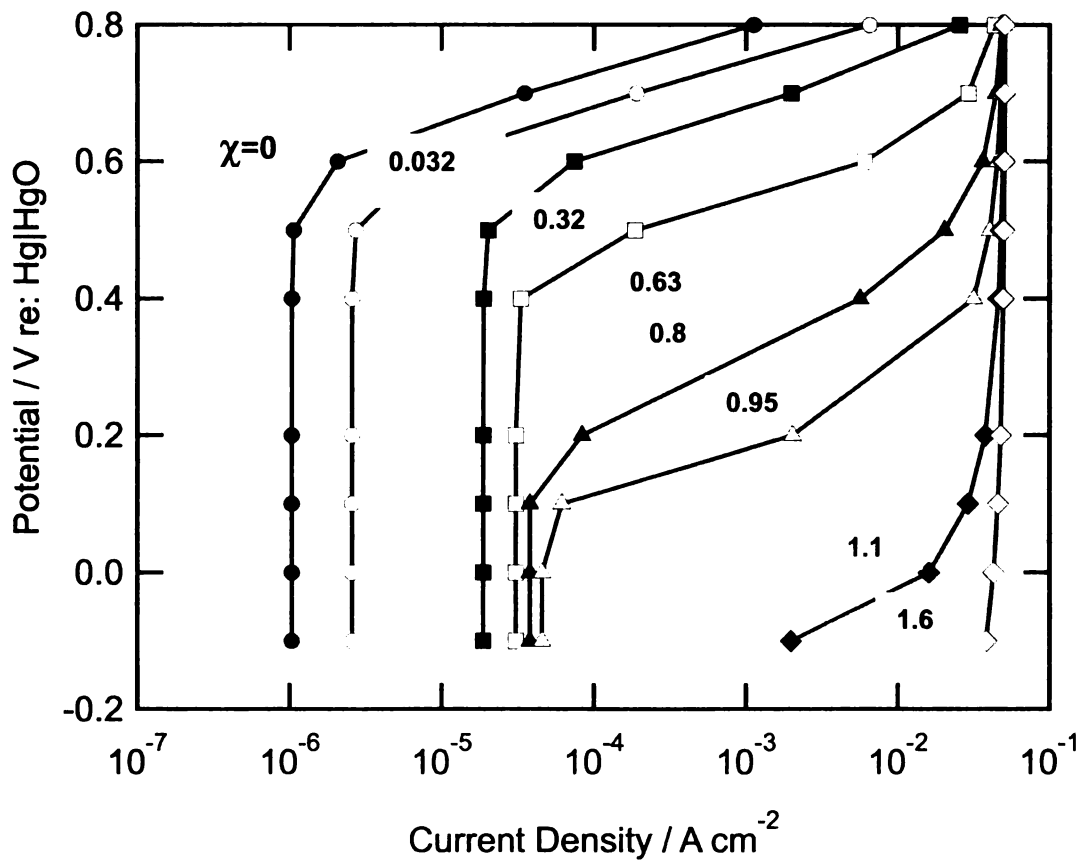


Figure 4-12: Calculated anodic polarization curve from mode

The model bounds the current density between i_{pass} and i_{lim} , the passive and limiting currents, respectively. Since the steel is passive in alkaline media, the active region is not considered in this model. If desired, the Tafel equation can be included to model the active region. The parameters β_p and β_l are similar to the Tafel slopes and control the slope of the transpassive region. As Figure 4-9 shows, as χ increased, the limiting current, i_{lim} , was roughly constant at about $45 \pm 5 \text{ mA cm}^{-2}$, but the other parameters depend on the chloride concentration. The parameters i_{pass} and E_{pit} were expressed as a function of χ earlier, and β_p and β_l can be expressed as:

$$\beta_i = \gamma_i \chi^n + \gamma_i' \quad i = \text{p or l} \quad (4-6)$$

It is possible to calculate the anodic polarization curve for steel in alkaline media at varying chloride concentrations by using the above equations with the parameters given in

Table 4-4 and the polarization curve for alkaline solutions with $\chi = 0$. The curve can be used to quantitatively define the transition from passive to the transpassive and limiting regions due to increasing $[\text{Cl}^-]/[\text{OH}^-]$ ratio. Figure 4-12 shows polarization curves for steel in the alkaline test solution obtained from the model, using parameters from

Table 4-4. Comparison of Figure 4-9 and Figure 4-12 shows that the experimental results agree well with the model. The surface plot Figure 4-13 shows the overall effect of chloride concentration on the anodic behavior of steel in alkaline media. From this plot it is possible to easily distinguish the passive, transpassive and limiting

current region at various potentials and $[\text{Cl}^-]/[\text{OH}^-]$ ratios. If the cathodic polarization curve associated with oxygen reduction (described below) intersects the surface at the transpassive and limiting current region, then corrosion is likely. From this plot it is also possible to obtain the corrosion potential at any chloride concentration by its intersection with the cathodic polarization curve.

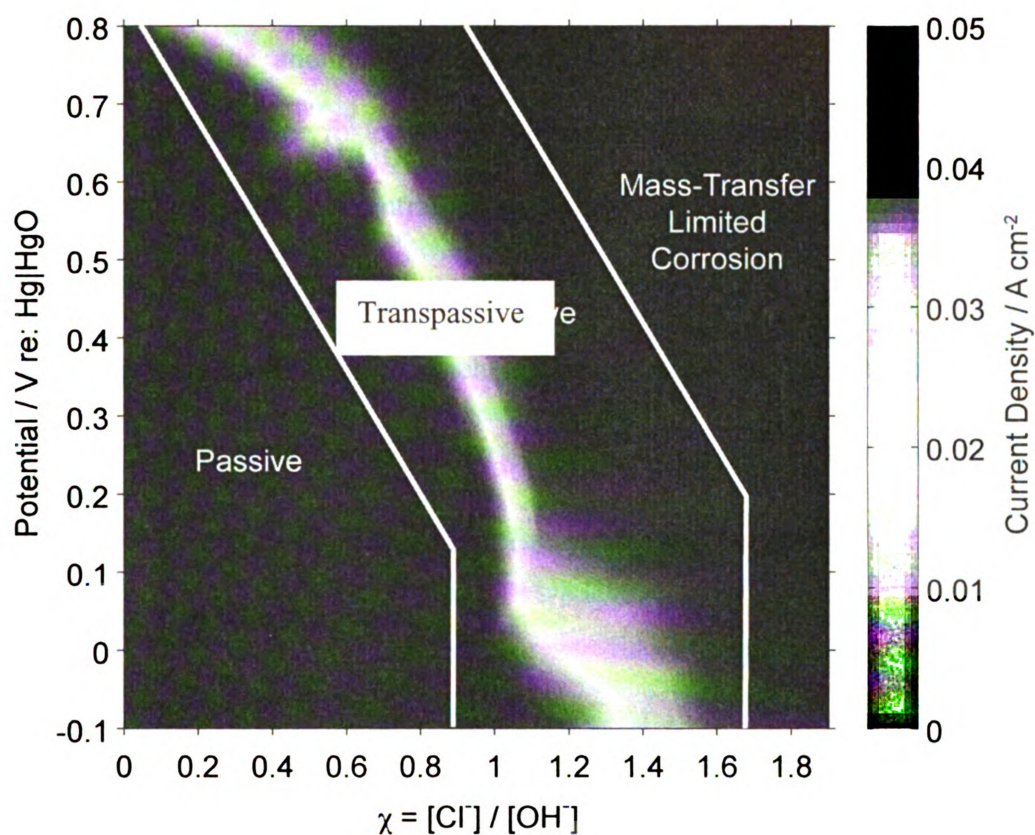


Figure 4-13: Change in steel polarization due to varying $[\text{Cl}^-]/[\text{OH}^-]$ ratio (polarization surface)

Table 4-4: Parameters used in Equation 4-6

	Parameter	Value (Error)
β_p	n	1.5
	γ_p (V)	1.62×10^{-1} (6.62×10^{-3})
	γ'_p (V)	3.45×10^{-3} (6.26×10^{-3})

	n	2
β_1	γ_1 (V)	-9.87×10^{-3} (2.91×10^{-4})
	γ_1 (V)	2.86×10^{-2} (3.17×10^{-4})

4.2.5 Cathodic Polarization Curve

The reduction of oxygen is the cathodic reaction for steel corrosion inside concrete in the presence of chloride ions. As explained earlier, chloride ions have a dramatic effect on the anodic polarization curve and explains why the presence of chloride ions can initiate corrosion of steel. The cathodic reaction is also not completely independent of chloride concentration and chloride ions can affect the cathodic polarization curve by changing the environmental condition.

The cathodic polarization branch is controlled by the Tafel equation given by Equation 2-5 in Chapter 2. Using $\beta_c = 0.05$ and $i_0 = 4 \times 10^{-12} \text{ A/cm}^2$ for the oxygen reduction reaction in high alkaline media (Bournazel and Moranville 1997) Equation 2-4 in Chapter 2 may be expressed as:

$$E^c = E_0^c + \beta_c \ln \left(\frac{i_c}{i_0^c} \right) \quad (4-7)$$

$$E_0^c = 0.401 + \frac{2.33RT}{4F} (4(14 - pH) + \log([O_2])) \quad (4-8)$$

where $[O_2]$ is the concentration of dissolved oxygen adjacent to the electrode, R is the universal gas constant, T is the temperature in $^{\circ}K$, and F is Faraday's constant. As Equation 4-8 indicates, there are different factors that affect E_c such as the pH and $[O_2]$.

Change of these parameters will change the overall polarization curve of oxygen reduction according to Equation 4-7. Effect of different parameters is studied in the next sections.

4.2.5.1 Effect of Chloride Concentration

When chloride is added to the solution, the concentration of chloride ions increases at the passive steel surface due to the attraction between the positively charged surface and the negatively charged chloride ions, since chloride ions adsorb preferentially on steel surfaces compared to hydroxide ions. Thus, the concentration of chloride ions around the steel passive surface is higher than in the bulk. The increase in chloride concentration decreases the hydroxide ion concentration by the electro-neutrality rule and thereby lowers the pH of the solution near the steel surface.

In this model, it is assumed that a change in the chloride concentration does not significantly affect the value of the Tafel slope and exchange current density in Equation 4-7.

4.2.5.2 Effect of Oxygen Concentration

One of the other factors that can affect Equation 4-8 is the oxygen concentration. Figure 4-14 shows the effect of the oxygen concentration on the cathodic polarization curve. When the oxygen concentration increases the polarization curves shifts up and the anodic and cathodic polarization curves intersect at a higher current density. Therefore, when the oxygen concentration is increased, the current density increases in the active and transpassive regions.

4.2.5.3 Effect of pH

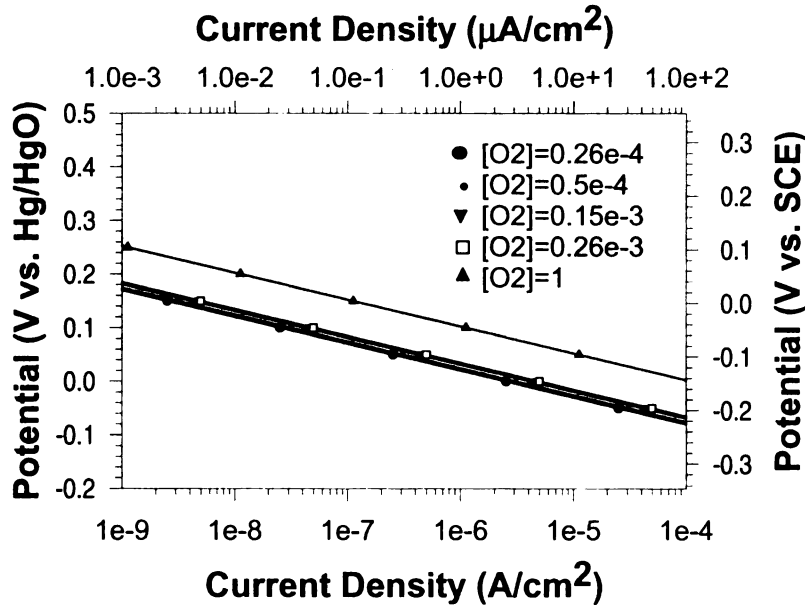


Figure 4-14: Effect of oxygen concentration on cathodic polarization curve

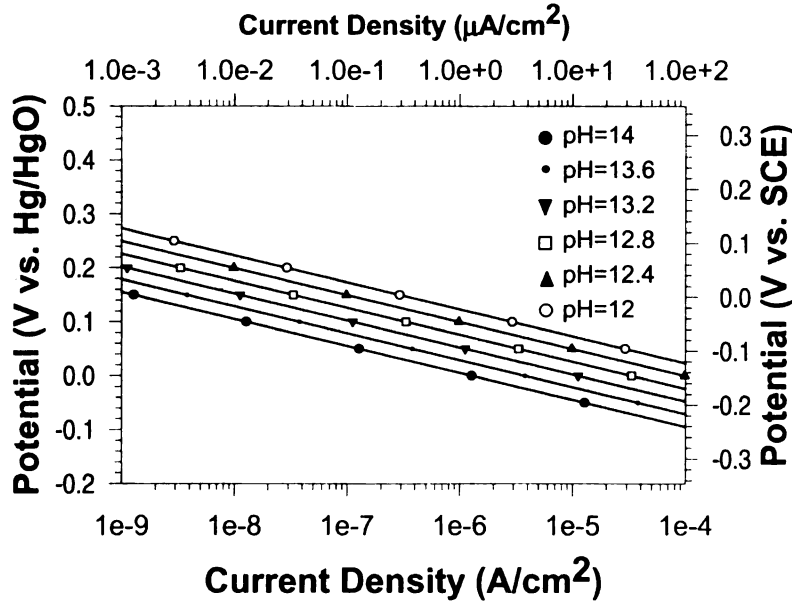


Figure 4-15: Effect of pH on the cathodic polarization curve.

The change of the pH also affects the polarization curve for oxygen reduction. For calculating the polarization curve for different pH values it was assumed that i_0 and β in Equation 4-7 are constant, which may not be true, but there is a lack of data regarding this. Figure 4-15 shows the effect of pH on the cathodic polarization curve. As expected, by decreasing the pH of the test solution the half cell potential increased and

consequently the current density in the active and transpassive zones, and hence possibility of corrosion, will increase.

4.3 Initial Corrosion Rate

As explained earlier, the experiments conducted and models proposed in the previous section were to enable understanding the effect of chloride ion concentration on depassivation and the corrosion rate. Now that the effect of chloride ions on both the anodic and cathodic polarization curves is known, it is possible to measure the corrosion rate based on the chloride concentration or χ . In natural corrosion, both half cell reactions (anodic and cathodic) occur simultaneously on the surface of a steel bar and the rate of oxidation is the same as the rate of reduction. By superimposing the anodic polarization curves for different chloride concentrations with the corresponding computed cathodic polarization curve, i_{corr} can be determined using the intersection between the two curves. As expected, and shown in Figure 4-16 for both the model and experimental data, when χ increases the anodic and cathodic polarization curves intersect at a higher current density and the potential is closer to E_{pit} . Pitting corrosion starts when the potential reaches E_{pit} .

An empirical equation for the corrosion current density of steel in alkaline solution as a function of the $[\text{Cl}^-]/[\text{OH}^-]$ ratio was developed by finding the intersection between the anodic and cathodic polarization curves and fitting a curve having the form:

$$\log\left(\frac{i}{i_{\text{passive0}}}\right) = \frac{\exp(\alpha(\chi))}{\beta + \gamma(\exp(\delta(\chi)))} \quad (4-9)$$

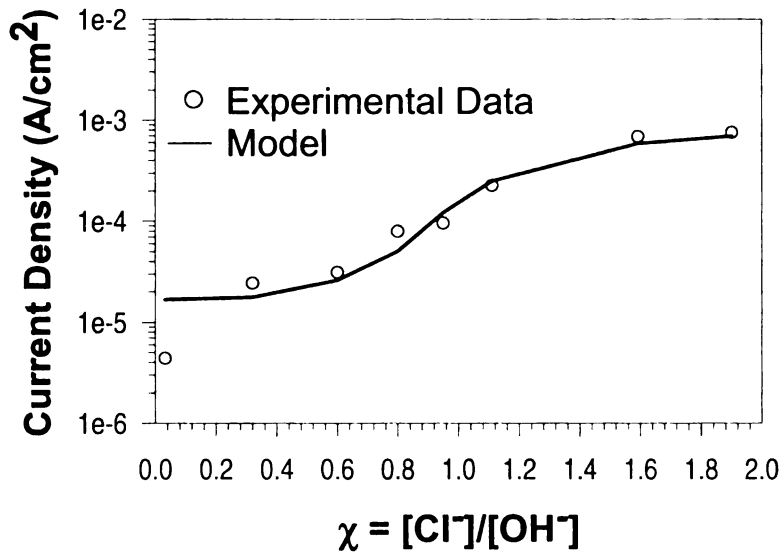


Figure 4-16: Variation of corrosion current with χ

good.

Equation 4-9 does not account for any limiting current based on either the reduction of oxygen or the oxidation of steel, and can be used to estimate the initial corrosion current before the lack of oxygen in concrete limits corrosion. Once oxygen is depleted, the corrosion will be controlled by the oxygen limiting current. Equation 4-9 should be used with care even at the initial stage of corrosion since it yields the corrosion current only at the pit and cannot be applied to the total corrosion over the bar.

where α, β, γ and δ are the empirical constants calibrated using the experimental data. Figure 4-16 shows the comparison between the experimental data and the proposed equation for different chloride concentrations and the agreement is quite

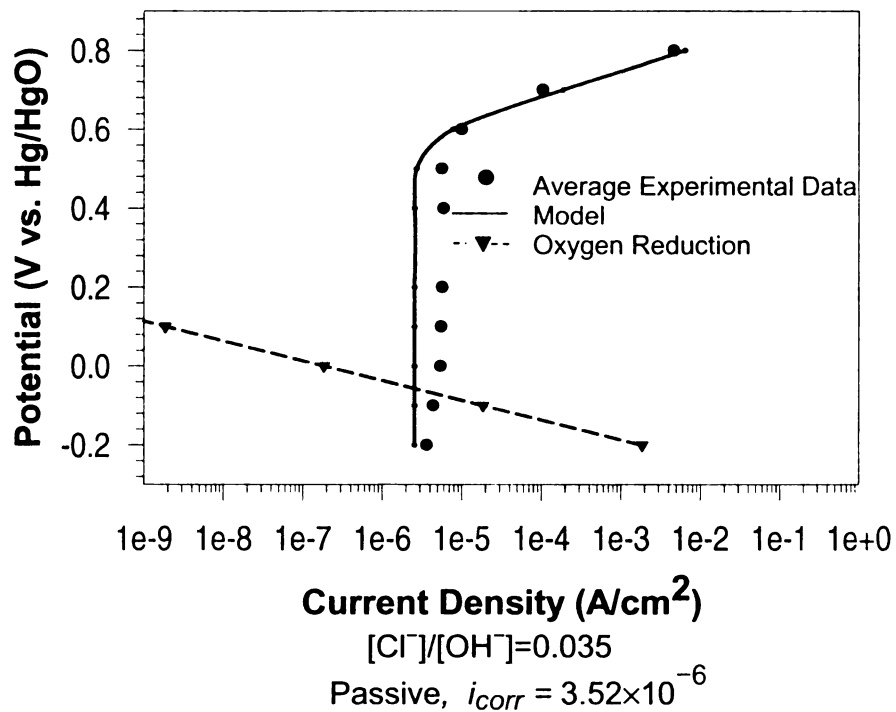
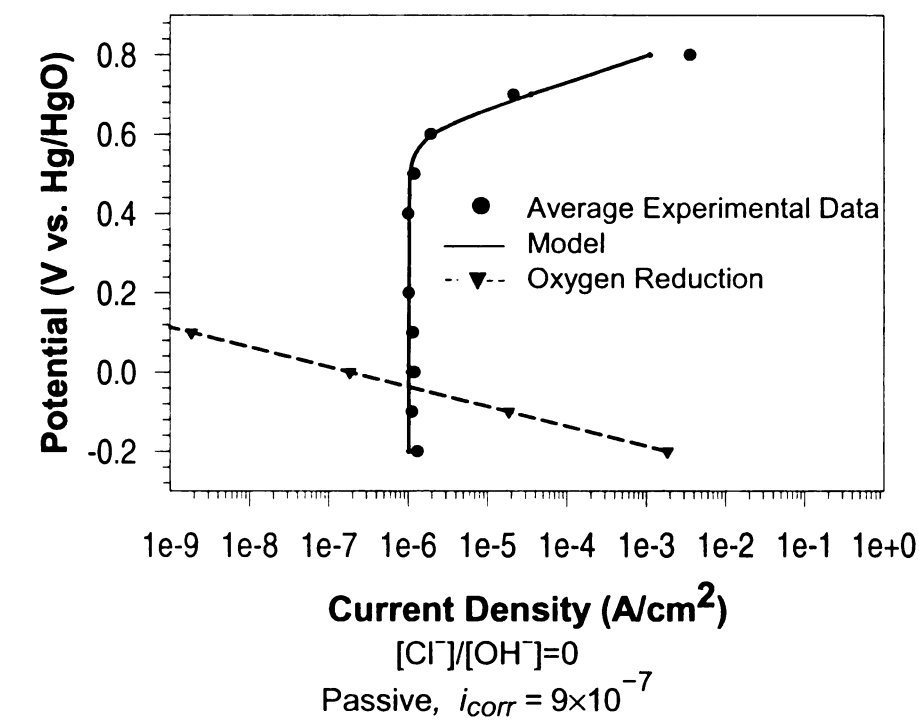


Figure 4-17: Comparison between experimental data and model, and the corrosion current

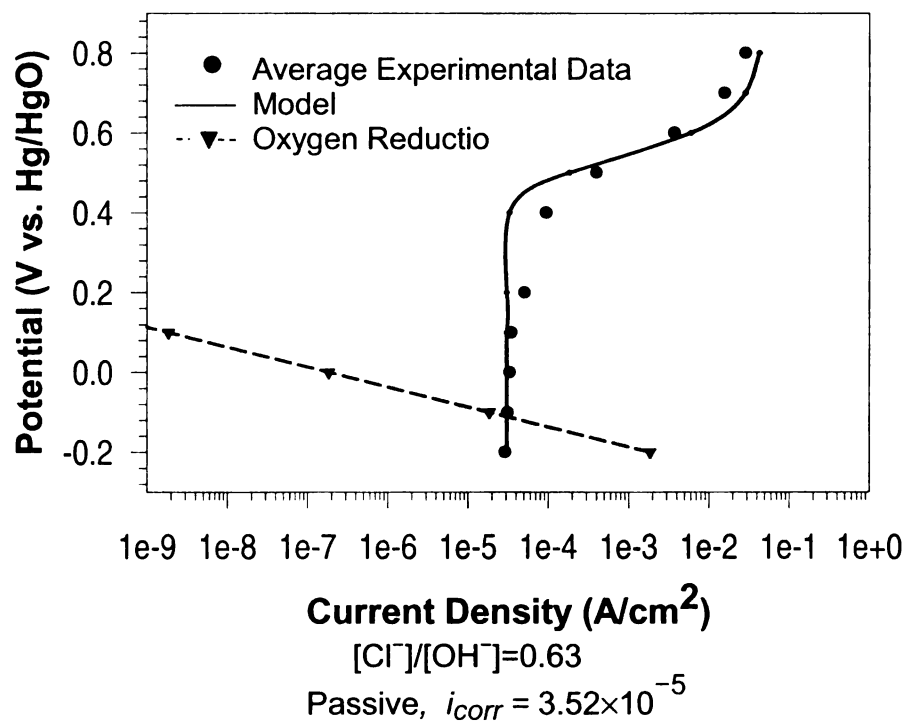
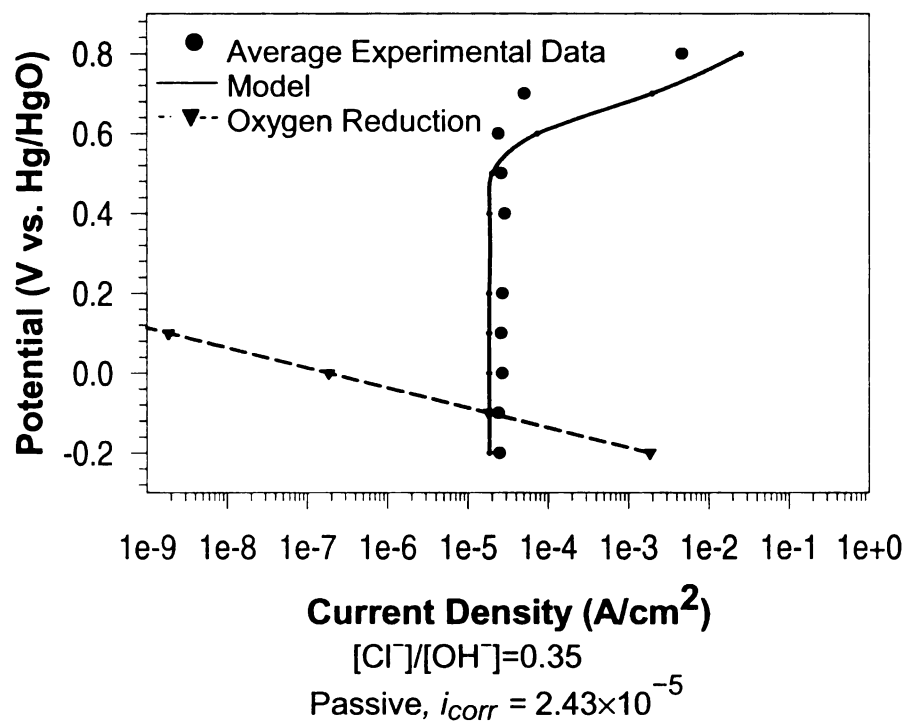


Figure 4-17 Cont'd: Comparison between experimental data and model, and the corrosion current

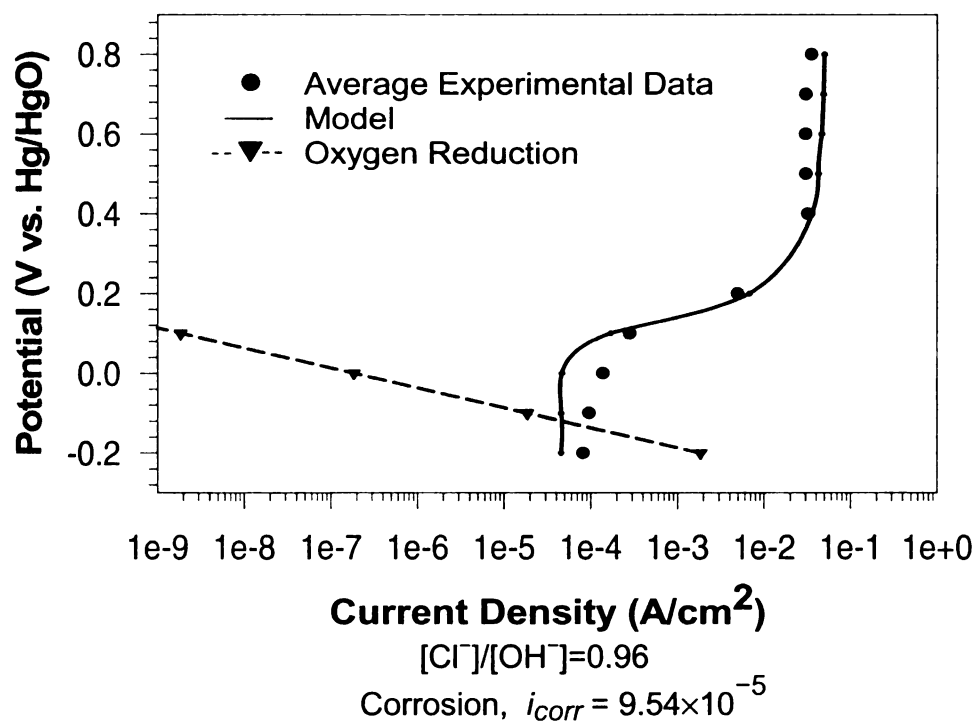
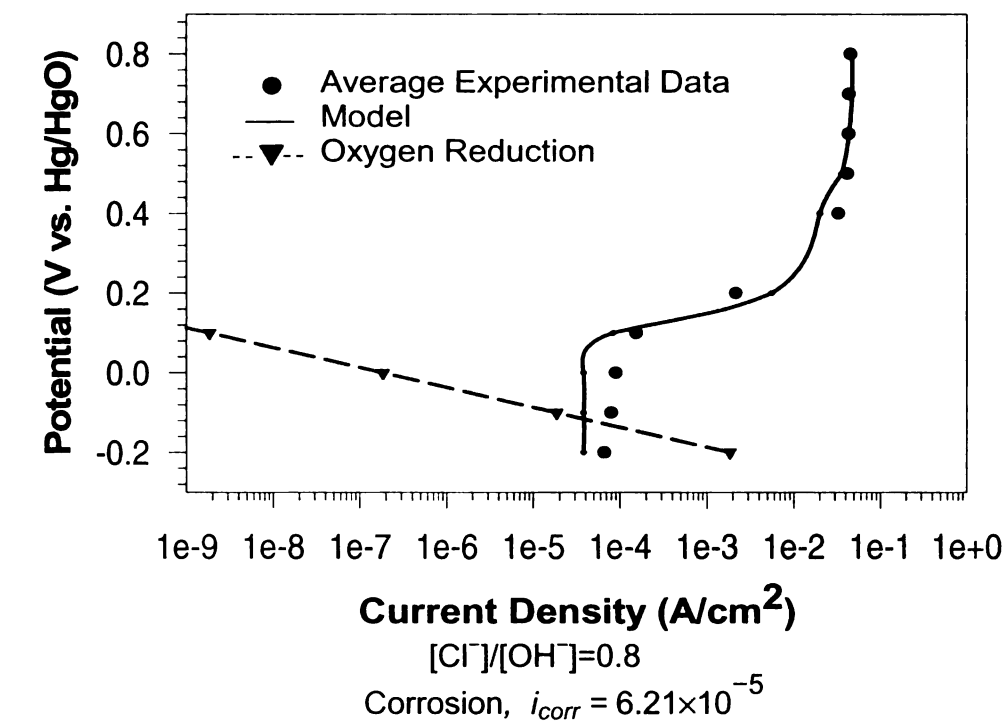


Figure 4-17 Cont'd: Comparison between experimental data and model, and the corrosion current

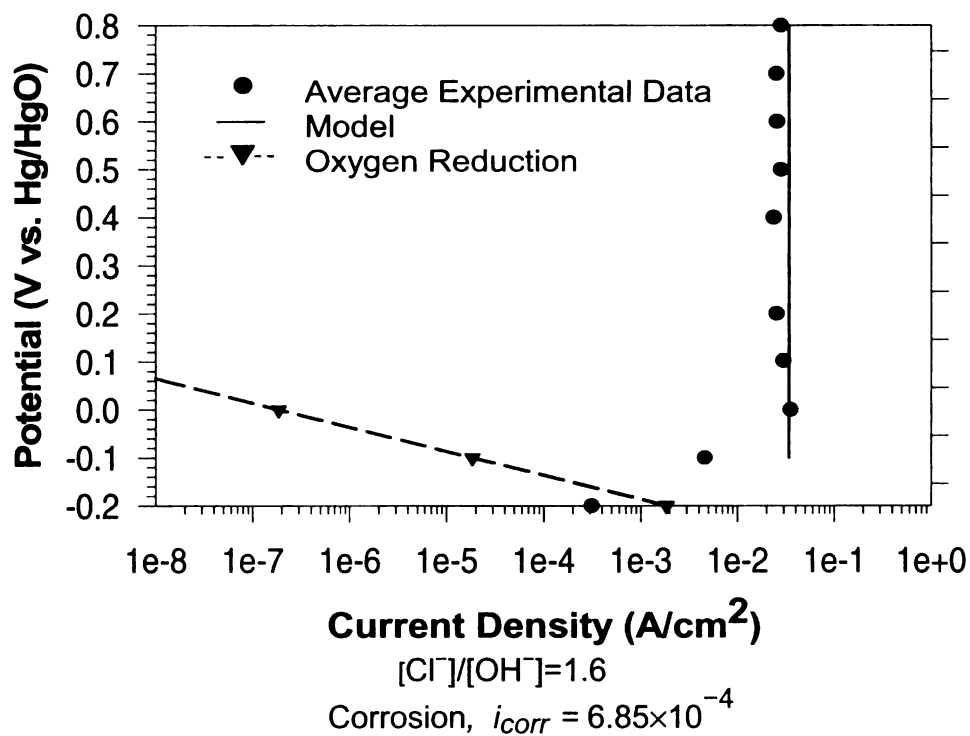
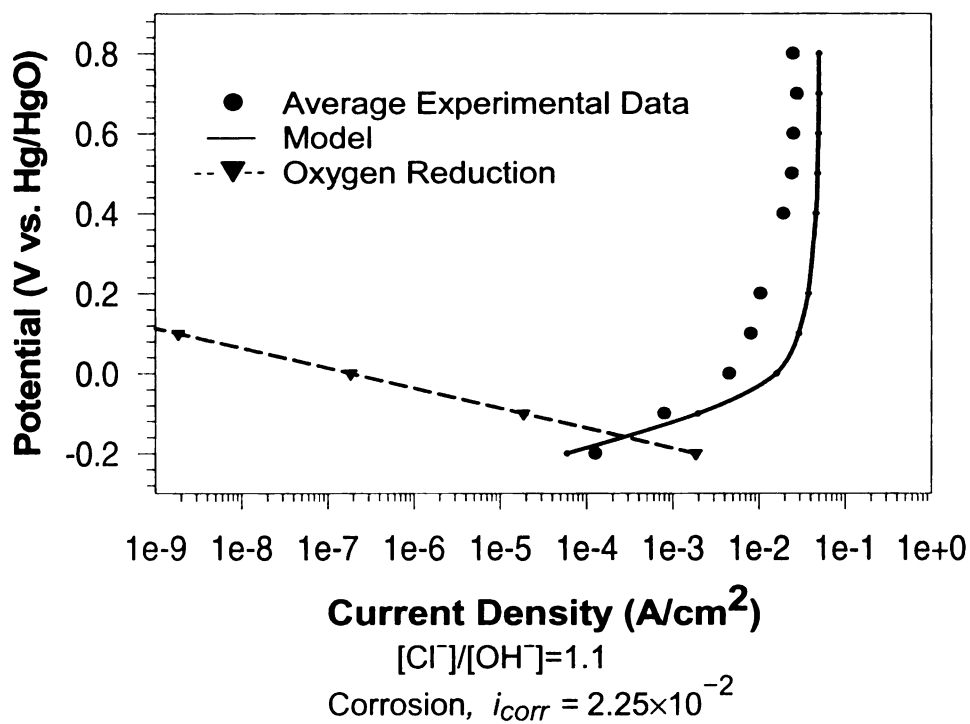


Figure 4-17 Cont'd: Comparison between experimental data and model, and the corrosion current

4.4 Limiting Corrosion Rate

When there is no limitation of oxygen in the corroding system, the corrosion current will increase with increasing chloride concentration. However, as Figure 4-9 shows even if oxygen is available the corrosion current will reach the anodic limiting current because the diffusion of corrosion products away from the anode is limited. This kind of limiting current is in very high. For modeling the corrosion of steel in concrete, the main factor that controls the corrosion current is the availability of oxygen after corrosion starts. For determining the availability of oxygen for corrosion to continue it is necessary to determine the pit structure and the oxygen diffusion path.

4.4.1 Corrosion Scale

One of the unknown features of corrosion that is essential for better estimation of the corrosion rate is the corrosion scale and the type of corrosion products. The composition and structure of the corrosion products in concrete is necessary not only to estimate the corrosion expansion and pressure applied on the concrete cover, but also to estimate the corrosion rate based on the limiting current, diffusion of oxidation, and reduction of species inside and outside the pit. The structure of the pit and corrosion products depends on the aqueous phase of the pore solution, steel type, and pressure adjacent to the bar. In general, the composition of the expansive corrosion products may be expressed as $\{a.\text{Fe}(\text{OH})_2 + b.\text{Fe}(\text{OH})_3 + c.\text{H}_2\text{O}\}$ (Bhagava et al. 2005), where a , b and c are variables that depend on the alkalinity of the pore water solution of the concrete, the oxygen supply, and the moisture content. For example, black rust (Fe_2O_3) will form

mostly in concrete immersed in deep water where the oxygen availability is low (Bazant 1979).

Table 4-5: Weight and Volume of Various Corrosion Products (Bhagava et al. 2005)

Parameter	Name of corrosion product					
	FeO	Fe ₃ O ₄	Fe ₂ O ₃	Fe(OH) ₂	Fe(OH) ₃	Fe(OH) ₃ +3H ₂ O
α	0.777	0.724	0.699	0.622	0.523	0.347
β	1.8	2.00	2.20	3.75	4.20	6.4

α : ratio of molecular weight of iron to molecular weight of the corrosion product

β : ratio of volume of corrosion products to the volume of iron consumed in corrosion

The model proposed herein for the corrosion scale is based on the literature (Jones 1992, Sarin et al. 2004) and experimental observation of the corroded specimens under the scanning electron microscope (SEM). In the model, the scale consists of two main layers, the inside part (core layer), and the outer part (top layer). These two layers are separated by a hard shell layer.

The core layer is assumed to be a porous mass made up of small particles of different component phases. Fe(II) is expected to dominate the core part of the scale due to a lack of hydroxide ions since the cathodic reaction will take place outside the core layer. The pores in the core layer act as corrosion pits and will have high chloride ion concentration and possibly low pH. The porous core is a conductive layer since the Fe(II) products are more conductive than Fe(III) products that can transfer electrons outside this layer for other reactions.

The wet outside region of the scale is exposed to air and the ferrous hydroxide is rapidly oxidized to the ferric components Fe(OH)₃ and Fe(OH)₃+3H₂O. This layer is expected to be fully saturated with concrete pore water. Along the top surface layer at the

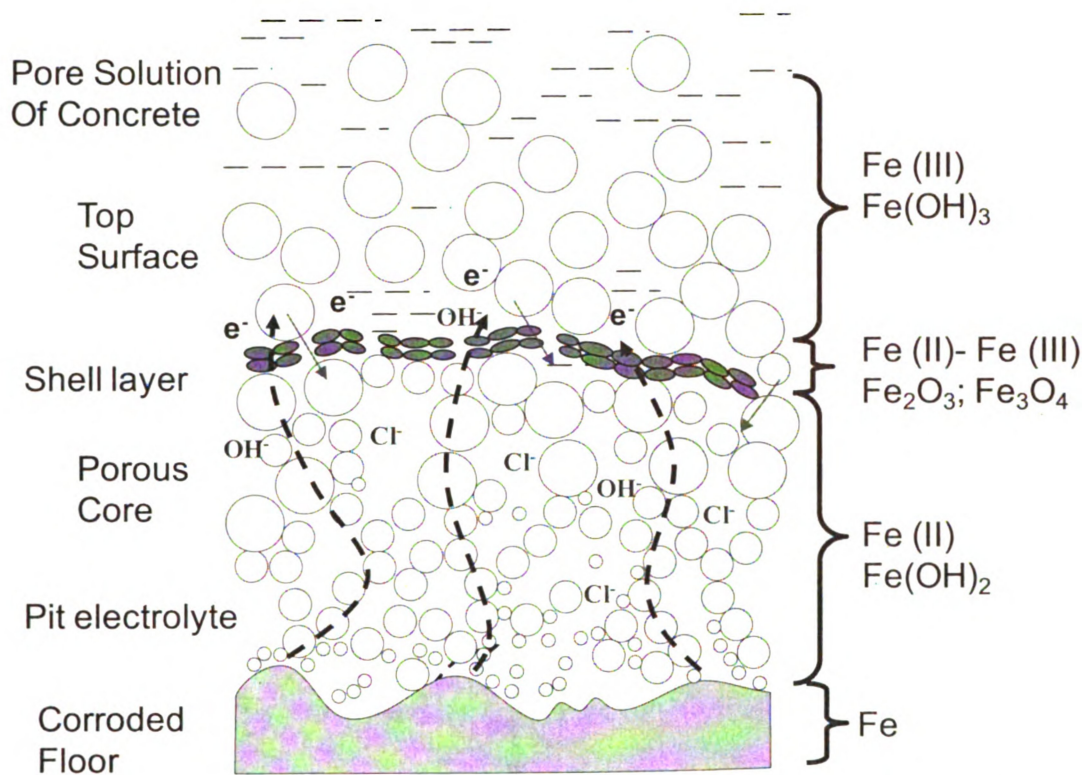


Figure 4-18: Corrosion scale model (adapted from Jones 1992, Sarin et al. 2004)

concrete interface, particles are loosely held and can be easily transferred to the concrete pore water under the pressure that is produced. Figure 4-18 shows the schematic of the corrosion scale.

4.5 Corrosion Current

In an alkaline environment, corrosion of steel starts when the chloride concentration reaches a certain threshold value. Most existing models treat the corrosion rate as a steady state phenomenon, although it is known that the corrosion rate varies with change in temperature, chloride content, and corrosion level (Liu 1996). No quantitative model has been developed to take all of these factors into account. Initially, the rate of corrosion will depend on the chloride concentration and the rate of the anodic reaction.

As the corrosion becomes more severe and the rust layers build up, the corrosion rate will be controlled by the cathodic reaction and the availability of oxygen at the cathode.

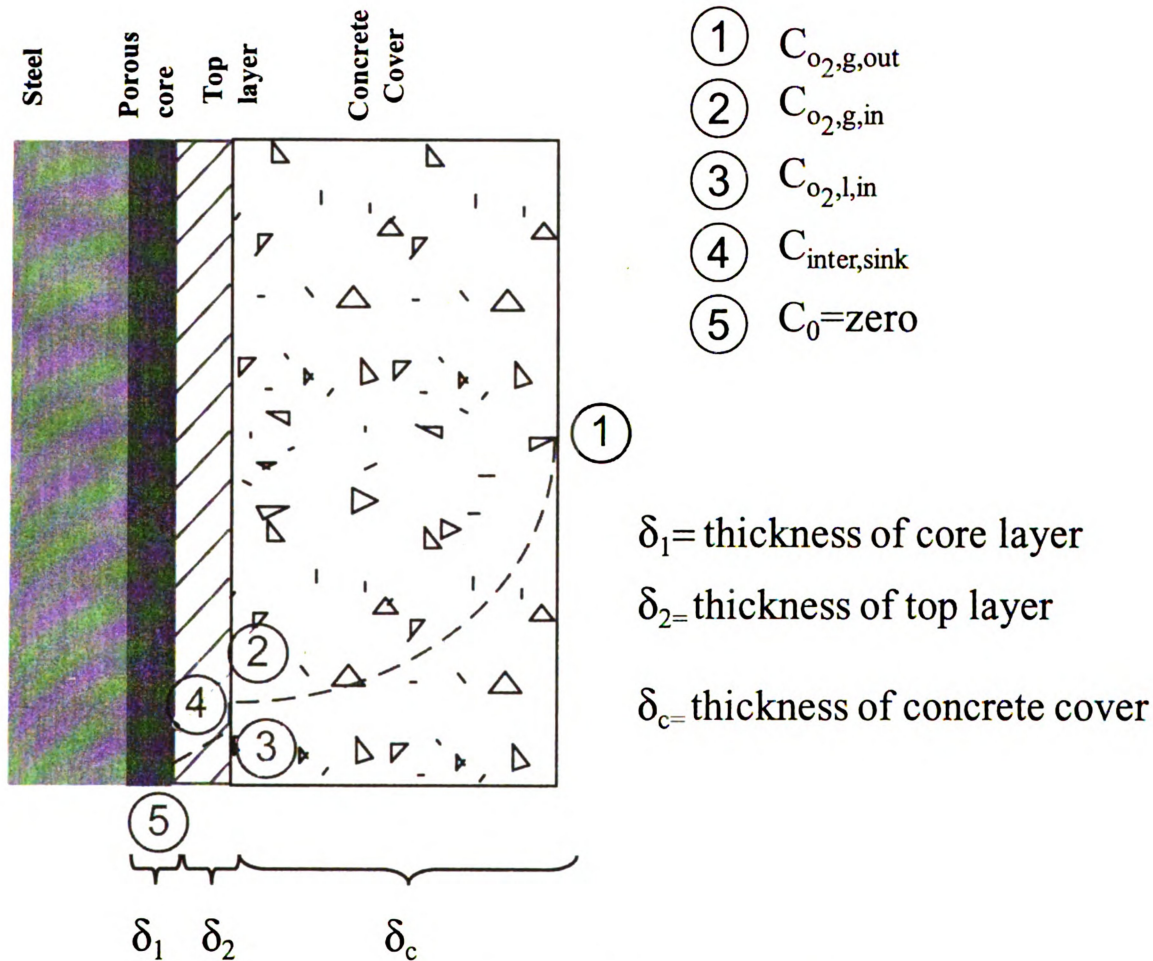


Figure 4-19: Oxygen diffusion path

Equation 4-9 can be used to determinate the start of corrosion when there is enough oxygen inside the concrete at the bar level. It should be noted that Equation 4-9 was obtained using the maximum dissolved oxygen concentration in water, since the only oxygen that can be used in the corrosion process is the dissolved oxygen. If for any reason the concentration of dissolved oxygen is different than normal due to change in temperature or pressure, the equation parameter can be updated by updating the cathodic

polarization curve and finding the intersection with the same anodic polarization curve, since the anodic polarization curve is independent of the oxygen concentration, and only depends on the chloride concentration and perhaps temperature.

The corrosion current will continue according to Equations 4-9 until it reaches the limiting current due to lack of oxygen at the steel surface. The limiting current at each time can be calculated through:

$$i_{corr} = n_{O_2} \cdot F \cdot j_{O_2,used} \quad (4-10)$$

where $j_{O_2,used}$ is the flux of the oxygen consumed at the cathode, n_{O_2} is 4 for the reduction of oxygen in the corrosion reaction, and F is Faraday's constant.

At the current limiting stage the oxygen flux into the cathode is a dominating factor. Figure 4-19 shows a simplified model of the different stages of oxygen diffusion to the anode. The flux of oxygen to the steel bar can be divided into three stages. In the first stage oxygen diffuses through the concrete cover, and will follow Fick's Second Law:

$$\frac{\partial C_O}{\partial t} = D_O \frac{\partial^2 C_O}{\partial x^2} \quad (4-11)$$

where C_O is the oxygen concentration, and D_O is the coefficient for diffusion of oxygen into the concrete cover. At any time, the concentration of oxygen gas in the concrete adjacent to the bar is denoted by $C_{O_2,g,in}$. Since only the dissolved oxygen can be used in the cathodic reaction, it is assumed that the dissolved oxygen is in thermodynamic

equilibrium with the oxygen partial pressure ($C_{O_2,g,in}$) in the gaseous phase, and according to Henry's Law

$$C_{O_2,l,in} = C_{O_2,g,in} \frac{RT}{K_H} \quad (4-12)$$

where $C_{O_2,l,in}$ is the dissolved oxygen concentration.

It is assumed that the water content of the concrete will reach equilibrium with the outside relative humidity. The semi-empirical equations proposed by Bazant (1978, 1979) were used to calculate the water content of the concrete.

$$m_L = \left\{ \begin{array}{ll} \rho_{CEM} \left(\frac{m_0}{\rho_{CEM}} \frac{P_v}{P_{SAT}} \right)^{1/m(T)} & , \frac{P_v}{P_{SAT}} \leq 0.96 \\ m_{0.96} + \left(\frac{P_v}{P_{SAT}} - 0.96 \right) \frac{m_{1.04} - m_{0.96}}{0.08} & , 0.96 < \frac{P_v}{P_{SAT}} < 1.04 \\ m_{L0} \left[1 + 0.12 \left(\frac{P_v}{P_{SAT}} - 1.04 \right) \right] & , \frac{P_v}{P_{SAT}} \geq 1.04 \end{array} \right\} \quad (4-13)$$

where

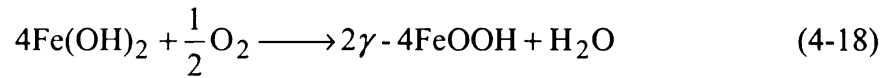
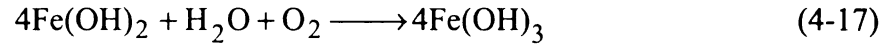
$$m(T) = 1.04 - \frac{(T + 10)^2}{22.3(T_0 + 10)^2 + (T + 10)^2} \quad (4-14)$$

$$m_{0.96} = \rho_{cem} (0.96 \frac{m_0}{m_{pem}})^{1/m(T)} \quad (4-15)$$

$$m_{1.04} = m_{L0} \quad (4-16)$$

where T is temperature in $^{\circ}C$, T_0 is $25^{\circ}C$, ρ_{cem} is the mass of the cement per cubic meter of concrete in the initial concrete mix. m_{L0} is the initial mass of water in the mix

and m_0 is the saturation water content at $25^\circ C$ and P_V/P_{SAT} is the relative outside humidity. $C_{O_2,l,in}$ diffuses across the top layer of the rust scale since this layer is assumed to be fully saturated. The top layer consumes some of the oxygen in the secondary non-electrochemical reaction, in which Fe(II) is oxidized to Fe(III):



Assuming that the top layer is a homogeneous porous medium, Fick's First Law can be used to predict the flux of the diffused oxygen through the rust layer:

$$J_{O_2,used} = (D_{o,r} \frac{\partial C_{O_2}}{\partial x}) \quad (4-19)$$

where $D_{O,r}$ is the coefficient for diffusion of oxygen into the rust layer, and can be calculated from the general equation for diffusion in porous media (Equation 2-14). The limiting current occurs when C_0 reaches zero, and all the diffused oxygen is consumed. The limiting oxygen flux can be estimated from

$$\frac{\partial C}{\partial x} = \frac{C_{O_2,i,in} - C_{O_2,consumed}}{\delta^2} \quad (4-20)$$

The final limiting current will be

$$i_{lim} = n_{O_2} \cdot f \cdot D_{o,r} \cdot \left(\frac{C_{O_2,i,in} - C_{O_2,consumed}}{\delta^2} \right) \quad (4-21)$$

where $C_{O_2,consumed}$ is the loss in oxygen concentration due to consumption of oxygen in the top layer. The corrosion current will then be

$$i_{corr} = \min(i_{corr}, i_{lim}) \quad (4-22)$$

According to Faraday's Law, the flux of the Fe^{2+} produced will be

$$j_{Fe(OH)_2} = \frac{i_{corr}}{n_{Fe} \cdot F} \quad (4-23)$$

Assuming that Equation 4-18 dominates the secondary reaction:

$$j_{Fe(OH)_2} = k_r \cdot j_{Fe(OH)_2} \quad (4-24)$$

where k_r needs to be determined experimentally or obtained from the literature. k_r can be assumed to be 1.0 in air since $Fe(OH)_2$ is not a stable product when sufficient oxygen is available, and for corrosion of steel in concrete it can vary from 1.0 to less than 0.5 depending on the availability of oxygen. A parametric study was done to evaluate the effect of this factor on the limiting current.

$C_{O_2,consumed}$ can be calculated from Equation 4-18 since the flux of the consumed oxygen is four times smaller than the flux of the $Fe(OH)_3$ produced (see Equation 4-13). Thus

$$\frac{dC_{O_2,consumed}}{dt} = \frac{j_{Fe(OH)_3}}{4 \cdot \delta_2} \quad (4-25)$$

Assuming that the density of the porous core and top layer is a function of pressure and 3.75 and 4.20 times smaller than the density of steel, respectively (see Table 4-5), the rate of build-up of corrosion products is:

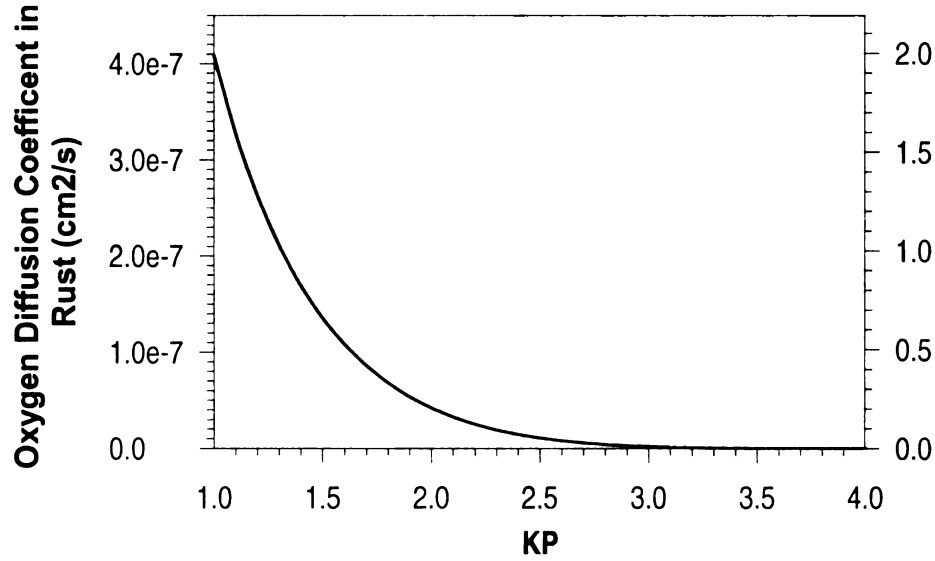


Figure 4-20: Effect of K_P factor on oxygen diffusion coefficient

$$\frac{d\delta_1}{dt} = \frac{j_{Fe(OH)_2} \cdot A_{Fe(OH)_2}}{\rho_{Fe(OH)_2}} = \frac{3.75(J_{Fe(OH)_2} - J_{Fe(OH)_3}) \cdot A_{Fe(OH)_2}}{\rho_{Fe} \cdot K_P} \quad (4-26)$$

$$\frac{d\delta_2}{dt} = \frac{j_{Fe(OH)_3} \cdot A_{Fe(OH)_3}}{\rho_{Fe(OH)_3}} = \frac{4.20(J_{Fe(OH)_3}) \cdot A_{Fe(OH)_2}}{\rho_{Fe} \cdot K_P} \quad (4-27)$$

K_P is a correction factor that accounts for pressure dependency of the density of the corrosion products. K_P was calibrated using the experimental data from Chapter 3 and microscopic image analysis

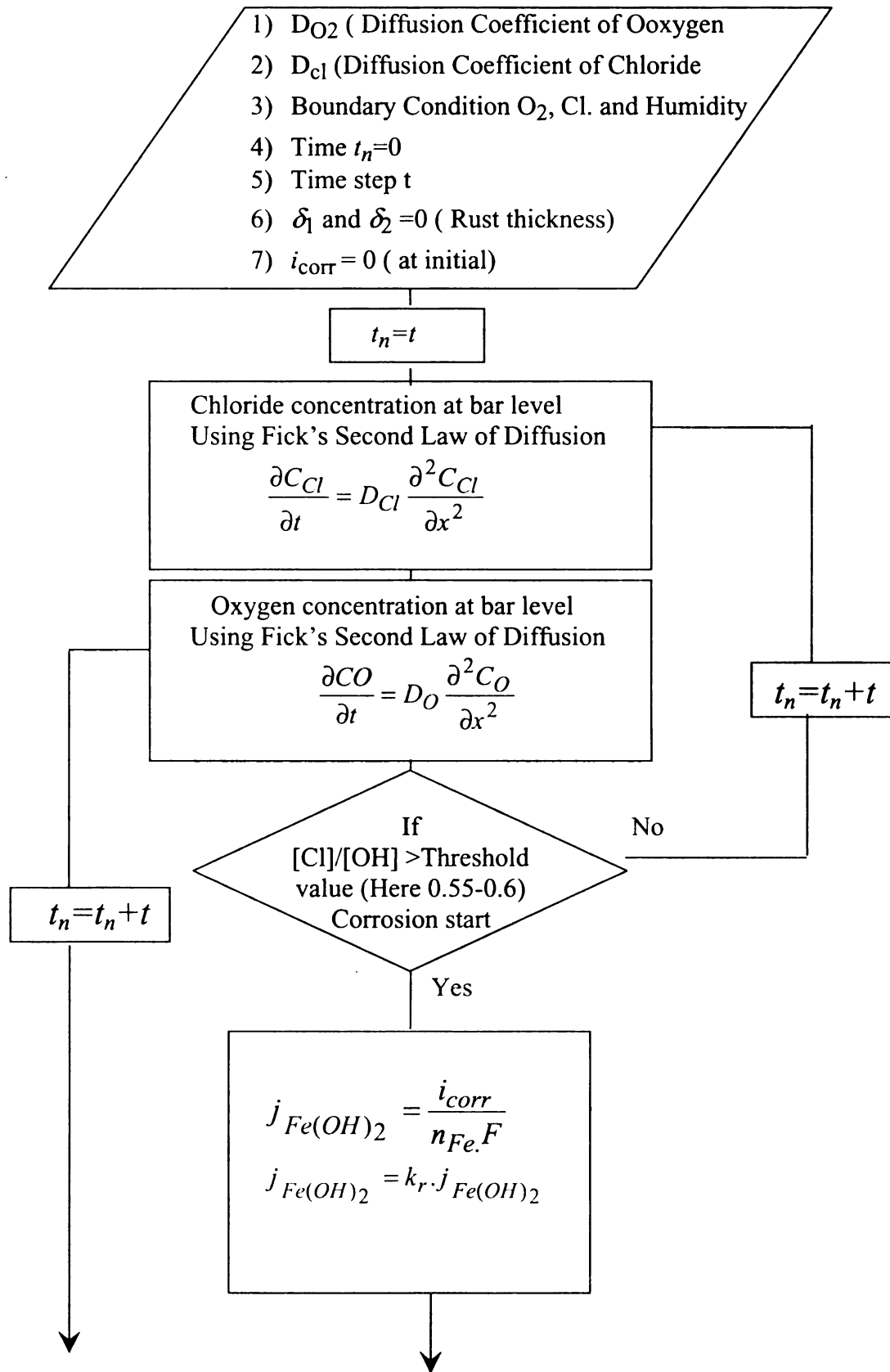


Figure 4-21: Flowchart of the model

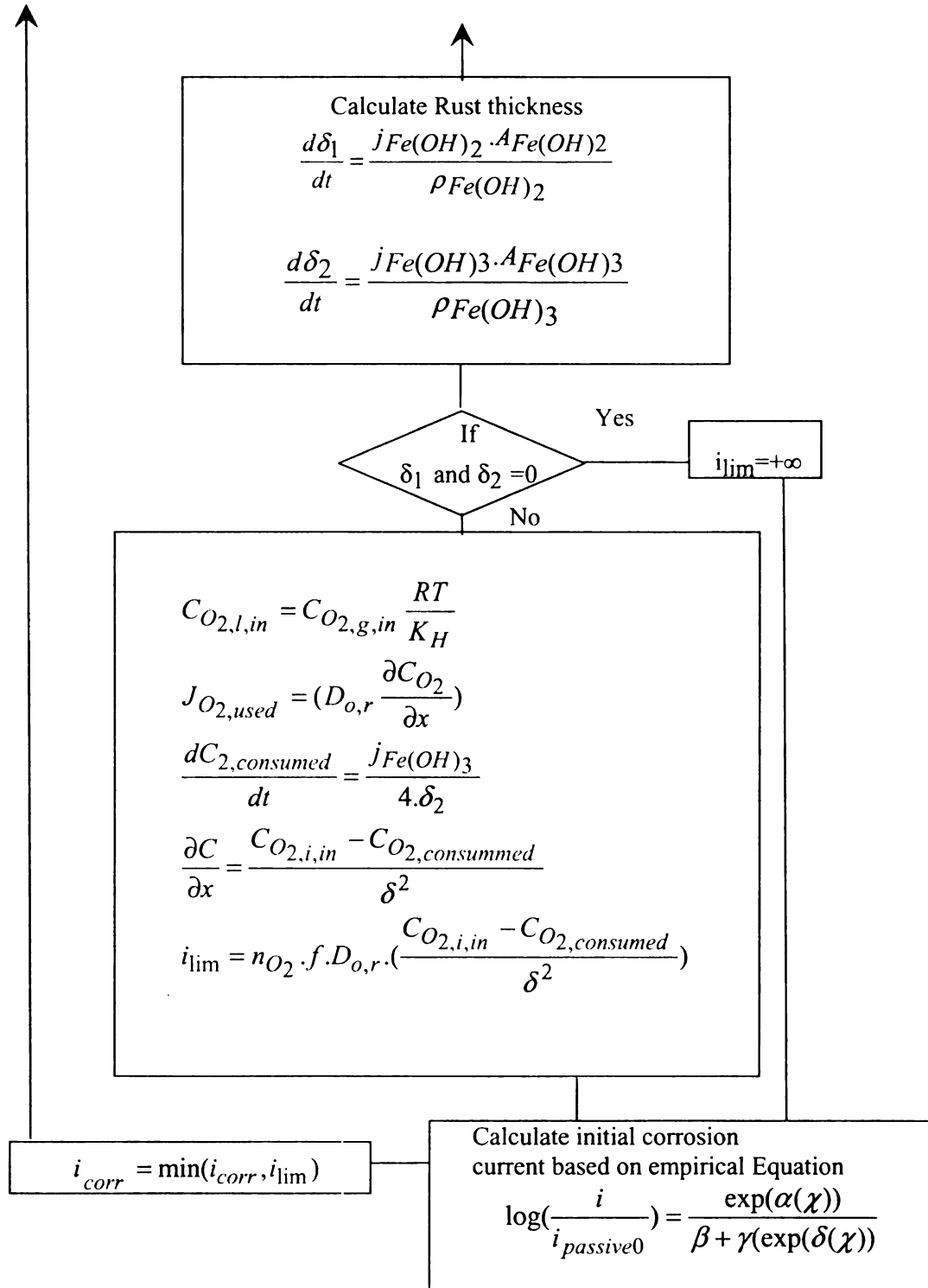


Figure 4-21 Cont'd: Flowchart of the model

explained in the next section. K_P is a very important parameter it affects the pressure applied to the concrete cover, the rust thickness that controls the oxygen diffusion, and the diffusion coefficient of oxygen in the rust in Equation 4-21. Figure 4-20 shows the effect of K_P on the oxygen diffusion coefficient in the rust layer.

4.6 Calibration with Experimental Data

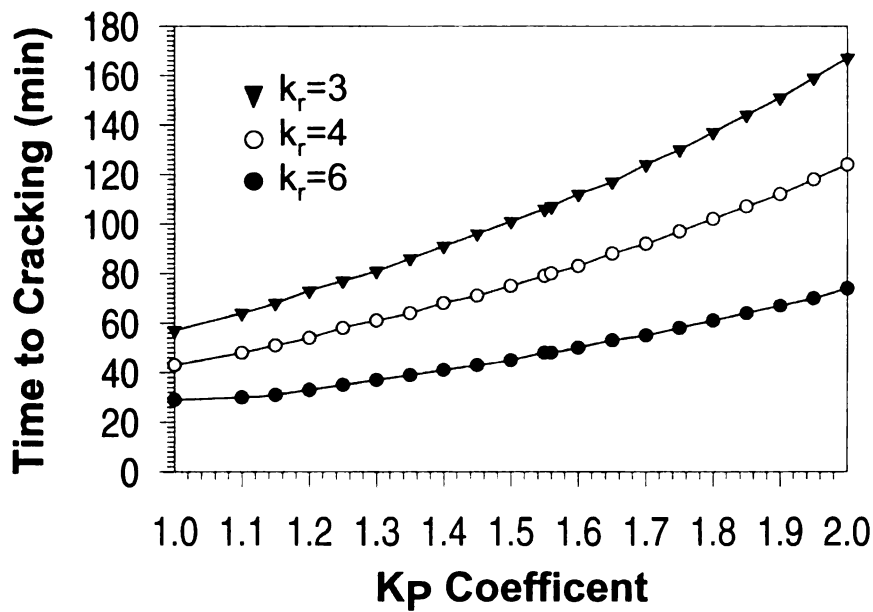


Figure 4-22: Time to cracking as function of K_P , using the model.

function of the corrosion current. For calibrating K_P the model proposed in this chapter was used to predict the rust thickness and cracking time for the experimental specimens described in Chapter 3 by using a constant current density of 0.0045 A/cm^2 as applied in the accelerated corrosion test. K_P was varied from 1 to 2. K_P was calibrated based on the time to the cracking of the concrete cover. The goal was to establish a unique K_P factor

As explained in Chapter 3, experimental tests were performed to establish the rust thickness at the time the concrete cover cracks as a

for different k_r values using experimental data for the time to cracking. After calibration, the rust thickness obtained from the experimental test and the model was compared to establish the accuracy of the model. Figure 4-22 shows the time to cracking as a function of K_P for all three k_r ratios. Figure 4-23 to Figure 4-25 shows the cracking time from experimental tests and the model for individual k_r ratios. These results help to calibrate the model for all three k_r ratios to obtain a unique K_P factor.

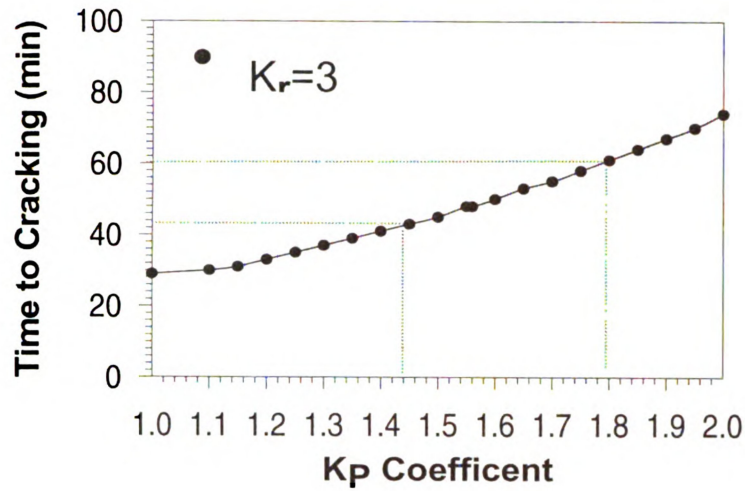


Figure 4-23: Model calibration results for $k_r = 3$

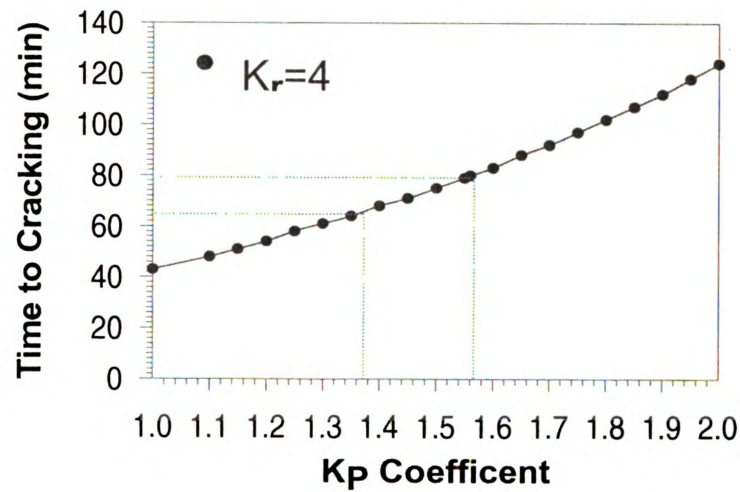


Figure 4-24: Model calibration results for $k_r = 4$

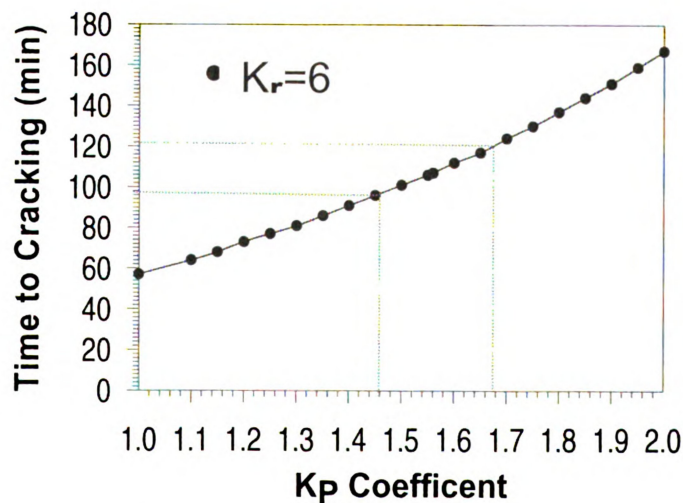


Figure 4-25: Model calibration results for $k_r = 6$

As Figure 4-23 for $k_r = 3$ shows, in the experiment the time to cracking (see Figure 3-12) was between 45 and 60 minutes, which yields a K_P coefficient between 1.50 and 1.8, with an average of 1.65. For $k_r = 4$, the cracking time from experiments was between 65 and 80 minutes, which yields a K_P coefficient between 1.35 and 1.56, with an average of 1.45. For $k_r = 6$ the cracking time was between 95 and 125 minutes, which yields a K_P factor between 1.45 and 1.7 with an average of 1.58. The average of all three average values of 1.65, 1.45, and 1.58 is 1.56. Also, all the K_P values overlap between 1.5 to 1.56, and a representative value of 1.56 can be used. A K_P value of 1.56 yields cracking times of 48, 79, and 107 minutes compared to average cracking times of 53, 72.5, and 110 minutes from experimental results for k_r value of 3, 4 and 6, respectively.

The experimental results of the rust thickness over time are shown in Figure 3-12 of Chapter 3. Figure 4-26 shows the same graph superimposed with the rust thickness predicted by the model with $K_P = 1.56$. It should be noted that the rust thickness predicted by the model is independent of k_r . The build up of rust thickness in the proposed model is a not function of concrete cover when the current density is constant (see Equations 4-22 and 4-23). Figure 4-26 shows that the experimental results and model with $K_P = 1.56$ are in very good agreement especially up to cracking of the concrete for all k_r values. After cracking of the concrete, the value of K_P will change since the

pressure due to the confinement effect of the surrounding concrete will decrease and also, the crack will provide a migration path for rust products.

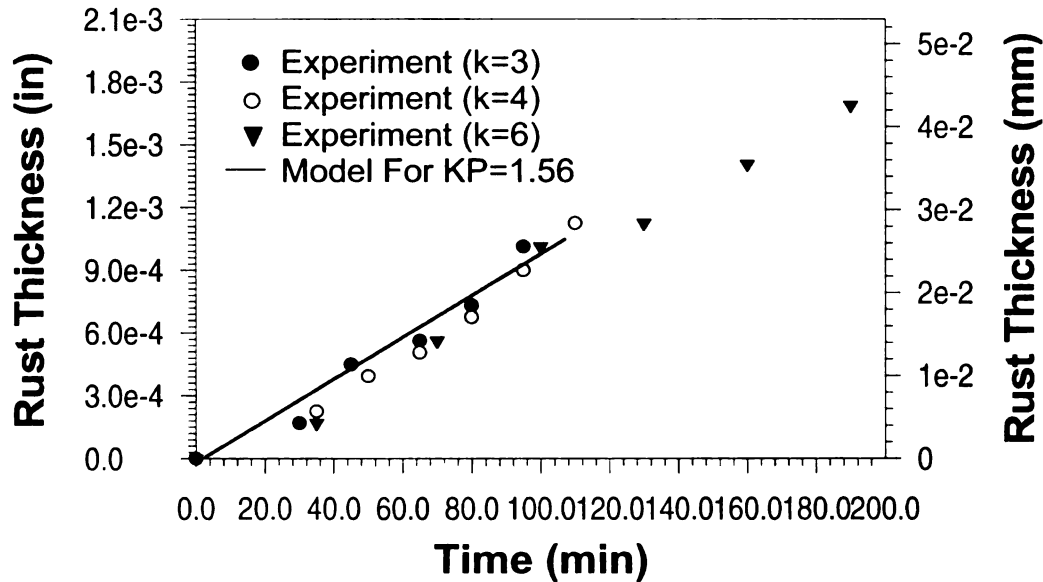


Figure 4-26: Comparison between model and experiment of rust thickness over time

Since the goal of this research is to predict the cracking time of the concrete cover, no attempt is made to develop a corrosion model after cracking occurs. The corrosion current model is only valid before cracking of the concrete cover, since after cracking the assumption that the corrosion current is limited based on the limitation of oxygen inside the concrete is not valid anymore as the crack provides free access to oxygen and a path for chloride ingress into the corrosion pit. The corrosion current will therefore increase dramatically after cracking and lead to spalling of the concrete cover due to multiple cracks.

4.7 Results and Discussion

After calibrating the corrosion model using experimental test results, the model was used to analyze the effect of different boundary conditions, concrete cover thicknesses, and concrete quality as a function of the water-cement ratio (w/c ratio).

Table 4-6: Different Concentrations Boundary Conditions (lb/in³)

Boundary Condition	Oxygen Concentration	Chloride Concentration
Type 1	1.1×10^{-5}	5.4×10^{-5}
Type 2	1.1×10^{-5}	4.7×10^{-4}
Type 3	2.6×10^{-7}	6.9×10^{-4}

Table 4-7: Geometry

Ratio (k_r)	D (outside diameter, in.)	d (inside diameter, in.)
3	3	1
4	4	1
6	6	1

Three different boundary conditions, three concrete cover thickness, and water cement ratios of 0.4, 0.5, and 0.6 were used to study the effect of these factors on the corrosion current. Table 4-6 and 4-7 show the values of the oxygen and chloride concentrations at the boundary for each condition and the chosen geometry condition. The geometry was chosen to yield the same k_r values as the experimental specimens, but with dimensions close to those of full size structures. Only the corrosion current is reported in this chapter and the time to cracking of the concrete cover after corrosion starts is described in more detail in the next chapter.

4.7.1 *Effect of Boundary Condition*

The chloride on the concrete surface can originate from various sources. Bridge structural components can be categorized as superstructure components (type 1), splash zone components (type 2), and submerged components (type 3). For submerged components, there is a constant supply of water and chloride on the surface of the concrete. However, corrosion of steel may be limited by the lack of oxygen dissolved in the water. In the splash zone, there is a constant supply of both oxygen and chloride, and these components experience the greatest corrosion. For the superstructure, the chloride supply can limit the corrosion process since it is supplied mainly by deicing salts.

Figure 4-30 to Figure 4-32 show the calculated corrosion current for the first 200 days after corrosion starts. The figure that shows the corrosion current is initially high but after the rust layer thickens and limits the oxygen diffusion into the corrosion cell, the corrosion current decreases. The decrease in the corrosion current continues over the duration of corrosion until cracking of the concrete. The relationship between the corrosion current and the rust thickness for different boundary conditions is explained in detail later in this section.

The corrosion rate for boundary condition types 1 and 2 (BC1 and BC2) does not vary much. In the model, the corrosion rate is controlled by the available oxygen and in both cases the oxygen accessibility is equal before the concrete cracks. Nevertheless, as the figures show, the corrosion current is more for BC2 compared to BC1 due to the availability of water in the concrete pores. As Equation 4-12 indicates, in the model only dissolved oxygen in water can contribute to the corrosion process, and the difference in

corrosion current between BC1 and BC2, even with the oxygen concentration being the same, is due to this. The water content calculated from the outside humidity equilibrium (Equation 4-13) is lower and causes a lower corrosion current in BC1. This is more evident in Figure 4-30 for the w/c ratio of 0.4 since porosity of the concrete is smaller, the water content is lower, and also the permeability of concrete is lower, all of which limit the mobility of water. For the higher water cement ratios (see Figure 4-31: and Figure 4-32:) the difference between BC1 and BC2 is smaller because of the higher water content in the concrete, but yet for comparable diameters the corrosion current is still slightly higher in BC2 compared to BC1. For boundary condition 3, the corrosion current is an order of magnitude smaller than for BC1 and BC2 because the oxygen availability is much more. This can increase the life of the structure by more than an order of magnitude.

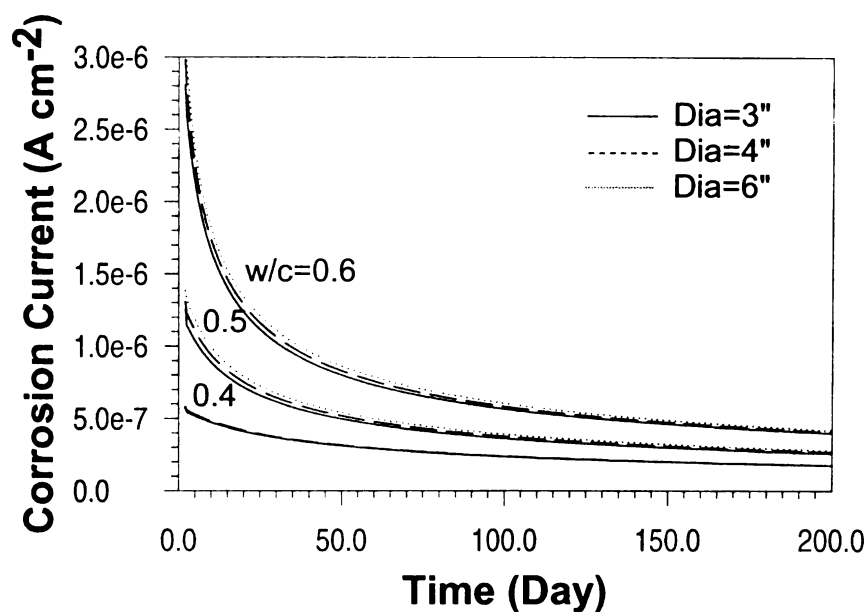


Figure 4-27: Corrosion current for BC1

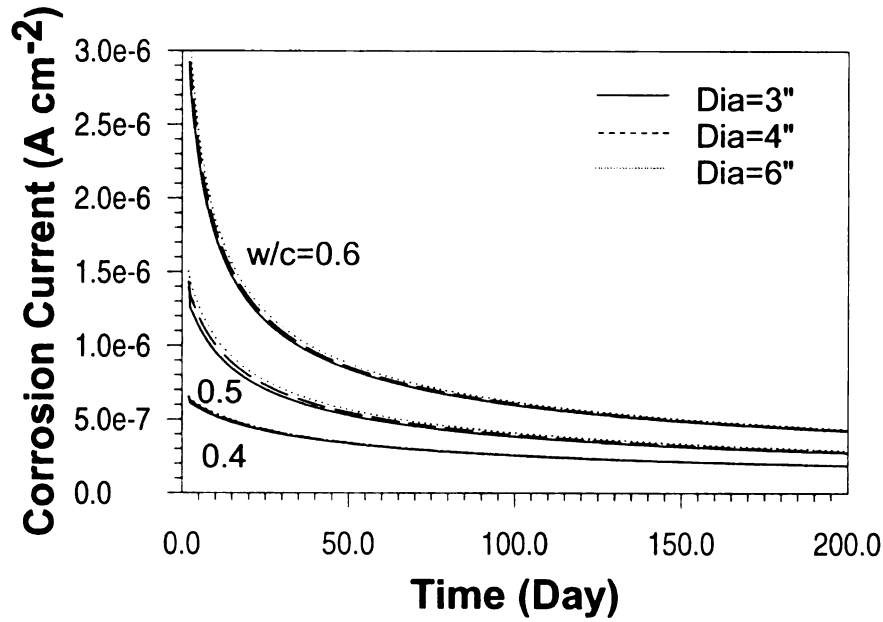


Figure 4-28: Corrosion current for BC2

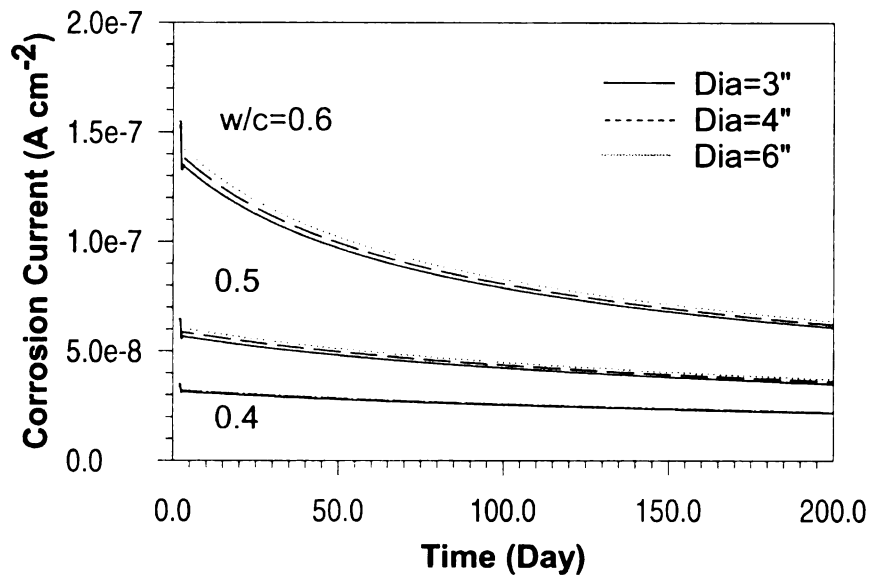


Figure 4-29: Corrosion current for BC3

The boundary condition not only affects the corrosion current and time to cracking of the concrete cover, but it can also impact the time for initiation of corrosion, t_1 . A comparison between the time for initiation of corrosion and the time from the initiation of corrosion to first cracking of the concrete cover is presented in the next chapter.

4.7.2 *Effect of Water-Cement Ratio*

The concrete quality is controlled mainly by the water/cement ratio. Figure 4-27 to Figure 4-29 show the effect of the water/cement ratio (w/c) on the corrosion rate. Concrete with a high w/c ratio has high porosity and therefore a high corrosion rate. The corrosion rate at the limiting current stage is strongly dependent on the oxygen diffusion to the top rust layer that is independent of the water/cement ratio. However, as Figure 4-19 shows, the oxygen has to diffuse through different regions including the concrete cover and is highly dependent on the concrete porosity and water/cement ratio. Using concrete with low w/c ratio has a considerable effect on decreasing the corrosion current. Decreasing the water/cement ratio from 0.6 to 0.5 reduces the corrosion current by about 45% and decreasing the water/cement ratio from 0.5 to 0.4 reduces corrosion about another 45%.

4.7.3 *Effect of Concrete Cover*

Although the concrete cover has a significant effect on the time for initiation of corrosion, t_1 , it does not seem to have significant effect on the corrosion rate. As Figure 4-29 to Figure 4-30 show, the corrosion current is always slightly higher for higher k_r ratios (i.e., higher concrete cover). It is not apparent why this is the case. The only possible explanation is numerical error arising from the different increment used in solving the model for different concrete cover thickness. A thicker concrete cover is likely to affect the time to corrosion initiation and also increase the critical pressure that causes the concrete to crack as discussed in the next chapter.

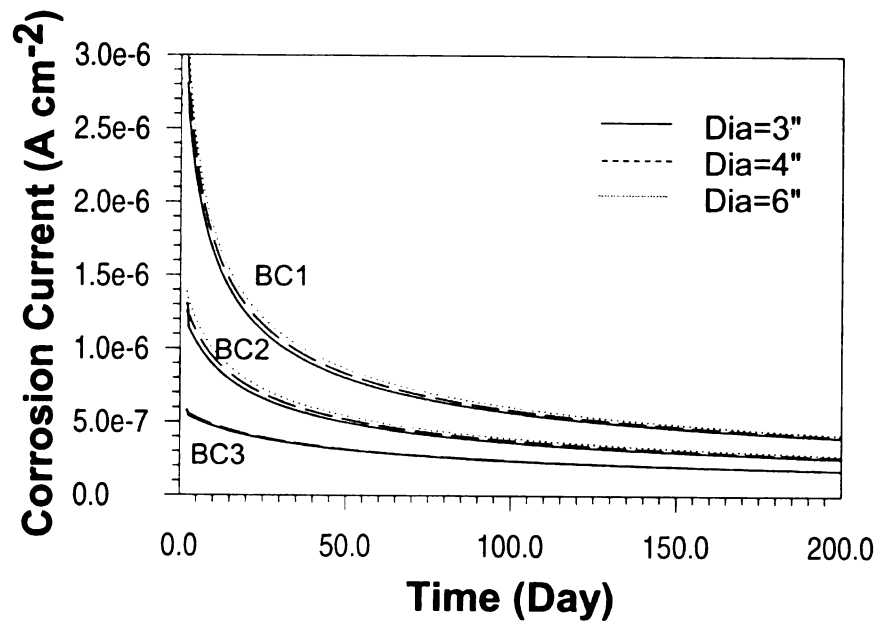


Figure 4-30: Corrosion current for W/C of 0.4

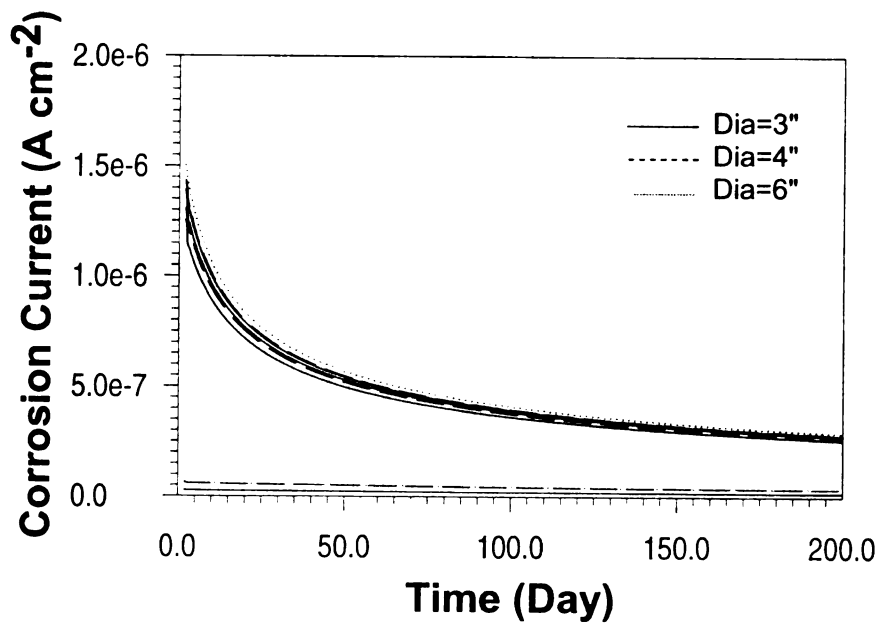


Figure 4-31: Corrosion current for W/C of 0.5

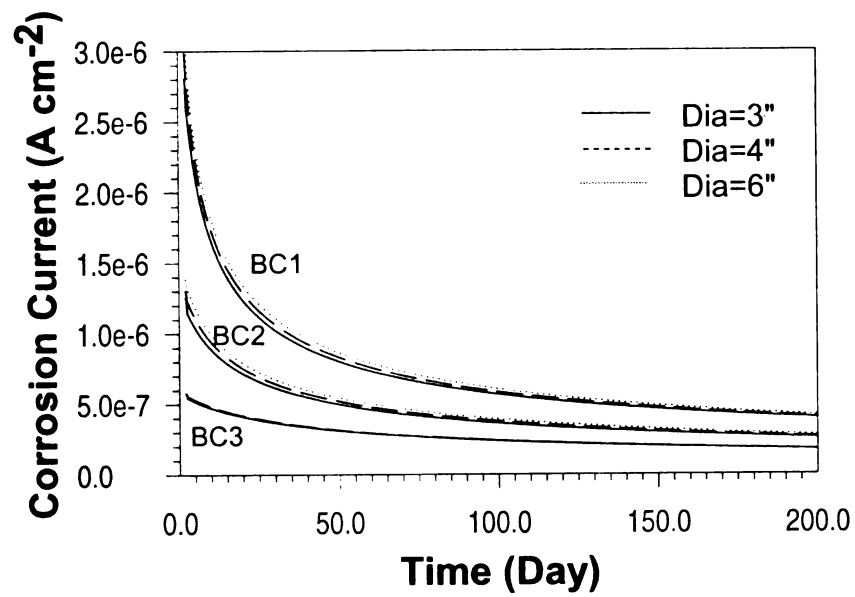


Figure 4-30: Corrosion current for W/C of 0.4

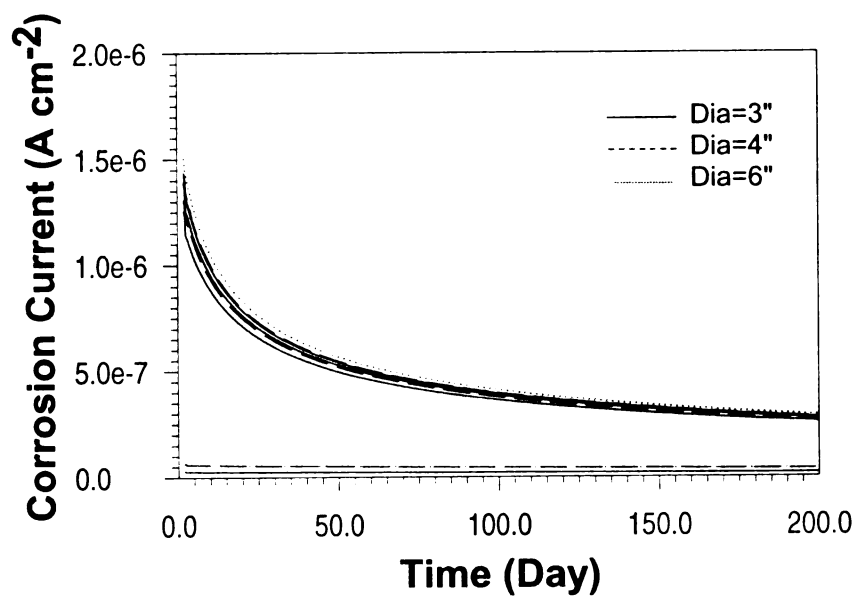


Figure 4-31: Corrosion current for W/C of 0.5

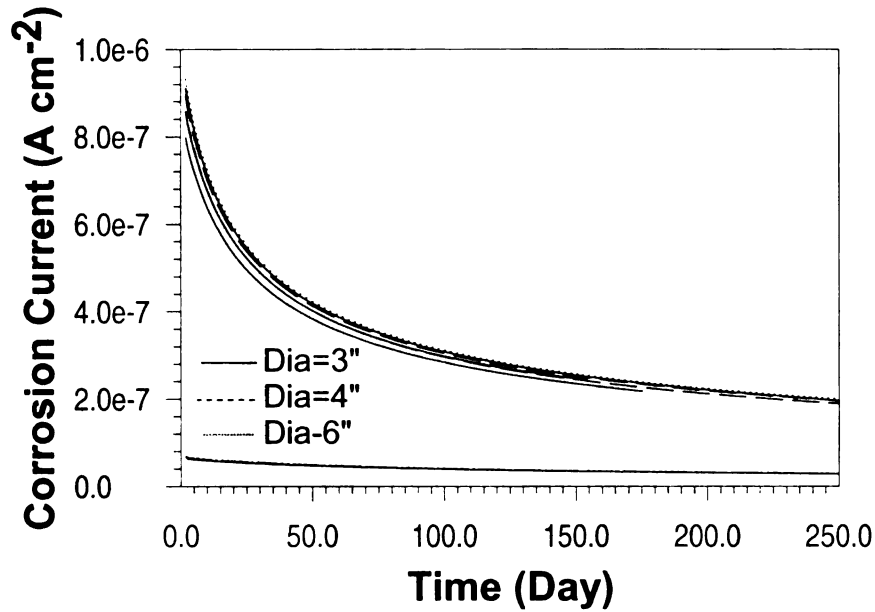


Figure 4-32: Corrosion current for W/C of 0.6

4.7.3.1 Relationship between Corrosion Current and Rust Thickness

There is a relationship between rust thickness and corrosion current. The corrosion current is mostly controlled by oxygen availability and as the rust thickness increases the oxygen diffusion through the rust layer slows down, thereby limiting the corrosion rate.

Figure 4-33 shows the relationship between the corrosion current and rust thickness for $k_r = 3$ and boundary condition type 2. This trend is very similar for other conditions.

As Figure 4-33 shows, the corrosion current is nonlinearly related to the thickness and the relationship may be modeled by

$$t_{Rust} = \alpha i_{corr}^{\beta} \quad (4-28)$$

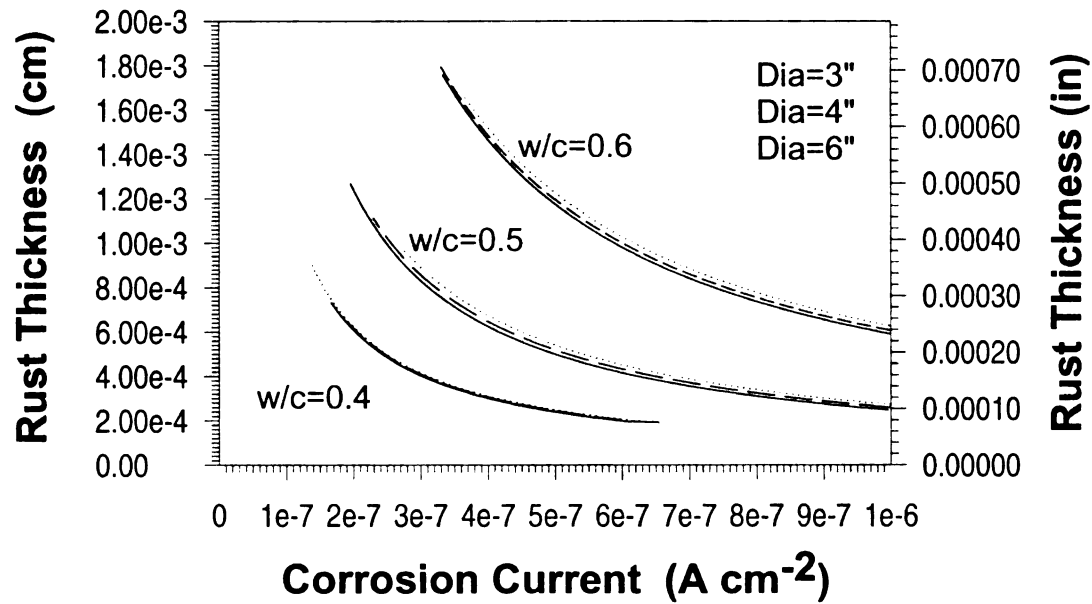


Figure 4-33: Corrosion Current and rust thickness for BC2

where α and β are parameters that can be calibrated for different conditions. Both parameters are functions of the boundary condition and water/cement ratio.

4.7.4 Comparison of Results with Literature

In this section, the results of the proposed model are compared with both theoretical and experimental results reported by others

4.7.4.1 Experimental Data

Since natural corrosion is a very long term phenomenon, not much experimental data is available in literature regarding it. Most of the experimental work on the corrosion of steel in concrete has been done using an accelerated corrosion test rather than natural corrosion. Further, it is not possible to accurately measure the corrosion current directly when the steel bar is inside the concrete and no direct measurement methods exist.

Corrosion monitoring techniques such as the half cell potential method measure the potential of the rebar but not measure the corrosion current. It is possible to estimate the

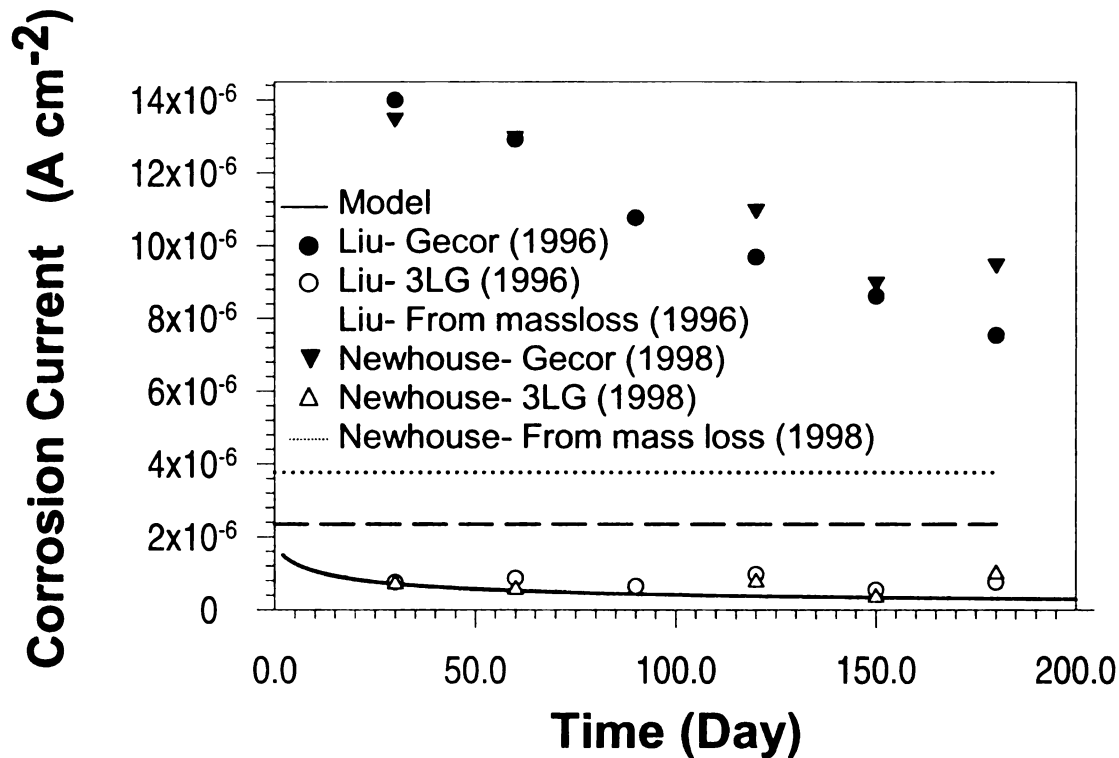


Figure 4-34: A comparison between literature test data and proposed model

average corrosion current by measuring the overall mass loss over a period of time and back calculating corrosion current density using Faraday's Law. While this method can give a good estimate of the average corrosion current, it can not capture the decay or possible fluctuation of the corrosion current over time.

Although the results of this study are categorized by different conditions such as the concrete properties or boundary conditions, it is difficult to find similar conditions in the literature to compare the results to. However, two sets of results from literature can be compared with.

Figure 4-34 shows a comparison between experimental tests on natural corrosion, and the results measured from two commercially available devices that can measure the corrosion current at different stages, the average corrosion current calculated from the mass loss, and predictions from the proposed model for similar conditions (Liu 1996, Newhouse and Wayer 1998). As the results shows the proposed model is in good agreement with readings from the 3LG device and also the decay in corrosion rate is in agreement. The proposed model predicts that the corrosion current will decay as the rust thickness grows with time. The corrosion rate calculated using the mass loss can not show the change in corrosion current with time, and as Figure 4-35 shows, the average corrosion rate is higher than that predicted by the model. However, back calculating the corrosion current density from the total mass loss over the bar length may yield error due to over cleaning the bar and assuming all rust products are Fe^{2+} oxides.

As Figure 4-34 shows, and as mentioned in the literature (Winston 2000 Liu 1996), the corrosion currents measured using the 3LG and Gecor devices have almost up to an order of magnitude difference. Also, none of the above instrument measurements are in agreement with the calculated corrosion current using the final mass loss. General broad criteria for corrosion acting developed from field and laboratory investigations using corrosion monitoring devices are shown in Table 4-8.

Table 4-8: Corrosion Current Guide (Broomfield 1996)

Corrosion Current $\mu\text{A}/\text{cm}^{-2}$	Condition
$I_{corr} < 0.1$	Passive condition
$0.5 > I_{corr} > 0.1$	Low Corrosion
$0.5 > I_{corr} > 1$	Moderate Corrosion
$I_{corr} > 1$	High Corrosion

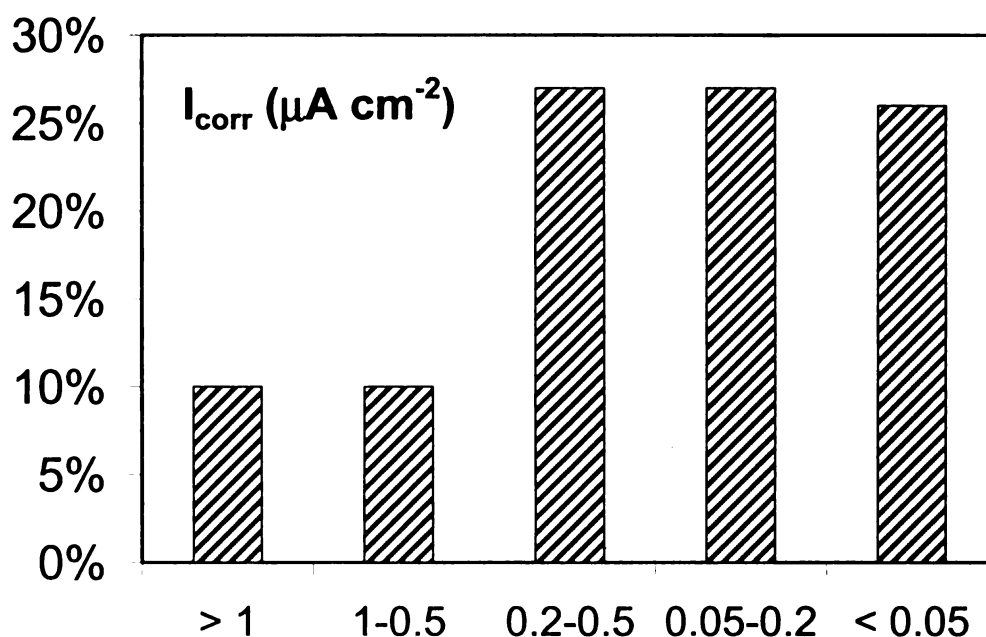


Figure 4-35: Field measurement of corrosion current (Broomfield 1996)

In the field, more than 80% of the half cell potential measurements indicate less than $0.5\ \mu A/cm^{-2}$ corrosion. Figure 4-35 shows the results of field measurements of the corrosion current.

As the results indicate, the corrosion current calculated using the model proposed in this study is generally in good agreement with field measurements. A detailed comparison is not possible because the age, concrete properties, length of corrosion activity etc, are often unknown.

4.7.4.2 Models

There are very few models for predicting the corrosion current. Different models have been proposed for predicting concrete cracking based on a constant corrosion

current (Maaddawy and Soudki 2007, Pantazopoulou and Papoulia 2001). Most models predict the corrosion current due to carbonation of the concrete cover (Liang et al. 2004 Huet et al. 2006). Others, such as Liu's model (1996) is purely empirical in Figure 4-37, the proposed model is compared with predictions by Liu's empirical model and experimental results from mass loss experiments to conducted (Liu 1996).

As Figure 4-35 shows, the model proposed in this work is in better agreement with the experiment test results than Liu's empirical equation.

4.8 Summary and Conclusions

This chapter focused on modeling the corrosion rate of steel inside concrete. First, the effect of chloride concentration on the anodic polarization curves for the corrosion of mild steel in alkaline media were experimentally obtained at varying chloride concentrations. As the ratio $\chi = [\text{Cl}^-]/[\text{OH}^-]$ increased to values greater than 0.6 at a pH of 13.46, the passivation current increased linearly with χ to maintain the passive layer. Pitting corrosion of steel occurs when $\chi > 0.6$. The pitting potential decreases cubically as χ increases. These data provide the basis for an empirical model of steel corrosion in alkaline environments containing chloride that is directly applicable to reinforced concrete structures.

After calculation of the initial corrosion current, the limiting current was modeled based on the cathodic limiting reaction and oxygen diffusion in the rust layer. The corrosion current was calculated for different boundary conditions, concrete properties and concrete cover. The concrete cover did not have significant effect on the corrosion current. The two main factors that influence the corrosion current are the boundary

conditions and the concrete quality. For high water/cement ratio, the concrete quality decreases the permeability of concrete increases, the diffusion of oxygen and water into the concrete increase, and consequently the corrosion current increases. Using good quality concrete with a low w/c ratio is in itself the first step in protecting the concrete structure from corrosion damage. Boundary conditions also have an effect on the corrosion current especially in the case of submerged structures. For superstructures and concrete elements in splash zones, when the chloride concentration reaches the threshold value, the corrosion current would be very similar to that before cracking of the concrete. However, the corrosion current would be little higher in splash zones due to the higher water content of concrete.

The corrosion current was compared with those obtained other in experiments, field measurements and corrosion models. The proposed model shows good agreement with experimental tests and some field measurement.

Chapter 5

Mechanical Modeling for Concrete Cover Cracking

5.1 Introduction

The previous chapter focused on electrochemical modeling of the corrosion current, and how the corrosion current decreases over time due to many factors. The effect of different parameters such as the water-cement (w/c) ratio, boundary condition and concrete cover on the corrosion current of a steel bar in concrete due to chloride ions was studied. The results showed that the w/c ratio has the most effect and can increase the corrosion current by almost 45%. This chapter focuses on the time for cracking of the concrete cover due to corrosion, t_2 , and how the corrosion current controls this time. The

time for chloride diffusion to initiate corrosion, t_1 , is also compared with t_2 for different conditions.

The time to cracking of the concrete cover, t_2 , is based on the corrosion rate calculated in Chapter 4. First, the rust thickness calculated in Chapter 4 is used to estimate the pressure applied to the concrete cover, accounting for the amount of the rust products that diffuse into the concrete pores. The inelastic behavior of concrete is used to calculate the pressure due to the thickening rust layer. The critical pressure that makes the concrete crack is calculated based on a proposed model that is calibrated with finite element analysis and experimental data from the literature (Shah and Swartz 1987).

Since abundant oxygen and chloride is available at the corrosion pit after the concrete cracks, the current will increase dramatically, spalling and delamination of the concrete cover will occur quickly, and the time t_3 from first crack to spalling is the shortest of the times for all three corrosion steps. As mentioned earlier, the focus of this research is on the time t_2 , and calculation of the time t_3 is beyond the scope of this work.

5.2 Mechanistic Model of Concrete Cover Cracking

Durability problems in concrete are at the crossroad between chemistry and mechanics (Bournazel and Mornaville 1997). This statement is true for all durability problems in concrete, including corrosion of the steel reinforcement. Concrete durability problems are usually caused by undesirable chemical reactions that induce stresses and strains in the concrete. The cracking of concrete induced by internal stresses and strains falls within the realm of mechanics.

5.2.1 Development of Internal Pressure

Concrete surrounding the rebar will be subjected to an internal radial pressure due to the expansive corrosion products. It is assumed that the corrosion occurs uniformly around the steel bar, although it is known that this is not the case in reality (Du et al. 2006). The radial strain is:

$$\varepsilon_r = \frac{du}{dr} + \nu \cdot \frac{u}{r} \quad (5-1)$$

where u is the radial displacement, ν is Poisson's ratio, and $\varepsilon_\theta = u/r$ is the circumferential strain. The rate of radial and circumferential strain due to thickening of the corrosion products are:

$$\frac{d\varepsilon_r}{dt} = \frac{d(\delta_1 + (\delta_2 - \delta_0) - \delta_3)}{dt \cdot \delta} + \nu \cdot \frac{d\varepsilon_\theta}{dt} \quad (5-2)$$

and

$$\frac{d\varepsilon_\theta}{dt} = 2 \cdot \frac{d(\delta_1 + (\delta_2 - \delta_0) - \delta_3)}{d_{bar} \cdot dt} \quad (5-3)$$

where δ_3 is the reduction in diameter of the steel bar due to corrosion that can be calculated using Faraday's Law, and δ_0 is the reduction in the rust thickness due to diffusion of rust products into the concrete. Calculation of δ_1 and δ_2 was explained in Chapter 4 (Equations 4-26 and 4-27). δ_3 can be calculated through:

$$\frac{d\delta_3}{dt} = \frac{j_{Fe}}{\rho_{Fe}} \quad (5-4)$$

The rate of pressure growth at the steel surface due to the thickness of the rust layer was calculated using the nonlinear concrete constitutive relation given by Todeschini's plasticity model (MacGregor 1997):

$$P_{in} = \frac{2P_{cri}(\frac{\epsilon_r}{\epsilon_0})}{1 + (\frac{\epsilon_r}{\epsilon_0})^2} \quad (5-5)$$

where P_{cri} is the critical pressure that causes the concrete to crack. ϵ_r is the radial strain obtained from Equation 5-2 and ϵ_0 can be calculated using (Mac Gregor 1997):

$$\epsilon_0 = \frac{1.71f_t}{E_{con}} \quad (5-6)$$

Equation 5-5 and 5-6 were used to estimate the applied strain and developed pressure on the concrete cover. The accuracy of these equations was investigated using finite element analysis as explained in more detail later in this chapter.

In this study the pressure is assumed to be uniform around the bar, although this may not be true in reality. Most studies on corrosion-induced cracking of concrete make this assumption for simplicity. This pressure may cause a small amount of corrosion products (mainly red rust in the top layer) to diffuse into the concrete pores surrounding the steel rebar before the concrete cracks. Thoft (2000) and Maaddawy and Soudki (2007) accounted for the diffusion of rust into the pores by assuming that the rust filled a hypothetical porous layer of 10 to 20 μm thickness around the steel bar. They calibrated this thickness using experimental test results of the time for cracking of the concrete cover and not based on the accumulated rust thickness. In this study, the diffusion of rust

product into the concrete pores is modeled and calculated and the results for δ_0 are compared with results reported in the literature.

5.2.2 Loss of Rust Thickness (δ_0)

The migration of rust from the top layer into the concrete pores will reduce the amount of accumulated pressure around the bar and this can slightly increase the time for the concrete to crack. The migration of rust into the concrete pores is modeled as described below.

Conservation of mass yields:

$$(j_{Fe(OH)_3} + dj_{Fe(OH)_3} - j_{Fe(OH)_3})A = \frac{\partial w}{\partial t}(V_t) \quad (5-7)$$

$$\frac{dj_{Fe(OH)_3}}{dx} = \frac{\partial w}{\partial t} \quad (5-8)$$

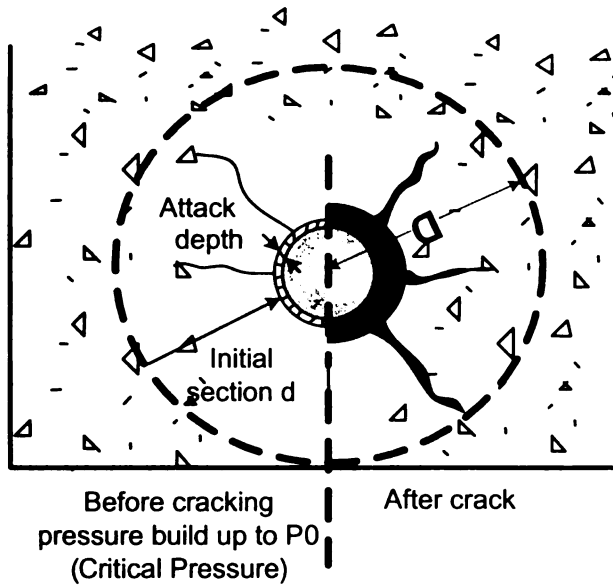


Figure 5-1: Diffusion of rust inside concrete

where A is the cross sectional area, $j_{Fe(OH)_3}$ is the flux of the top layer corrosion products into the concrete pores, w is the mass of $Fe(OH)_3$ per volume of concrete, n is porosity, and V_t is the total volume of concrete. In terms of the saturation

$$s = \frac{w}{n} \quad (5-9)$$

Equation (5-8) may be written as

$$\frac{dj_{Fe(OH)_3}}{dx} = n \frac{\partial s}{\partial t} \quad (5-10)$$

Using Darcy's equation:

$$j_{Fe(OH)_3} = K \frac{dp}{dx} \quad (5-11)$$

where p is the pore pressure and K is the conductivity of the water inside the concrete.

Substituting Equation 5-10 into Equation 5-11 yields:

$$\frac{d}{dx} \left(K \frac{dp}{dx} \right) = n \frac{\partial s}{\partial t} \quad (5-12)$$

Using the Van Genuchten relation between pore pressure and saturation (Monlouis et al. 2004, Van Genuchten 1980) developed for flow of liquid and gas in porous media:

$$p = M \left(s^{\frac{1}{m}} - 1 \right)^{1-m} \quad (5-13)$$

where M and m are empirical constants available in the literature for moisture diffusion into concrete (Monlouis et al. 2004). **Error! Reference source not found.** shows the relationship between the pore pressure and saturation. In Equation 5-12, K needs to be modified to account for the fact that moisture is mixed with rust particles, and replaced by:

$$k = \frac{K}{\eta_r} \quad (5-14)$$

where η_r is the relative density of water mixed with rust. Equations 5-13 and 5-14 can be substituted into Equation 5-12 to yield a composite form of the differential equation for flow of rust into the concrete pores.

Using the set of equations outlined above, the internal pressure can be computed in an incremental time step procedure. After corrosion starts, the pressure begins to accumulate. This pressure pushes some amount of corrosion products produced in the top layer (mostly red rust) into the concrete pores depending on the concrete properties, and this would reduce the pressure around the bar slightly. When the pressure of rust suspension inside the concrete pores exceeds the strength of the concrete, the concrete will crack.

5.2.3 Critical Pressure

The development of cracking in the concrete cover is highly dependent on the ratio of the concrete cover or half the distance between bars to the diameter of the bar, defined in Chapter 4 as the k_r ratio. The empirical model from the literature was adopted in this study and calibrated and validated using finite element analyses using the ABAQUS (HKS 2006) commercial software. According to the model, for $k < 5$, cracking occurs when the mean value of the circumferential stress reaches the tensile strength of the concrete (Shah and Swart 1987), i.e., when

$$\bar{\sigma}_t = \sigma_m \quad (5-15)$$

Equation 5-15 implies that cracking occurs when the final pressure on the concrete cover is

$$p_{in} - p_{out} = (k - 1) \cdot \sigma_m \quad (5-16)$$

where σ_m is the splitting tensile strength of the concrete.

However, for $k > 5$, the first crack opens before the circumferential stress reaches the tensile strength of the concrete, i.e., when

$$\bar{\sigma}_t = \alpha \sigma_m \quad (5-17)$$

or

$$p_{in} - p_{out} = (\alpha k) \cdot \sigma_m \quad (5-18)$$

where α is a factor established in the literature through experiments. In this study, finite element analysis was used to calibrate the α factor to yield $\alpha = 0.72$, which compares well with the value $\alpha = 0.8$ reported in the literature (Shah and Swart 1987).

5.3 Calibration and Validation with Finite Element Analysis

The development of finite element models to calibrate and validate parts of the cracking model used in this study is presented in this section. The first part that needs to be validated is the relationship between the rust thickness and the resulting pressure based on the nonlinear concrete constitutive model. The second part is to calibrate the α coefficient in Equations 5-17 and 5-18 and compare it with experimental values reported in the literature. The ABAQUS (HKS 2006) general purpose finite element package was used for all the analyses. Also, the effect of parameters such as the concrete compressive strength and k_r was evaluated as a part of the parametric study.

5.3.1 Finite Element Model

Since corrosion causes radial expansion, a 2-D plane strain model can be used to study the mechanical behavior of concrete. The major limitation of experimental investigation is that it cannot provide detailed information regarding the relationship between applied pressure and rust thickness. The experimental results can only indicate the time to cracking as a function of the corrosion current. Also, performing many experiments for concrete with different compressive strengths can be expensive and time consuming. Finite element analysis is expedient for detailed parametric studies.

5.3.1.1 Geometry and Boundary Conditions

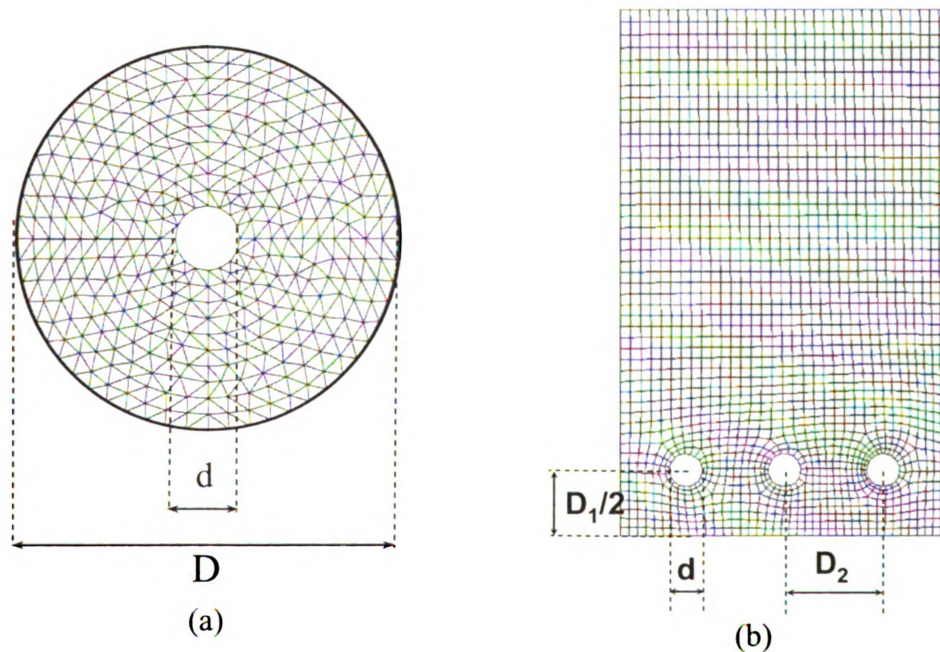


Figure 5-2: Geometry of the FE models: (a) experimental unit, and (b) real structure

As mentioned in Chapter 3, the geometry of the experimental specimens were designed to be convenient and yield the most common k_r ratios in concrete structures, but

the cover thicknesses and bar sizes in actual structures vary considerably. It was important to maintain the same k_r ratios in both the experiment and the model since this is the main factor controlling the cracking time and not the concrete cover thickness. The three different k_r ratios of 3, 4 and 6 that were the same as in the experimental test were chosen in the finite element models, but a bar diameter of one inch for all three cases and concrete cylinder diameters of 3, 4 and 6 inches were used. Figure 5-2(a) shows the geometry of the FE models. Due to symmetry of the model, only half of each specimen was modeled and appropriate boundary conditions were applied. The steel bar was replaced by a cavity at the center and an outward radial pressure was applied around the circumference of the cavity.

The validity of representing the concrete around a bar in a rectangular beam or column by a concrete cylinder was verified using the model shown in Figure 5-3(b). If the critical pressure required for cover cracking is similar for the models in Figure 5-2(a) and (b), then Equations 5-18 and 5-16 can be used for any concrete structure with a non-symmetrical shape as in Figure 5-2(b) with k_r being the ratio of the steel bar diameter to the shorter of the concrete cover thickness or half the distance between bars.

5.3.1.2 Concrete Material Model

There are currently three different models in ABAQUS (version 6.4, 2006) to model plain and reinforced concrete. These include the smeared cracking model, concrete damage plasticity model, and cracking model. In this study, the concrete damage plasticity model was used to model concrete.

The damage plasticity model is very versatile and capable of predicting the behavior of concrete structures subjected to monotonic, cyclic and/or dynamic loading. It assumes the main failure mechanism to be tensile cracking and compressive crushing. In compression the model uses a multi-axial plasticity model with a non-associated flow rule and isotropic strain hardening. In tension the model uses a multi-axial damage elasticity model. Concrete in tension is considered to be a linear elastic material until the uni-axial tensile stress at which concrete cracks, f_t , is attained and softening behavior is assumed thereafter. A linear softening model is used to represent the post-failure behavior in tension.

The softening rate depends on the post-failure behavior in tension. In the analysis, the number of failed elements was large because of the high tensile stresses, ABAQUS does not have any provision to model the possible high crack widths, and the analysis terminated prematurely. To resolve this problem, a large tension stiffening value was used to continue the analysis up to failure. The behavior of the model in uni-axial tension and compression is shown in Figure 5-3. Figure 5-4 shows the combined uni-axial stress-strain curve.

The input required for defining the concrete material model are: (a) the uni-axial compression stress-strain curve; (b) the uni-axial tension stiffening stress-strain curve; (c) the volumetric dilation angle ψ ; (d) the bi-axial compression ratio; and (e) the ratio of tensile-to-compressive meridian K . These inputs are described below.

The uni-axial compression stress-strain curve was defined using the Todeschini empirical stress-strain model. A typical uni-axial compressive and tensile stress-strain

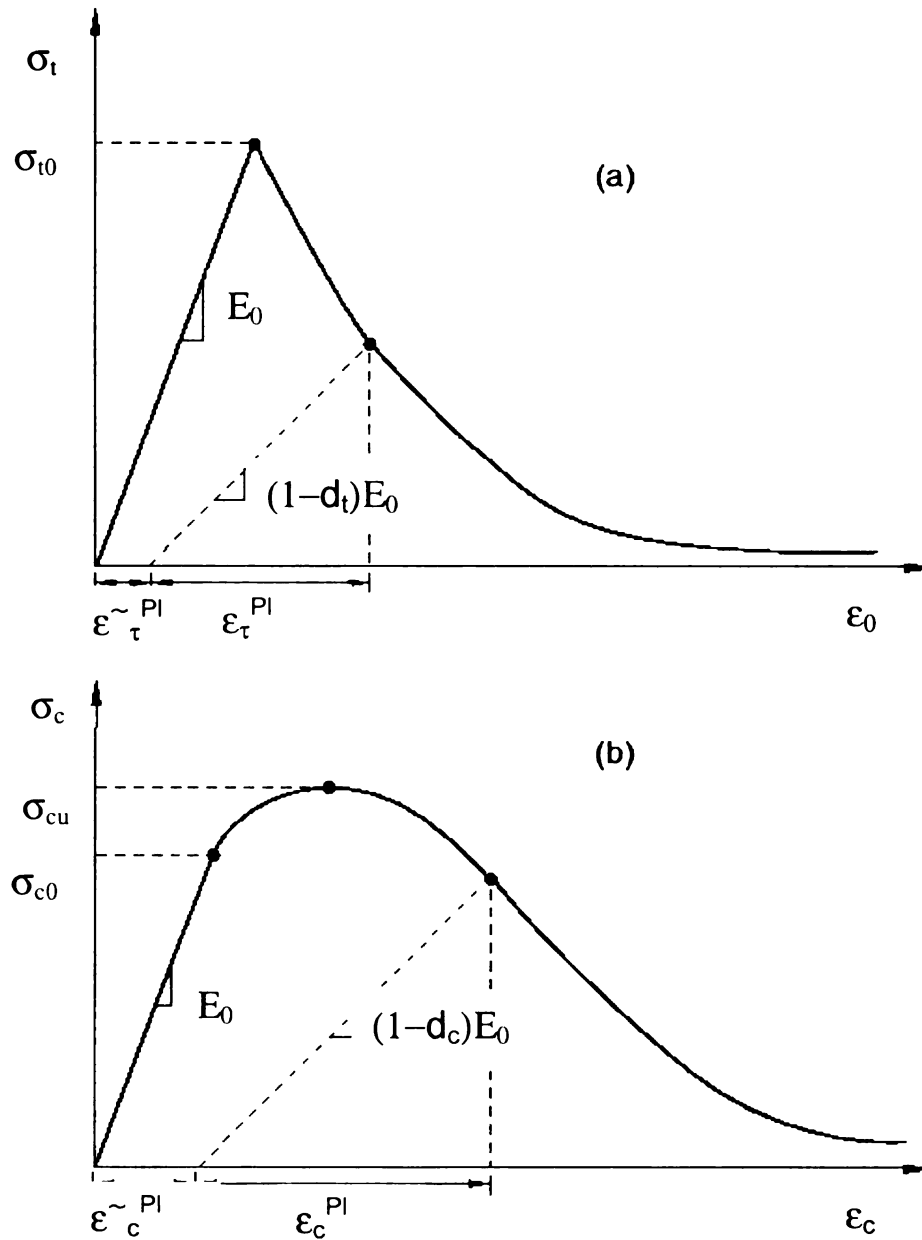


Figure 5-3: Typical concrete uni-axial stress-strain curve in (a) tension and (b) compression (ABAQUS User Manual)

curve for 3500 psi (24.1 MPa) concrete is shown in Figure 5-4. As explained earlier, the concrete is assumed to have elastic-plastic behavior under tensile loading. The concrete compression stress-strain relationship is given by

$$f_c = \frac{2f'_c (\epsilon/\epsilon_0)}{1 + (\epsilon/\epsilon_0)^2} \quad (5-19)$$

$$\varepsilon_0 = \frac{1.71f'_c}{E_c} \quad (5-20)$$

$$f''_c = 0.9f'_c \quad (5-21)$$

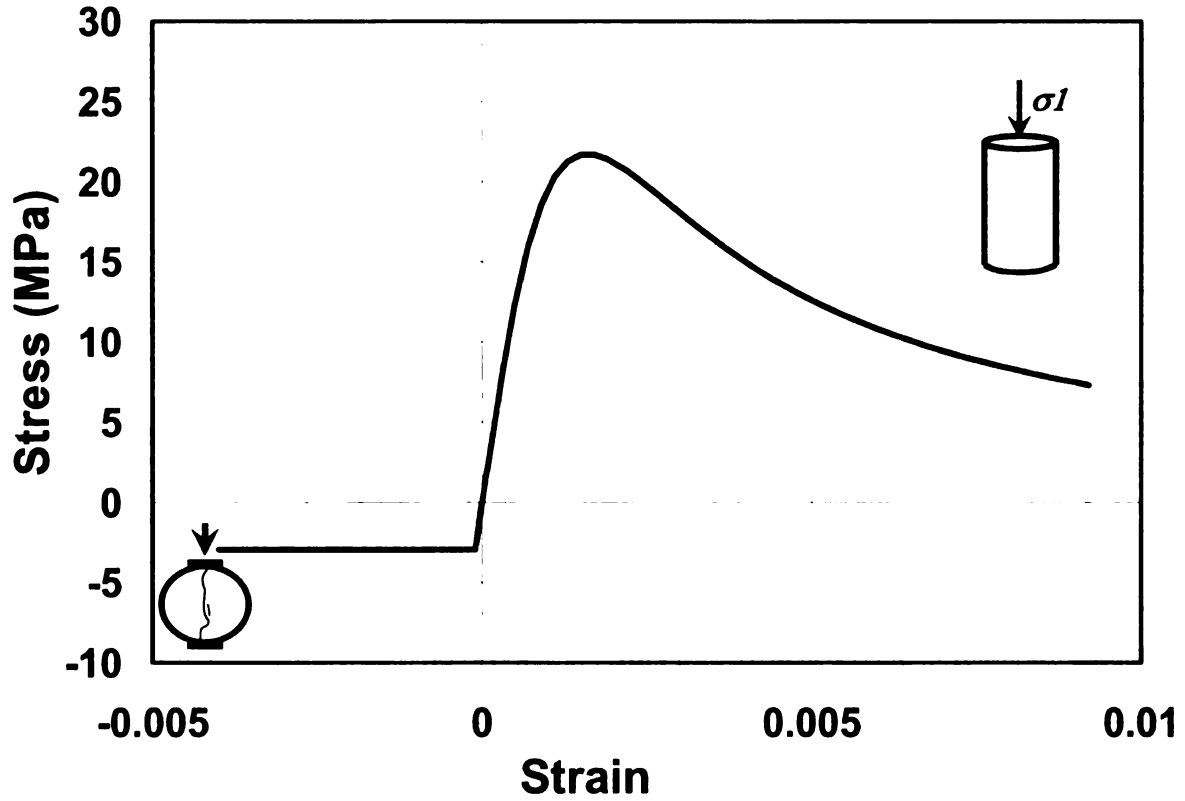


Figure 5-4: Stress-strain curve used for the concrete

The calculation for the dilation angle involves complex mathematical derivations, and assumptions using the yield surface of the concrete damage plasticity model. The dilation angle for unconfined concrete in this study was assumed to be 30° . The bi-axial stress ratio and the tensile to compressive meridian ratio were assumed to be 1.16 and 0.667, respectively.

5.3.1.3 Loading Condition

When the rebars corrode, the corroded steel swells to about 2 to 6 times of its initial volume (Mehta 1993). However, some of the corrosion products will fill pore voids within the concrete. The expansion of the rust products will apply internal pressure to the concrete cover. This expansion causes the concrete cover to crack and eventually spall.

The objective of the FE analysis was to find the pressure-displacement relationship and calibrate the α coefficient in Equations 5-17 and 5-18. The reinforcing steel was replaced by a uniform radially outward pressure that was applied in increments over time steps until the concrete cover cracked. Since the ABAQUS concrete plasticity model cannot account for the opening of a large crack, the analysis terminates when the crack opens. The amount of pressure at this time step was considered to be the critical pressure, and the α factor was calibrated using this pressure.

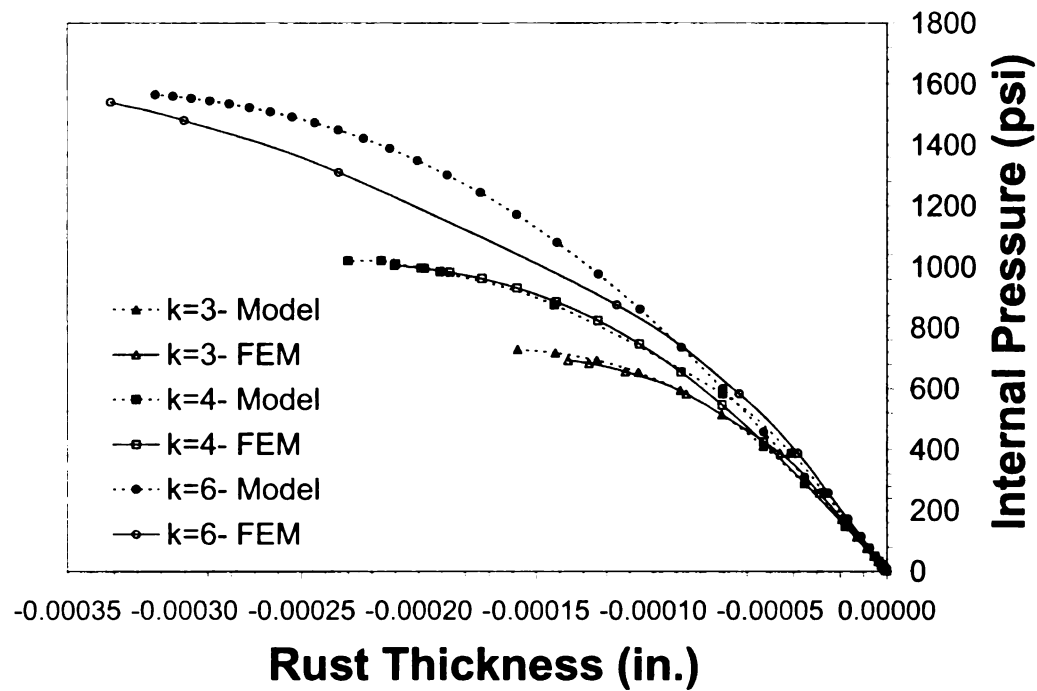
5.3.2 *Finite Element Analyses*

The results of the finite element analyses are presented in this section. These results were only used to calibrate the α factor and also validate the displacement-pressure constitutive relationship used in model.

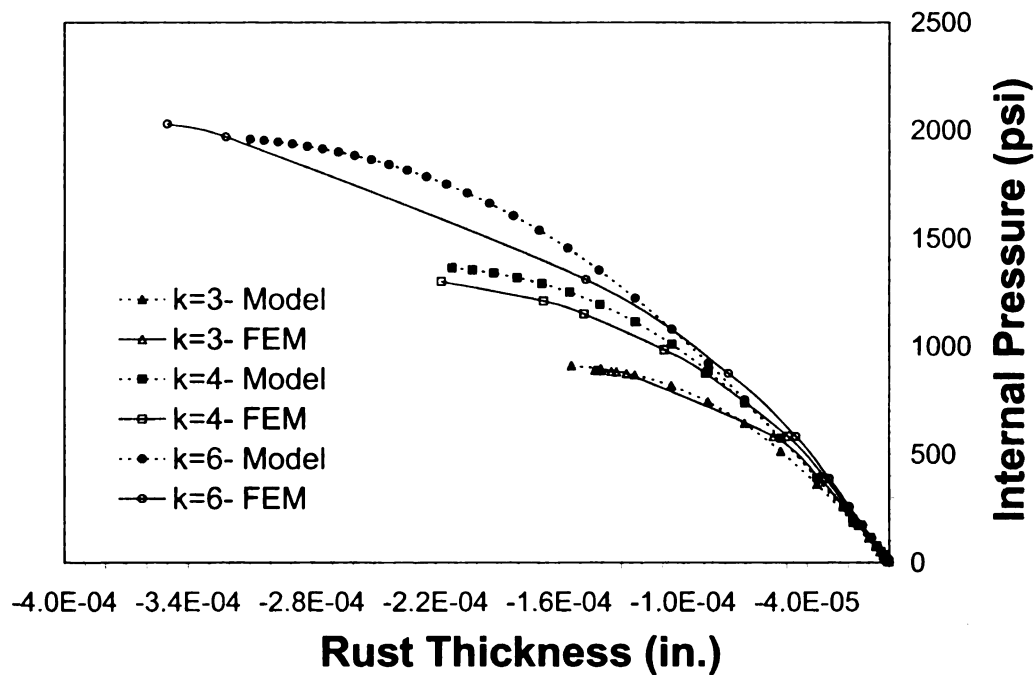
5.3.2.1 Strain-Pressure Relations

One of the most important factors that controls cracking of the concrete cover due to corrosion of a steel bar in concrete is the relationship between the rust thicknesses and the applied pressure. As mentioned before, a concrete plastic constitutive model was

chosen to describe this relationship, and the results were compared with finite element analysis to validate the use of Equations 5-3 and 5-4.



(a)



(b)

Figure 5-5: Rust thickens vs. pressure from model and FEM

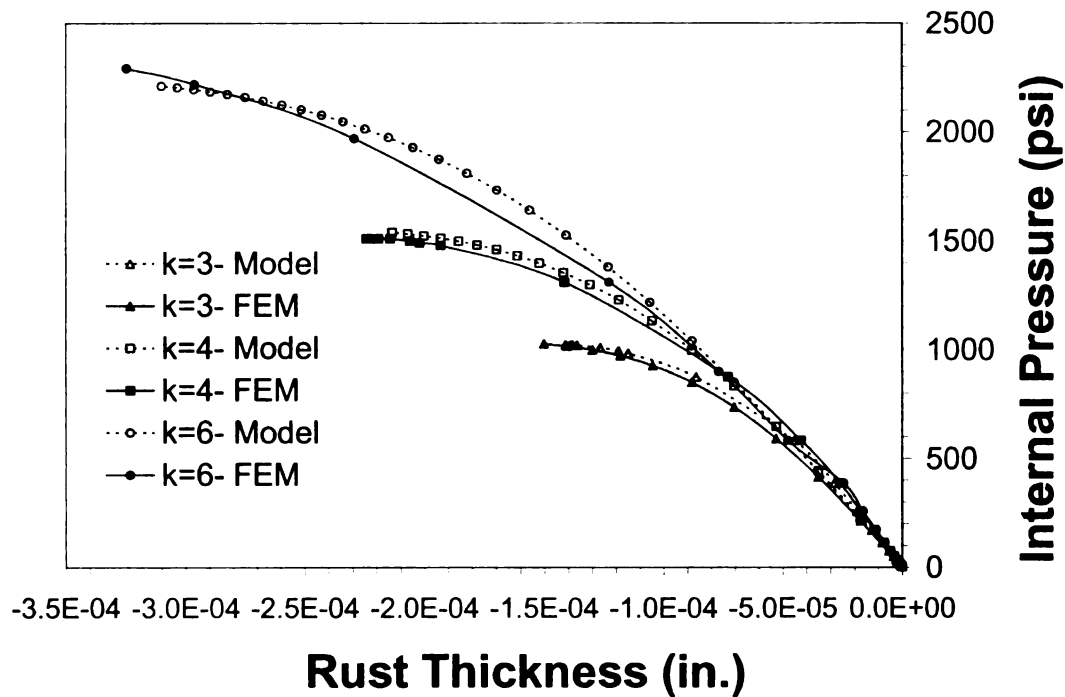


Figure 5-6 cont'd: Rust thickens vs. pressure from model and FEM

Uniform outward radial pressure was applied along the bar circumference and the pressure was increased in time steps until the concrete cracked. The pressure verses radial displacement was plotted for different cases. It should be noted that in the model the input strain for Equation 5-5 was calculated using Equation 5-2 and the effect of hoop strain was also considered. In Figure 5-6, the rust thickness verses applied pressure from the model and FE analysis is plotted for different concrete cover thicknesses and compressive strengths. For the finite element analysis the coefficient in Equation 5-6 was taken to be 1.71. However, the best match using Equations 5-3 and 5-4 were obtained when this coefficient was increased to 1.75, and the model predictions in Figure 5-6 are based on this coefficient value. The proposed model matches the FE results well and can be used to calculate the pressure developed due to thickening of the rust layer.

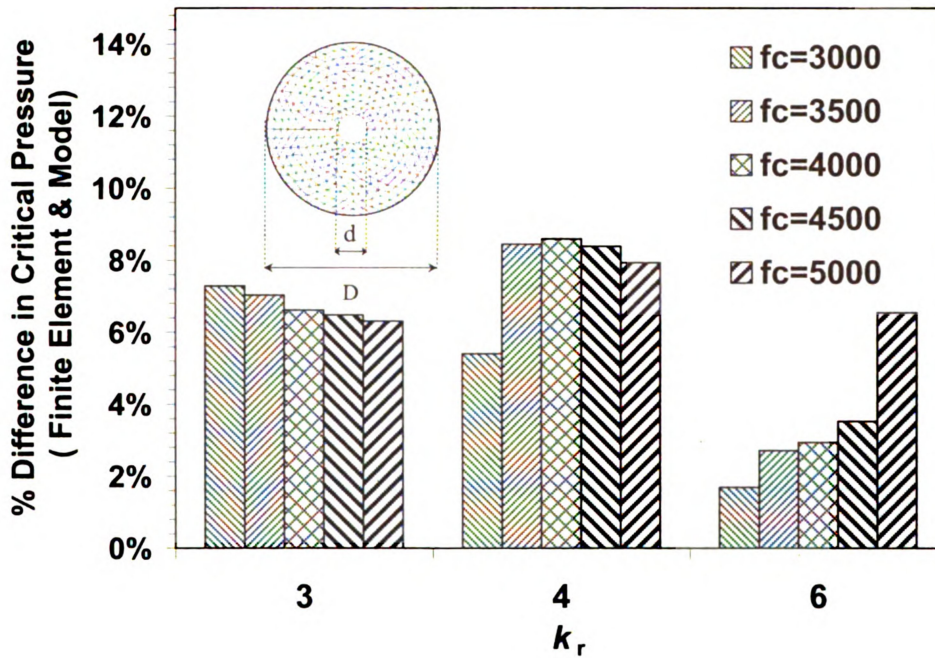


Figure 5-6: Critical pressure for different k_r ratios

5.3.2.2 Critical Pressure

Figure 5-6 shows the finite element results of the critical pressure for concrete cover cracking. As mentioned earlier, the experimental value obtained for the α factor was 0.7 (Shah and Swartz 1987). The α factor was also calibrated using the finite element analysis and yielded a value of 0.72, which is in very good agreement with the experimental results. It should be noted that Equation 5-19 was used in the proposed model to avoid complicated nonlinear finite element analysis.

5.3.2.3 Effect of Concrete Cover vs. Bar Distance

The second factor that needed to be evaluated using finite element analysis was the effect of the concrete cover thickness and bar spacing on the cracking time of the

concrete cover due to the corrosion. Depending on dimensions, concrete cover cracking or delamination may occur as shown in Figure 5-7.

Table 5-1: Case Study on Finite Element to calibrate a factor in asymmetric situation

	d (in.)	D_1 , Cover (in.)	D_2 , Between (in.)	$k_{r, \min}(d/D)$
Case 1	1	3	4	3, cover
Case 2	1	3	6	3, cover
Case 3	1	4	3	3, between
Case 4	1	6	3	3, between

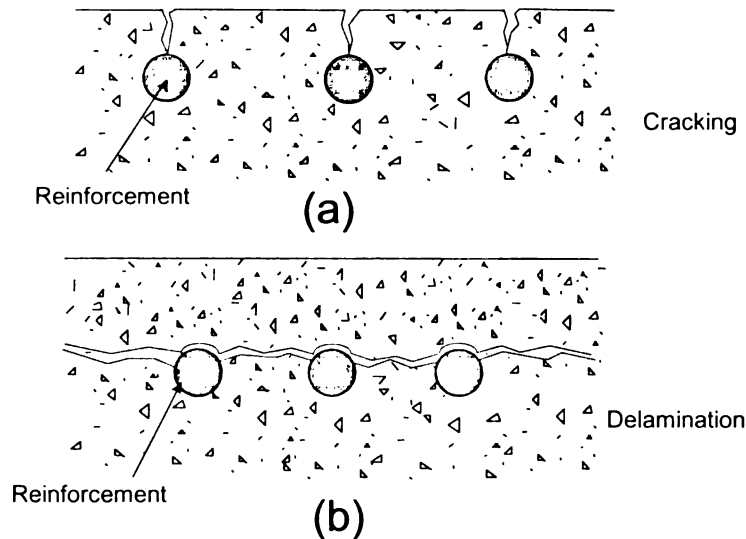


Figure 5-7: Effect of concrete cover and bar distance on type of damage:
(a) cover < half of bar distance, and (b) cover > half of bar distance

The actual dimensions to be used in 1-D analysis and the appropriate factor for the two cases shown in Figure 5-7 needs to be established. The cases shown in Table 5-1 were considered and analyzed using the FE models shown in Figure 5-3.

The finite element results of the different cases are presented in Figure 5-8. The results indicate that when half the bar spacing and cover thickness are not equal, D can be

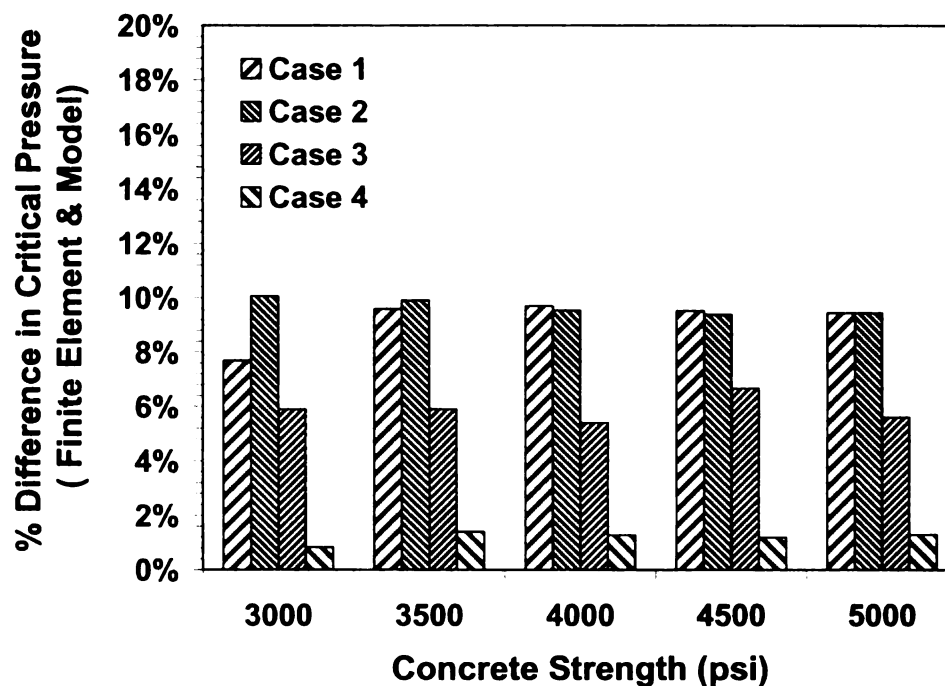


Figure 5-8: Finite element result for unsymmetrical situation

considered to be the smaller of the two. Using $\alpha = 0.72$, and the 1-D model yields a critical pressure that is within 10% of the value obtained through nonlinear 2-D FE analysis.

5.4 Results and Discussion

5.4.1 Rust Thickness Growth

Growth of the rust thickness has been studied over past years as mentioned in Chapter 2. Many models such as linear, parabolic, and more complicated power models were proposed. Unfortunately, these models were not calibrated with experimental tests or corrosion rate models. Also, the amount of rust that diffuses into the concrete was never explicitly modeled and only an assumption about rust filling a hypothetical porous

zone around the steel bar was made and calibrated with experimental tests on the time for cracking (Thoft 2000, Bhargava et al 2005, and Maaddawy and Soudki 2007).

In this section, the results of rust thickness growth over time and the amount of rust that diffuses into the concrete pores based on the developed model are described.

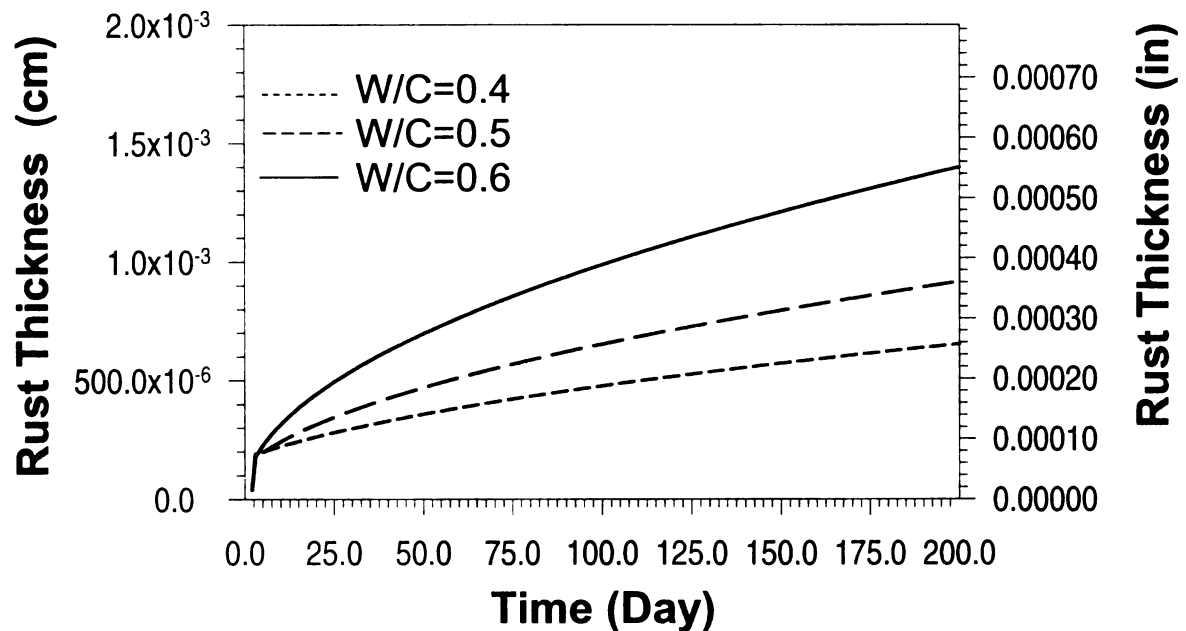


Figure 5-9: Rust growth over time for different w/c ratio and $k_r = 6$

5.4.1.1 Rust Build-Up

Figure 5-9 shows the results of the rust growth over time for the different conditions studied in this research. The model indicates that the rate of rust growth is not affected by the concrete cover and the only factors that have a significant effect are boundary conditions and the water cement ratio.

Although the proposed model has a more complicated equation to calculate the rust thickness growth over time than the simple ones presented in the literature, it has a

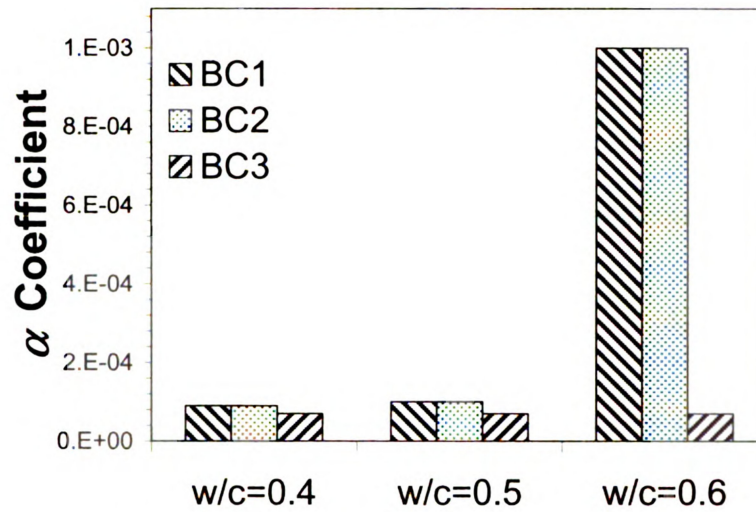


Figure 5-10: α coefficient for different conditions

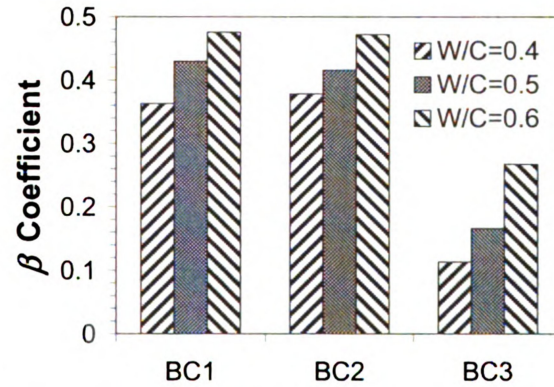


Figure 5-11: β coefficient for different conditions

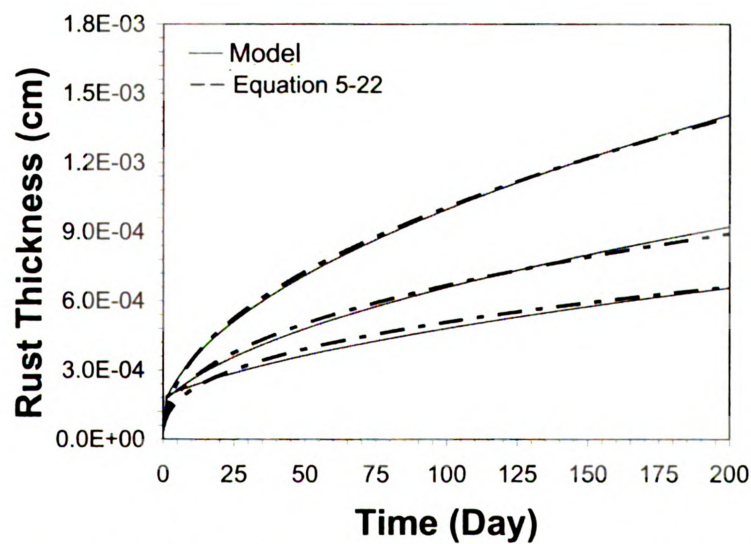


Figure 5-12: Comparison Between Model and Equation 5-22

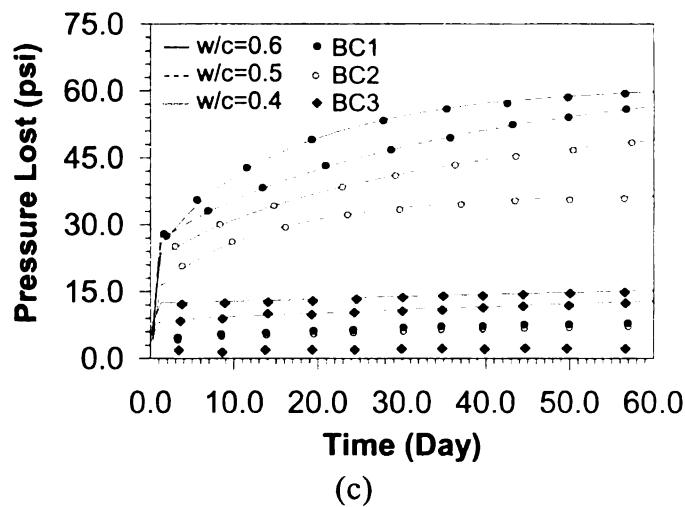
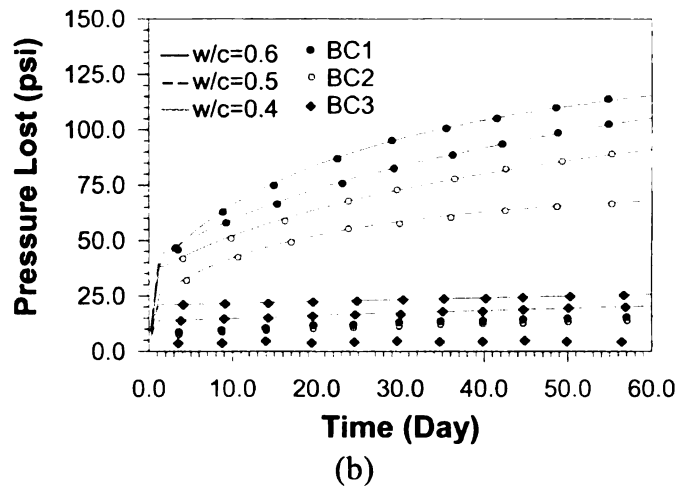
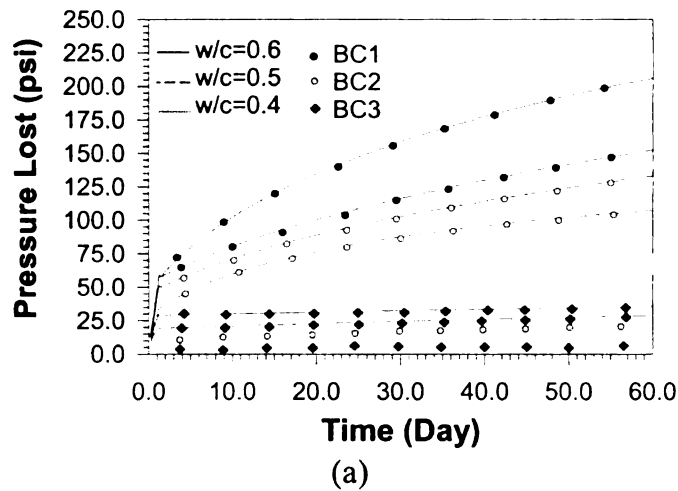


Figure 5-13: Pressure loss due to rust diffusing into concrete pores

similar trend to Equation 2-9.

Figure 5-12 shows the comparison between the results from model and the equation:

$$\delta_{total} = \alpha t^{\beta} \quad (5-22)$$

in which α and β are empirical coefficient that need to be calibrated experimentally. In this work, these coefficients were calibrated based on the model results. It should be noted that the proposed model is more sophisticated than just the simple empirical equation and different values for α and β as shown in Figure 5-10 and Figure 5-11 would be needed for different boundary conditions and w/c ratios in order for the empirical equation to match the rust growth predicted by the model.

The α factor controls the

initial rust thickness before the corrosion current reaches it is limiting value and is approximately the same for BC1 and BC2, is lower for BC3, and the water-cement ratio does not have a significant effect on it. The β factor controls the rate of decay and is influenced mainly by the water-cement ratio.

5.4.1.2 Rust Diffusion into Pores

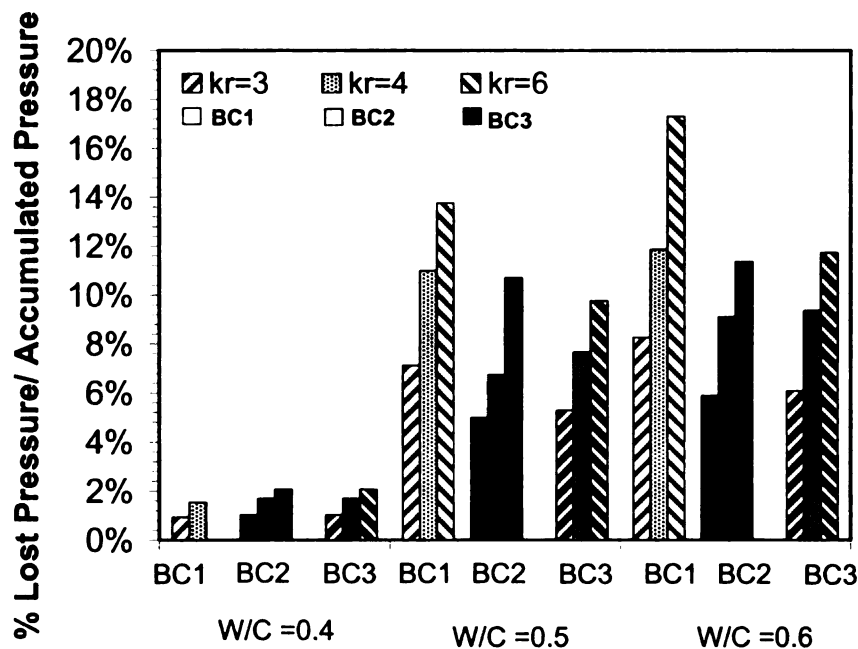


Figure 5-14: Reduction in pressure as a percentage of the final pressure

The rust diffusion into concrete pores has not been effectively modeled in the past. Equations 5-7 to 5-14 show the model developed in

this work for diffusion of the rust into the concrete pores around the steel bar. Figure 5-13 shows the pressure lost due to rust diffusion into the concrete pores based on the model (i.e., p_{out}) for different boundary conditions and water-cement ratios. The rust only diffuses to a certain depth before cracking of the concrete. The calculated depth according to the proposed model can be between 0.1 to 0.6 inches, depending on factors such as the w/c ratio and boundary conditions.

The diffusion of rust decreases the amount of accumulated pressure and increases the time to cracking depending on the situation. Figure 5-14 shows the percent reduction in accumulated pressure (i.e., $p_{out} / (p_{in} - p_{out})$). The loss in pressure increases as the water-cement ratio increases since the porosity of the concrete becomes larger.

The other factor that affects the loss in pressure is the boundary condition. Lower saturation allows more rust to fill the pores. The amount of rust that diffuses is 2% for a water-cement ratio of 0.4, and between 5 to 17% for water cement ratios of 0.5 and 0.6. The amount of rust that diffuses into the surrounding concrete is highest for BC1 due to the lower degree of saturation, and similar but lower for BC2 and BC3.

5.4.2 Stress in Concrete Cover

Hoop and radial strain and stress on the concrete cover around the steel bar were calculated. The results of the stress on the concrete cover at the time of cracking are shown in Figure 5-16 for k_r values of 3, 4, and 6. The averages of the stress distributions over the cover thickness are shown within the table in each figure and the tensile strength of the concrete is shown as horizontal lines.

As expected from Equations 5-16 and 5-18, for the $k_r < 5$ the concrete cover cracks when the average hoop stress is close to the tensile strength of the concrete, but for $k_r > 5$, the concrete starts cracking when the average hoop stress is slightly smaller than the tensile strength of the concrete. This behavior is consistent with experimental observations made by Shah and Swart (1987).

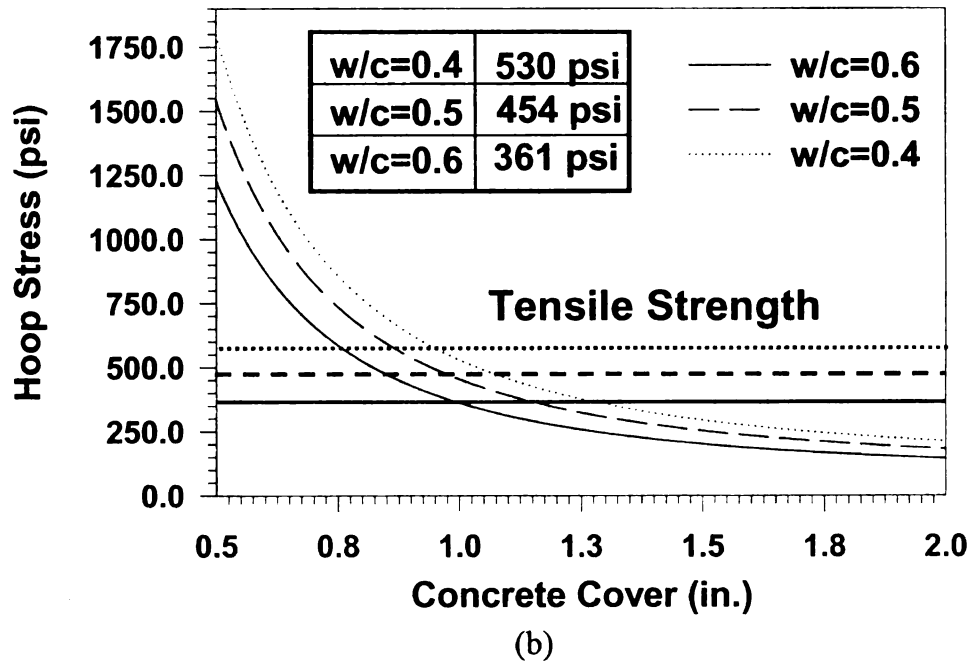
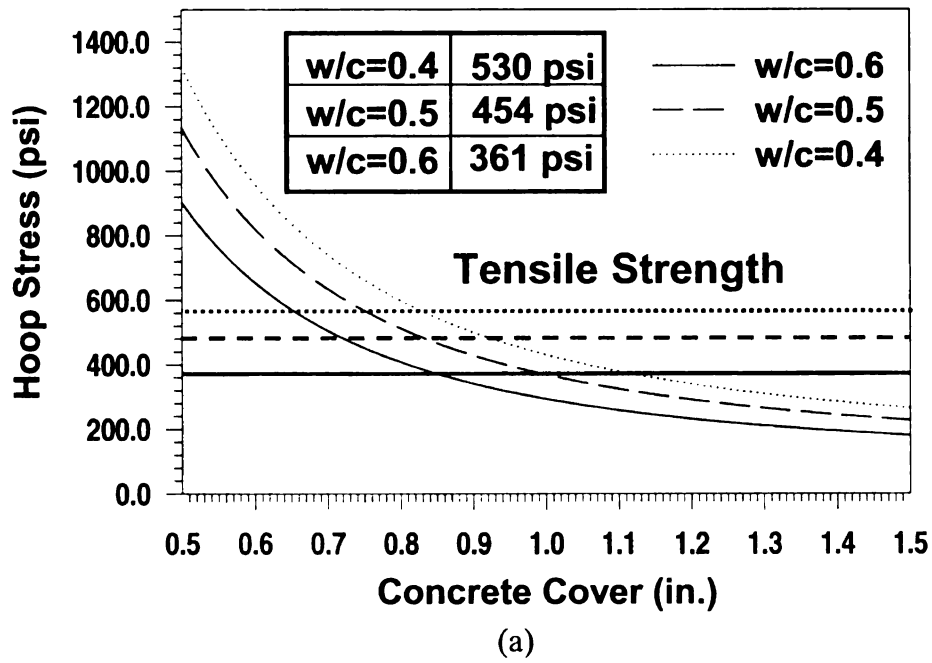


Figure 5-15: Hoop stress from model for different k_r . (a) $k_r = 3$, (b) $k_r = 4$, and (c) $k_r = 6$

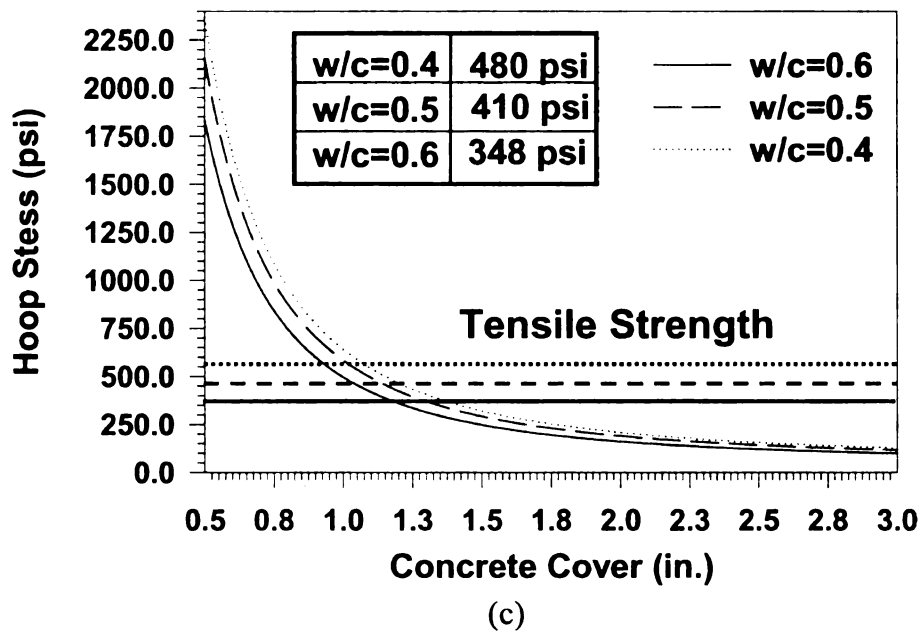


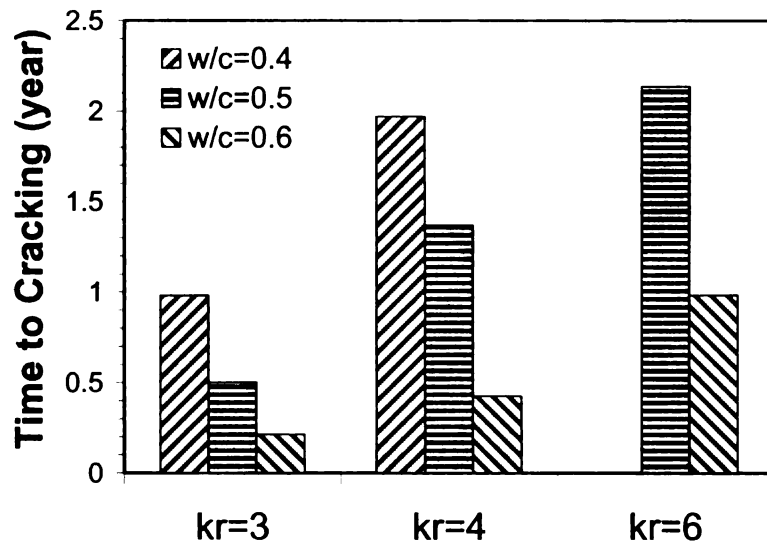
Figure 5-15 cont'd : Hoop stress from model for different k_r . (a) $k_r = 3$, (b) $k_r = 4$, and (c) $k_r = 6$

5.4.3 Cracking Time, t_2

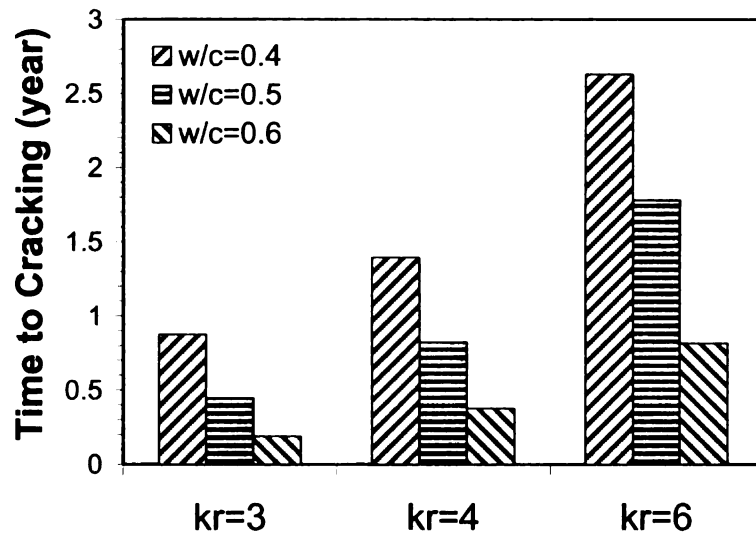
After calibration and validation of the model, the time for cracking of the concrete cover, t_2 , was predicted using the model for different boundary conditions, water-cement ratios, and the D values shown in Tables 4-6 and 4-7. Results from the model also are compared with available experimental data and results from different models.

5.4.3.1 Effect of Boundary Condition

The boundary condition was one of the factors that had an effect on the corrosion current. As described in Chapter 4, the boundary condition influences the corrosion current over time due to the availability of oxygen in the concrete. The difference in the corrosion current between BC1 and BC2 was about 5%. However, for BC3 the corrosion current was almost 10 times lower than for BC1 and BC2. The time for cracking of the concrete cover was not calculated for BC3 in this study because it was computationally



(a)



(b)

Figure 5-16: Effect of water cement ratio on concrete cracking time:
(a) BC1 and (b) BC2

very expensive and the concrete cover would not be crack even after more than 25 years for the smaller cover thickness ($k_r = 3$).

The time for cracking of the concrete cover for different conditions is shown in Figure 5-16 and Figure 5-17. The 5% increase in corrosion current from BC1 to BC2 due to the higher water content of the

concrete can decrease the life of a concrete structure by 10% and in some cases even by up to 25%.

5.4.3.2 Effect of Concrete Quality

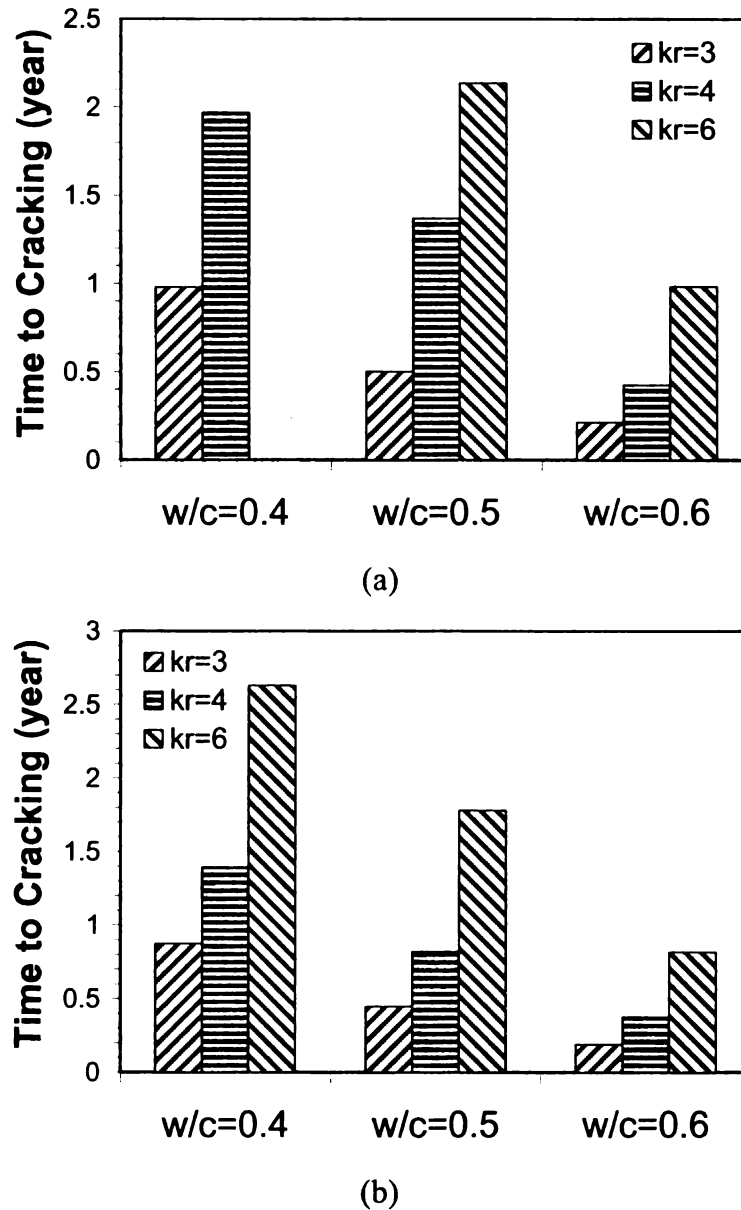


Figure 5-17: Effect of concrete cover on cracking time (a) BC1 and (b) BC2

The main factor that controls concrete quality is the w/c ratio. As Figures 4-31 to 4-33 show, decreasing the w/c ratio significantly decreases the corrosion current, but this is not the only effect that the w/c ratio has on the cracking time. As the water-cement ratio decreases the concrete strength also increases roughly linearly. Decreasing the w/c ratio by 0.1 increases the concrete strength by almost 1000 to 1500 psi

(Neville 2000).

Figure 5-16 shows the effect of the w/c ratio on the cracking time. Increasing the w/c ratio by 0.1 decreases the cracking time by 1.5 to 3 times depending on the k_r ratio. The

time to cracking is very large for a w/c ratio of 0.4 and k_r of 0.6 and is not shown in Figure 5-16(a).

5.4.3.3 Effect of Concrete Cover

After concrete quality, the second most important factor that has an effect on the time for cracking of the concrete cover is the k_r factor. As mentioned in Chapter 4, k_r or the concrete cover thickness does not have an important effect on the corrosion current since the oxygen concentration across the concrete cover is near steady state when corrosion starts. The concrete cover can increase the time to the initiation of corrosion, t_1 , due to chloride penetration, but does not have a direct effect on the corrosion current. However, an increase in the w/c ratio reduces the concrete strength and, as shown in Figure 5-17, reduces the time for cracking of the cover.

5.4.4 Comparison of Results with the Literature

To verify the proposed model, the results from the model were compared with results from different theoretical models and experimental work available in the literature. The largest study on natural corrosion of reinforcing steel in concrete was done by Liu (1996), who investigated different specimens with different bar diameter to cover thickness ratios. The measured corrosion current from Liu's study was compared to that from the proposed model in Chapter 4. The model was in very good agreement with one of the measurements, but almost 50% lower than the average mass loss measurements from other cases. However, as mentioned in Chapter 4, estimating the corrosion current

from the average mass loss may not be very accurate because use of a different valency number for iron oxidation can yield significantly different results.

Here, the time for cracking of the cover from the proposed model is compared with experimental value reported by Liu from experiments for comparable cases. Liu used concrete with compressive strengths of 5400 to 5700 psi and the only close k_r (bar radius to concrete cover thickness) ratio was 6.5 and 4.1. These conditions are compared to the model results with k_r of 4 and 6, a w/c ratio of 0.5, and a compressive strength of 5500 psi.

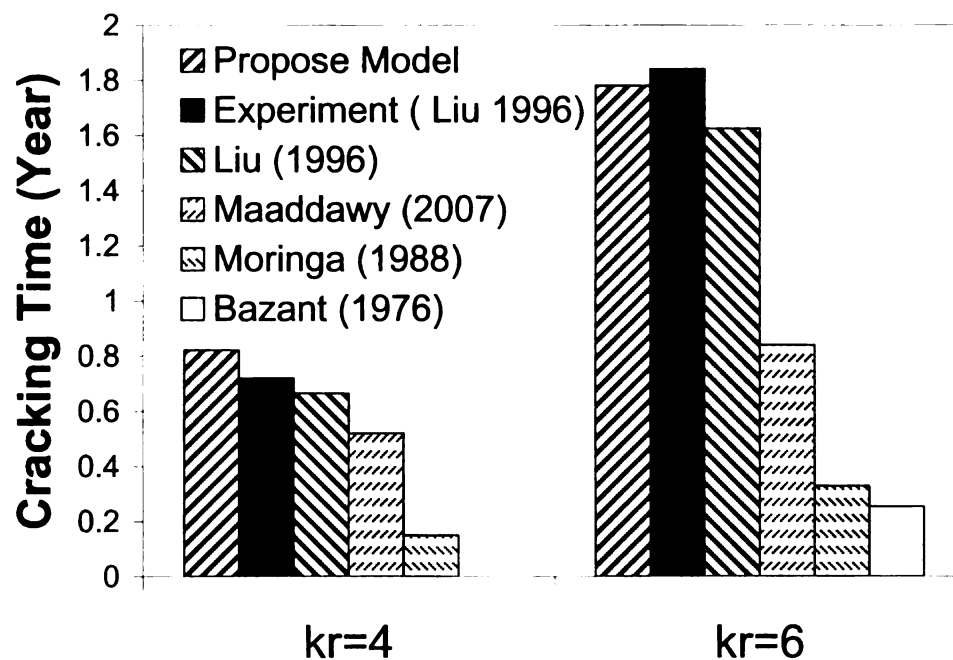


Figure 5-18: Comparison between proposed model and literature

The results from the model were also compared to those from some other concrete cracking models in the literature: Bazant (1976), Morinaga (1988), Liu (1966), and Maaddawy and Soudki (2007). The comparisons are shown in Figure 5-19. There are two main problems with all of the above models. First, they are based on a constant

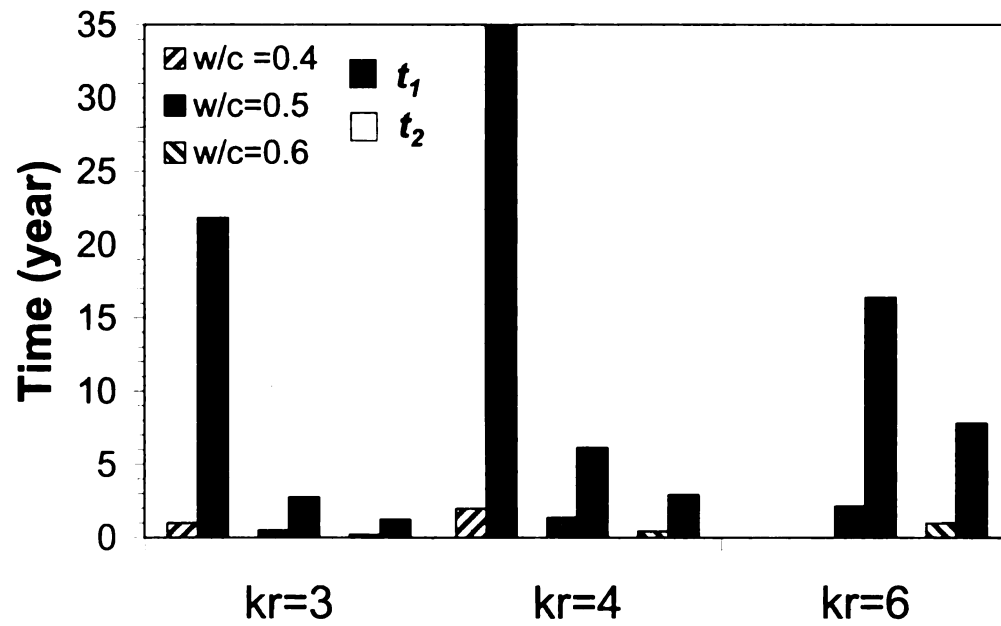
corrosion current. Second, most of the models assume a porous zone with a thickness between 10 to 20 μm adjacent to the steel bar. They assume that this porous zone will first be filled by rust and then the rust will accumulate and apply pressure to the concrete. This was assumed based on calibration with experimentally measured time to cracking of the concrete and there is no evidence that this layer exists.

In this study, the rust growth with time is related to the corrosion current and it is assumed that due to confinement the rust products may not have a volume expansion of 3.75 to 4.2 times the volume of the corroded steel. The K_P factor was used represent the densification of rust and was calibrated to be 1.56.

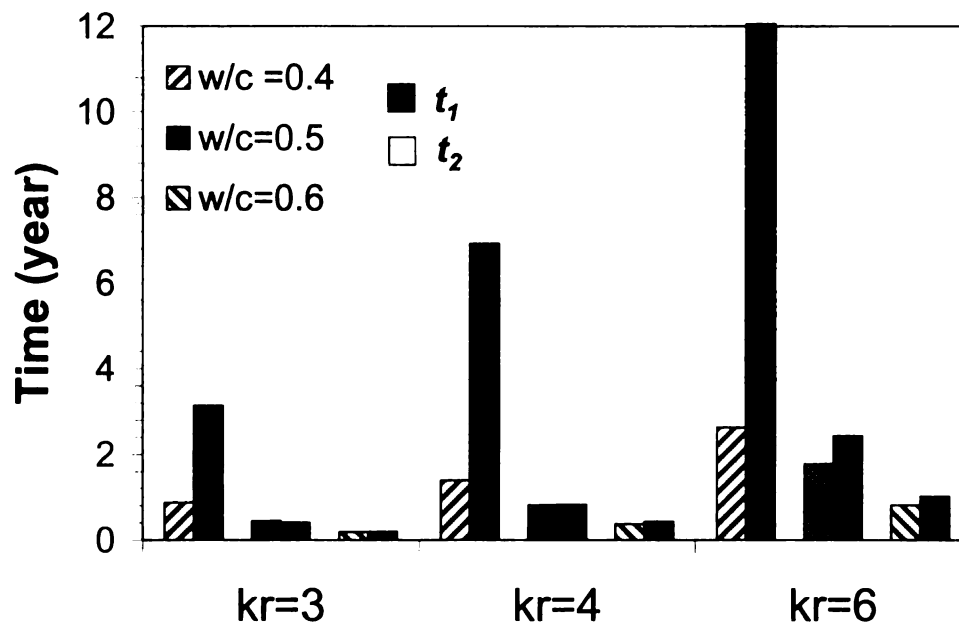
In the proposed model the amount of rust that diffused into the concrete was also calculated and found to be much less than that required to fill a hypothetical porous zone of 10 to 20 μm adjacent to the steel bar.

5.4.5 Effect of Time t_1 Compared to t_2

As shown in Figure 4-1, the corrosion initiation time, t_1 , and the time to cracking of the concrete cover, t_2 , are the two main phases of the life of a concrete structure exposed to chloride. It is often assumed that t_1 dominates the life of a concrete structure, and t_2 can be ignored compared to t_1 . In order to verify this assumption, the time t_1 calculated using the model described in Section 2.3 is compared to the time t_2 obtained from the proposed model in Figure 5-19.



(a)



(b)

Figure 5-19: Comparison between time t_1 and t_2 for different conditions: (a) BC1 and (b) BC2

As Figure 5-19 shows, t_1 is considerably higher than t_2 for BC1 in all cases since the availability of chloride is more limited at the boundaries and t_1 dominates the life of a concrete structure under chloride attack. However, for BC2, t_1 and t_2 are almost equal for the higher water-cement ratios of 0.5 and 0.6 and both times should be considered when estimating the life of a concrete structure. For a w/c ratio of 0.4 the chloride diffusion coefficient is low and t_1 is larger than t_2 . While the contribution of t_2 to the life of a concrete structure may be neglected for BC1, it cannot be neglected for BC2.

For BC3, although model calculations were not performed, t_2 will dominate the life of a concrete structure because abundant chloride is available and will reach the steel reinforcement in a short time (i.e., t_1 will be very small).

5.5 Summary and Conclusions

The boundary condition (BC) is one of the factors that has a significant effect on the corrosion current. The difference in the rate of corrosion for BC1 and BC2 is only about 5% since the availability of oxygen in both cases is about the same but the water content is higher in BC2. However, for BC3 the corrosion current is almost 10 times lower than for BC1 and BC2 due to the lack of oxygen at boundaries. Since the corrosion rate was too small, cracking of the concrete cover for BC3 was not calculated in this study. The 5% increase in corrosion current from BC1 to BC2 can decrease the life of the concrete structure by 10% and in some cases even by up to 25%. Also, an increase in the w/c ratio by 0.1 decreases the time for cracking of the concrete cover by a factor of 1.5 to

3, depending on other factors. The second important factor that can affect the time for cracking of the concrete cover is the cover thickness. The life of a concrete structure from the start of corrosion to cracking can increase by factor of 2 if the concrete cover is increased from 1.5 to 2 inches, and by about the same percentage when the concrete cover is increased from 2 to 3 inches. This increase in life of a concrete structure excluded the increase in the time for corrosion initiation, t_1 , due to diffusion of chloride through the concrete cover.

The corrosion initiation time, t_1 , and concrete cover cracking time, t_2 , are the two main phases of the life of a concrete structure exposed to chloride. It is often believed that t_1 dominates the life of a concrete structure and the contribution of t_2 can be neglected. However, estimates of t_1 and t_2 from the models presented herein show that although t_1 is considerably higher for BC1 in all cases, the two times are about the same for BC2 for the higher water-cement ratios of 0.5 and 0.6 and are equally important in estimating the life of a concrete structure. t_2 may be neglected in comparison to t_1 for a w/c ratio of 0.4 and BC1, but for BC2, t_2 is not small enough in comparison to t_1 to be neglected. For BC3, t_2 will dominate the life of a concrete structure.

Chapter 6

Effect of Concrete Repairs on Corrosion Behavior

6.1 Introduction

The previous chapters focused mainly on corrosion rate modeling and time to cracking of the concrete cover. After the first crack, the corrosion rate will increase very rapidly since access of oxygen would not be limited and the crack propagation time would be shorter than both t_1 and t_2 .

In this chapter, the effect of different repairs on the corrosion rate and the critical cracking pressure are studied. In concrete repaired with a patch, unavoidable restrained shrinkage of the patch material leads to cracking of the patch. The main factor

influencing the limiting corrosion rate is the presence of oxygen as described in Chapter -

4. After cracking of the patch the corrosion problem becomes worse because cracks facilitate the intrusion of oxygen and chloride ions to the steel bar. Shrinkage cracking of the patch material is unavoidable and even with the most promising patch materials the repair system will crack soon after application. Use of a barrier that can reduce the diffusion of oxygen should be able to decrease the corrosion rate considerably. The effect of using a fiber reinforcement polymer (FRP) overlay as a secondary reinforcement on top of a traditional patch on the corrosion rate was studied experimentally. Experimental investigation of the durability and performance of concrete with and without a patch was performed using the accelerated corrosion test.

Also, the model developed in Chapter 4 and 5 was adjusted so that it can provide results of the cover cracking time for the patched concrete as well as the dual repair system consisting of the patch and FRP.

6.2 Overview of Patching System

Structures damaged by corrosion are usually repaired by patching, typically with a polymer cement mortar (PCM). In many situations, even after repairing damaged concrete, corrosion continues to induce damage. Sometimes the corrosion rate is higher in the steel bar after patching the damaged concrete. This can be due to different reasons such as the patch material having higher porosity than concrete, early shrinkage cracking of the patch, and electrochemical incompatibilities between the repair and the concrete substrate (Beaudette 2001). In the following sections, the properties, advantages and disadvantages of different repair methods are briefly described.

6.2.1 Traditional Patch

Polymer cement mortar is a modified mortar in which part (10 to 15% by weight) of the cement binder is replaced by a synthetic organic polymer. Modification of the mortar with a polymer latex (colloidal dispersion of polymer particles in water) results in greatly improved properties. A great variety of latexes are now available for use in polymer cement concrete products and mortars. The most common latexes are based on polymethyl methacrylate (also called acrylic latex), polyvinyl acetate, vinyl chloride copolymers, polyvinylidene chloride, styrene-butadiene copolymer, nitrile rubber and natural rubber. Each polymer produces characteristic physical properties. The acrylic latex provides a very good water-resistant bond between the modifying polymer and concrete components, whereas use of latexes of styrene-based polymers results in a high compressive strength.

Curing of latex PCM is different from that of conventional mortar, because the polymer forms a film on the surface of the product, retaining some of the internal moisture needed for continuous cement hydration. Because of the film-forming feature, the curing time for latex products is generally shorter. Generally, PCM made with polymer latex exhibits better bonding to steel reinforcement and to old concrete, good ductility, resistance to penetration of water and aqueous salt solutions because of lower permeability, and resistance to freeze-thaw damage. The flexural strength and toughness of PCM are usually higher than those of unmodified concrete. The modulus of elasticity of PCM may or may not be higher than that of unmodified mortar, depending on the polymer latex used. The drying shrinkage of PCM is generally lower than that of conventional concrete. The amount of shrinkage depends on the water cement ratio,

cement content, polymer content, and curing conditions. PCM is more susceptible to higher temperatures than ordinary cement concrete. For example, creep increases with temperature to a greater extent than in ordinary cement concrete, whereas flexural strength, flexural modulus and modulus of elasticity decrease. These effects are greater in materials made with elastomeric latex (e.g., styrene-butadiene rubber) than in those made with thermoplastic polymers (e.g., acrylic). Typically, at about 45°C, PCM made with thermoplastic latex retains only approximately 50 percent of its flexural strength and modulus of elasticity. Because of lower shrinkage, good resistance to permeation by various liquids such as water and salt solutions, and good bonding properties to old concrete, PCM is particularly suitable for thin (even less than 1-inch) floor toppings, concrete bridge deck overlays, anticorrosive overlays, concrete repairs, and patching (Blaga and Beaudoin 1985)

6.2.2 Patch and FRP Overlay

The poor performance of shallow depth surface patches applied to concrete structures is generally due to two reasons. The rapid cure patches, typically consisting of latex modified concrete, demonstrate extensive cracking due to high shrinkage during curing and subsequent aging. As a result of the restraint provided by the substrate at the interface and periphery, drying shrinkage cannot occur freely. This leads to the development of various stress components, the interaction of which can lead to premature degradation of the patch (Baluch et al. 2002). After cracking, the problem is further exacerbated if the repaired structure is subjected to an aggressive environment, where cracks provide free access for intrusion of chloride ions and diffusion of carbon dioxide.

In order to have longer and better lifetime performance it is necessary for the repair to retain its integrity and display few or no cracks. Thus, the performance criterion should be that of a minimum, or crack-free, repair layer (Baluch et al. 2002). Theoretically, it should be possible to develop improved patching materials that bond well to concrete, are shrinkage resistant, have coefficients of thermal expansion that are compatible with that of concrete, and are resistant to environmental damage. However, the development of such materials will involve costly research, product development and field-testing before these materials are likely to be adopted in practice. On the other hand, the use of fiber reinforced polymer (FRP) fabrics applied in a “bandaid” fashion over traditional patching materials that are currently used, has a strong potential to provide highly durable patches. The FRP fabric will serve as:

- Temporary formwork to hold the filler material in place after initial application, thereby providing construction cost savings;
- A physical barrier that retards the ingress of chlorides and moisture into the filler material; and
- Secondary reinforcement to hold the filler material in place if it should debond from the concrete due to shrinkage and environmental effects.

In order to obtain the desired performance under field conditions, the complex conditions leading to the buildup of stress in the repair zone needs to be understood (Baluch et al. 2002, Mangat et al. 2000). The role of different parameters has to be identified to allow the identification of suitable materials and procedures for repair

(Mangat et al. 2000). Thus, a quantitative assessment of the compatibility of basic properties such as elastic modulus, shrinkage and creep on the long-term service life of the repair is needed. Unfortunately, most repair material selection is based on short-term response and most standards and recommendations are based only on limited quantitative knowledge of structural interaction between the concrete substrate and the repair patch throughout its service life (Mangat et al. 2000). In the research reported herein, two and three-dimensional finite element analyses as well as laboratory testing was employed to study the performance of repairs.

6.3 *Experimental Test*

Experimental tests were conducted to determine the effect of the dual patching system on the cracking time of the repaired concrete and compare it with that for a traditional patch and plain concrete. Fabrication of the specimens consisted of making wooden molds, casting the concrete specimens, surface preparation, patching the specimens, and applying the FRP overlay. Each of these above mentioned steps are explained in more detail below.

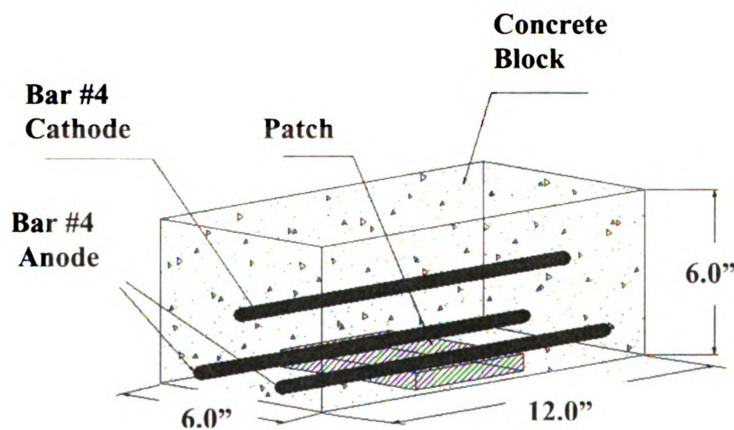
6.3.1 *Sample Preparation*

Wooden molds were constructed for fabricating the specimens to be used for experimental studies. Concrete specimens (6" × 6" × 12") with three #4 reinforcing bars, two near the bottom face (anodes or corroding bars) and one near the top face (cathode), were used. The bottom bars were placed such that half of each bar cross section was exposed to the patching material, and the cathode was placed at the middle of the

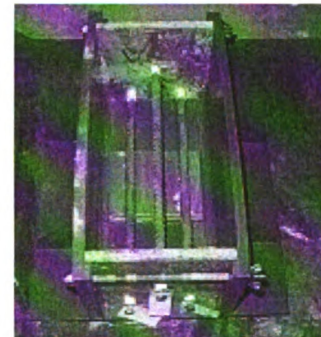
specimens. A piece of wood with the same dimension of the patch was used to create a cavity in the concrete substrate for six specimens. Three specimens did not have a cavity.

Figure 6-1 shows the molds for the test specimens before casting, the location of the patch part and the steel bar inside the molds. A total of 9 specimens were cast for the corrosion test with 3 specimens in each of three different groups: Group 1- repaired with patch and FRP; Group 2- repaired with patch only; and Group 3- plain concrete.

Ready-mix concrete conforming to the M-DOT Grade S2 mix design was used with a water reducer. This concrete mix is usually used for bridges. The fresh properties of the concrete mix determined at the time of casting, as well as some mechanical properties of the cured concrete, are given in Table 6-1.



(a)



(b)

Figure 6-1: Corrosion test specimens

The reinforcement bars for the corrosion test needed to be cleaned to remove all rust and other particles on the surface before casting. The bars were weighed after cleaning so that the mass loss could be measured after the corrosion test. The ASTM G1-

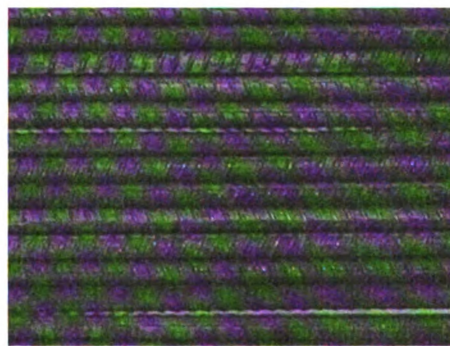
90 procedure was used to prepare clean and evaluate corrosion test specimens. Following the ASTM procedure, the steel bars first were degreased by soaking in saturated lime solution (CaCO_3) and then was pickled in an acid solution (5% HCl). After weighing, each bar, was named with a unique identifier and tagged. Figure 6-2 shows the corrosion steel bars before and after cleaning.

Table 6-1: Mechanical and Fresh Properties of Concrete

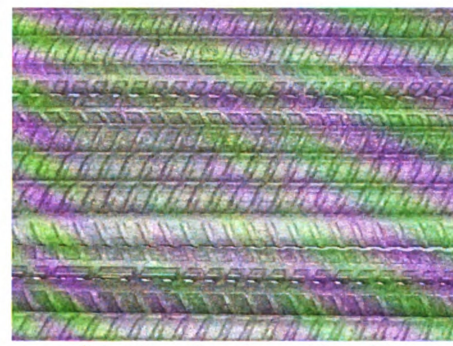
	Fresh	7 Days	14 Days	28 Days
Compression Strength (psi)	-	3789	4647	4896
Tensile Strength (psi)*	-	306	316	371
Slump	3.5-in.-max	-	-	-
Total Air Content	7	-	-	-

*From split tensile test

After casting, the specimens were immediately covered with polyethylene sheets which remained in place for more than 24 hours before demolding. After demolding the specimens were transferred to the curing room.



(a) After degreasing



(b) After cleaning with acid

Figure 6-2: Steel bars after degreasing and cleaning

6.3.1.1 Surface Preparation

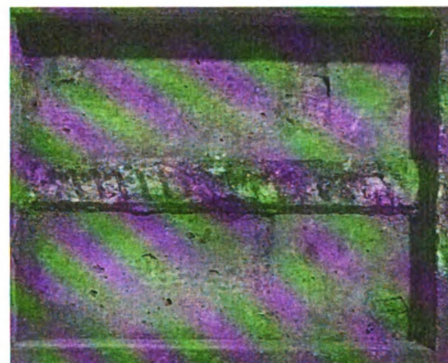
Repair practices commonly require that surface preparation techniques consist of high pressure water blasting, abrasive blasting or other techniques. Surface preparation improves the bond strength between the patch and concrete substrate.

The specimens to be filled with a patch were sand blasted on all sides of the cavity. Sandblasting was performed with the nozzle nearly perpendicular to the surface and was continued for at least 1 minute until no visible change on the surface was observed. After sand blasting, the surface was blown with compressed air and then washed. Figure 6-3 shows the cavity in the specimens before and after sand blasting.

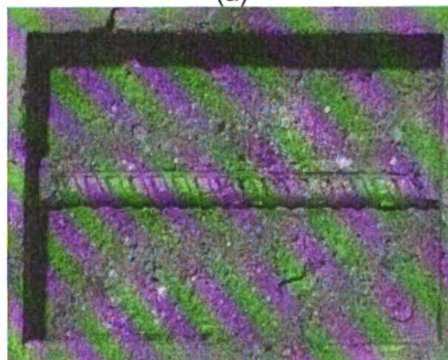
6.3.1.2 Repair of the Specimens

A PCM patch material used to fill the cavities in 6 specimens. A bidirectional glass FRP overlay was applied to 3 patched specimens. The patch and FRP application were done according to the material data sheets.

According to the material data sheet, the concrete surface should be “saturate dry” before applying the patch material. To accomplish this, the cavity was filled with water for about 8 hours before applying the



(a)



(b)

Figure 6-3: Specimens (a) before and (b) after sand blasting

patch material. However, when applying the patch the surface was still dry and water was sprayed on the surfaces to moisten them. The specimens were placed in an overhead position before applying the patch to simulate real field conditions.

The patch material was a two-component polymer-modified, lightweight mortar and was mixed according to the material data sheet. Since the quantity of material needed was less than the minimum recommended in the data sheet, the mixture quantities were reduced in proportion to the required amount, and the repair mortar was mixed in partial batches. After applying the repair mortar to six specimens, the FRP overlay was placed over the uncured repair mortar on three of the repaired specimens. After placing the FRP overlay, all the specimens were kept in an overhead position for curing.

6.3.2 Installing Strain Gages

Strain gages were used to monitor the strain in the FRP overlay and concrete due to corrosion-induced radial expansion. For specimens with an FRP overlay the strain gages were mounted on the overlay. For specimens without an FRP overlay, (Group 2 and 3) a 1/2-inch wide strip of FRP was bonded around the specimens at specific locations and strain gages were mounted on these strips. The strain gages were applied on the specimen sides, and also on the bottom surface of the patch exactly below of the steel reinforcement. Strain measurements were taken on two sides of the specimens at the level of the rebar. The strain was monitored every other day at the same time for all specimens.

6.3.3 Test Set-Up

The specimens were subjected to accelerated corrosion for three weeks. Due to equipment limitations, the accelerated corrosion test was done in two batches of 3 and 6 specimens. A constant voltage of 12 V was supplied from the single bar (cathode) to the other two reinforcing bars (anodes) using an

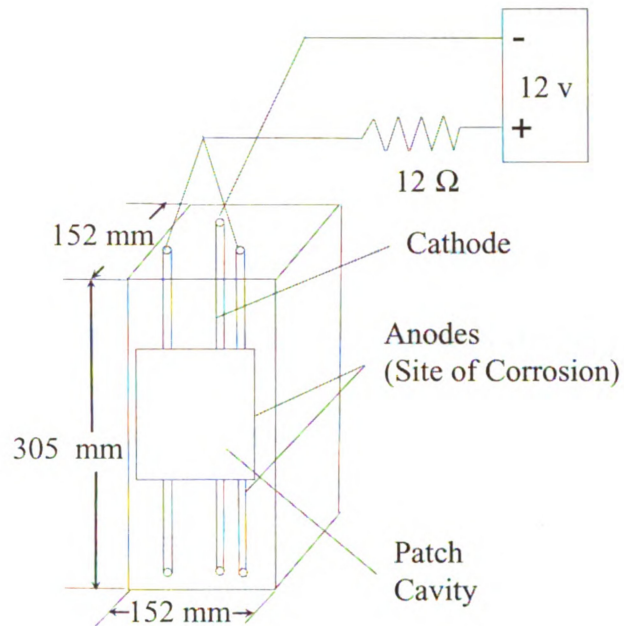


Figure 6-4: Experimental setup for the corrosion test

external power source. A 3.5 percent sodium chloride solution (by weight) was used to wet the concrete specimens for one hour in each 12-hour period. The moisture in the concrete specimens and the applied current induced corrosion in the anodic reinforcing bars in an accelerated fashion. Figure 6-4 shows the experimental setup for the corrosion test.

The applied current was monitored at two-minute intervals with a voltage data-logging unit (Omega Engineering Inc., AD128-10T2), since this can be used to estimate the total corrosion in the reinforcing bar.

The mass loss was calculated using two methods. In the first method the real mass loss of the steel bar was measured by weighing the bars before and after the corrosion

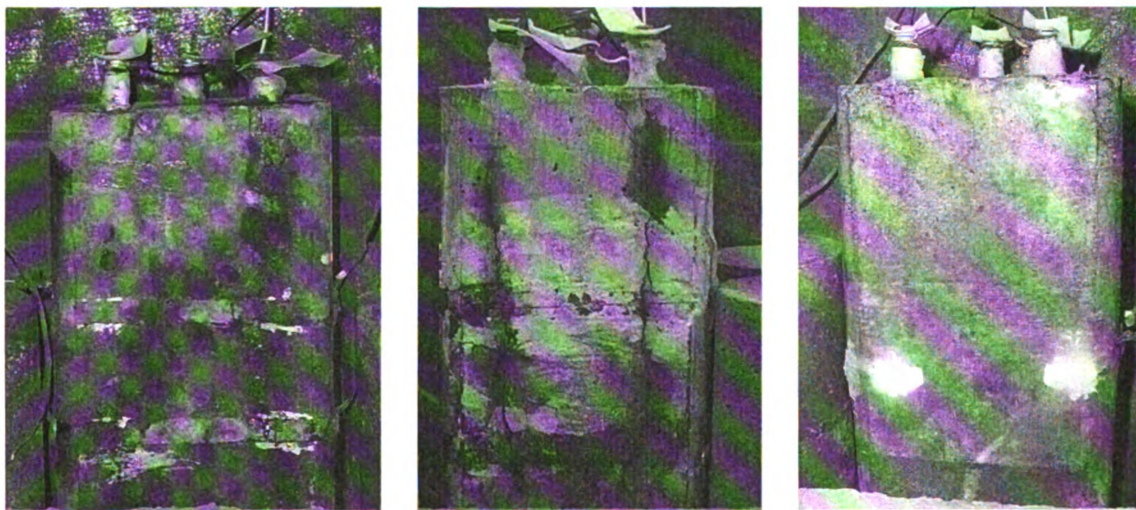
test. In the second method the mass loss was estimated using the recorded current and using Faraday's Law (Phillips 1992, Pantazopoulou 2001):

$$\Delta W = \frac{A_m}{F \times Z} \int_0^T I(t) dt \quad (6-1)$$

where ΔW = steel loss in grams, $I(t)$ = measured current at time t in amperes, t = duration of the test in seconds, A_m = atomic mass of Fe, z = valency (assuming that the rust product is mainly Fe(OH)_2 , $z = 2$), and F = Faraday's constant.

6.3.4 Results and Discussion

As shown in Figure 6-5, all specimens suffered severe cracking. However, specimens with the FRP overlay had fewer cracks and less damage than unrepaired specimens and repaired specimens without FRP. The crack pattern due to the corrosion-induced expansion was monitored in more detail for each group of specimens.



(a) Sample from Group 3

(b) Sample from Group 2

(c) Sample from Group 1

Figure 6-5: Samples from each group after 6 weeks of accelerated corrosion testing

6.3.4.1 Crack Path

Two different crack patterns were observed in the three types of specimens. Figure 6-6 shows schematics and photographs of the two crack patterns.

Specimens with the FRP overlay had a single dominant crack along the side surface of the specimens parallel to the FRP overlay and reinforcing bar as shown in Figure 6-6 (a). This crack path is henceforth referred to as a Pattern 1 crack. Some cracks were observed in the concrete cover, but they did not extend to the patch. Also, some debonding of the FRP overlay was observed around the crack path.

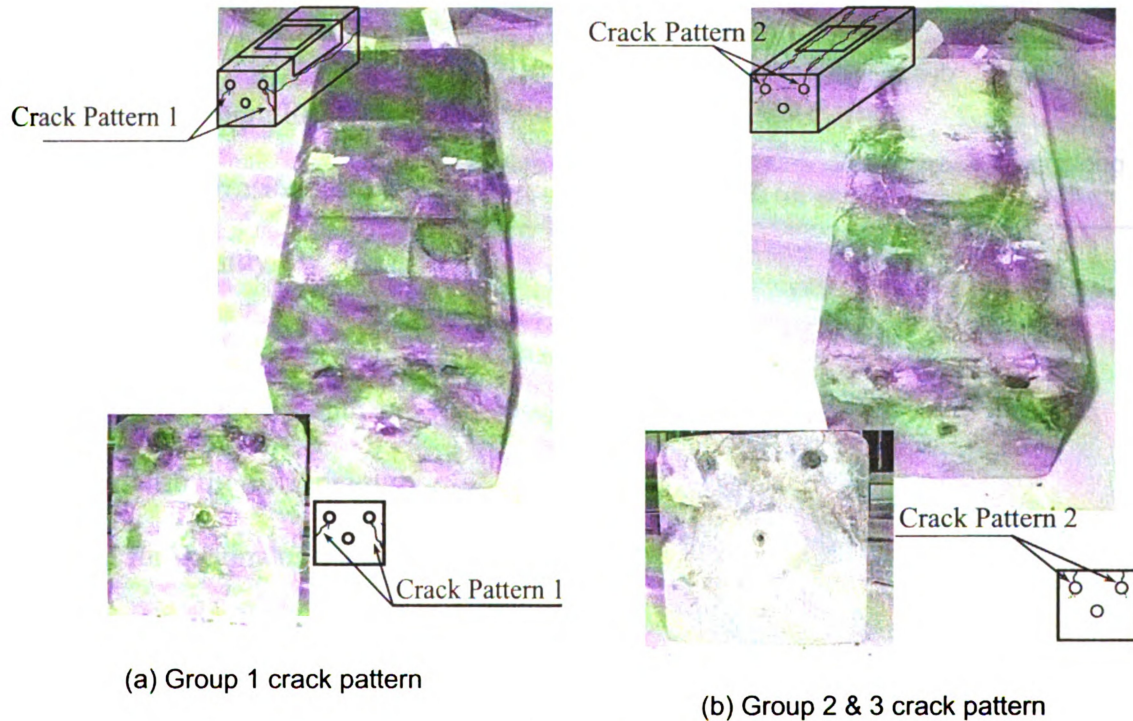


Figure 6-6: Crack pattern due to corrosion

Specimens with a patch and no FRP overlay, and unrepaired specimens with no patch or overlay, had a dominant crack at the bottom surface of the specimens parallel to the reinforcing bar. This crack is henceforth referred to as a Pattern 2 crack. Some specimens without FRP also had internal cracks from one corroding bar to the other

(anodes), and some internal cracks radiating outward from the reinforcing bar into the concrete.

6.3.4.2 Strain Gage Readings

As both Figure 6-7 and Figure 6-8 show, the maximum strain at the sides for the specimens with FRP are almost 10 times smaller than the maximum strain at the bottom for specimens without FRP. This indicates that corrosion can be reduced significantly by using the FRP overlay. The crack widths ranged from 0.2 mm on specimens with the FRP overlay to 1.5 mm for specimens without the overlay. Thus the FRP overlay also reduced crack widths.

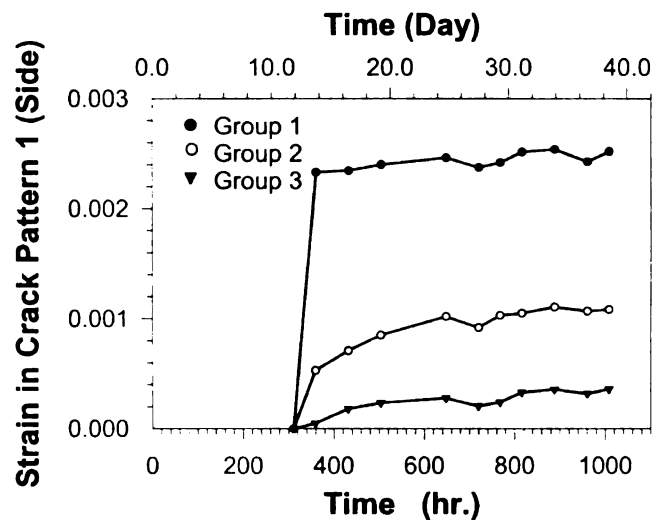


Figure 6-7: Maximum strains in the corrosion test along the crack path for crack pattern 1

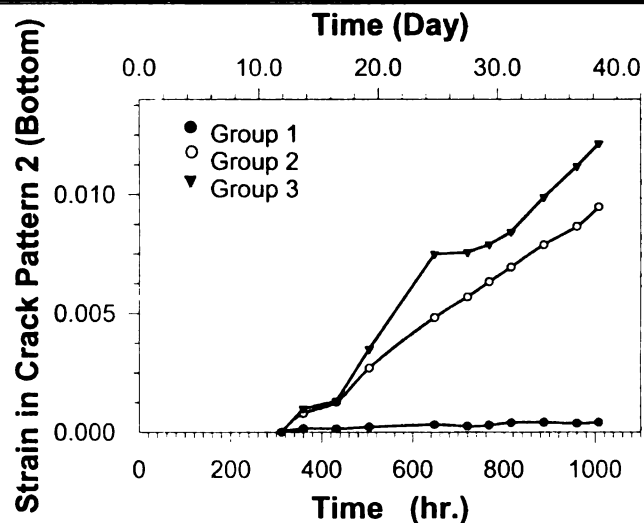


Figure 6-8: Maximum strains in the corrosion test along the crack path for crack pattern 2

6.3.4.3 Crack Pattern

Specimens with and without FRP showed very different crack patterns and measured strains under the accelerated corrosion test. 3-D FE analysis of these specimens was

conducted to understand why the FRP overlay changed the crack pattern and reduced

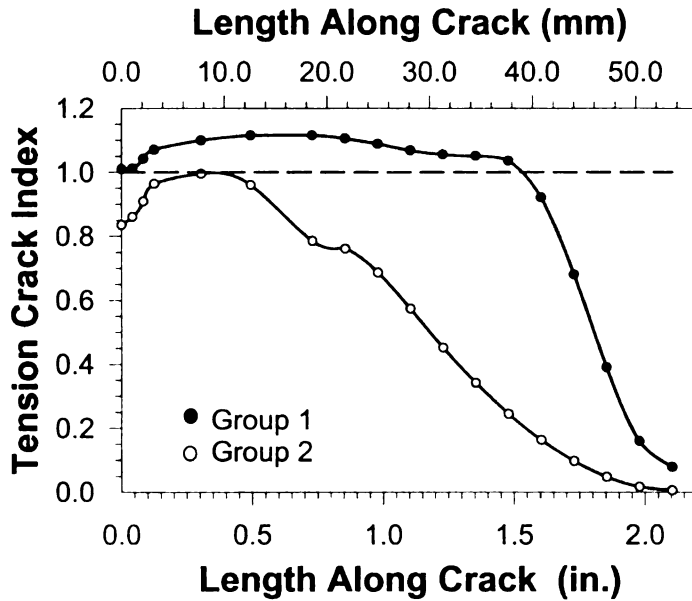


Figure 6-9: TCI along crack pattern 1

crack widths. The properties shown in Table 6-2 were used in the analysis. The expansive behavior due to rebar corrosion of the reinforcement was modeled using a uniform expansion of $17500 \mu\epsilon$ on the rebar cross section

based on calibration with prior research (Harichandran and Nossoni 2008). In order to understand the overall effect of the FRP overlay on the stress distribution and crack pattern in the concrete substrate and patch material, the tension crack index (TCI):

$$TCI = \frac{\sigma_{P_{max}}}{f_t} \quad (6-2)$$

was calculated in the cross section of the model along the two most probable crack paths that were obtained in the experiment, where $\sigma_{P_{max}}$ is the maximum tension principal stress, and f_t is the tensile strength of the patch material. Tension cracking occurs when $TCI > 1$.

Figure 6-9 and Figure 6-10 show the calculated TCI in the concrete and patch material along the crack paths observed in the experiment and confirm that Pattern 1 cracks will occur for FRP specimens but not for patch specimens, while Pattern 2 cracks

will occur for patch specimens but not for FRP specimens. The FE analysis indicated that when 14% of the corrosion expansion strain is applied on the patch specimens (without FRP) the first crack opens in the patch material as in Pattern 2, and when the first crack is fully opened the concrete substrate is not yet cracked.

On the other hand, the first crack opens as in Pattern 1 after applying 58% of the expansion strain on specimens with the FRP overlay. The numerical results match the crack patterns observed in the experiment, and cracking is delayed when the FRP overlay is used. The match between experimental and numerical results show that the FE analysis

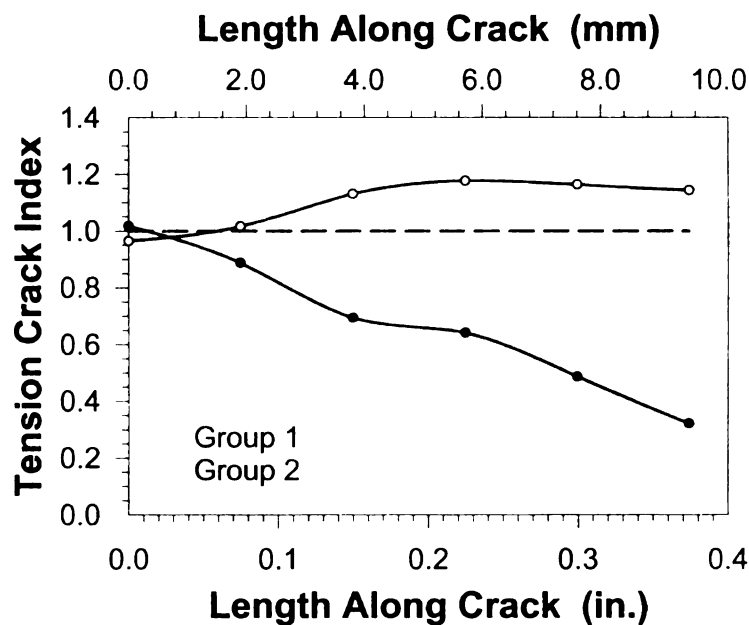


Figure 6-10: TCI along different crack pattern 2

with the rebar corrosion modeled as an initial expansion strain applied uniformly across the entire cross section of the bar gives reasonable results. The FE analysis also is able to explain the mechanical effect of the

FRP overlay on the crack pattern and how it delays the onset of cracking.

It is apparent that the cracking of the concrete is a direct consequence of the radial expansion of the corroded reinforcement bar. Internal cracking always starts at the location of the maximum expansion and extends in the direction of the weakest region, which in most cases is the cover region when the patch material is not reinforced by an FRP overlay. However, when an overlay is used, the overall stress distribution changes

and the crack propagate sideways away from the region influenced by the overlay. In this case, the crack initiates in the concrete substrate instead of the patch, and since the concrete is stronger than the patch the cracking is delayed as predicted by the FE model.

Table 6-2: Mechanical and Physical Properties of the Glass FRP and Patch Material used

	Type	Elastic modulus (psi)	Tensile Strength (psi)	Thickness (in.)	Compressive Strength (psi)	Shrinkage Strain (μ s)	Shear Strength (psi)
FRP (Glass)	Glass Bidirectional	2.47×10^6	4.40×10^4	0.013	-	-	-
Patch Material	PMC	2.0×10^6	590		5000	350	2700

6.3.4.4 Mass Loss

As mentioned earlier, the mass loss due to corrosion was calculated using Faraday's Law (Equation 6-1) and also measured using the ASTM G1-90 procedure. In the ASTM procedure the bars were cleaned and weighed before casting. The covered bars were initially cleaned with a wire brush to remove all the loose rust products and concrete from the steel bars, and then they were immersed in 35% hydrochloric acid for 25 minutes at room temperature for deep cleaning inside the corrosion pits. More time was needed in some cases to remove heavy rust. The steel bars were washed, dried in an oven, and weighed. This procedure was continued until the weight of the bars reached a steady state. Table 6-3 shows the measured mass loss for the two batches of specimens as a percentage of the initial weight of the steel bar.

The first batch had 3 specimens and, the second batch had 6 specimens. For the second batch, the applied voltage was 12.83 V, while for the first batch it was 12 V. This

is likely to be the cause for the increased mass loss in the second batch compared to the first batch for all groups.

Table 6-3: Average Mass Loss for Each Group in the Corrosion Test

	With Patch & FRP	With Patch	Unrepaired
First Batch	4.90%	12.20%	10.06%
Second Batch	5.67%	17.31%	16.93%

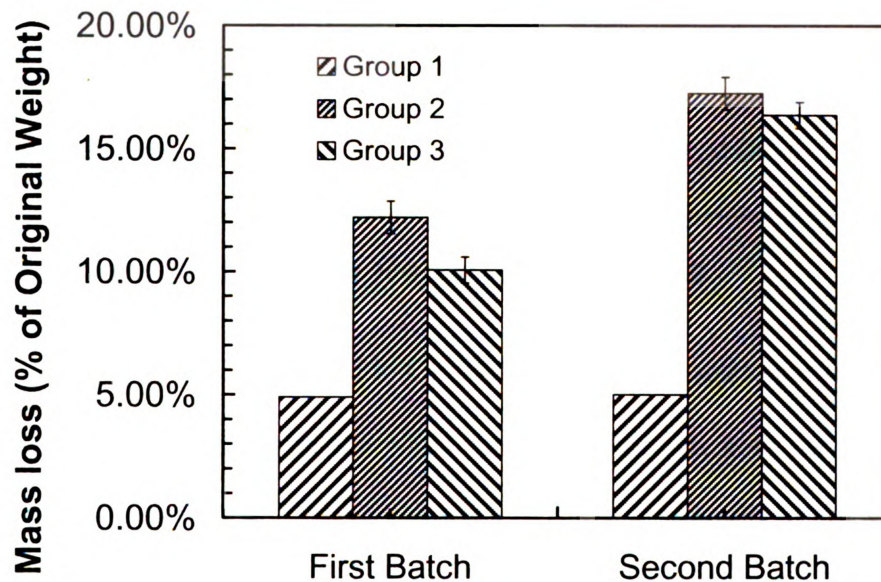


Figure 6-11: Corrosion mass loss for each group

Figure 6-11 indicates that the corrosion level is similar for patched and unrepaired specimens and concrete.

Table 6-3 and Figure 6-12 also indicate that the corrosion level was significantly reduced when the FRP overlay was used. This confirms the inference made earlier from strain gage readings. The most likely reason for the overlay reducing corrosion is the reduction in diffusion of chloride ions, moisture and air through the concrete and patch due to the overlay acting as a barrier. As explained in Chapter 3, when there is

insufficient chloride available in the system, even impressed current does not corrode the steel bars.

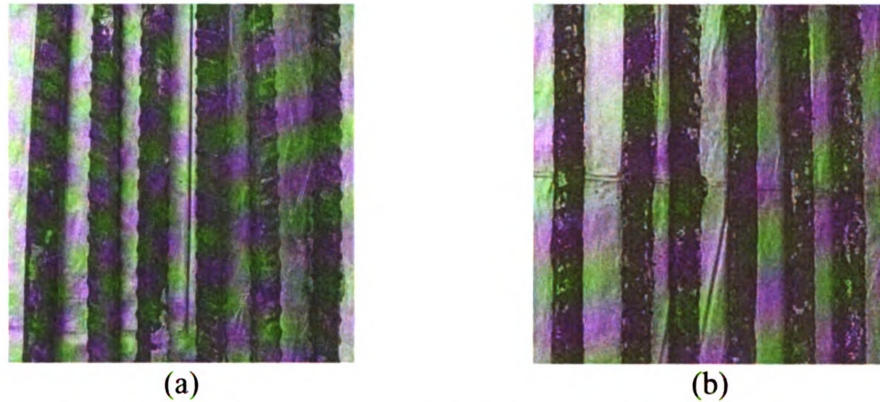


Figure 6-12: Bars after six weeks of accelerated corrosion testing (a) Group 1 (b) Group 2 & 3

6.4 Corrosion Modeling in Repaired Concrete

The corrosion model presented in Chapter 4 and 5 was used to predict the corrosion rate for specimens repaired with the patch material, and with both the patch and FRP overlay. Also, a finite element model was used to estimate the critical cracking pressure for both patching systems as explained in Chapter 5.

6.4.1 Corrosion Rate

The corrosion rates for unrepaired specimens (Group 3), specimens repaired with the patch material (Group 2), and specimens repaired with both the patch and FRP overlay (Group 1) were compared using the developed model assuming that the chloride concentration was the same for all three cases, and that the only factor governing the rate of corrosion was the rate of diffusion of oxygen into the concrete and rust layer as described in Chapter 4.

Since the porosity of the patching mortar is higher than that of concrete and micro-cracking due to restrained shrinkage further increases the oxygen diffusion coefficient, it was assumed that the oxygen diffusion coefficient for concrete repaired with patch

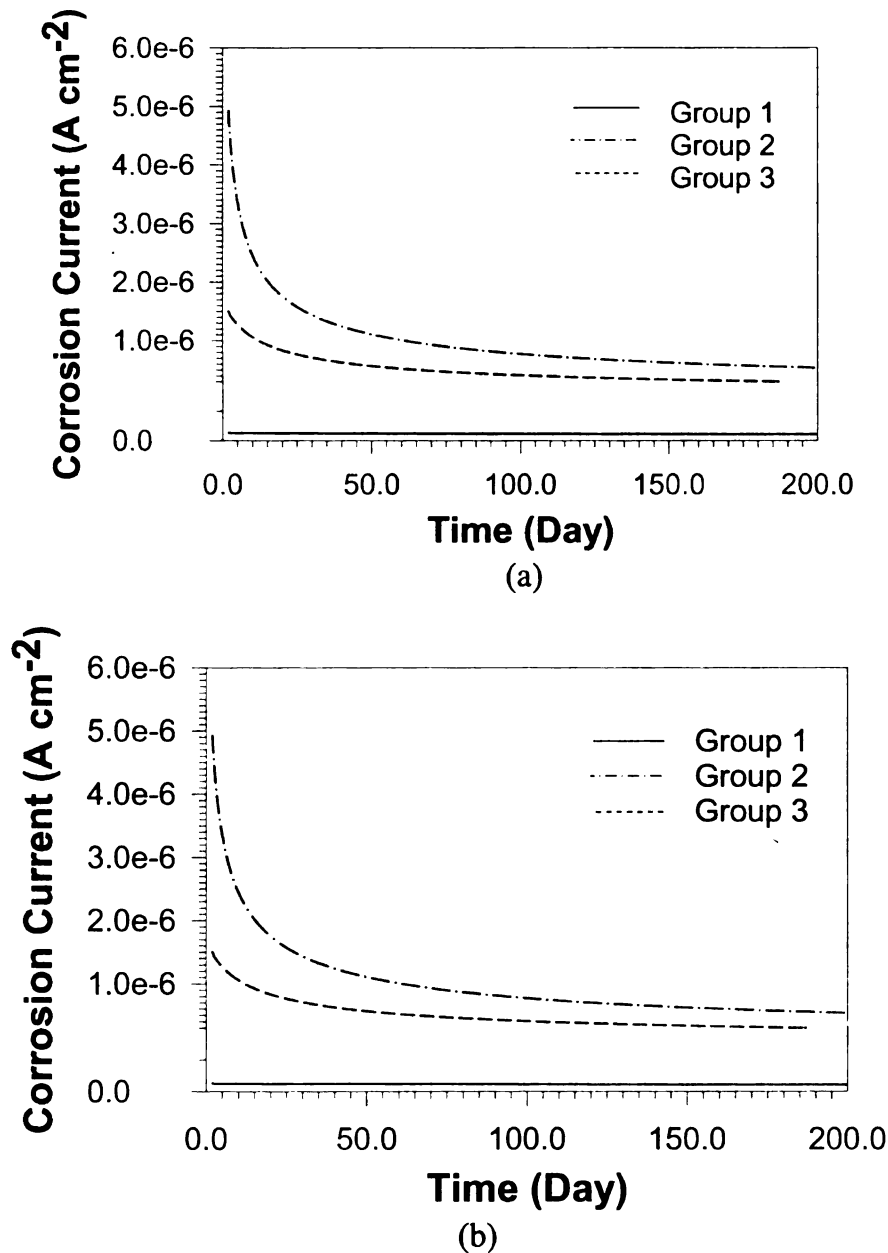
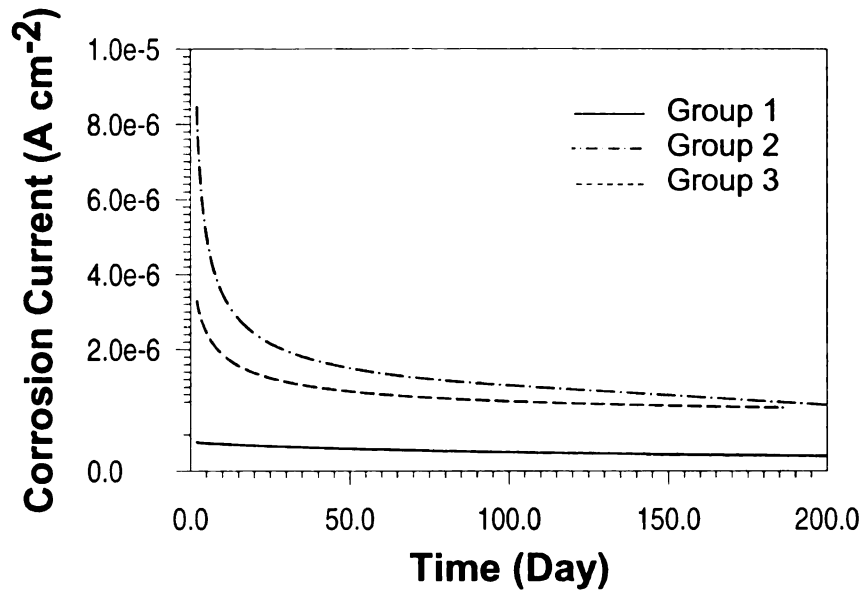


Figure 6-13: Corrosion rate for different patching system, BC2 and a) w/c =0.4, b) w/c =0.5 and c) w/c =0.6



(c)

Figure 6-13 cont'd: Corrosion rate for different patching system, BC2 and a) w/c = 0.4, b) w/c = 0.5 and c) w/c = 0.6

material was 1.5 times that of concrete. When an FRP overlay is used, the oxygen diffusion coefficient is almost 100 times lower than the oxygen diffusion coefficient for concrete (Chowdhury et al. 2007). It is therefore reasonable to neglect the oxygen diffusing through the FRP. Consequently, the oxygen needs to travel a longer distance from the top surface or sides of the concrete element to reach the corrosion cell depending on the geometry of the repaired part. Figure 6-13 shows a comparison of the corrosion rates as a function of time for the three different cases with boundary condition type 2 as described in section 4-7.

The results show that the corrosion rate increases by 20-30% when the patch material is used compared to unrepaired concrete. However, the corrosion rate decreases dramatically by 85-95% when an FRP overlay is used on top of the patch material.

6.4.2 Cracking Pressure

The concrete surrounding the reinforcing bar will be subjected to an internal radial pressure due to the expansion of corrosion products. The pressure adjacent to the bar increases due to

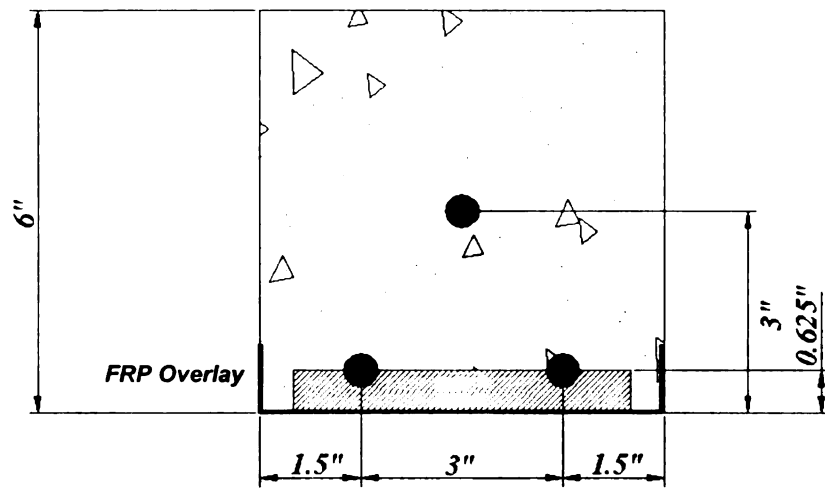


Figure 6-14: Geometry of the FE model with and without FRP

accumulation of the rust products, and the concrete will eventually crack and spall. The development of cracks and spalling of the concrete is highly dependent on the ratio of the concrete cover and distance between bars to the bar diameter (k_r), as explained in previous chapters.

Finite element analysis was performed for the repair with the FRP overlay to investigate the effect of the overlay on the critical pressure and cracking time of the concrete cover. Figure 6-14 shows the geometry of the finite element models and Table 6-2 shows the material properties used.

The FRP overlay increased the pressure required to crack the concrete cover by about a factor of 4 compared to the pressure required to crack plain concrete for this specific geometry. When an overlay is used, the overall stress distribution changes and the crack propagates away from the region influenced by the overlay (Nossoni and

Harichandran 2008). In other words, the FRP overlay strengthens the weakest region that is the concrete cover and increases the service life of the patch repair.

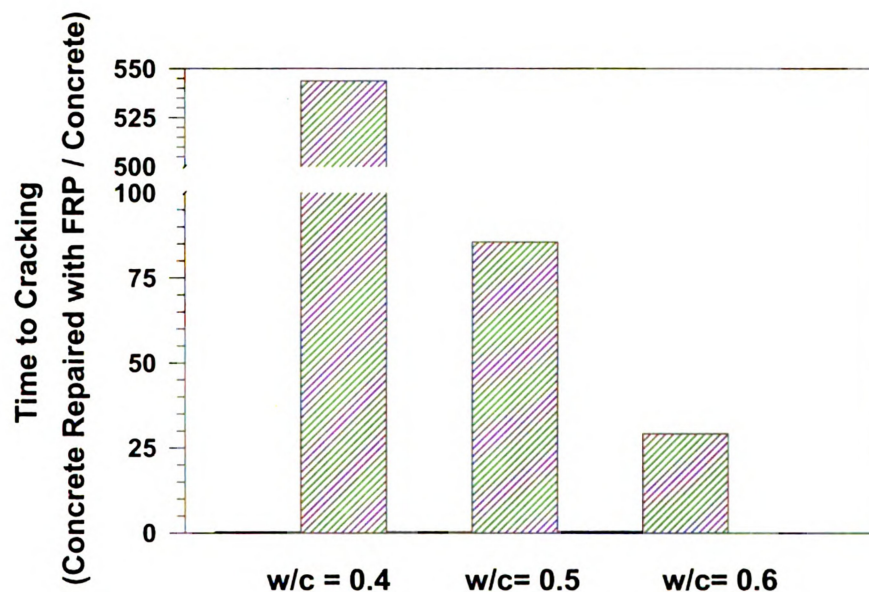


Figure 6-15: Concrete cover cracking for different condition for BC2, and $k_f = 6$

By reducing the corrosion rate and increasing the cracking pressure, use of the FRP overlay over a traditional patch can increase the life of the repair and reduce rehabilitation cost over the life of the concrete structure. Figure 6-15 shows a comparison between the cracking times for different water- cement ratios.

6.5 Summary and Conclusions

The corrosion rate and the critical pressure required to crack the concrete cover were determined for plain concrete, concrete repaired with a polymer concrete patching compound, and concrete repaired with a patch and an FRP overlay. The results indicate that use of an FRP overlay on top of a traditional patch repair significantly reduces the corrosion rate and increases the critical pressure required to crack the concrete cover. The combination of both effects dramatically increases the durability of the patch repair

enhanced with the FRP overlay. The results agree well with those obtained from accelerated corrosion tests on reinforced concrete specimens with and without repairs.

Chapter 7

Summary, Conclusions, and Recommendations for Future Research

7.1 Introduction

This chapter contains the summary and conclusions of the experimental investigation and the theoretical modeling of the corrosion current and concrete cover cracking for different conditions. Recommendations for future research in this area are also provided.

7.2 Significance of Research

Corrosion of steel in concrete has attracted the attention of many researchers in civil engineering, material science and chemistry over the past 100 years. It is a fascinating topic at the intersection of science and engineering.

Reinforced concrete is one of the most common construction materials. High quality concrete is a very durable material and can remain maintenance free for many years when it is properly designed. Steel reinforcement is used to improve the tensile strength of concrete structures, and more generally the mechanical resistance. The high alkalinity of concrete can prevent the reinforcing steel from corroding inside concrete; in other words steel is passive inside concrete. Depassivation of steel reinforcement embedded in concrete and the onset of active corrosion can arise due to two causes: carbonation of the concrete, or chloride diffusion.

There has not been much work done on the effect of chloride ions on the electrochemical behavior of iron in alkaline media and how depassivation of steel in concrete occurs from an electrochemical point of view. There also was not much work done on modeling the corrosion current as a function of time, and explaining how and why the corrosion current decreases with time. Available models for cracking of the concrete cover assumed a constant corrosion current. No work was done to model the amount of rust products that diffuse into concrete pores and at best researchers used a hypothetical porous zone of 10 to 20 μm around the steel bar to account for the loss of pressure build-up.

This work is a comprehensive study on the effect of chloride ions on the durability of concrete structures. The study begins with the effect of chloride ions on the depassivation of steel bars inside concrete, and the overall electrochemical behavior of steel in alkaline media. Then the corrosion rate of steel inside concrete was studied and the corrosion current was modeled as a function of the different chemical species that can affect it. At the early stage of corrosion the chloride concentration controls the corrosion

rate, but the limiting corrosion current that depends on the availability of oxygen is quickly reached and controls the corrosion rate until cracking of the concrete cover. A comprehensive experimental study was conducted and a theoretical model of corrosion describing depassivation, and the initial and limiting corrosion currents was developed. This is an original contribution since other available models are based on observation or assumption rather than on a clear understanding of the physical and chemical processes involved and a complete understanding of the effects of chloride and other factors on the electrochemistry of corrosion. After estimating the corrosion current for different conditions, the time for cracking of the concrete cover due to corrosion, t_2 , was calculated. First, the growth of the rust layer was calculated using the rate of corrosion and then it was used to estimate the pressure applied to the concrete cover. The amount of corrosion products that diffuse into the concrete pores was also modeled. The critical pressure that causes the concrete cover to crack was estimated based on the rust build-up and inelastic behavior of concrete, and calibrated with finite element analysis and experimental data. Additional experimental tests were conducted to calibrate and verify both the corrosion rate and concrete cover cracking model.

The time for chloride diffusion to the rebar, t_1 , was calculated and compared with the time for cracking of the concrete cover, t_2 , to better understand the factors that control the life of concrete structures.

Finally, the effect of different concrete repairs on the corrosion rate and the critical cracking pressure were studied. In concrete repaired with a polymer mortar patch, unavoidable restrained shrinkage of the patch material leads to cracking of the patch.

After cracking of the patch the corrosion problem becomes worse because cracks facilitate the intrusion of oxygen and chloride ions to the steel bar. Use of a barrier that can reduce the diffusion of oxygen should be able to decrease the corrosion rate considerably. The effect of using a fiber reinforced polymer (FRP) overlay as a secondary reinforcement on top of a traditional patch on the corrosion rate was studied experimentally. Also, the proposed model was adjusted so that it can provide results of the cover cracking time for the patched concrete as well as the dual repair system consisting of the patch and FRP. The dual patching system can significantly increase the life of concrete repairs. The models developed in this research can be used to assess the benefits of using improved materials and structural configuration for the next generation of sustainable concrete infrastructure.

7.3 Summary, Conclusions

A summary of this comprehensive study on the electrochemical modeling of the corrosion current and mechanical modeling of concrete cover cracking, and resulting conclusions and recommendations are given below.

7.3.1 Effect of Chloride Ions on Steel Behavior

The anodic polarization curves for the corrosion of mild steel in alkaline media were experimentally measured at varying chloride concentrations. As the ratio $\chi = [\text{Cl}^-]/[\text{OH}^-]$ increased, the passivation current increased linearly with χ to maintain the passive layer. At a pH of 13.46 pitting corrosion of steel occurred approximately when $\chi > 0.6$ and the pitting potential decreased cubically as χ increased. The initiation of

corrosion at a threshold chloride concentration of about $\chi = 0.6$ occurs due to changes in the underlying electrochemistry of corrosion. These data provided the basis for an empirical model of steel corrosion in chloride-containing alkaline environments that is directly applicable to the prediction of corrosion-induced damage in steel-reinforced concrete structures.

7.3.2 Corrosion Current

The initial corrosion current was modeled empirically using measured anodic polarization curves and the calculated reduction polarization curve. The limiting current was modeled based on the cathodic limiting reaction and oxygen diffusion in the rust layer. The corrosion current was calculated for different boundary conditions, concrete properties, and concrete cover thicknesses. The concrete cover thickness did not significantly affect the corrosion current. The only two factors that had a significant impact on the corrosion current were the boundary conditions and the concrete quality. As the concrete quality decreases the permeability of concrete increases, and the diffusion of oxygen and the water content of concrete also increases resulting in an increase of the corrosion current. Using good quality concrete with a low water-cement (w/c) ratio is the first step in protecting concrete structures from corrosion damage. Boundary conditions also have some effect on the corrosion current, especially in the case of submerged structures. However, concrete superstructures and elements in the splash zone have similar corrosion currents after the chloride concentration reaches the threshold value.

The corrosion current predicted by the model was compared with data from experiments, field measurements and corrosion models reported in the literature. Although there is considerable scatter in the data reported in the literature, the proposed model showed good agreement with some experimental test results and field measurements.

7.3.3 Concrete Cracking

The boundary condition is one of the factors that had an effect on the corrosion current. The difference in the rate of corrosion for superstructures and elements in the splash zone (referred to as BC1 and BC2 in this work) is only about 5% because the availability of oxygen for both cases is about the same. However, for submerged structures (BC3) the corrosion current is almost 10 times lower than for BC1 and BC2 due to the lack of oxygen at the boundaries. Because the corrosion rate was extremely small, the time for cracking of the concrete cover for BC3 was not calculated in this study. The 5% increase in corrosion current from BC1 to BC2 due to the higher water content of concrete can decrease the life of the concrete structures by 10% to 25%. An increase in the w/c ratio by 0.1 decreases the time for cracking of the concrete cover by a factor of 1.5 to 3 depending on other factors. Another important factor that affects the time for cracking of the concrete cover is cover thickness. The life of a concrete structure from the start of corrosion to cracking of the cover can be increased by a factor of two if the concrete cover is increased from 1.5 to 2 inches, and by same proportion again when the concrete cover is increased from 2 to 3 inches. If the increase in the time of diffusion

of chloride to the steel, t_1 , is included, then the increase in the life of concrete structures due to an increase in cover thickness is even more significant.

The time for corrosion initiation due to chloride diffusion, t_1 , and the time for cracking of the concrete cover, t_2 , are the two main parts of the life of a concrete structure exposed to chloride. It is commonly believed that the time t_1 dominates the life of the concrete structure and that the time t_2 can be neglected. This study shows that t_1 is considerably higher for BC1 for all w/c ratios, but for BC2 t_1 and t_2 are almost equal when the w/c ratio is 0.5 or larger and both times are equally important in estimating the life of a concrete structure. Even for a w/c ratio of 0.4 in BC2, t_2 cannot be neglected.

7.3.4 Effect of Repair on Corrosion Rate

The corrosion rate and the critical pressure required to crack the concrete cover were determined for plain concrete, concrete repaired with a polymer concrete patching compound, and concrete repaired with a patch and an FRP overlay. The results indicated that use of an FRP overlay on top of a traditional patch repair significantly reduces the corrosion rate and increases the critical pressure required to crack the concrete cover. The combination of both effects dramatically increases the durability of the patch repair enhanced with the FRP overlay. The results agree well with those obtained from accelerated corrosion tests on reinforced concrete specimens with and without repairs.

7.3.5 Experiments on Accelerated Corrosion Test and Rust

Thickness Growth

A comprehensive experimental investigation was performed on accelerated corrosion testing using an impressed current to investigate the accuracy of using Faraday's Law to calculate mass loss. This test was used to calibrate the relationship between the corrosion current and rust thickness, and establishing a situation where Faraday's Law gave accurate results was very important. Tests were performed in both solution and concrete to better understand the reactions that take place at the anode and cathode. The solution was chosen to be similar to the pore solution of concrete. The results of the tests in solution and concrete had similar trends, and indicated that Faraday's Law does not always give an accurate estimation of the mass loss. The accuracy depends on the chloride concentration in the system as well as the amplitude of the impressed current. Two competing reactions, the oxidation of steel and production of oxygen due to the splitting the water, occur at the anode. When the chloride concentration exceeds the amount required for natural corrosion to begin (i.e., $[\text{Cl}^-]/[\text{OH}^-] \geq 0.6$) and when there is no limitation of water in the system, the current efficiency (ratio of the real mass loss to the mass loss calculated using Faraday's Law) is close to unity. In this situation, Faraday's Law may be used to accurately estimate the mass loss in the accelerated corrosion test as long as the current is not too high.

Accelerated corrosion testing using a constant impressed current was performed under a microscope to establish the relationship between rust thickness and corrosion current. The test was done under conditions where all the corrosion current would be spent on corrosion rather than on splitting water to oxygen and hydrogen. The accumulated rust thickness varied approximately linearly with corrosion current until cracking of the concrete cover. The linear

relationship between rust thickness and time may not hold under natural corrosion since the corrosion current will not be constant. The results of the test under the microscope were used to calibrate and validate the corrosion current and concrete cover cracking models.

7.4 Recommendations for Future Research

Future work in the area of corrosion-induced cracking should focus on developing methods for more accurate nondestructive measurement of the corrosion current, and the development of sensors that can measure oxygen and chloride concentrations. Data from such measurement techniques would be useful for validating the corrosion model.

Image-based techniques of measuring the corrosion-induced strain field over the cross section of specimens tested in the laboratory offer significant promise. Data from these techniques can be useful for validating and refining prediction of the time for cracking of the concrete cover.

A nondestructive method for observing the accumulated rust thickness within concrete specimens at any stage of corrosion would be very valuable but will probably be very hard to develop.

The ability to identify the corrosion products at different locations in the rust layer would help further understand and validate the chemical reactions involved in corrosion. The development of methods to control the rust products could be used to favor products such as black rust over red rust that would reduce the volume expansion and reduce damage to concrete.

Finally, the properties of corrosion products under various confinement pressures, such as their density, permeability and the coefficient for the diffusion of oxygen in them,

are not well-established. Laboratory measurements of these would improve the accuracy of the proposed model.

APPENDIX

Main program

```

clc, clear all;
vary1D
filename=['vary1D.mat'];
save(filename);
%%%%%%%%%%%%%%%%%%%%%%%%%%%%%%%%%%%%%%%%%%%%%%%%%%%%%%%%%%%%%%%%%%%%%%%%
%%%%%%%%%%%%%%%%%%%%%%%%%%%%%%%%%%%%%%%%%%%%%%%%%%%%%%%%%%%%%%%%%%%%%%%% Data need to save %%%%%%%%%
rustthicknesshist1=[];rustthicknesshist=[];pshist=[];p1hist=[];monthhist=[];clhist=[];o1hist=[];dayhist=[];clohrhist=[];oconshist=[];O1hist=[];icorr1hist=[];icorrhist=[];ilimhist=[];delta3hist=[];delta2hist=[];delta1hist=[];delta0hist=[];
Pinrhist=[];Poutrhist=[];strainrhist=[];strainrouthist=[];
%%%%%%%%%%%%%%%%%%%%%%%%%%%%%%%%%%%%%%%%%%%%%%%%%%%%%%%%%%%%%%%%%%%%%%%%
sat=sat0;
p1=p0;
for yr=1:100
for month=1:12
for day=1:30
ai=yr*365+(month-1)*30+day;
[outcl,cl1]=chloride(1,ai); % chloride diffusion
cl1(end,1);
cl=cl1(end,1)*27679904/(35.5*w1); %mol/cm3 of water
clohr=cl*1000/oh
if clohr>0.55
[outo,o1]=oxygen(1,oi); % oxygen diffusion grm/cm3
o1(end,1);
o=o1(end,1)*27.679904/(32); %mol/cm3 of concrete
daycor=daycor+1
icorr1=ipass*(10+10^(alfa1*exp(alfa*clohr)/(beta+gama*exp(delta*clohr)))); % the
empirical equation from tests
for hr=1:4
hr;
O1l=(o-ocons)*R*Tt/KH; % concentration of oxygen
Mol/cm3 of water
O1=O1l*w1/10^6;
if ilim<0
ilim=0;
else
icorr=min(icorr1,ilim);
end
jFe2=icorr/(nFe*F); %mol/cm2*s
jFe3=krate*jFe2; %mol/cm2*s
delta1=delta1+jFe2*6*AFe*(60*60)/ro; %cm
delta2=delta2+(3.75*(jFe2-jFe3)*AFe*6*(60*60))/(ro*Kperssure); %cm

```

```

delta3=(delta3)+(4.20*jFe3*AFe*6*(60*60))/(ro*Kperssure); %cm
ocons=ocons+jFe3*(60*60)*6/(4*delta*100);
rustthickness=delta3+delta2-delta1-delta0;
rustthickness1=delta3+delta2-delta0;
straint=(rustthickness)/(d*100+rustthickness);
strainr=((rustthickness)/(delta*100))+(poisson*straint);
Pinr=(2*0.95*Pcrit*((strainr)/strainr0))/(1+((strainr)/strainr0)^2) %Mpas
Pfinal=Pinr;
P0=p0-(Pfinal)*P10;
%%%%%%%%%%%%%%
bi=(daycor-1)*24+hr*6;
bi;
if icorr>0
[outp,p]=pressure(1,bi,P0,p1,no); %Diffusion of rust in
concrete
ps=p(end,:);
sat=((ps/Mm).^(1/(1-m))+1).^(-m))-sat0;
Sat=mean(sat(:,1:matrix size));
VofFe3out=(Vp*0.3)*(Sat)*Vcon;
if VofFe3out<=0;
VofFe3out=0;
end
delta00=sqrt((delta2+(d*50-delta1)+delta3)^2-(VofFe3out/pi));
delta0=(delta2+(d*50-delta1)+delta3)-delta00;
else
delta0=delta0;
end
strainrout=delta0/(delta*100);
Poutr=(2*0.95*Pcrit*((strainrout)/strainr0))/(1+((strainrout)/strainr0)^2)
ilim=no2*F*Dor*(O1)/(delta2-delta0);
oi=0;
rustthicknesshist1=[rustthicknesshist1;rustthickness1];rustthicknesshist=[rustthicknesshist;rustthickness];pshist=[pshist;p1];p1hist=[p1hist;p1];dayhist=[dayhist;day];icorr1hist=[icorr1hist;icorr1];ilimhist=[ilimhist;ilim];delta3hist=[delta3hist;delta3];delta2hist=[delta2hist;delta2];delta1hist=[delta1hist;delta1];delta0hist=[delta0hist;delta0];
Pinrhist=[Pinrhist;Pinr];Poutrhist=[Poutrhist;Poutr];strainrhist=[strainrhist;strainr];strainrouthist=[strainrouthist;strainrout];oconshist=[oconshist;ocons];O1hist=[O1hist;O1];icorrhist=[icorrhist;icorr];
if Pfinal>Pcrit %
break
end
if Pfinal>Pcrit
break
end
end
end

```

```

monthhist=[monthhist,ai];clhist=[clhist;cl(end,1)];olhist=[olhist;ol(end,1)];clohrhist=[cl
ohrhist,clohr];
end
if Pfinal>Pcrit
    break
end
end
if Pfinal>Pcrit
    break
end
end
if Pfinal>Pcrit
    break
end
end

```

Diffusion of Chloride Subroutine

```

function [outcl,solcl]=chloride(geom,tmax)
% -----

    nt=4; %each time step is one day
    x=linspace(0.5,thickness,150);
    t=linspace(0,tmax,tmax);
    solcl=pdepe(geom,@pdefun,@icfun,@bcfun,x,t);
    outcl.x=x;
    outcl.t=t;
    outcl.solcl=solcl;

%semilogx(t,solcl(:,1),'-o');figure(gcf)

% -----
function [c,f,s] = pdefun(x,t,u,DuDx)
    % Here, u is the concentration to avoid confusion with c.
    dcl=2.5606e-008;
    wcement=358000;
    w1=75263;
    alfa=4.2;
    c=1;          % c is a coefficient of DcDt

    D=((dcl)/(1+((alfa*(wcement/100)*(35.5*w1/1000))/((1*(35.5*w1)/1000)+(3.2*(u*(453.
    59237/(1.6387064E-5))))^2))))*0.155*24*60*60;          % Concentration-dependent
    diffusion coefficient with lots of unit converting
    f=D*DuDx;      % f is a flux expression
    s=0;           % s is the source term

```



```
end %pdefun
```

```
% -----  
function c0=icfun(x)
```

```
    c0=0;    % c=0 everywhere initially
```

```
end %icfun
```

```
% -----  
function [pl,ql,pr,qr] = bcfun(xl,cl,xr,cr,t)
```

```
    % BC's defined as  $p + q \cdot f = 0$  at both boundaries
```

```
    pl = 0;    % On left side ( $x=0$ )  $f=D \cdot Dc/Dx=0$   
    ql = 1;
```

```
    pr = cr- Chloride Boundary Condition depending on case;    % On right side  
    (x=1) c=1; gr/cm3  
    qr = 0;
```

```
end %bcfun
```

```
end %main
```

Diffusion of Oxygen Subroutine

```
function [outo ,solo]=oxygen(geom,tmax,oin)  
% -----
```

```
    nt=4;  
    x=linspace(0.5,thickness1,150);  
    t=linspace(0,tmax,tmax);  
    %t=[0,logspace(-3,0,nt-1)]*tmax;  
    solo= pdepe(geom,@pdefun,@icfun,@bcfun,x,t);
```

```
    outo.x=x;  
    outo.t=t;  
    outo.solo=solo;
```

```
    %semilogx(t,solo(:,1),'-o');figure(gcf)
```

```
% -----  
function [c,f,s] = pdefun(x,t,u,DuDx)
```

```

% Here, u is the concentration to avoid confusion with c.

c=1;          % c is a coefficient of DcDt
D=0.508/(365*24); % Concentration-dependent diffusion coefficient in2/hr
f=D*DuDx;     % f is a flux expression
s=0;          % s is the source term

end %pdefun

% -----
function c0=icfun(x)

c0=oin;       % c=0 everywhere initially

end %icfun

% -----
function [pl,ql,pr,qr] = bcfun(xl,cl,xr,cr,t)

% BC's defined as  $p + q*f = 0$  at both boundaries

    pl = 0;      % On left side ( $x=0$ )  $f=D*DcDx=0$ 
    ql = 1;

    pr = cr-Oxygen Boundary Condition Depending on Case; % On right side
    (x=1) c=1;
    qr = 0;

end %bcfun

end %main

```

Diffusion of the Rust Subroutine

```

function [outp,solp]=pressure(geom,tmax,pbc,pin,n)
% -----
    pbc=pbc;
    nt=4; %each time step is one day
    x=linspace(0.5,thickness,150);
    t=linspace(0,tmax,tmax);
    solp= pdepe(geom,@pdefun,@icfun,@bcfun,x,t);

    outp.x=x;
    outp.t=t;
    outp.solp=solp;

```

```

%semilogx(t,solp(:,1),'-o');figure(gcf)

% -----
function [p,f,s] = pdefun(x,t,u,DuDx)

    % Here, u is the concentration to avoid confusion with c.
    m=0.46;
    Mm=5444.75;
    k=0.0124/(365*24);
    alpha=0.7;
    wcr=0.5;
    Vp=((wcr-0.36*alpha)/(wcr+0.32));
    kp1=k/(Vp*0.3*n*0.06785);
    p=1;          % p is a coefficient of DcDth
    D=kp1/(m*(((u/Mm)^(1/(1-m))+1)^(-1-m)*((u)^((1/(1-m))-1)/(((m-1))*Mm^(1/(1-
m)))))); % Concentration-dependent diffusion coefficient cm/day
    f=D*DuDx;    % f is a flux expression
    s=0;         % s is the source term

end %pdefun

% -----
function p0=icfun(x)

    p0=pin;      % p=0 everywhere initially

end %icfun

% -----
function [pl,ql,pr,qr] = bcfun(xl,cl,xr,cr,t)

    % BC's defined as  $p + q*f = 0$  at both boundaries

    pl = 0;      % On left side (x=0)  $f=D*DcDx=0$ 
    ql = 1;

    pr = cr-pbc; % On right side (x=1)  $c=1$ ;
    qr = 0;

end %bcfun

end %main

```

REFERENCES

- Ababneh, A., Benboudjema, F., and Xi, Y. (2003). "Chloride Penetration in Nonsaturated Concrete," *Journal of Materials in Civil Engineering*, ASCE, Vol. 15, No. 2, pp. 183-191.
- Ahmad, S. (2003). "Reinforcement Corrosion in Concrete Structures, its Monitoring and Service Life Prediction- A Review." *Cement and Concrete Composite*, Vol. 25., pp. 459-471
- Allan, M.L. (1995). "Probability of Corrosion Induced Cracking in Reinforced Concrete." *Cement and Concrete research*, Vol. 25, No. 6, pp. 1179-1190.
- Applied Instrument Group, (2002). *Princeton Applied Research, Basics of Corrosion Measurement*. Princeton, NJ.
- ASTM (2002). "Standard Practice for Preparing, Cleaning, and Evaluating Corrosion Test Specimens." *ASTM Designation: G 1-90*, pp. 9-15.
- ASTM (2008). "Standard Specification for Carbon Structural Steel." *ASTM Designation: A 36/A36M-05*.
- Baluch M. H., Rahman M. K., Al-Gadhib, A. H., (2002). "Risks of Cracking and Delamination in Patch Repair." *Journal of Materials in Civil Engineering*, July/August, 294-302.
- Barneyback, R. S., Diamand, S. (1981). "Expression and Analysis from Pore Fluids from Hardened Cement Paste and Mortars." *Cement and Concrete Research*, vol. 11, pp. 279-285.
- Baiyasi, I. M., and Harichandran, R. S.(2001). "Corrosion and Wrap strains in Concrete Bridge Columns Repaired with FRP Wraps," *Proceedings (CD-ROM), 80th Annual Meeting of the Transportation Research Board*, Washington, D.C., Paper No. 01-2609.
- Bazant, Z. P., Najjar, L. J. (1972). "Nonlinear Water Diffusion of Nonsaturated Concrete." *Materiaux et Constructions*, 5 (25).
- Bazant, Z. P. (1979). "Physical Model for Steel Corrosion in Sea Structure-Application," *Journal of Structural Division, ASCE*, Vol. 105, pp. 1155-1166.
- Bazant, Z., and Thonguthai, W. (1979). "Pore Pressure in Heated Concrete Walls: Theoretical Prediction." *Magazine of Concrete Research*, Vol. 31, No. 107, pp. 67-76.

- Bazant, Z., Thonguthai, W. (1978). "Pore Pressure and Drying of Concrete at High Temperature." *Journal of the Engineering Mechanics Division*, pp. 1059-1079.
- Batis, G., and Routoulas, T. (1999). "Steel Rebars Corrosion Investigation with Strain Gages." *Cement and Concrete Composites*, Vol. 21, no. 3, pp. 163-171.
- Berke, S. N., and Hicks, C. M (2004). "Predicting Long Term Durability of Steel Reinforced Concrete with Calcium Nitrite Corrosion Inhibitor." *Journal of Cement and Concrete Composite*, Vol. 26, pp. 191-198.
- Berkeley, K. G. C., and Pathmanaban, S., (1987). "Practical Potential Monitoring in the Concrete." UK CORROSION '87, Brighton, U.K, Oct, 115-131.
- Beaudette, M.R, (2001). "Investigation of Patch Accelerated Corrosion with Galvashield Xp." *Interim Report*.
- Bertolini, L., Elsener, B., Pedferri, P., and Polder, R. B. (2004). "Corrosion of Steel in Concrete." *Transport Processes in Concrete*, WILEY-VCH Verlag GmbH & Co. KGaA.
- Bhagava, K., Ghosh, A.K., Mori, Y, and Ramanujam (2005). "Modeling of Time to Corrosion-Induced Cover Cracking in Reinforced Concrete Structures" *Journal of Cement and Concrete Research*, Vol. 35, pp. 2203-2218.
- Browning J., (2007). "Effect of Cracking on Chloride Content in Concrete Bridge Decks." *Proceedings, 86th Annual meeting of the Transportation Research Board*, Washington DC.
- Bournazel, J. P., and Moranville, M. (1997). "Durability of Concrete: The Crossroad between Chemistry and Mechanics." *Cement and Concrete Research*, Vol. 27, No. 10., pp. 1543-1552.
- Boulfiza, M., Sakai, K., Banthia, N., and Yoshida, H. (2001). "Prediction of Cracking Effect on the Penetration of Chloride Ions in Reinforced Concrete."
- Boyar, B., Warren, C., Somayaji, S., and Heidersbach, R. (1990). "Mechanism of Corrosion of Steel in Concrete." *Corrosion Rates for Steel in Concrete ASTM SPT 1065*.
- Broomfield J. P. (1996) "Field Measurement of the Corrosion Rate of Steel in Concrete Using a Microscope Controlled Unit with a Monitored Guard Ring for Signal Confinement." *Techniques to Assess the Corrosion Activity of Steel Reinforcement Concrete Structure*. ASTM, STP 1276
- Caddy, P. D., and Weyers, R. E. (1983). "Chloride Penetration and Deterioration of Concrete Bridge Decks." *Cement, Concrete, and Aggregate*, Vol. 5, No. 2, pp. 81-87.

Carassiti, F., Proverbio, E., and Valente, T., (1991). "Corrosion State Evaluation of Steel in Concrete by Receptivity and Polarization Resistance Measurement." *Electrochemical Methods in Corrosion Research, Proceeding of 4th International Symposiums*, Espoo, Finland, July, pp. 647-658.

Castellote M., Alonso C., Andrade C., Chadbourn G.A., Page C.L., (2001). "Oxygen and Chloride diffusion in Cement Pastes as a Validation of Chloride Diffusion Coefficients Obtained by Steady-State Migration Test." *Cement and Concrete Research*, Vol. 31, pp. 621-625.

Christensen, R. M. (1979). *Mechanistic of Composite Material*. Wiley, New York.

Collepordi, M., Marcialis, A., and Tuniziani, R. (1972). "Penetration of Chloride Ions into Cement Paste and Concrete." *Journal of American Ceramic Society*, Vol. 55, pp. 534-535.

Costa, A., and Appleton, J. (1998). "Chloride Penetration into Concrete in Marine Environment - Part I: Main Parameters Affecting Chloride Penetration." *Materials and Structures/MaMriaux et Constructions*, Vol. 32, pp. 252-259.

Coussy, O., Dangla, P., T. Lassabatere, T., and Baroghel-Bouny, V. (2004). "The Equivalent Pore Pressure and the Swelling and Shrinkage of Cement-Based Materials." *Materials and Structures / Concrete Science and Engineering*, Vol. 37, pp 15-20.

Crnot, A., Frateur, I., Marcus, P., and Tribollet, B., (2002). "Corrosion Mechanism of Steel Concrete Moulds in the Presence of Demolding Agent." *Journal of Applied Electrochemistry*, pp 865-869.

Du, Y.G., Chan, A. H. C. and Clark, L.A (2006). "Finite Element Analysis of the Effects of Radial Expansion of Corroded Reinforcement." *Computers and Structures*, Vol. 84, No. 13-14, pp. 917-929.

Elsener, B., and Bohini, H., (1991). "Electrochemical Methods for Inspection for Reinforcement Concrete Structure –Field Experience." *Electrochemical Methods in Corrosion Research, Proceeding of 4th International Symposiums*, Espoo, Finland, July , pp. 635-646.

El Maaddawy, T., Chahrou, A., Soudki, K.(2006) "Effect of Fiber Reinforced Polymer Wraps on Corrosion Activity and Concrete Cracking in Chloride-Contaminated Concrete Cylinders." *Journal of Composites for Construction, ASCE*, April, Vol. 10, No. 2, pp. 139-147.

El Maaddawy T, Soudki, K, (2007) "A model for Prediction of Time from Corrosion Initiation to Corrosion Cracking." *Cement & Concrete Composites* 29, pp. 168–175.

Fasullo, E. J. (1992). "Infrastructure: The Battlefield of Corrosion, Corrosion Forms and Control for Infrastructures, ASTM STP 1137, pp. 1-16.

Glass, G.K., Buenfeld, N.R. (2000). "The Influence of Chloride Binding on the Chloride Induced Corrosion Risk in Reinforced Concrete." *Journal of Corrosion Science*, Vol. 42, pp. 329-344.

Glass, G. K., Stevenson, G. M., Buenfeld, N. R., (1998). "Chloride-Binding Isotherm from Cell Test." *Cement and Concrete Research*, Vol. 28, No. 7, pp. 939-945.

Harichandran, R. S., and Nossoni, G.(2008). "Improved Shallow Depth Patches for Concrete Structures." *Report No. RC-1502*, Michigan Department of Transportation, Lansing, Michigan.

Hartt, W.H. (1979). "Laboratory Method for Corrosion Testing of Reinforce Concrete using Impressed Current." *Corrosion*, No 133.

Hope, B. B., Ip, A. K., and Manning , D., (1985). "Corrosion and Electrical Impedance in Concrete." *Cement and Concrete Research*, Vol. 15, pp.525-534.

Jones, D. A. (1992). *Principles and Prevention of Corrosion*. Macimillan, New York

Lee, C.; Bonacci, J. F., Thomas, M.D.A., Maalej, M., Khajehpour, S., Hearn, N., Pantazopoulou, S., and Sheikh, S.(2000) "Accelerated Corrosion and Repair of Reinforced Concrete Columns using Carbon Fiber Reinforced Polymer Sheets." *Canadian Journal of Civil Engineering*, Oct, pp. 941-948.

Liang, M. T., Jin, W. L., Yang, R.J., and Huang, N. (2005). "Predeterminate Model of Corrosion Rate of Steel in Concrete." *Cement and Concrete Research*, Vol. 35, pp. 1827–1833.

Kassir, K. M., and Ghosn, M. (2002). "Chloride-Induced Corrosion of Reinforced Concrete Bridge Decks," *Cement and Concrete Research*, Vol. 32, pp. 139–143.

Kobayashi, K., and Shuttoh K. (1991). " Oxygen Diffusion of Various Cementitious Materials." *Cem. Concr. Res.*, vol. 21, pp. 273-284.

Liu, Y., (1996). "Modeling the Time to Corrosion Cracking of the Cover Concrete in Chloride Contaminated Reinforced Concrete Structure." *Doctoral Thesis*, Virginia Polytechnic Instituted, Blackburg, VA.

MacGregor, J. G., and Wight, K. J (1997). *Reinforced Concrete: Mechanics and Design*. Prentice-Hall, New Jersey.

Metha, P. K. (1993). *Concrete Structure, Properties and Materials*. Prentice-Hall, New Jersey.

Mindess, S. Young, J. F., and Darwin, D. (2003), *Concrete*. Second Edition, Prentice Hall, New Jersey.

Morinaga, S. (1989). "Prediction of Service Lives of Reinforced Concrete Building Based on Rate of Corrosion of Reinforcing Steel." Special Report of the Institute of Technology, Skimiza Corporation, Japan.

Monlouis, J.P, Verdier, J., and Perrin, B. (2004). "Predication of the Relative Permeability to Gas Flow of Cement-Based Materials." *Journal of Cement and Concrete Research*, Vol. 34, pp. 737-744.

Neville, A. M. (2000). *Properties of Concrete*, Fourth Edition, Prentice-Hall, New Jersey.

Newhouse, C. D., and Weyers, R. E. (1996). "Modeling the Measured Time to Cracking." *Corrosion Activity of Reinforced Concrete Structure*, In ASTM STP 1276, pp. 3-21.

Newhouse, C. D. (1993). "Corrosion Rates and the Time to Cracking Model for Critically Contaminated Reinforced Concrete Structure." *Master of Science Thesis*, Virginia Polytechnic Instituted, Blackburg, VA.

Nossoni, G., and R.S. Harichandran, (2007). "Improved Durability of Patched Concrete Bridges against Corrosion by using an FRP Overlay." *Proceedings (CD-ROM), 86th Annual Meeting of the Transportation Research Board*, Washington, D.C..

Page,C.L., and Treadaway K. W. J (1982). "Aspect of the Electrochemistry of Steel in Concrete." *Nature*, Vol. 297, pp. 109-115.

Page, C. L., Short, N. R., and El Tarras, A. (1981). "Diffusion of Chloride Ions in Hardened Cement paste." *Cement and Concrete Research* vol. 11 (3), pp.395-406.

Palle, T. C. (2002). "Deterioration of Concrete Structures." *Proceedings*, First Kassir, K. M., and Ghosn, M. (2002). "Chloride-Induced Corrosion of Reinforced Concrete Bridge Decks," *Cement and Concrete Research*, Vol. 32, pp. 139-143.

Pantazopoulou, J., and Papoulia, K. (2001). "Modeling Cover-Cracking due to Reinforcement Corrosion in RC Structures." *Journal of Engineering Mechanics*, Vol. 127, No. 4, pp.342-451.

Peterson, J. E. (1993). "A Time to Cracking Model for Critically Contaminated Reinforced Concrete Structure." *Master of Science Thesis*, Virginia Polytechnic Instituted, Blackburg, VA.

Pourbiacx, M. (1976). *Atlas of Electrochemical Equation in Aqueous Solutions*. Pergamon, London

Sarin, P., Snoeyink, V. L., Lytle, D. A., and, Kriven, W. M. (2004). "Iron Corrosion Scale: Model for Scale Growth, Iron Release, and Colored Water Formation." *Journal of Environmental Engineering, ASCE*, pp. 364-373.

Shah, S. P., and Swart, S. E. (1987). *Fracture of Concrete and Rocks*. Springer-Verlag, New York

Speller, F. (1951). *Corrosion*. McGraw-Hill London

Stearn, M., and Greay A., L., (1957). "Electrochemical Polarization No.1: The Theoretical Analysis of the Shapes of Polarization Curve." *Journal of Electrochemical Society*, Vol. 104, pp. 56-64.

Tang, L. (1999). "Concentration Dependence of Diffusion and Migration of Chloride Ions- Part 2. Experimental Evaluations." *Cement and Concrete Research*, Vol. 29, No. 9, pp. 1469–1474.

Thangavel, K., and Rengaswamy, N.S. (1998). "Relationship between Chloride/Hydroxide Ratio and Corrosion Rate of Steel in Concrete." *Cement and Concrete Composite*, Vol. 20, pp. 283-292.

Timoshenko, S., and Goodier, J. N. (1959). *Theory of Elasticity*. McGraw-Hill, New York.

Tomoshov, N. D. (1966). *Theory of Corrosion and Protection of Metals*. McMillan Co., New York.

Townsend, H. E., Cleary H. J., Allegra L. (1981). "Breakdown of Oxide films in Steel Exposure to Chloride Solutions." *Corrosion - NACE*, Vol. 37, pp. 384-391.

Tuutti, K. (1982). "Corrosion of Steel in Concrete." *Swedish Cement and Concrete Research Institute*, Stockholm.

Van Genuchten, M. Th. (1980). "A Close Form Equation for Predicting the Hydraulic Conductivity of Unsaturated Soils." *Journal of the Soil Science Society of America*, pp. 892-898.

Verbeck G. J. (1975). "Mechanism of Corrosion in Concrete." In *Corrosion of Metals in Concrete*, ACI SP-49.

Wang, X. M. and Zhao, H.Y. (1993). "The Residual Service Life Prediction of R.C. Structures. In *Durability of Building Materials and Components 6*, S. Nagataki *et al.* E & FN Spon, pp. 1107–1114.

Winston Revie, R. (2000). *Uhlig's Corrosion Handbook*. Second Edition. Wiley, New York.

Xi. Y., (1994). "A Model for Moisture Capacities of Composite Materials Part II: Application to Concrete." *Computational Materials Science*, p.p. 78-92.

Yoshiki, T., Hirotaka, K., and Hiroshi, W., (2001). "Study a Required Cover Depth of Concrete Highway Bridge in Coastal Areas." *17th U.S.-Japan Engineering workshop*, Tsukuba, pp. 1-16.